Precision Delivery of Multi-Scale Payloads to Tissue-Specific Targets in Plants

by

Yunteng Cao

B.Eng. Engineering Mechanics, Shanghai Jiao Tong University (2013)
M.Eng. Solid Mechanics, Xi'an Jiaotong University (2016)

Submitted to the Department of Civil and Environmental Engineering
in partial fulfillment of the requirements for the Degree of

Doctor of Philosophy

in Civil and Environmental Engineering

at the

MASSACHUSETTS INSTITUTE OF TECHNOLOGY

September 2022

Signature of Author ……...
Department of Civil and Environmental Engineering
August 10, 2022

Certified by ……...
Benedetto Marelli, Ph.D.
Associate Professor of Civil and Environmental Engineering
Thesis Supervisor

Accepted by……...
Colette L. Heald, Ph.D.
Professor of Civil and Environmental Engineering
Chair, Graduate Program Committee

Precision Delivery of Multi-Scale Payloads to Tissue-Specific Targets in Plants

by
Yunteng Cao

Submitted to the Department of Civil and Environmental Engineering on August 10, 2022
in partial fulfillment of the requirements for the degree of
Doctor of Philosophy in Civil and Environmental Engineering

Abstract

Agrochemicals delivery is of crucial importance in modern agriculture to ensure the healthy growth of crops and productivity, therefore food security, particularly under current pressures, including escalating growing conditions associated with climate change (e.g., extreme weather, the spread of plant diseases and pests, lower soil quality), an ever-increasing human population, scarcity of arable land, and limited resources. However, conventional practices suffer from low efficiency and significant payload loss to the environment, conflicting with societal and environmental sustainability requirements. Therefore, there is a dire need for new techniques for precise, efficient delivery.

This thesis studies the use of biomaterials and drug delivery principles to engineer the precise deployment of payloads in plants. Specifically, the thesis designs a novel silk-based biomaterial and fabricates a microneedle-like device capable of delivering a variety of payloads ranging from small molecules to large proteins into specific loci of various plant tissues. Precisely sampling plant sap is also demonstrated by tuning the material composition. Silk-based microneedles further show minimal wounding responses, activation of gibberellic acid (GA_3) responses post-injection of GA_3-loaded microneedles, and promotion of bolting and inhibition flower formation by GA_3 on *Arabidopsis thaliana* mutant *ft-10*. This method is proved to be more efficient and effective in delivering GA_3 than foliar spray. Potential applications of silk-based microneedles in agriculture are also confirmed by the successful deployment of GA_3 in several crops. In addition, hollow microneedles are fabricated using silk fibroin assembly and inorganic nucleation at their phase fronts, providing new tools to bridge the biotic/abiotic interface by interrogating pathways for biomolecules transport in plants and enabling early-stage detection of bioaccumulation of environmental contaminants, such as cadmium and arsenic.

Thesis Supervisor: Benedetto Marelli
Title: Associate Professor of Civil and Environmental Engineering

Acknowledgements

It is a great honor for me to study and research in a CEE doctoral program at MIT. Full of happiness, I am getting my doctoral degree. I want to thank all the people who helped me be here and the people I worked with.

Many thanks to my advisor Professor Benedetto Marelli. He guided and encouraged me in research as I navigated through the highly interdisciplinary journey related to biomaterials, plants, and agriculture with a mechanical engineering background. He provided great support during the darkest period in my life. I am deeply thankful for the kindness, patience, support, and advice Benedetto has offered for my research and my own career development as a researcher.

I would also like to thank Professor David L. Des Marais and Professor Darrell J. Irvine for serving on my thesis committee. Their expertise and insights are very helpful in adjusting my research plan, technique troubleshooting, and completing my program. I am very grateful for the opportunity to visit the group of Professor Nam-Hai Chua in Singapore, and I thank Professor Chua for his support and mentoring.

Many thanks to Roberta Pizzinato, Kathleen Briana, Kiley Clapper, and Sarah Smith for their mental support, which is essential for my research and life. Their smiling is so impressive and contagious. I would also thank the logistical support from Roby and CEE headquarter. Particularly, I want to thank Stephen Rudolph, the magic, legendary engineer, for his technical support for my research, from microneedle fabrication to lab instrument installation.

I definitely could not have done this without the support of my friends. Thanks to those who helped me be here – Benhua Zhu, Xiaobo Gong, Xi Chen, Yilun Liu, Youlong Chen, Yongmei Zhang, Xiaobin Deng, Jialv Zhou, Liangliang Zhu, and many others. Thanks to my colleagues - Eugene Lim, Doyoon Kim, Sally Shuxian Koh, Kathleen Cormier, Augustine Zvinavashe, Pil Joong Chung, Tao Yao, Hui-Zhu Mao, Nicole Bohn, Benedetta Petracca, Anita Mollo, Muchun Liu, Yue Hu, Zeina Barghouti, Haruka Sakurai, Yangyang Han, Raju Cheerlavancha and many others - for your invaluable help in research. Thanks to my friends I met here –, Guiyin Xu, Menglong Xu, Jiawei Xu, Yongji Wang, Huijun Chen, Shi Kuang, Xiaoming Li, Xiaoyu Chen, Chengxi Li, Yi Jia, and many others - thank you all for making my time here so enjoyable.

Most importantly, I would like to thank my parents and my brother for everything they have done for me, particularly my mom; she is always with me. Their unconditioned love, encouragement, and support made me who I am today.

Lastly, I am grateful for the financial support from Singapore-MIT Alliance for Research & Technology, National Research Foundation, Prime Minister's Office, Singapore under its Campus for Research Excellence and Technological Enterprise (CREATE) program and Abdul Latif Jameel Water and Food Systems Lab (J-WAFS).

This thesis is dedicated to my family.

Table of Contents

List of Figures

List of Tables

Chapter 1 Introduction

Part of the contents in this chapter was in preparation as: Yunteng Cao [1] and Benedetto Marelli [1,*]

Department of Civil and Environmental Engineering, Massachusetts Institute of Technology, 77 Massachusetts Avenue, Cambridge, 02139, MA. United States.

"Precise payload delivery into plants"

Part of the contents in this chapter was published in the Advanced Functional Materials as: Hui Sun [1], Yunteng Cao [1], Doyoon Kim [1] and Benedetto Marelli [1,*]

Department of Civil and Environmental Engineering, Massachusetts Institute of Technology, 77 Massachusetts Avenue, Cambridge, 02139, MA. United States.

"Biomaterials Technology for AgroFood Resilience." Published, Advanced Functional Materials, 2201930, May 12, 2022. DOI: 10.1002/adfm.202201930

2.2. Precision Payload Delivery to Plants and part of 2.3. Summary and Outlook in the review were written by Yunteng Cao and reproduced here.

1.1 Payload Delivery to Plants in Agriculture

The population is projected to be 9.7 billion by 2050, indicating a ~70% increase in food demand.[1] However, there are grand limitations on agricultural productivity resulting from resource deficiency and abiotic/biotic stresses. For example, 30-60% of arable lands undergo quality decline.[2] Agriculture used almost 70% of extracted water (~2.8 trillion cubic meters) and has caused water deficiency worldwide, particularly in water-scarce areas such as the Middle East-Western Asia.[2] To address these limitations, two main strategies have been deployed, i.e., a) enhancing crops' yield and resistance to stresses and b) providing a suitable environment for crops. The former relates to gene operation, evolving from traditional crossbreeding to plant genetic engineering that enables precise addition, deletion, and modification of target genes. It requires the delivery of specific genetic payloads and carriers to target plant cells and organelles.[3] The latter strategy involves the application of agrochemicals, including fertilizers containing macronutrients and micronutrients, protectors against biotic stresses (e.g., pesticides, herbicides, antibiotics), and plant growth regulators and stimulants facilitating plants' growth and development. It requires the

delivery of agrochemicals onto and into plant tissues. While no available data quantifies genetic payloads used for breeding due to the relatively small scale, modern agriculture relies heavily on agrochemicals. For example, demand for macronutrients fertilizers (nitrogen, phosphorus, and potassium) was estimated to be 184 million tons in 2015 and reach 201 million tons in 2020.[4] The global market for micronutrients is estimated at USD 4.3 billion in 2022 and projected to be USD 6.4 billion by 2027.[5] The global pesticide usage was estimated to increase up to 3.5 million tons by the end of 2019.[6] The demand for antibiotics, gibberellic acid, auxin, and stimulants are also increasing.[7]

Genes associated with desired traits have been introduced by crossbreeding for thousands of years, which requires little human manipulation and is time-consuming and limited to species without reproductive isolation. After recognition of specific genes, a plethora of methods, such as the commonly used bombardment, electroporation, Agrobacterium-mediated delivery, and polymer-mediated delivery, have been developed to deliver genes as well as other genetic cargos.[8] However, these methods are mainly suitable for protoplasts and explants, requiring time-consuming, complex tissue culture and showing low efficiency. Agrobacteria can deliver genetic payloads to leaf cells and flowers in intact plants but are limited to host species.[8] Currently, nanomaterials have attracted considerable attention and demonstrated successful delivery of genetic payloads to intact plants and plant species independence, circumventing drawbacks of conventional delivery methods and showing the potency of a versatile carrier in plant engineering.[3,8,9] Unfortunately, nanomaterials are delivered mainly via foliar infiltration, whose target tissue is limited to leaves of intact plants. Interestingly, nanomaterials have also demonstrated utility in imparting organelles with new and enhanced functions, termed plant nanobionics,[10] and in the detection and monitoring

of signaling molecules in plants as nanosensors.[11] These emerging and promising functional nanomaterials were also delivered by foliar infiltration, which hinders their wide applications.[10-13] On the other hand, the heavy application of agrochemicals since the green revolution employs plants' evolved pathways for material uptake, categorized by the applied tissues as root application, stem application (i.e., trunk/petiole injection), and foliar application.[14] The root is the primary tissue of most crops physiologically used to take up water and minerals, which is therefore employed in the delivery of water, fertilizers for macronutrients and micronutrients, and pesticides. Stem application mainly employs the xylem of vasculature, the pathway transporting water and minerals from root to canopy. An external reservoir is typically connected to vasculature after the mechanical removal of primary barriers (e.g., bark). Leaves have the largest surface area, are readily accessible, and are the main pathway for transpiration and gas exchange. Foliar spray, therefore, is proposed. Foliar infiltration is also based on the leaf structure for transpiration and gas exchange, i.e., stomata. However, the evolved pathways are specially built for plants' physiology and those involved compounds, not for exogenous materials. The selectivity of these pathways rendered by the tissue barriers (e.g., Casparian strip, cuticles) and tissue structures (e.g., fewer stomata on the adaxial side of a leaf) result in limited permeability of payloads and pathetically low delivery efficiency. For example, more than 70% of the nanoparticles are blocked by the cuticle.[14,15] Nanomaterials requiring systemic transportation further undergo blockage due to perforation plate, pit membrane, and sieve plate. In addition, these practices have intrinsic drawbacks, further lowering delivery efficiency. In foliar spray, payloads will undergo high off-target application (30-40% by careful application),[14] quick degradation in the sun (43.8% in natural sunlight 1 day for oxytetracycline), and quick run-off in the rain (67.2% in 2 minutes in 44 mm h^{-1} rain).[16] Nitrogen fertilizers applied by root application lose 50-70% in the environment.[17]

Nanoparticles applied to the soil can be taken up only at the order of 0.1%.[14] Trunk injection has significant payload loss to the pith under high pressure.[18] In addition, such agrochemicals leakage into the environment, particularly toxic compounds and minerals, has caused severe environmental issues such as biodiversity loss, soil salinity, eutrophication, and food safety and health concerns.[19] In sum, agrochemicals suffer from low delivery efficiency and, therefore, low utilization efficiency, besides other delivery method-specific drawbacks.

To increase the utilization efficiency and efficacy, great efforts have been made in precision agriculture, focusing on two fields, i.e., information collection and analysis and efficient payload delivery. Information collection and analysis are achieved via advances in detection, including soil sensors, plant wearables,[20] nanosensors,[11] and other portable detectors,[21] and progress in big data analytics, aiming to figure out plants' needs. Efficient payload delivery depends mainly on controlled and/or stimuli-responsive release of agrochemicals with integrated functions such as protecting liable payloads, increasing permeability across biological barriers, and enhancing adhesion on plants.[3] While these innovations significantly enhance the utilization efficiency, the aforementioned traditional methods are still used for delivering payloads onto/into plants; the innovations are experiencing poor delivery, for example, the 30-40% off-target in foliar application. Therefore, we found an opportunity to target specific tissues, particularly vasculature, for precise payload delivery, aiming to further enhance the utilization efficiency.

1.2 Current Efforts of Precision Payload Delivery to Plants

Precision delivery of agrochemicals that fulfills plant needs while avoiding run off and side effects to the environment is of great importance in agriculture to ensure high crop yields and at the same time minimize their environmental impacts. Besides, genetic cargos used in plant genetic engineering to introduce new traits, including DNA, RNA and CRISPR-Cas9, must be precisely delivered into plant cells or subcellular organelles in order for them to function properly. In this

regard, conventional delivery methods generally suffer from low efficiency, limited cargo types, damage to plant tissues, and specificity to a narrow range of plant species. Development of a more efficient, versatile and species-independent biomolecule delivery platform is therefore in urgent need. Current efforts for precision delivery to plants can be categorized in two domains – (i) precise cargo delivery into targeted tissues/organelles/vasculatures and (ii) optimization of cargo release profiles. The former focuses on spatial precision while the latter emphasizes temporal precision (i.e. sustained or on-demand release). Combination of spatial and temporal precision in delivering cargo molecules to plants is also emerging and represents the ultimate goal. In this sub-section, biomaterials-based precision delivery platforms for plants are first discussed, followed by an overview of strategies to optimize the release profiles of various agrochemicals.

1.2.1. Biomaterials-based precision delivery systems

Precision delivery systems refer to solutions facilitating cargo molecules delivery to targeted tissues through several barriers, including cuticle, epidermis, Casparian strip, plant cell wall, and membranes of the cell and organelles. Various strategies have been proposed to overcome tissue barriers, including loss of barrier function by mechanical or enzymatic damage, enhancement of permeability using chemical or electric treatments, developing carriers that can travel through tissue and cellular barriers, and designing devices that can reach target loci. Common delivery practices, such as trunk injection, foliar infiltration, vacuum infiltration, and bombardment, are not discussed here as priority is given to biomaterials-based precision delivery systems (e.g., microneedles and nanomaterials) and the roles of biomaterials to establish a material/plant interface.

1.2.1.1 Biomaterials-based microneedles

Biomaterials-based microneedles have been investigated for decades in biomedicine for transdermal and intradermal drug delivery and vaccination as an easily deployable, rapid, pain-

free method to overcome the drug delivery barrier imposed by the skin's outer stratum corneum layer[22-24]. Similar principles are now applied to plants, where the use of microneedles has been recently demonstrated. Although steel microneedles were proposed to increase bark permeability for agrochemical delivery[25] as used for medical applications, polymeric microneedles are now more investigated, given their versatile encapsulation of payloads and materials safety and sustainability. Cao et al. used silk fibroin extracted from *Bombyx mori* cocoons and its derivatives (i.e., proteins) to fabricate microneedles with controlled solubility in plant saps for material delivery and sampling (Figure 1.1a)[26]. The authors designed the microneedles according to the target tissue histological analysis. Therefore, they delivered small molecules, proteins, and bacteria to various plant tissues, such as xylem and phloem of tomato plants and leaves and meristem of tobacco, via punching through tissue barriers, including cuticles and epidermis (Figure 1.1b). This design principle for delivery precision differs from microneedles for transdermal drug delivery systems in medicine where microneedles do not target vasculature as the main motivation for microneedles is low invasiveness, pain free, and ease of application without the need of medical training. However, this design renders microneedles a similar role to steel needles for intravenous injection, which was considered impossible in plants due to anatomical and physiological constraints, such as the dimension of the vasculature and negative pressure in xylem. While trunk injection enables access to vasculature, it is time-consuming and invasive compared to applying a "sticker". Microneedles can also access meristem, a promising target locus for genetic engineering accessing stem cells, particularly for non-heritable and current generation genetic modification. The authors also showed that biopolymers-based microneedles are mechanically robust for plant tissue injection.

Isomalt, a small molecule made from sugar, was also used for precision delivery in a microneedle-like format. Fiorello et al. developed a microhook array by casting cargos and melted isomalt mixtures for precise delivery to leaf tissues (Figure 1.1c,d)[27]. They presented the small molecule delivery and mobility through the vascular tissue using a fluorescein-loaded isomalt array after injection onto *V. lambrusca* leaves. Such microhooks can easily lose features under environmental humidity due to the high affinity of isomalt to water, demanding protective post-treatment or specific storage conditions. Note that the high temperature (100 ºC) used during fabrication is unsuitable for temperature-sensitive and labile cargos.

Unlike the extensive research done in the biomedical field, using microneedles for precision delivery to plants is emergent, and its versatility is far from being fully unveiled. Combining advanced microneedle fabrication techniques (i.e., drawing, 3D printing, molding, and layer-by-layer fabrication) with rational modification of biomaterials (i.e., formation of micro/nano particles and functionalization of surface groups) will help narrow the research gap. In fact, most reported nanocarriers for plants were first delivered via foliar and vacuum infiltration to plant leaves and explants to circumvent most of the barriers. However, these laborious practices cannot be used in field and for non-leaf tissues *in vivo*.

1.2.1.2 Nanomaterials with desirable physiochemical properties

Nanomaterials provide time-controlled, target-specific, programmed, stimuli-responsive, and multifunctional drug delivery capabilities. Their applications in plant genetic engineering, agrochemical delivery, and consequent environmental impacts have been extensively reviewed[8,14,28-30]. Particularly intriguing is the possibility to deliver *in vivo* cargos (e.g., DNAs, RNAs, proteins, CRISPR/Cas9 complexes) to engineer plants and regulate their metabolic activity. Delivery to intact plant cells *in vivo*, compared to delivery to isolated protoplasts, is more attractive as it circumvents the laborious and time-consuming regeneration procedure and limitations in plant

species.

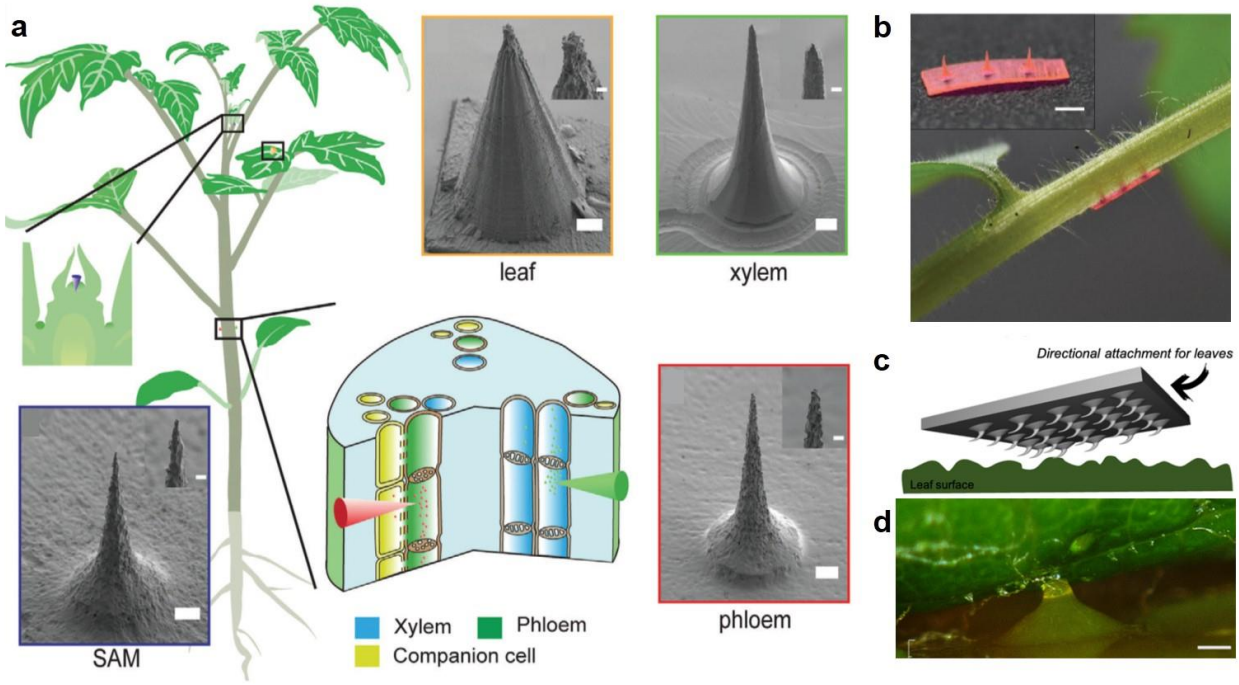

Figure 1.1. Microneedles for precision delivery. a) Scanning electron micrographs of silk microneedles (scale bar, 100 µm) designed for injection in shoot apical meristem (SAM), leaf, xylem, and phloem. The insets show the corresponding injector tips (scale bar, 20 µm). b) A tomato plant injected in the petiole by an array of microneedles loaded with rhodamine 6G. Scale bar of the top left image, 1 mm. Reproduced with permission[26]. Copyright 2020, Wiley-VCH. c) Microhook-based directional attachment system on leaves. d) Self-dissolving isomalt microhooks loaded with fluorescein interlocking with leaf surface. Scale bar, 200 µm. Reproduced with permission[27]. Copyright 2021, Springer Nature.

Size exclusion limit (SEL) is a key design factor for nanomaterials delivery into intact cells and organelles. SEL identifies the upper limit of a molecule size allowing its free transport through a biological membrane. The SEL of cuticle, Casparian strip, and plant cell wall are <10 nm, <1 nm, and 5-20 nm, respectively, even though nanoparticles up to 50 nm were reported to permeate cell wall in plants via unclear mechanisms. Indeed, studies on metallic nanoparticles have demonstrated that most nanoparticles applied via foliar spray are blocked/trapped by the cuticle. For example, >70% of the rod-shaped CeO_2 nanoparticles (~8 nm) were easily removed after spray[15], and 20–50 nm CuO nanoparticles aggregated to 230–400 nm agglomerates on lettuce leaf

after 2 h[31], and those reaching plant cells undergo poor dislocation[14,15,32]. Furthermore, the delivery efficiency does not significantly increase for nanoparticles inducing larger pores in cuticles (e.g., TiO_2 nanoparticles damage cuticles probably by photocatalytic properties)[32]. Similarly, nanomaterials suffer from low delivery efficiency via root application (~0.1% or less)[33]. Bombardment of biomaterials, including mesoporous silica and gold nanoparticles with large size (around 600 nm in diameter with 10 nm pores), was reported to deliver cargos to plant leaves[34]. However, these are only suitable for superficial tissues with thin barriers because of the particles' limited kinetic energy. Another strategy is exposing nanoparticles to plant cells directly with the assistance of foliar infiltration or via trunk injection. This strategy has been widely deployed to enable nanoparticles to circumvent the permeation through barriers with extremely small SELs, whereby nanoparticles cope with cell wall (SEL 5-20 nm) and membranes of the cell and organelles (SEL >500 nm).

Preparation and/or modification of nanomaterials with size below the SEL of cell wall is one path to precise delivery for plant, especially those have demonstrated successful delivery to mammalian cells and isolated plant cell protoplasts, for example, metallic/magnetic nanoparticles, carbon-based nanomaterials (e.g., fullerene, carbon nanotube, graphene), silicon-based nanoparticles (e.g., silica nanoparticle, mesoporous silica nanoparticle). These nanomaterials can be directly used for delivery to intact plant cells because they already meet all the SEL requirements. Of particular interest is carbon nanotubes which demonstrated extraordinary performances and versatility as a nanocarrier for biomolecules delivery to plants owing to their high aspect ratio, exceptional tensile strength, capability to protect biomolecules from cellular metabolism and degradation, and biocompatibility. Meanwhile, the potential applications of the referred nanomaterials raise safety concerns related to their environmental impacts, translocation and fate in plants and health

risks[35,36]. Policy makers are taking precautionary principles that may not be scientifically justified when making regulations. For instance, carbon nanotubes were added to the so-called SIN ('Substitute It Now') list of chemicals as a single substance category[37].

Natural inorganic materials and polymers have also been fabricated in nanoparticles formats to overcome such concerns and potential regulations due to their intrinsic nontoxicity. For example, Naqvi et al. produced calcium phosphate nanoparticles (size: 15–32 nm and zeta potential: -25.6 mV) to encapsulate a reporter gene and reached a transformation efficiency of ~80.7%[38]. The self-assembly of DNA molecules through Watson–Crick base pairing allows construction of various custom designed two- and three-dimensional nanostructures with accurately controlled size ranging down to 2.5nm, well below the SEL of the plant cell walls[39-41]. DNA nanostructures have also been used for drug, DNA, RNA, and protein delivery in animal systems[42,43]. These findings infer that DNA nanostructures may facilitate cargo delivery to intact plant cells. Zhang et al. systematically assessed different DNA nanostructures for their ability to internalize into leaf cells of tobacco, arugula, and watercress (Figure 1.2a)[39]. They reconfirmed that structural and mechanical properties (e.g., size, shape, compactness, and stiffness) of DNA nanostructures determine their internalization into intact plant cells, consistent with the results in mammalian cells[44]. Interestingly, they observed an abrupt decline in the internalization efficiencies between the 8.8- and 12.6-nm tetrahedrons, which suggested the SEL of the plant cell wall was less than 12.6 nm. As a functional molecular model, siRNA was hybridized to DNA nanostructures and delivered to leaves of transgenic mGFP5 *Nicotiana benthamiana*. Efficient gene silencing was achieved, ascertaining DNA nanostructures for cargo delivery to intact plant cells. Later studies found that the magnitude of the zeta potential of nanoparticles is another key factor in determining whether a particle can spontaneously penetrate the lipid membrane of cells and organelles[45,46].

Other natural biomaterials such as proteins[47], cellulose[48], and chitin[49] can also assemble into nanocrystals with size below the SEL of the plant cell wall and may be used as nanocarriers. The loading capacity of these nanocarriers however, may be limited due to their ultra-small size.

Fabricating pure polymeric nanoparticles with a uniform size below the SELs is challenging. Therefore, polymeric biomaterials are used to modify and functionalize other nanomaterials (e.g., silica, metal, carbon nanotubes) that can be easily fabricated and highly monodispersed. Modification of surface charge is one major strategy. For example, polycationic chitosan was used to form complexes with single-walled carbon nanotubes, enabling negatively charged plasmid DNA binding to the nanocarriers via electrostatic interactions[50]. Strano and colleagues proposed a mathematical model of the lipid exchange envelope and penetration (LEEP) mechanism for translocation through lipid bilayers based on their findings that particle size and the zeta potential are pivotal factors determining the particle trap within the organelle[45]. Surprisingly, the sign of the zeta potential has little influence in this process, although the lipid bilayer is negatively charged. In addition, the theory counterintuitively indicates that smaller nanoparticles require larger surface potentials to penetrate the lipid bilayer. Despite its assumptions and not dealing with cell wall, the LEEP model successfully predicted the ability or inability of various nanoparticles to penetrate the chloroplast. Modification of amphiphilicity, porosity, and morphology (aspect ratio) is likely to affect the interactions among cargos, nanoparticles, and cell wall and membranes, yet little has been reported. Still, concerns for safety related to nanomaterials applications in plants and crops and policy barriers are inevitable challenges for the deployment of nanomaterials technologies in drug delivery for plants.

1.2.1.3 Nanomaterials decorated with physiologically functional molecules

While many studies focus on relating the physicochemical properties of nanoparticles with their structure and function, the physiological roles of biomolecules and existing material translocation

mechanisms in cells and organelles are often neglected. Cell-penetrating peptides (CPPs), typically made with up to 30 amino acids, are the domains responsible for the rapid penetration of such peptides through plasma membrane. They have been used as a powerful tool to translocate and internalize a wide variety of cargos into mammalian cells[51-53] and isolated plant protoplasts[54-56], despite a lack of understanding of the exact mechanism. Their application is also expanding to payloads delivery to intact plant cells, *in vitro* and *in vivo*.

Lakshmanan et al. designed a peptide-based gene carrier consisting of a CPP (Bp100 or Tat_2) fused with a polycation (Figure 1.2b)[57]. The polycationic peptide interacts with negatively charged pDNA to form complexes, while the CPP transports the complexes into plant cells by penetrating the cell walls and plasma membranes. The carrier demonstrated rapid and efficient transient transfections into intact leaf cells of *Nicotiana benthamiana* and *Arabidopsis thaliana*. The fusion peptides demonstrated significantly higher transfection efficiency than the non-fused CPP peptides alone. It is noteworthy that the pDNA–peptide complex is around 300 nm in diameter and negatively charged. The same group also delivered double-stranded RNA into intact leaf cells of *Arabidopsis thaliana*, via this peptide-based gene carrier[58]. The dsRNA–peptide complex is 100–300 nm in diameter and weakly positively charged. Double-stranded DNA[59] introduction into intact *Nicotiana benthamiana* and protein delivery to rice callus[60] and *Arabidopsis thaliana*[61] were also demonstrated. Transfection behavior can be changed and controlled by selecting peptide-based gene carriers with appropriate amino acid sequences. For example, CPP structure and properties were optimized to facilitate DNA release from the polycation polymer via the formation of a bioreducible cyclic domain (Figure 1.2c)[62]. Combination of CPP with other existing carriers to impart/enhance desired properties was also reported. Cas9 ribonucleoprotein complexes[63] and enzymes[64] were successfully delivered to *Arabidopsis thaliana* callus and to the root hair cells of

Arabidopsis thaliana seedlings via a cell penetrating peptide--polyion complex vesicle, respectively. An artificial peptide, composed of cationic cell-penetrating and hydrophobic endosomal escape domains and CPP fusion peptide, enabled more efficient transfection of callus cells than the CPP fusion peptide alone[65]. Similarly, an endosome-escaping micelle, composed of plasmid DNA condensed with cationic peptides and dually modified with CPP and endosome-disrupting peptides, was reported to avoid endosomal entrapment and subsequent vacuolar degradation of the DNA cargo[66]. These results suggest the feasibility of superposition of functionality by adding components and structures.

CPPs alone enable non-specific delivery to cytosol, while more precise delivery targeting plastids such as chloroplasts and mitochondria is of great interest owing to the metabolisms occurring in these compartments. Incorporation of organelle-targeting biomolecules has been explored. Hurt et al. have shown that the first 12 amino acids of the yeast cytochrome c oxidase subunit IV pre-sequence were sufficient to direct dihydrofolate reductase into the mitochondrial matrix[67] and can be used as a mitochondria-targeting peptide. Using a combination of this mitochondria-targeting peptide (MTP) and cell-penetrating peptide (CPP), Chuah et al. reported the intracellular delivery of plasmid DNA to the mitochondria of Arabidopsis thaliana via negatively charged CPP_{KH}-MTP_{KH}-pDNA with hydrodynamic diameters of 160–280 nm[68]. Remarkable increases in transfection levels were observed compared to that of MTP_{KH}-pDNA complexes, indicating the critical internalization role of CPPs. The group further developed a peptide-based gene carrier consisting of BP100 and chloroplast-targeting peptides (CTP, $(KH)_9$-OEP34) for DNA delivery (Figure 1.2d)[69]. Interestingly, the chloroplast-targeting peptide showed recognition of many plastids instead of exclusive recognition of chloroplast. In addition, dimeric CPP has shown significantly higher gene transfection efficiency than monomeric CPP, probably by enhancing the

cell-penetrating power of the carrier peptide. The complexes were positively charged and displayed hydrodynamic diameters above 200 nm. The results from studies using CPP for cargo delivery to intact plant cells seems circumventing the SEL of cell wall through unclear mechanisms. Despite the large hydrodynamic diameters reported, the complexes showed much smaller sizes in AFM results, where the heights were around 10 nm. Therefore, the complexes may deform and reduce size during their travel through the cell wall. It is also possible that some complexes are smaller than SEL as the complexes have a large polydispersity index. The charge of the complexes, either positive or negative, does not seem to block their internalization. Overall, the penetrating mechanism of CPPs through plant cell walls needs to be further investigated.

Incorporating organelle-targeting biomolecules into nanomaterials (e.g., quantum dots, carbon nanotubes) enables more precise delivery compared to those depending on physical factors (i.e., pH difference)[50]. Santana et al. combined MTP with quantum dots (as a marker) and β-cyclodextrin (as a molecular basket) to deliver small molecules (i.e., ascorbic acid and methyl viologen) to the chloroplast, achieving tuning of the organelle's oxidative status[70]. However, chronic or high-level uses of Cd-based quantum dots (QDs) in agriculture applications raise food and environmental safety concerns.

In sum, the delivery of cargo molecules into intact plant cells and organelles needs to overcome biological barriers with stringent geometrical, biochemical, and physical properties. To address these requirements, nanostructures have been rationally designed to cross biological membranes and promote internalization in cells and organelles by adopting three main strategies, i.e. (i) fabrication of nanoparticles with characteristic dimensions below SEL, (ii) engineering of nanoparticles with shapes facilitating internalization, and (iii) modification of nanoparticles with physiologically functional molecules. The first strategy focuses on fabricating nanomaterials less

than the smallest SEL found in cell walls (~20 nm). Additionally, nanomaterials with negative charges are preferable since they will not be trapped by the also negatively charged cell wall. The second strategy also considers physicochemical interactions between the nanomaterials and the barriers. Nanomaterials with high aspect ratio, i.e. 1D materials (i.e., nanotubes or rods) and 2D nanosheets, experimentally demonstrated internalization, even if their dimension is larger than the SEL, as shown in the use of corona phase carbon nanotubes for targeted delivery of plasmids. The third strategy focuses on the decoration of the nanomaterial with biomolecules that can favor translocation across the membrane. This strategy is particularly important to circumvent size limit and charge requirements that can be technologically difficult to achieve, at scale.

1.2.2. Optimization of release profiles

Controlled release and stimuli-responsive release of agrochemicals are two main strategies for the optimization of drug release profiles. Controlled release refers to the release of agrochemicals, mainly fertilizers, herbicides, and pesticides, over a prolonged period, unlike the conventional burst release approaches. For decades, it has been proposed to administer agrochemicals in a safer, more economical, and efficient way, with the ultimate goals of reducing input resources, mitigating environmental impact, and enhancing safety for growers and consumers[17,71-73]. Most of the technologies for controlled payload release approximate environmental conditions as constant and neglect critical fluctuating parameters, such as soil biochemical conditions, weather, and plant life cycle stages. These variables may however be used to design stimuli-responsive release technologies that employs triggers, such as pH, enzyme, and temperature, to dynamically control precise administration of agrochemicals.

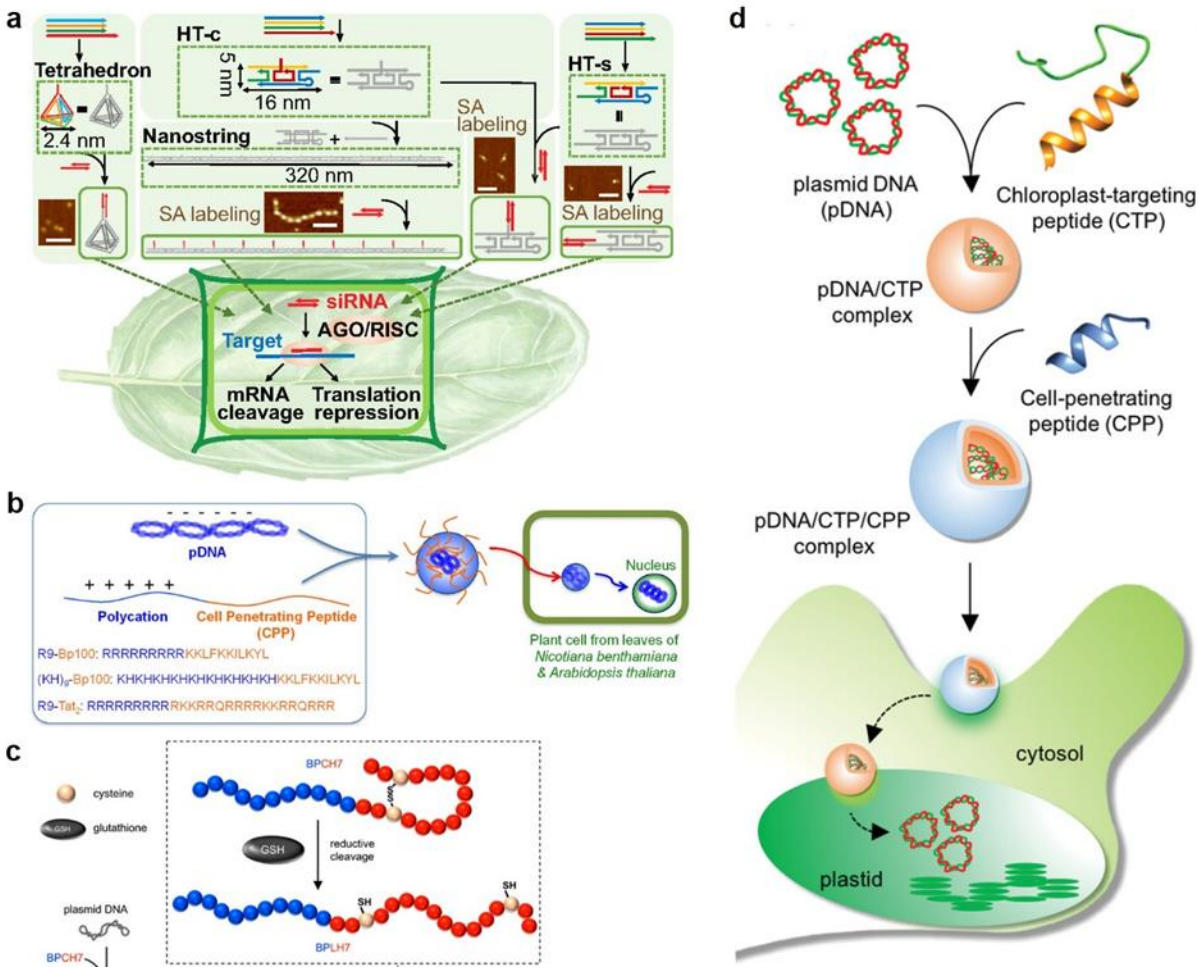

Figure 1.2. Engineered nanomaterials for precision delivery. a) DNA nanostructure synthesis and plant infiltration. The tetrahedron and HT monomer were synthesized from four single strand DNA sequences, and the 1D nanostring structure was synthesized by polymerization of HT monomers with the introduction of an initiator strand. The cargo was attached at the apex of the tetrahedron, along the nanostring, and at the side (HT-s) or center (HT-c) of each HT nanostructure, respectively. Insets show AFM images of streptavidin-bound biotinylated HT monomers. DNA nanostructures loaded with cargos are infiltrated into the transgenic mGFP5 Nb plant leaves for downstream studies. Scale bars, 100 nm. Reproduced with permission[39]. Copyright 2019, National Academy of Sciences. b) Peptide-based gene delivery to intact plant cells. The negatively charged pDNA and designed peptides formed complexes via electrostatic interaction. The pDNA complexes penetrated throughh the cell wall and the cell membrane after foliar infiltration and genes on pDNA were expressed throughout the cell. Reproduced with permission[57]. Copyright 2012, American Chemical Society. c) Schematic representation of the Glutathione Reducible Peptide (BPCH7). Reproduced with permission[62]. Copyright 2018, American Chemical Society. d) Schematic formulation of the clustered pDNA/CTP/CPP complexes and plastid transformation to a plant cell. Reproduced with permission[69]. Copyright 2019, Wiley-VCH.

As used for medical applications, carriers for controlled release of agrochemicals have been developed from a variety of materials, ranging from inorganic materials, such as sulfur and silica, to organic materials, such as lipids, proteins, synthetic and natural polymers, with varying sizes, surface physicochemical properties, and architectures. However, these agrochemical carriers must comply with unique requirements that arise from large-scale in-field applications and the sustainability of the economy and the ecosystem. Additionally, environmentally friendly, and safer materials are preferred by policymakers due to public awareness of environmental sustainability. Such requirements hinder the wide application of commonly studied materials, such as toxic heavy metal-based QDs and non-degradable synthetic polymers[74], despite their outstanding performance. Degradable biomaterials, including biopolymers and their derivatives, such as chitosan, cellulose, lignin, and starch, have been explored as carriers for the controlled release of agrochemicals due to their desirable features, such as low toxicity, circular life, ease of functionalization, and large availability. This section describes degradable biomaterials-based strategies for controlled release and stimuli-responsive release of agrochemicals.

1.2.2.1 Controlled Release

Macronutrient fertilizers (nitrogen, phosphorus, and potassium) are the largest used agrochemical (demand was estimated to be 184 million tons in 2015 and is forecast to reach 201 million tons in 2020)[4]. They are deployed mostly via poorly effective soil application, causing circa 50-70% of loss with detrimental effects on the environment, resource management, and soil health. Controlled release of nutrients in soil/plant systems that synchronizes the release of macronutrients from fertilizers and their uptake into plants is an effective method to increase fertilizer usage efficiency[73,75]. The European Standardization Committee Task Force recommends the criteria that no more than 75% of the nutrients should be released within 28 days[76]. Urea is the most widely used fertilizer and as such has been explored as a fertilizer model for controlled release studies.

The strategy of controlled release is based on the reduction of water and urea permeability by surface coating or strongly binding urea with a substrate.

Early studies of controlled release of fertilizers, also known as slow-release fertilizers, utilized inorganic materials with/without modification and showed limited capability in controlling the nutrient release[73,77-81]. Polymeric coating dramatically extended the release time by forming a release barrier or strongly binding fertilizers on carriers[82,83]. However, environmental concerns are raised by non-degradable polymers. Recent regulations, such as the European Union's Directive on Single-Use Plastics and Limitation in the use of Intentionally Added Microplastics in Products[84,85], will ban certain use of non-degradable plastics, driving the research focus to degradable polymers, particularly natural polymers (e.g., starch, cellulose, chitin, lignin) that are low cost, abundant (several million tons per year), and suitable for large-scale production. Despite the efforts to optimize the performances of natural polymers as a coating material, few studies have met the criteria and a high loading capacity (>95%). For instance, the hydrophilic nature of starch prevents it from being a suitable coating material for urea, regardless of the combination with other materials and modification of starch[86-89]. Chemical modification of cellulose by reaction with its hydroxy groups was also deployed, and the relationship between release rate and structure of cellulose-based materials was discussed[90], but the results did not meet the criteria[91]. While Faez and coworkers reported potassium-containing microspheres based on chitosan and montmorillonite clay that sustained K^+ release for more than 55 days and maintained a relatively constant concentration of potassium in the soil, the high polymer content (>46%) make the solution of difficult commercialization[92]. However, many hydrophilic polymers showed excellent release properties when used as superabsorbent polymers at the nanoscale, including starch, alginate[93], and cellulose derivatives[94].

Owing to their superior performances as adhesives, coatings, and sealants, biobased polyurethanes[95], a greener alternative to fossil-based polyurethanes, have also been explored as carriers for the controlled release of fertilizers. Soybean oil[96,97], castor oil[82,96,98], palm oil[99], and corn stover[100] were reported as the raw materials to extract polyol for the synthesis of biobased polyurethanes for coating urea. The uniform coating of urea by biobased polyurethanes significantly prolonged the 75% release duration, from 35 days to 80 days. Despite their superior performances, the degradation profiles of these biobased polyurethanes in soil have not been investigated yet.

Micronutrients, phytohormones, and pesticides usually have distinct properties from macronutrients and are required at much lower amounts (micronutrients <0.01% dry weight of plants, phytohormones and pesticides < 10μM). In addition, deficiency of micronutrients results in physiological and metabolic disorders, and excess of micronutrients causes toxicity[101,102], which technically necessitates controlled release to deliver the precise dosage. Furthermore, targeted delivery using biomaterials formats (coatings, particles, fibers, sheets) that foster deployment close to the plant tissues as opposed to the wide application through foliar spray or soil applications should be favored. Metal and metal oxide nanoparticles are common micronutrient sources, while other biomaterials are incorporated as surface modification, coating, matrix etc., to control release profile and/or as carriers to facilitate plant uptake and translocation. Martins et al. immobilized ZnO nanoparticles onto biopolymers (microcrystalline cellulose, chitosan, and alginate) to form composites for micronutrient delivery[103]. ZnO nanoparticles/alginate beads showed a lower but enough Zn release for the maize growth while avoiding the early-stage Zn toxicity caused by conventional Zn supplies. While researchers have also explored the application of carbon-based materials, including graphene, graphene oxide, CNTs, and carbon nanofibers (CNFs), as carriers

for nutrient nanoparticles due to limited plant toxicity and uptake by plants[104], the regulatory restriction may apply as previously mentioned. Controlled release of phytohormones was achieved via strong binding to matrix or encapsulation. Yang et al. developed inclusion complexes of GA_3 with cyclodextrins derivative (HP-β-CD) that showed slow release of GA_3 due to the binding ability of the HP-β-CD[105]. Alginate/chitosan and chitosan/tripolyphosphate nanoparticles containing gibberellic acid (GA_3) were reported for seed priming of *Solanum lycopersicum*[106].

Controlled release of toxic agrochemicals (e.g., pesticides, herbicides) was employed as an effective strategy to reduce toxicity and side environmental effects compared to a burst release. For example, Grillo et al. prepared chitosan-based nanoparticles to encapsulate paraquat (1,1'-dimethyl-4,4'-bipyridinium dichloride), a fast-acting nonselective contact herbicide[107]. These nanoparticles showed preserved herbicidal activity but reduced toxicity compared to the pure compound. Similarly, calcium alginate nanocarriers were suggested as a promising and safe candidate for sustained and slow release of cypermethrin, which may decrease the use of cypermethrin and mitigate related environmental pollution[108]. Functional biomolecules embedded in degradable nanomaterials for disease control were also investigated. Mitter et al. loaded designed dsRNA into non-toxic, degradable, layered double hydroxide clay nanosheets to target pepper mild mottle virus (PMMoV) and cucumber mosaic virus (CMV)[109]. Clay nanosheets were slowly degraded into biocompatible residues by atmospheric CO_2 and moisture, releasing dsRNA in a controlled manner over 30 days. The results showed dsRNA uptake into plant cells and silencing of homologous RNA. Liu et al. developed a gene silencing method for efficiently preventing Tomato yellow leaf curl virus (TYLCV) infection in tomato plants by combining artificial microRNA and clay nanosheets[110].

1.2.2.2 Stimuli-Responsive Release

The on-demand release of agrochemicals to fulfill real-time plants' nutritional needs and engineer their response to stressors can be achieved via stimuli-responsive release, which uses pH, temperature, ionic strength, light, enzyme, or magnetic fields, as triggers for cargo deployment[111]. Multi-stimuli-responsive systems were also reported. For example, Hou et al. designed macrospheres loaded with salicylic acid, whose release could be triggered in the presence of hydrogen peroxide (oxidant) and cellulase (enzyme)[112]. A novel pH and redox dual-responsive cellulose-based nanogel was also reported[113]. Yang et al. constructed a smart plant hormone delivery system for gibberellic acid based on metal-organic frameworks (MOFs) and supramolecular nanovalves that exhibited multi-stimuli-responsive release under external stimuli including pH, temperature, and competitive agent spermine[114]. Using plants' environment or response to stressors as triggering principles comes with many limitations. Plants have a limited impact on their local environment, especially at the early stage of stress. Stimuli that can trigger the release of cargo molecules should leverage changes in plant physiology and metabolism, such as physicochemical properties of sap, hormones, and signaling molecules in the vasculature and the release of volatile organic compounds. Extensive investigations of plant responses to various abiotic and biotic stresses have been carried out. Physiologically associated signs of biotic and abiotic stresses were found and have been used in plant sensors and plant wearables for plant monitoring and diagnosis, as we previously reviewed[20]. However, changes in plant physiological indicators and metabolic activity can be associated with several abiotic stressors. So far, only a few studies have shown a successful development of in planta stimuli-responsive release that can mitigate the emergence of such stressors. Major challenges are, in fact, associated with the causality of the stimulus since several stressors or needs may induce the same triggering signal.

The straightforward causation between the appearance of specific biomolecules and biotic stressors (i.e., pathogen infections) makes disease control the pioneer field for stimuli-responsive release. For example, bacterial and fungal pathogens will secret specific enzymes and/or toxins in hosts that do not exist in healthy plants. These secretions can be considered as a fingerprint of infection and used as a stimulus due to their uniqueness. Lignin, one major component of the plant cell wall, is a target for some lignin-degrading enzymes (e.g., laccases and peroxidases) and has been investigated as infection-responsive nanocarriers for disease control. Fischer et al. presented enzyme-responsive lignin nanocarriers encapsulating fungicide against fungal trunk infections of grapevine plants (Figure 1.3a)[115]. Drug loaded lignin nanocarriers were delivered to grapevine plants by trunk injection. Only upon Esca infection, lignin-degrading enzymes secreted by the Esca-associated fungi, degrade the lignin substrate and release the fungicide to kill fungi. These infection-responsive nanocarriers enabled selective, on-demand drug release for plants. *Trichoderma* spores were also encapsulated in nanoparticles to enable an enzyme-responsive biofungicides (Figure 1.3b-d)[116]. The spores displayed germination selectively triggered by the pathogenic fungi *in vitro*, which antagonized the pathogenic fungi and finally supplanted the pathogen. Beckers et al. further explored the fate of polymeric nanocarriers in several plant models, including grapevine, apple, and peach, regarding the chemical composition, size, surface charge, or surfactant of the nanocarriers[117]. They found that negatively charged carriers remained macroscopically stable while some aggregation occurred for cationic nanocarriers. Xylan-based nanocarriers loaded with fungicides were reported to be active in vitro against several pathogenic fungi associated with plant diseases[118]. Interestingly, empty xylan-based nanocarriers stimulated the growth of fungal mycelium, indicating the degradation of xylan in the presence of the fungi. This analogy to lignin makes it a candidate for infection-responsive fungicide. Cellulose-based

and pectin-based nanocarriers loaded with fungicides were also reported to target cellulase-segregating and pectinase-segregating fungi[119,120]. However, these carriers respond to enzymes instead of specific pathogens, thus their selectivity is generally limited.

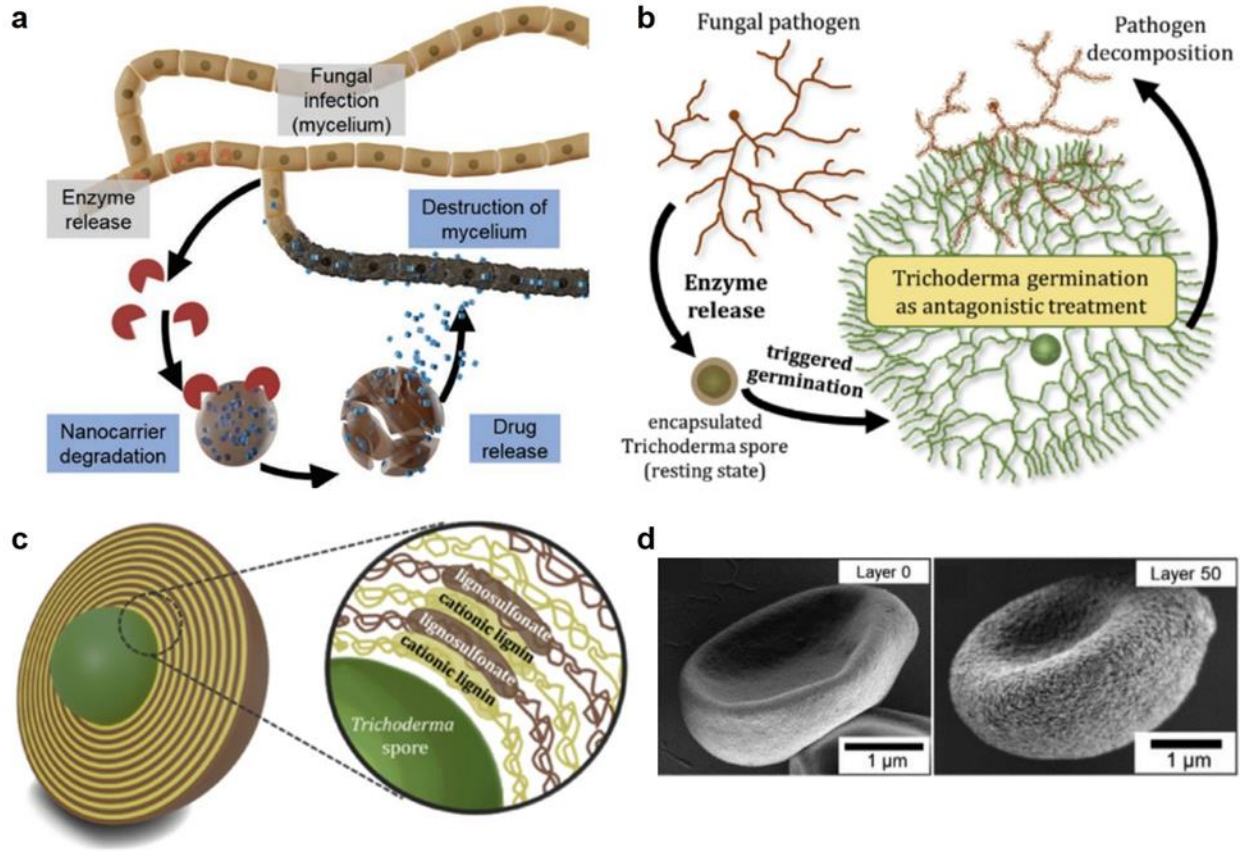

Figure 1.3. Delivery systems with stimuli-responsive release for disease control. a) Schematic of the mechanism of lignin nanocarriers. Fungicide-loaded lignin nanocarriers release the drug only when the Esca fungi secrete lignin-degrading enzymes. Reproduced with permission[115]. Copyright 2019, Wiley-VCH. b) Conceptual illustration of *Trichoderma* spores delivery as a biological control agent. c) Schematic of the structure of a coated *Trichoderma* spore where the coating is composed of alternating cationic Kraft lignin and anionic lignosulfonate formed via a layer by layer deposition. d) SEM images of Trichoderma spores before coating and after 50 layers of coating. Reproduced with permission[116]. Copyright 2020, Elsevier.

To sum, the triggered release of cargo molecules offers unprecedented opportunities to enhance the precise administration of agrochemicals in response to biotic and abiotic stressors, but current technologies still need to show applicability in real-life conditions. The technological bottleneck lies in the sensitivity to and selectivity of the molecules that plants use as a signal for stress events.

For example, small signaling molecules and hormones have been investigated extensively, but they are usually involved in multiple metabolic responses. Recent studies have revealed that peptides and RNA also function as signaling molecules. It is possible that these signaling molecules provide more specificity for stressor-specific signaling and can trigger payload release at physiological concentrations. Innovation at the interface between plant and biomaterials will result in new release triggering mechanisms that enhance precise plant care in stress management. Moreover, monitoring internal stimuli mandates exposure to stimuli-responsive cargos in plant tissues that are often remote and difficult to interrogate. Deployment of stimuli-responsive carriers using previously mentioned spatial precision delivery tools such as microneedles may be a good solution.

Chapter 2 Statement of the Problem

Agrochemicals delivery is of crucial importance in modern agriculture to ensure the healthy growth of crops and, therefore productivity and food security, particularly under current pressures including escalating growing conditions associated with climate change (e.g., extreme weather, the spread of plant diseases and pests, lower soil quality), an ever-increasing human population, scarcity of arable land, and limited resources. However, conventional practices suffer from low efficiency and significant mass loss to the environment, which conflicts with our concerns about sustainability. Therefore, there is a dire need for new techniques for precise, efficient delivery. Given the tremendous effects of biomaterials and nanotechnology in biomedicine (e.g., drug delivery) and microbiology, there is an increasing interest and great opportunities in the deployment of these technologies in plant science and crop production. The use of biomaterials and drug delivery principles to engineering the precise deployment of payloads in plants is thus proposed. Specifically, the dissertation will propose a silk materials-based microneedle device for precise delivery of payloads to multi plant tissues. Chapter 3 designs a silk fibroin-based biomaterial that is suitable for materials delivery to plants, fabricates new microneedle devices for precise delivery to multi plant tissues, and investigates their performance. Chapter 4 explores the utility of silk-based microneedles in delivering gibberellic acid to model plants and several crop species with minimal injection-induced wounding responses. Chapter 5 extends the application of microneedles to sampling via hollow microneedles that are fabricated using silk fibroin assembly and inorganic nucleation at their phase fronts, providing new tools to bridge the biotic/abiotic interface by interrogating pathways for biomolecules transport in plants and enabling early-stage detection of bioaccumulation of environmental contaminants, such as cadmium and arsenic.

Chapter 3 Precision Delivery of Multi-Scale Payloads to Tissue Specific Targets in Plants

The contents of this chapter were published in Advanced Science as: Yunteng Cao[1], Eugene Lim[1], Menglong Xu[2], Jing-Ke Weng[2,3], Benedetto Marelli[1*]

[1]Department of Civil and Environmental Engineering, Massachusetts Institute of Technology, 77 Massachusetts Avenue, Cambridge, 02139, MA. United States.

[2]Whitehead Institute for Biomedical Research Cambridge, MA 02142, USA.

[3]Department of Biology Massachusetts Institute of Technology Cambridge, MA 02139, USA.

"Precision Delivery of Multiscale Payloads to Tissue-Specific Targets in Plants." Published, Advanced Science, 7.13: 1903551, April 22, 2020. DOI: 10.1002/advs.201903551.

3.1 Abstract

The precise deployment of functional payloads to plant tissues is a new approach to help advance fundamental understanding of plant biology and accelerate plant engineering. Here, the design of a novel silk-based biomaterial is reported to fabricate a microneedle-like device, dubbed phytoinjector, capable of delivering a variety of payloads ranging from small molecules to large proteins into specific loci of various plant tissues. It is shown that phytoinjector can be used to deliver payloads into plant vasculature to study material transport in xylem and phloem and to perform complex biochemical reactions in situ. In another application, it is demonstrated Agrobacterium-mediated gene transfer to shoot apical meristem and leaves at various stages of growth. Tuning of the material composition enables the fabrication of another device, dubbed phytosampler, which is used to precisely sample plant sap. The design of plant-specific biomaterials to fabricate devices for drug delivery in planta opens new avenues to enhance plant resistance to biotic and abiotic stresses, provides new tools for diagnostics, and enables new opportunities in plant engineering.

3.2 Main Text

A projected world population of 9.7 billion people in 2050 may result in a 70% increase of food demand and pose a severe strain to global food security[1]. To address these challenges, innovations in plant genetic engineering and precision agriculture are highly sought to enhance crop productivity, impart and/or enhance plants' resistances to diseases and stresses and increase the sustainability of crop production[121-123]. In this scenario, there is an increasing interest in the use of biomaterials and nanotechnology to plant science and crop production, provided the tremendous effects of these technologies in biomedicine (e.g. drug delivery) and microbiology. For example, nanomaterials have been used in plants as bactericides and fertilizers[14,29,109,115], microneedles have been applied on leaves to sample pathogenic bacteria[124] and nanobionics has been developed to impart new function to plants' organelles[10,12,50]. Nonetheless, the use of biomaterials and drug delivery principles to engineer the precise deployment of payloads in plants has been largely overseen. This has also resulted in limited technical capability in dealing with diseases that target plant vasculature (e.g. phloem- or xylem- restricted bacteria[125,126]) and is a limiting factor in plant engineering, where nanoparticles are delivered to plant tissues by complex and inefficient methods. The most commonly used delivery methods for plants are foliar spray, root application, and trunk injection/petiole feeding[14]. Although foliar spray and root application are easy to implement, they suffer from significant material loss and low efficiency due to plant's barrier tissues such as cuticle and epidermis. Trunk injection and petiole feeding overcome the challenges caused by plant barrier tissues by damaging these barriers mechanically and accessing vasculature directly. They have a higher delivery efficiency and can be used to deliver large amount of payloads. However, they are suitable for large, woody plants due to their invasive application process. Valuable and labile payloads are also not suitable to be delivered by these methods. Foliar infiltration and pressurized

bath infusion[12] widely used in lab also have a low delivery efficiency since most materials are left in leaves‘ intercellular space.

Silk fibroin (derived from *Bombyx mori*) has been extensively studied as a technical material in a wide range of fields including drug delivery and regenerative medicine[127], optoelectronics[128], and food coatings[129] due to its unique properties that include nontoxicity (degradation into amino acids), mechanical robustness, tunable degradation via hydrolysis, preservation of heat-labile payloads, and ease of fabrication. In biological sciences, the structural protein has been investigated for drug delivery as it can be fabricated into implantable devices that preserve and release payloads *in vivo* while not providing an adverse reaction upon implantation[130]. Silk fibroin degradation in host human tissues can be modulated by controlling the protein polymorphism, i.e. the amount of beta sheets present in the end-material, as more ordered molecular structures are more resistant to proteolytic degradation[131]. These features are attractive also for the design of a plant-specific biomaterial for drug delivery. However, limited free water and low concentration of proteases in plant sap fluid result in prolonged silk fibroin stability and limited release of cargo molecules[132]. To overcome these challenges, we engineered a new biomaterial based on silk fibroin that was formatted in a device capable of delivering a variety of payloads ranging from small molecules to large proteins into specific loci of various plant tissues.

Optimization of material’s mechanical robustness and solubility was controlled by tuning the relative amount of hydrophobic/hydrophilic domains and enabled the design and fabrication of an array of injectors (namely phytoinjector) capable of targeting plant vasculature by penetrating plant dermal and ground tissues. The dimensions of tissue-specific phytoinjectors were determined by histological analysis of the target tissue. Using specific phytoinjectors, payloads (ranging in size from small molecules to large proteins) were deployed in tomato plant xylem and phloem and

their transport to sink and source was observed and modeled. *Agrobacterium*-loaded phytoinjectors also showed gene transfer to and expression in tobacco shoot apical meristem (SAM) and in leaves at various stages of growth. Tuning of material composition also enabled the fabrication of a device to sample xylem sap.

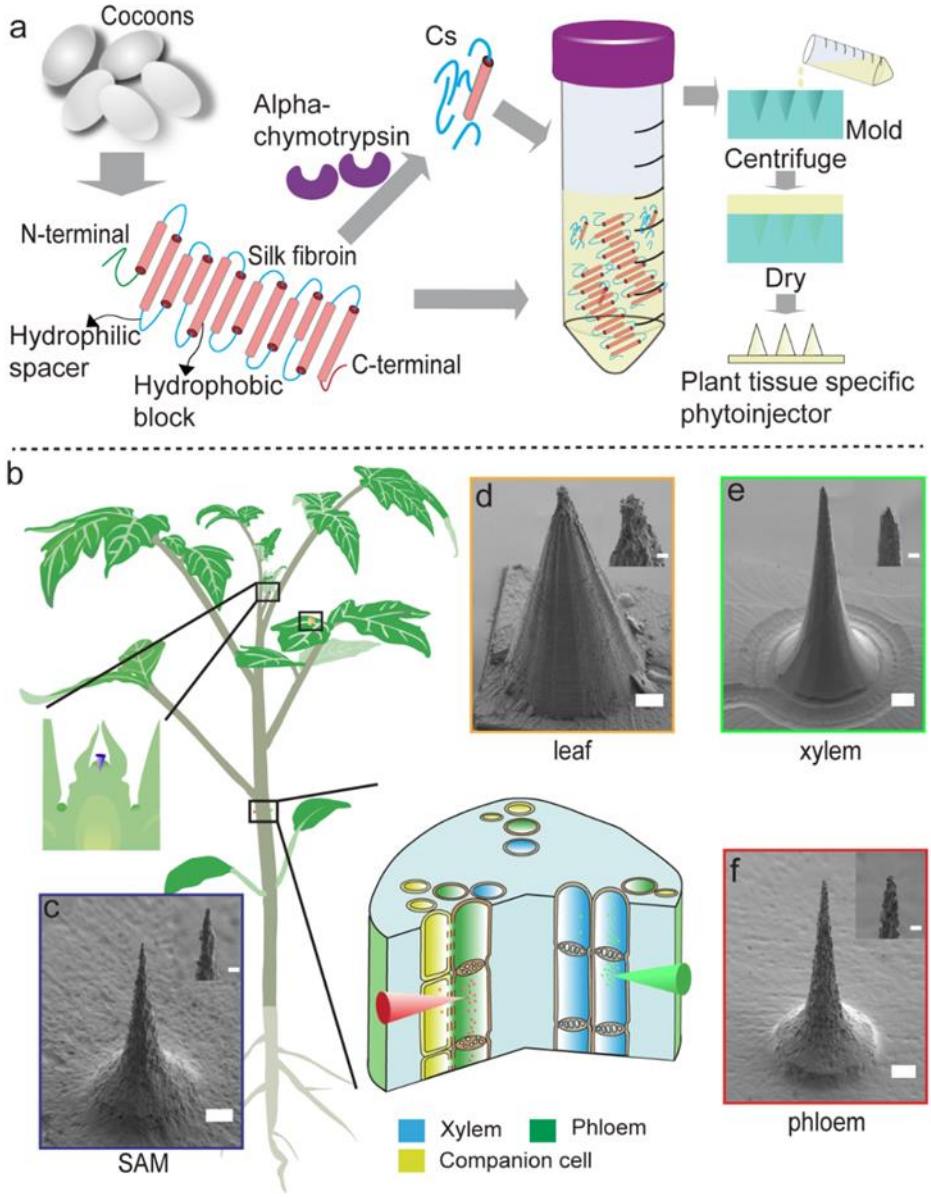

Figure 3.1. Material and device design for multiscale, multitissue precise delivery of payloads in plants. a, Material design. Silk materials were engineered to perform in plants. Silk fibroin is first extracted from *Bombyx mori* cocoons; the 390 kDa heavy chain is composed of 12 hydrophobic blocks (red cylinders) staggered by 11 hydrophilic spacers (blue lines). By using alpha-chymotrypsin, the hydrophilic spacers (Cs) can be extracted. The final material is a blend of

Cs and silk fibroin, which is fabricated intoplant tissue specific phytoinjectors via PDMS molds. **b**, Silk fibroin materials can be fabricated in phytoinjectors of desired size and shape for precise payloads delivery in different plant tissues. In the schematic, injection in foliar tissue, shoot apical meristem and plant vasculature are represented. In particular, the green and red injectors indicate delivery to xylem and phloem, respectively. The left inset indicates delivery to shoot apical meristem (SAM). **c, d, e, f**. Scanning electron micrographs of phytoinjectors designed for delivery to SAM, leaf, xylem, and phloem, respectively. The inlets show the injectors tips. Scale bar: 100 μm, scale bar of inlet: 20 μm.

Silk fibroin heavy chain (~390kDa) is composed of 12 large, hydrophobic amino acid domains that amount for more than 75% of the protein and that are linked by 11 short, hydrophilic spacers (**Figure 3.1**a). Preliminary investigations using silk fibroin showed limited payload release in xylem and phloem saps. Partial insolubility in plant sap may negatively affect sap flow in xylem and phloem by vascular blockage. To overcome these challenges, we used a top-down synthetic approach to increase the hydrophilic content of the silk end-material and decrease the size of the protein biodegradation byproducts by extracting hydrophilic silk fibroin-derived polypeptides (Cs) (Figure 3.1a, Figure S3.1)[133]. α-chymotrypsin allows to extract silk fibroin-derived soluble peptides (Cs)[133] that can be mixed with silk fibroin water suspensions, yielding a more hydrophilic silk material that also disrupts the hydrophobic effect-derived aggregation of silk molecules in nanomicelles. In aqueous suspension, Cs does not show noticeable influence on silk nanomicelle size (Figure S3.1). In terms of composition, Cs is composed of negatively charged peptides with a molecular weight of 2-10 kDa (Figure S3.1) and a primary structure that accounts for only 10-15% of hydrophobic amino acids. As a result, Cs is highly soluble but also yields very brittle materials, which makes it unsuitable (as a stand-alone entity) for the fabrication of payload delivery devices. However, Cs can be blended with silk fibroin with the weight ratio of the two biopolymers being tuned to modulate fundamental biomaterial end-properties such as solubility, degradation, mechanical strength, nanomicelle size, and preservation of payloads. Cs is incorporated in silk materials during the assembly process, when hydrogen bonds between silk nanomicelles and water

are replaced with intermolecular hydrogen bonds. During this step, nanomicelles coalesce and form a monolithic material. Cs would then participate in this assembly process as it is made by a portion of the silk fibroin primary structure. However, being of smaller MW, the incorporation of Cs results in the weakening of the interactions/entanglement between large silk fibroin molecules, ultimately enhancing material disassembly upon exposure to water. The intermolecular and intramolecular interaction of hydrophobic amino acid domains may also be weakened. To further explore this mechanism, we have conducted several investigations of silk fibroin-Cs interactions both in water suspension and in solid, monolithic materials (i.e. film format), which has been reported in SI. Materials characterization was also accomplished to identify the optimal composition for payload delivery into plants. In the manuscript, we denote a Cs 20% - Silk Fibroin 80% dry weight mixture as $Cs_{20}SF_{80}$. SF refers to pure silk fibroin.

Cs-silk fibroin biomaterials were characterized according to the following properties: solubility, nanomicelle size when re-solubilized, conformation, viability of preserved labile payloads, and mechanical robustness. Solubility in simulated sap increases dramatically with increased Cs content (**Figure 3.2**a). Compared to silk fibroin (89.8 mg ml^{-1}), the maximum concentration of $Cs_{20}SF_{80}$ in suspension is two times higher (184.1 mg ml^{-1}), while the concentration of pure Cs at saturation is five times higher (441.3 mg ml^{-1}). Nanomicelle size of resuspended $Cs_{20}SF_{80}$ has no significant difference from that of resuspended silk fibroin (Figure S3.1). The protein structure was investigated both in suspension by circular dichroism (CD) and in solid state (film form) by Attenuated Total Reflectance Fourier Transform Infrared Spectroscopy (ATR-FTIR), Raman Spectroscopy, Thermogravimetric analysis (TGA), and Differential scanning calorimetry (DSC). CD spectra of silk fibroin show a strong negative peak at 196nm, indicating large amounts of random coils and a weak negative peak at 216 nm, distinctive of limited amounts of β-sheets[134].

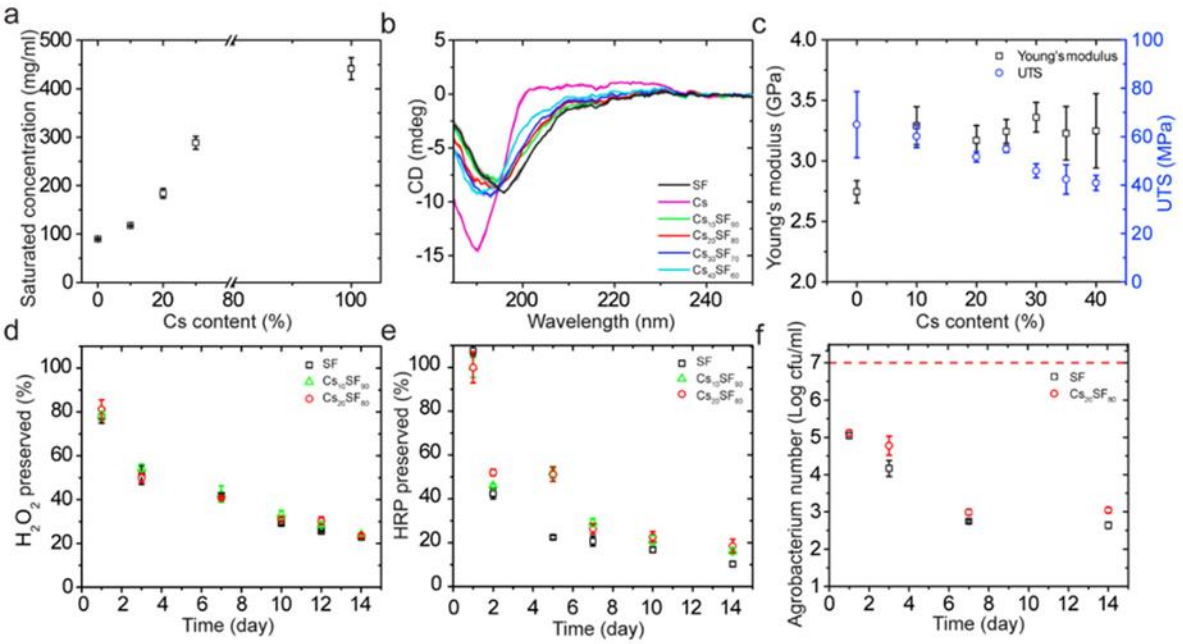

Figure 3.2. Material characterization of engineered silk material for in planta applications. **a**, Solubility of Cs-silk fibroin blends ($Cs_{xx}SF_{yy}$) in simulated sap fluid. Cs dramatically increases the solubility of CsSF blends, resulting in materials that can easily biodegrade in a sap-like environment. **b,** CD spectra of CsSF blends with various Cs content. **c**, Mechanical properties of CsSF films with various Cs content under tension. **d**, Hydrogen peroxide preservation in SF, $Cs_{10}SF_{90}$, and $Cs_{20}SF_{80}$. **e**, HRP preservation in SF, $Cs_{10}SF_{90}$, and $Cs_{20}SF_{80}$. **f**, Agrobacterium preservation in SF and $Cs_{20}SF_{80}$. Data are mean ± s.d (n is at least 3).

Pure Cs shows a strong negative peak at 190 nm and a weak negative peak at 216 nm, indicating the presence of β-turns and β-sheets, respectively (Figure 3.2b). No noticeable conformation changes occur due to the blending of Cs and silk fibroin. FTIR spectra also show little difference and Amide I absorbance is dominated by a resonance centered at 1645 cm^{-1} (Figure S3.2) that is characteristic of random coils[135]. Incorporation of increasing concentrations of Cs in the blends did not result in a change of beta sheet content (Figure S3.2), suggesting that Cs did not drive a random coil to beta-sheet transition during silk fibroin assembly. The slight increase of turns with Cs content increase may attribute to the intrinsic molecule properties of Cs. Analysis of the Amide bands in Raman Spectra (Figure S3.3) indicates that Cs does not hinder polymorphic changes of the structural protein[136,137]. The difference of decomposition temperature of Cs (180 °C), SF

(225 °C), and $Cs_{20}SF_{80}$ (205 °C) (Figure S3.4) indicates weakened molecular interaction between silk fibroin by Cs, which agrees with DSC results (Figure S3.4)[138,139].

Hydrogen peroxide was selected as a small molecule used for labile payload preservation due to its significant metabolic functions, which include lignification, ABA signaling in guard cells, programmed cell death and pathogen response[140]. Based on the mechanical properties of the CsSF blends (Figure 3.2c, discussed later), Cs content was limited to 20% or less. Hydrogen peroxide was well preserved in SF, $Cs_{10}SF_{90}$, and $Cs_{20}SF_{80}$, showing no significant differences among the three materials (Figure 3.2d). In $Cs_{20}SF_{80}$ films, 81% and 50% of entrapped hydrogen peroxide was preserved at day 1 and 3 post-drying, respectively. At day 14, 24% of hydrogen peroxide was preserved, and this preservation window can be extended beyond three weeks. This strong oxidant is trapped in the Cs-silk fibroin matrix without chemical reactions, similarly to the presence of free water in the material (Figure S3.5)[141]. Horseradish peroxidase (HRP) was used as a model to test preservation of enzymes and proteins. In this case, $Cs_{20}SF_{80}$ blends enhanced the preservation of the enzyme, which had 51% and 19% residual catalytic activity at days 5 and 14, respectively. To assess preservation of bacteria in Cs-silk fibroin blends, *Agrobacterium tumefaciens* was added to SF and $Cs_{20}SF_{80}$. The number of live bacteria preserved in dried SF and $Cs_{20}SF_{80}$ showed a 2-log reduction after 24h, due to the drying process. At day 7, a further 2-logs decrease in bacteria viability was measured. $Cs_{20}SF_{80}$ shows a slightly improved performance in preserving *Agrobacterium* than SF (Figure 3.2f). The feasibility of injecting CsSF mixtures in plants was first explored by investigating their mechanical properties via uniaxial tensile strength and nanoindentation measurements (Figure S3.6). SF Young's modulus was 2.75±0.09 GPa (Figure 3.2c), which is in the range of previously reported measurements[142]. The addition of Cs into silk fibroin materials enhances the Young's modulus by more than 15% but at the cost of ductility,

which further confirms our proposed mechanism of interaction between Cs and silk fibroin. Nanoindentation results also indicate that reduced modulus increases with increasing Cs content from 0% up to 40%.

Table 3.1. Tip breaking force of phytoinjectors.

	$Cs_{20}SF_{80}$ phloem phytoinjector	SF phloem phytoinjector	$Cs_{20}SF_{80}$ xylem phytoinjector	SF xylem phytoinjector
Tip breaking force [N]	0.142±0.022	0.151±0.015	0.392±0.043	0.400±0.080

Table 3.2. Plant tissue penetration force by a xylem phytoinjector.

Plant	Tomato			Tobacco		Citrus	
Tissue	Stem	Petiole	Leaflet	Petiole	Leaf	Branch	Leaf
Penetration force [mN]	30.4±10.1	24.0±8.4	5.2±0.5	23.3±1.0	9.1±2.7	32.2±4.6	22.8±1.0

Payload release profiles of silk fibroin constructs in sap fluid follows a *Super Case II* mechanism (see Supporting Information, Figure S3.7, and Table S3.2). To demonstrate targeted payload delivery to xylem and phloem, we combined $Cs_{20}SF_{80}$ with replica-molding to fabricate phytoinjectors of different sizes. To identify potential modes of entry to plant vasculature, we prepared and analyzed histological samples of tomato (*Solanum lycopersicum L.*) stem and petiole. We used tomato as the working model because of the well-defined structure of the vasculature, presence of compound leaves with long petiole (Figure S3.8), and importance as crop. The penetration depth, defined as the segment between the vasculature and the epidermis, is in the range of 840-1040 μm and 707-925 μm for xylem and phloem, respectively, and depends on the diameter of petiole (Figure S3.8). The reported diameters of xylem and phloem are of the order of tens and hundreds of μm, respectively[143]. Based on these parameters, phytoinjectors were designed with a tip diameter smaller than 35μm and 10μm for xylem and phloem, respectively (Figure 3.1b, Figure S3.8). Resuspended $Cs_{20}SF_{80}$ has a particle size of 3-7 nm (Figure S3.1), which suggests that it can be transported in xylem through the pit membrane (pore size 5-420 nm[144]) and in phloem

through the sieve plate (pore size 610±150 nm in *S. lycopersicum*[145]). Phytoinjectors exhibit appropriate mechanical robustness to for injection to various tissues of tomato plant, tobacco plant and citrus tree. (Table 3.1 and 3.2, Figure S3.9). To investigate payload delivery in planta, each payload was loaded to phytoinjectors at the point of material assembly before drying. Rhodamine 6G and 5(6)-carboxyfluorescein diacetate were incorporated into phytoinjectors to target phloem and xylem, respectively, and injected in tomatoes' petioles (**Figure 3.3**a). Petiole cross-section showed that the phytoinjectors reached the vasculature (Figure 3.3b). Histological analysis also corroborated these findings (Figure 3.3c). The injected petioles were sliced along the transverse section downstream and upstream at various distances from the injection site to investigate the presence of the delivered dyes. For phloem injections, rhodamine 6G was transported further downstream (i.e. from leaf to root for a mature leaf, >3.3 cm) than upstream (~0.3 cm) the injection site. This result is in accordance with reported translocation in phloem for mature leaves[143,146] (Figure 3.3d) and indicates that phytoinjectors successfully deployed payloads in the phloem that were translocated along the vascular tissue. In xylem, transport analysis was conducted by tangential sectioning of the stem (Figure 3.3e). Analysis of 5(6)-carboxyfluorescein diacetate indicated that the molecule was transported more than 7 cm downstream (i.e. from root to leaves), and 1 cm upstream from the injection site. Upstream transport was likely the result of pure diffusive phenomena. The longer transport detected in the xylem when compared to phloem may be attributed to a more efficient deployment in its conduits, which also facilitated analysis conditions due to their larger diameter and smaller background noise of green fluorescence. To quantify payloads transport, we integrated the fluorescence intensity in Figure 3.3e. The normalized intensity distribution evolves spatially and temporally (Figure 3.3f). Notably, the dye was also transported along the radial system of the vasculature. However, in this study we focus

on longitudinal material transport only, thus ignoring the radial phenomena by integration, which results in a simplified 1-dimensional (1D) problem (see 3.4.1.3).

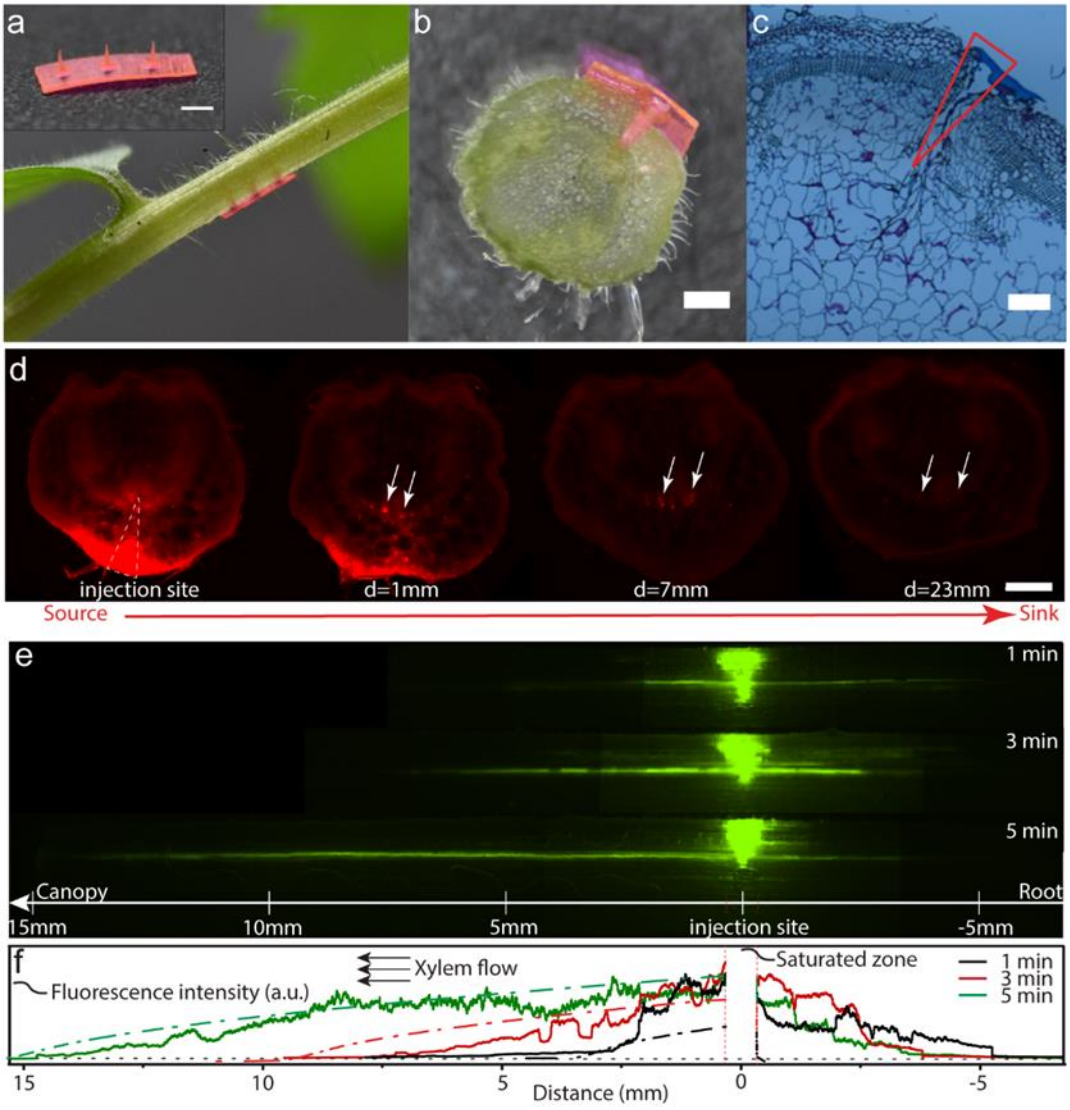

Figure 3.3. Payload delivery in stem's vasculature system. a, A tomato plant injected in the stem by an array of phytoinjectors loaded with rhodamine 6g. The phytoinjector array is showed on top left. Scale bar, 1 mm. **b,** Cross section of the injection site, depicting a phytoinjector that reaches tomato stem's vasculature system. Scale bar, 500 µm. **c,** Bright field image of a histological section of stem's cross section at injection site. Scale bar, 200 µm. **d,** Fluorescent microscope images showing rhodamine 6g delivered to and transported in phloem, from source to sink. The red spots highlighted by white arrows point to rhodamine 6g in phloem. Scale bar, 500 µm. **e,** Image assembly of fluorescent micrographs showing 5(6)-carboxyfluorescein diacetate delivered to and transported in xylem, from roots to canopy, 1, 3, and 5 minutes post injection. **f,** Corresponding fluorescent intensity depicting 5(6)-carboxyfluorescein diacetate distribution along xylem (1, 3, and 5 minutes post injection, respectively). Red dash line highlights the saturated zone

due to residue of the phytoinjetor, which is removed from experimental data. Black dot line is the background. Solid curves are experimental data while dash dot lines with the same color are corresponding model simulation.

There are numerous examples of small molecules, macromolecules, and bacteria that have been delivered in leaf tissue and roots to modify plants' genome, boost photosynthesis, and act as pesticide or fertilizer[109,115]. Injection in the stem (or trunk) has also been performed to deliver antibiotics, pesticides, and nutrients[147]. Here, to provide a proof of concept that silk-based phytoinjectors can precisely orchestrate the deployment of different payloads in plant vasculature, we have designed a multi-reagents delivery system that enables the well-known luciferin-luciferase bioluminescent reaction[12,148] in plant vasculature:

$$\text{Luciferin} + \text{ATP} + \text{O}_2 \xrightarrow[\text{Luciferase}]{\text{Mg}^{2+}} \text{Oxyluciferin} + \text{AMP} + \text{PPi} + \text{CO}_2 + h\nu \quad (1)$$

where AMP is adenosine monophosphate, ATP is adenosine triphosphate, PPi is inorganic pyrophosphate and *hv* is light. We deployed a bioluminescent system in plant vasculature as a model for the complex biochemical interactions occurring during transport of hormones, signaling molecules, and peptides. We chose to apply the phytoinjectors in petiole vasculature near the terminal leaflet to facilitate observation and imaging due to the limited amount of payloads delivered. At first, we deployed luciferin in the petiole's xylem while the other reagents were delivered by foliar infiltration to the leaf. The leaf tissues downstream the injection site showed luminescence (**Figure 3.4**a), indicating the occurrence of the reaction, thus the delivery of luciferin and mobility of small molecules through the vasculature into ground tissue. Interestingly, no noticeable luminescence was observed from main veins, suggesting impermeability of vein structure to some reagents, likely luciferase due to its size. Luciferin and luciferase were then loaded to different phytoinjectors and injected to the same petiole (Figure 3.4b), while the other reagents were infiltrated in the leaf ground tissue. Though faint, luminescence was detected in the

vein of the leaf (Figure 3.4b), indicating the delivery of multi reagents as well as a large protein via phytoinjectors.

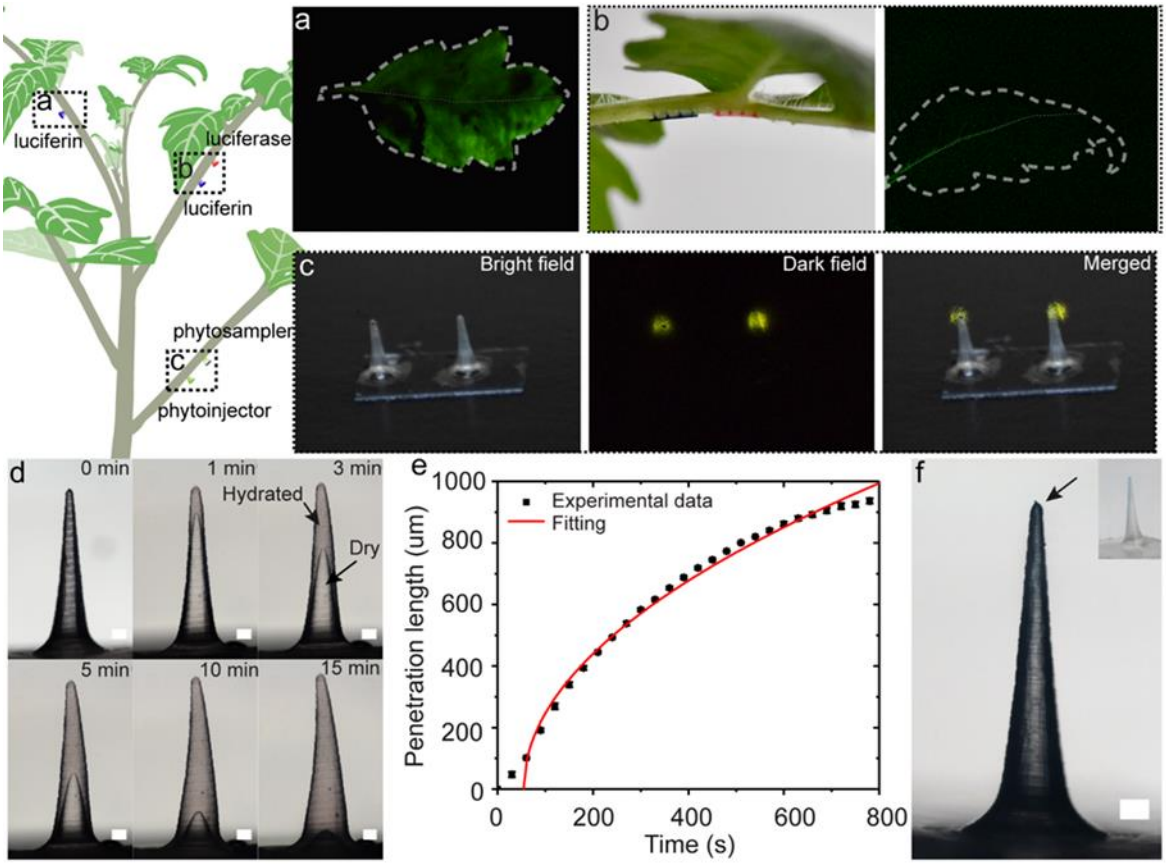

Figure 3.4. Delivery and sampling of biomolecules in xylem. a, Delivery of luciferin into the petiole xylem; by providing external luciferase, ATP, and Mg^{2+}, the whole leaf emits light. (Exposure time 30 seconds, image adjusted for display purpose) **b,** two arrays of phytoinjectors loaded with different payloads (luciferin for blue injectors and luciferase for red ones, blue and red here are only for display purpose) targeting petiole's xylem concurrently. By providing external ATP and Mg^{2+}, the leaf vein emits light (Exposure time 120 seconds, image adjusted for display purpose). **c,** Sampling of luciferin and Mg^{2+} delivered to petiole xylem by $Cs_{20}SF_{80}$ phytoinjectors using an SF phytosampler (Exposure time 30 seconds for dark field). **d,** Swelling of and water movement in a phytosampler injected into agar gel. indicating the possible use to sample plant fluids. **e,** Corresponding water penetration length with time. **f,** A phytosampler injected into toluidine blue agar gel becomes blue in 1 minute. Data are mean ± s.d (n=3).

Leveraging the polymorphic nature of silk materials, it was also possible to design water insoluble devices that reswell when exposed to sap fluid and can be removed post-injection. Such devices are here named phytosampler as they can be used to sample sap fluids. Since partial dissolution of

the phytosampler is undesired, we used pure silk fibroin as fabrication material. The efficacy of the phytosampler was assessed by deploying it in the xylem downstream to a phytoinjector loaded with luciferin and Mg^{2+}. Upon sampling, the phytosampler was exposed to the reaming reagent necessary for the bioluminescent reaction to occur. Generation of light indicated the successful sampling of luciferin and Mg^{2+} from the xylem (Figure 3.4c). The dislocation of phytoinjecor tip and luminescence spot in merged image is likely due to diffusion of luciferin into the solution drop of reagents and deformation of silk fibroin substrate when exposed to the reagents. Reswelling of the phytoinjectors and diffusion of metabolite and catabolite in silk phytosampler was modeled with a Lucas-Washburn equation[149] (Figure 3.4e) by investigating the diffusion of water and dyes like toluidine blue in the device (Figure 3.4d and 4f), although poroelastic models[150] could also be applied to take into account for the relaxation of the transient response of silk materials during reswelling. To assess targeted delivery of live microorganisms into plant tissues, we loaded *Agrobacterium tumefaciens* with a pEAQ-HT vector containing *gfp* gene into $Cs_{20}SF_{80}$ phytoinjectors, using tobacco (*Nicotiana benthamiana*) as a model plant. *A. tumefaciens* has been widely used as a powerful gene transformation vehicle in plant genetic engineering to optimize the crop production of the desired products, such as drugs or proteins[151]. *A. tumefaciens*-mediated genetic transformation can target: 1) developing tissues[152], 2) inflorescences via floral dipping, or 3) leaves via foliar infiltration. We targeted shoot apical meristems (SAMs), young growing leaves, and mature leaves. The phytoinjector dimensions were modified to optimize payload delivery via SAM injection and leaf injection (Figure 3.1f). At two weeks post-injection (when the SAM became a leaf), the leaves were harvested. Although all leaves exhibited GFP-induced fluorescence, the spatial distribution of GFP synthesis differed. Leaves derived from treated SAMs exhibited scattered GFP fluorescence across the leaf when excited with blue light (Figure 3.5a,ii). Using

fluorescence microscopy, GFP expression was detected in multiple spots situated across the entire leaf (Figure 3.5a,iii), indicating successful gene transfer in mesophyll cells. The scattered distribution of these cells may result from cell divisions and subsequent growth of SAM cells. Since some (but not all) of the SAM cells that were directly in contact with *A. tumefaciens* (released from the $Cs_{20}SF_{80}$ phytoinjector) demonstrated gene transfer, we hypothesize that GFP-expressing cells were isolated by non-GFP-expressing cells during leaf growth. The young leaves grew in the two weeks post-injection, and GFP fluorescence in the form of lines or scattered spots situated was observed away from the injection site (Figure 3.5b,iii). This differs from what was observed in mature leaves, where GFP expression was limited to cells that are close to the injection site (Figure 3.5c,iii). The limited degree of gene transfer in mature leaves suggests that *A. tumefaciens* has little to no mobility upon release in the leaf. This is validated by foliar infiltration, where GFP expression in mesophyll cells is generally limited to the area directly accessible to *A. tumefaciens*. In growing young leaves, mesophyll cells can divide and grow, so GFP-expressing mesophyll cells form lines and scattered spots, depending on the geometrical growth of the leaf. Altogether, these results demonstrate that *A. tumefaciens*–mediated gene transfer to plant tissues can be achieved using $Cs_{20}SF_{80}$ phytoinjectors.

Microneedles have been previously reported for pain-free transdermal drug delivery and vaccination[153-155]. In this study, we used principles of biomaterial design to fabricate phytoinjector and phytosampler devices to deliver cargo molecules to plants and to investigate material transport phenomena in plant vasculature. Our current design enables the delivery of tens of ng of cargo molecules per injector and cannot be used to deliver sufficient amounts of macronutrients for plants (Table S3.3). However, there is a large variety of payloads that function in plants at quantities that can be delivered with the current phytoinjector setup (Table S3.3 and S3.4).

Examples are: plant hormones, micronutrients, small interfering RNA (siRNA) and self-replicating microorganisms. Injection and silk degradation appeared to not compromise the functionality of both xylem and phloem and did not noticeably affect plant health, despite the formation of scar tissue around the injection site at day 14 post-injection (Figure S3.10). Immediate material degradation to nm-scale particles and the general bioinert nature of silk fibroin may, in fact, have resulted in a rapid recovery to physiological function upon flow disruption, with no evident adverse reaction to plant health at day 7 post-injection (Figure S3.10) and on sap flow (Figure 3). Future studies are however necessary to investigate plant responses to the injection, e.g. through studying Ca^{2+} [156] and jasmonic acid signaling[157]. The precise targeting of phloem here described may also open the door to future applications in systemic signaling molecules release in planta[158-161], which is currently not possible. Accessing the phloem has in fact always been a technological challenge that is currently addressed using Pico gauge[162] or by severing an aphid stylet during feeding[163,164]. Precise injection in SAM also enabled the modification of plant genotype to induce expression in the current generation. We have also expanded the function of silk-based phytoinjectors to achieve analyte sampling from plant vasculature. Potential sampling applications of insoluble phytoinjectors include detection of early-stage phloem- and xylem-limited pathogens, natural plant response to environmental cues, and engineered plant response to user-defined cues. In conclusion, the design of plant-specific biomaterials to fabricate devices for drug delivery in planta opens new avenues to enhance plant resistance to biotic and abiotic stresses, provides new tools for diagnostics, and enables new opportunities in plant engineering.

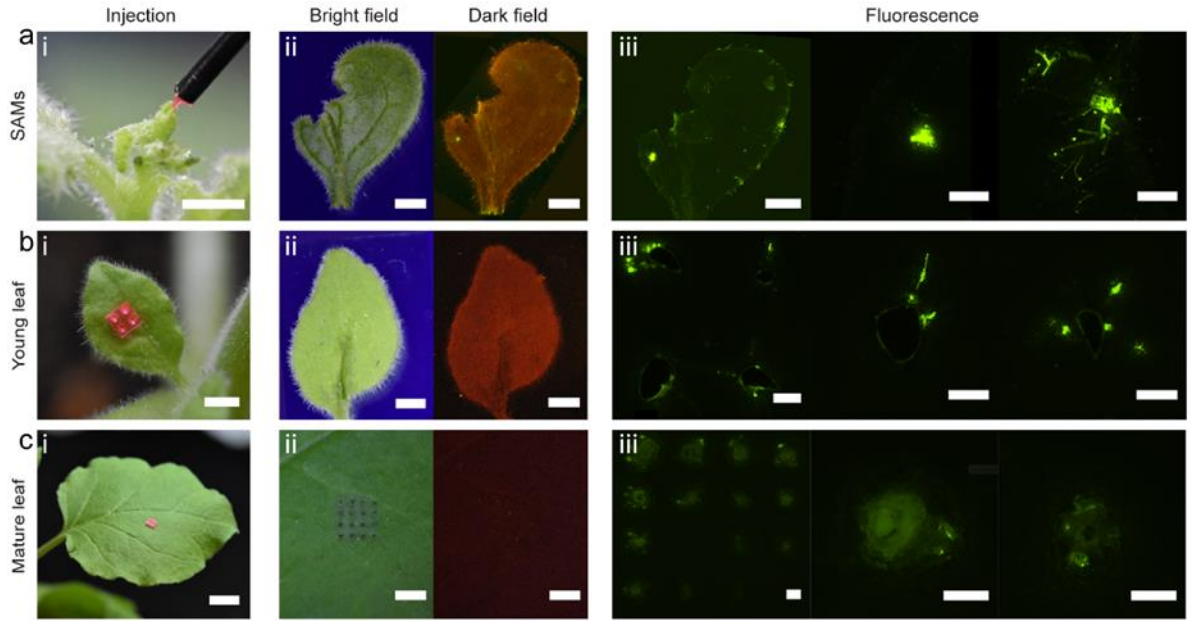

Figure 3.5. Agrobacterium-mediated gene transfer to shoot apical meristem and leaves. a, Agrobacterium delivered to the shoot apical meristem. i, shoot apical meristem (SAM) injected by a phytoinjector loaded with agrobacteria (rhodamine 6g was also loaded for display purpose); ii, bright and dark field images of the leaf from the shoot 2 weeks after the injection. Bright green spots in dark field indicating GFP expressed in leaf cells are distributed across the whole leaf; and iii, fluorescent microscope images of the leaf in ii. Agrobacterium delivered to a young leaf **b** and to a mature leaf **c**. i, ii, and iii are images when injected, bright and dark field images 2 weeks after injection, and fluorescent microscope images of the injected area on leaves. GFP is observed away from the injection site in a young leaf due to tissue growth, while it expressed only at the injection site in a mature leaf. Scale bar 2 mm for i and ii, 500 μm for iii. Exposure time, bright field 20 ms, dark field 5 seconds.

3.3 Experimental Section

Extraction of silk fibroin: The aqueous silk fibroin solution was prepared from *Bombyx mori* cocoons as described with modification[165]. Briefly, dime size cocoon pieces were boiled for 45 minutes to remove sericin in 0.02 M sodium carbonate solution and dried overnight after thorough rinse in MilliQ water. The dried silk fibroin fibers were then dissolved in 9.3 M lithium bromide solution at 60 ˚C for 4 h, followed by dialysis against MilliQ water in a Slide-a-Lyzer dialysis cassette (MWCO 3500, Pierce, Rockford, IL) for 48 h. After centrifuge, the supernatant was obtained and stored at 4 ˚C prior to use. The final concentration of silk fibroin is roughly 7% w/v, determined by weighing the residual of 1 mL solution.

Cs preparation: Cs was prepared following the method described previously with modification[133]. Alpha-chymotrypsin was added to aqueous silk fibroin solution by an enzyme to substrate weight ratio 1:100, followed by incubation at 37 ˚C for 24 h. The gel formed was then centrifuged at 4800 ×g for 30 minutes. The supernatant (Cs) was collected and kept at 80 ˚C for 20 minutes to denature alpha-chymotrypsin. The solution was centrifuged again, and the supernatant was stored at 4 ˚C prior to use. The concentration was determined by weighing dry residual.

Gel electrophoresis: The electrophoretic mobility of silk fibroin, Cs, and $Cs_{20}SF_{80}$ were determined using sodium dodecyl sulfate polyacrylamide gel electrophoresis (SDS-PAGE). 100 μg silk fibroin, 300 μg Cs, and 100 μg $Cs_{20}SF_{80}$ were mixed with 2X Laemmli Sample Buffer and loaded into a precast 4-15% polyacrylamide gel (Bio-Rad Laboratories, Hercules, CA). The gel was run for 23 minutes at 200 V with a prestained recombinant protein mixture as reference (Bio-Rad Laboratories). The gel was first washed twice with 5% (v/v) methanol in MilliQ water for 15 min each time. The gel was then stained by 0.001% crystal violet with 10% (v/v) methanol and 1.5% (v/v) acetic acid overnight.

Dynamic light scattering (DLS): Zeta Potential Analyzer (Brookhaven Instruments Corp., Holtsville, NY) was used to measure the particle size in resuspended solution at a concentration of 1 mg ml^{-1} dry material. Each measurement was 180 s and at least three measurements were carried out per sample's type.

Circular dichroism (CD): CD experiments were conducted with a JASCO Model J-1500 Circular Dichroism Spectrometer (JASCO Co., Japan). Aqueous solutions were diluted to 0.01% w/v, loaded into a 1 mm path quartz cell (Starna Cells, Inc., Atascadero, CA), and scanned at 25 °C with a resolution of 0.5 nm and a 4 s accumulation time at the rate of 50 nm min^{-1} from 250 nm to 185 nm wavelength. The results were averaged from three measurements.

Fourier Transform Infrared Spectroscopy (FTIR): IR measurements were carried out on a Spectrum 65 (PerkinElmer, Waltham, MA) equipped with an attenuated total reflection (ATR) generic UATR crystal, with a resolution of 4 cm^{-1} and accumulation of 32 scans from 4000 and 650 cm^{-1}. Films were cast on PDMS, dried overnight, and kept in a desiccator for 24 h to remove surface water. Analysis was performed based on the Amide I region (1595−1705 cm^{-1}) by OriginPro 2017 software (OriginLab Corporation, Northampton, MA), following the previously described method[135].

Raman spectroscopy: Raman spectra were obtained with a Renishaw inVia Raman Microscope (Renishaw PLC, Wotton-under-Edge, United Kingdom) with a laser 785 nm and a 10X objective. Data were collected and analyzed with software WiRE v5.2. Cs, silk fibroin, and $Cs_{20}SF_{80}$ were cast on PDMS and dried in a fume hood overnight. SF and $Cs_{20}SF_{80}$ films were immersed in 80% v/v methanol for 5 minutes described as 'methanol treatment' in the main text. Cs samples did not form a film but fragments, which were immersed into 1 ml 80% v/v methanol in a 6 mm petri dish until the completion of evaporation of liquid. H_2O_2 solution was mixed with $Cs_{20}SF_{80}$ solution at a material ratio of 5:1 and dried overnight in a hood. Three samples were tested for each case.

Thermogravimetric analysis (TGA): TGA curves were collected via a Discovery TGA model (TA instruments, New Castle, DE). Specimens were heated up at a rate of 10°C min^{-1} from 40°C to 500°C in nitrogen with a rate of 25.0 ml min^{-1}. Three samples were tested for each case.

Differential scanning calorimetry (DSC): DSC curves were collected via a Discovery DSC model (TA instruments, New Castle, DE). Specimens were heated up at a rate of 10°C min^{-1} from 40°C to 230°C (Cs) or 270°C (SF and $Cs_{20}SF_{80}$). Data were replotted with mass loss taken into consideration according to TGA results. Three samples were tested for each case.

Preservation of hydrogen peroxide and HRP: H_2O_2 can be enzymatically degraded by HRP, the product of which oxidizes 3,3',5,5'-Tetramethylbenzidine (TMB) and generates a deep blue color. Upon addition of acid solution, the blue color turns to yellow that can be recorded absorbance at 450 nm. Briefly, for hydrogen peroxide preservation, H_2O_2 was added to CsSF blend solution, with a final H_2O_2 concentration 0.1% w/v and CsSF material concentration 6% w/v. Films were prepared by dropping 50 µl solution on PDMS and drying overnight in a fume hood. Each film was dissolved in 500 µl water for absorbance reading. 5 µl of the sample solution was mixed with 80 µl of TMB solution and incubated for 1 minute at room temperature before the addition of 100 µl 0.1 M sulfuric acid. Absorbance was detected at 450 nm with reference at 620 nm by a Tecan microplate reader (Tecan Group Ltd, Switzerland). HRP preservation shared a similar protocol with the modification where HRP was added to CsSF blend solution to prepare films. The standard curve is in Figure S3.11.

Bacteria culture: *Rhizobium tropici* CIAT899 expressing bacterial GFP was obtained from Miguel Lara[166]. *R. tropici* was cultured at 30 °C to OD600 of 1 following the instructions before use. GFP gene was cloned into pEAQ-HT vector and transformed into *A. tumefaciens* strain (LBA4404). Transformants were cultivated and selected at 30 °C for 24-36 h to OD600 of 1.5 in YM medium (0.4 g L^{-1} yeast extract, 10 g L^{-1} mannitol, 0.1 g L^{-1} NaCl 0.2 g L^{-1} $MgSO_4 \cdot 7H_2O$, 0.5 g L^{-1} $K_2HPO_4 \cdot 3H_2O$, 15 g L^{-1} agar, pH 7) supplemented with 50 µg mL^{-1} rifampicin, 50 µg mL^{-1} kanamycin, and 50 µg mL^{-1} streptomycin.

Preservation of Agrobacterium tumefaciens: *A. tumefaciens* was cultured to OD600 1, centrifuged down at 3000 × g for 30 minutes and resuspended by SF and $Cs_{20}SF_{80}$ to the same volume. Films were prepared by dropping 50 µl suspension on PDMS and drying overnight in a fume hood. The

films were dissolved in 0.9% sterile NaCl solution and then spread on an agar plate for colony counting. A series of dilutions were prepared for better counting results.

Mechanical properties tests: Cs/silk fibroin solutions were cast on PDMS, dried overnight in a fume hood at room temperature, and cut into ribbons. Film tensile experiments were carried out on a Dynamic Mechanical Analysis (DMA) Q800 model (TA instruments, New Castle, DE) with a strain rate of 0.5% min^{-1} at room temperature. The static ultimate compression strength of phytoinjectors and puncture of plants' tissues were also conducted on a Dynamic Mechanical Analysis (DMA) Q850 model (TA instruments, New Castle, DE) using compression clamps at a loading speed of 1 mm min^{-1}. The sixth compound leaves from 7-week-old tomato plants (*Solanum lycopersicum*) having 13 compound leaves were collected to get tomato petiole and leaflet samples. Stems between the sixth and eighth leaves were collected from multiple plants as stem samples. The sixth leaves from 6-week-old tobacco (*Nicotiana benthamiana*) were collected as petiole and leaf samples. Green branches (not woody bark) and leaves of a navel orange tree (*Citrus sinensis*) were used as tissue samples. At least 3 samples were tested for each case. Nanoindentation measurements were performed on a Hysitron TriboIndenter with a nanoDMA transducer (Bruker, Billerica, MA). Samples were indented in load control mode with a peak force of 500 μN and a standard load-peak hold-unload function. Reduced modulus was calculated by fitting the unloading data (with upper and lower limits being 95% and 20%, respectively) using the Oliver-Pharr method. Each type of sample was prepared and indented in triplets to ensure good fabrication repeatability. For each sample, indentation was performed at a total of 49 points (7×7 grid with an increment of 20 μm in both directions) to ensure the statistical reliability of the modulus measurements.

Payloads release: Simulated sap was prepared according to the xylem exudate[132,167]. Rhodamine 6g and azoalbumin were added to SF and $Cs_{20}SF_{80}$ (6% w/v of dry materials) to get a final concentration of 0.1 mM and 2 mg ml^{-1}, respectively. R. tropici was centrifuged at 3000 × g for 30 minutes and resuspended by SF and $Cs_{20}SF_{80}$ to get an OD600 of 1. The solutions were then cast on PDMS and dried overnight in a hood. The films were then cut into discs and attached to the bottom of a well of a 48 well plate, enabling only one side of the disc exposed to simulated sap. 1 ml of fresh simulated sap was added after the previous solution was collected for measurement. Released rhodamine 6g and GFP-expressing *R. tropici* were monitored based on fluorescence intensity (excitation at 524 nm and 499 nm, emission at 550 nm and 520 nm). Released azoalbumin was monitored based on absorbance at 410 nm. At least three samples were tested for each case. The standard curve is in Figure S3.11.

Master and negative mold fabrication: The aluminum master was fabricated by computer numerical control (CNC) machining with a 1/32'' flat end mill for rough milling, followed by a 1/64'' ball end mill for finishing. The templates were then chemically etched to the desired topologies based on application by aluminum etchant type A (Transene, Danvers, MA). To produce negative, Poly(dimethyl siloxane) (PDMS) (Sylgard 184, Dow-Corning, Midland, MI) was cast over Al master in a 60 mm petri dish, degassed, and finally incubated at 70 ˚C for 2 h.

Phytoinjector fabrication: The desired amount of payloads were mixed with $Cs_{20}SF_{80}$ solution and added to negative PDMS molds, followed by centrifuge at 1200 ×g for 15 minutes. Molds were then kept in a fume hood to dry at room temperature overnight. The phytoinjector array was then cut into smaller arrays by a razor blade for tissue application.

Plant materials: Tobacco (*Nicotiana benthamiana*) and tomato (*Solanum lycopersicum*) plants were grown in pots in a plant chamber with ambient temperature 25 ˚C day/20 ˚C night and a 10

h photoperiod. Tobacco plants between 4-6 weeks old after germination are used for experiments, while tomato plants were used when they are 5-8 weeks old from seeds. A navel orange tree (*Citrus sinensis*) was grown in a 15' pot with regular water and fertilizer feeding in 25˚C day/20˚C night and 12 h photoperiod.

Histology: Tomato plant tissues of interest were collected and kept in 10% formalin for 24 h, followed by immersion in 70% ethanol before processing by a Rapid Biopsy Processing on the Vacuum Infiltrating Tissue Processor for paraffin filling. 10 μm thick slices were prepared by a microtone and stained by Safranin O stain and Fast Green after deparaffinization.

Payloads delivery to tomato plant: 5(6)-carboxyfluorescein diacetate (1 mM) and rhodamine 6G (1 mM) was mixed with 6% wt/v $Cs_{20}SF_{80}$ solution (volume ration 1:100) to fabricate phytoinjectors which were used to demonstrate the capability of phytoinjector to deliver payloads to xylem and phloem, repectively. The upstream and downstream cross-sections along the petiole were observed under microscope to record the appearance of fluorescence due to delivery and transport of 5(6)-carboxyfluorescein diacetate and rhodamine 6G with fixed light intensity and exposure time (20 ms). The petiole was also sliced longtutionally to image distribution profile of 5(6)-carboxyfluorescein diacetate in xylem. Images were analyzed with imageJ 1.52i. Fluorescence intensity was used to represent the concentration of 5(6)-carboxyfluorescein diacetate within the range we used. Fluorescence signal was integrated along the radial direction. 50 μl 15 mg/ml D-luciferin potassium salt solution was added to 2.5 ml 6% wt/v $Cs_{20}SF_{80}$ solution to fabricate luciferin loaded xylem phytoinjectors. Luciferin-loaded phytoinjectors were injected into petioles near a termial leaflet of a tomato compound leaf. Solution containing 150 uM ATP and 5 mM $MgCl_2$ and 10 μg ml^{-1} luciferase was delivered to the leaflet via foliar infiltration. The leaflet was then imaged in a dark room via a Nikon 3400 camera with an exposure time of 30 s.

Images were modified with an ad-hoc Matlab script to double the intensiy of the RGB signal for display purposes due to the original low luminescence intensiy. Similarly, luciferin and luciferase loaded phytoinjectors were injected on petiole near a leaflet and ATP and $MgCl_2$ were delivered externally. The leaflet was imaged with exposure time 120 s and ad-hoc Matlab script was applied to double the intensiy of the RGB signal for display purposes.

Sampling via xylem phytoinjector fabricated from pure SF: luciferin and $MgCl_2$ were loaded to $Cs_{20}SF_{80}$ xylem phytoinjectors, which were then injected to tomato petioles. Phytosamplers fabricated from pure silk fibroin were injected to the nearby position on the same petiole, supposing they reach the same xylem of $Cs_{20}SF_{80}$ xylem phytoinjectors. The phytosamplers were flipped on a glass slide and a drop of ATP and luciferase solution was added to image luminiscence. The camera exposure time was set to 30 s. 1% agar gel was prepared in a petri dish with thickness of ~3 mm in order to maintain high transparency. Phytosamplers were injected into the agar gel and images were taken with a Nikon TE2000-E microscope (Nikon Inc., Minato City, Tokyo, Japan) using a 4x objective at 10 s intervals to investigate the movement of water from the gel to inside the phytosampler, thus, the sampling behavior. The movement of the interface between dry silk fibroin and rehydrated silk fibroin along the phytosampler length direction was collected via imageJ and used to plot the penetration length *vs* time.

Agrobacterium mediated gene transfer to shoot apical meristem and leaves: Agrobacterium loaded phytoinjectors were injected into SAM, young leaf, and mature leaf of 5-week-old tobacco. Fluorescent leaves were imaged via a Invitrogen Safe Imager 2.0 Blue-Light Transilluminator (Thermo Fisher Scientific Inc., Waltham, MA) and Nikon TE2000-E microscope (Nikon Inc., Minato City, Tokyo, Japan) 2 weeks post injection when the SAM grew to a leaf.

Acknowledgements

This work was supported by the Office of Naval Research (award N000141812258, B.M.), the National Science Foundation (award CMMI-1752172, B.M.), and the Keck Foundation (J.K.W.). The authors acknowledge the Center for Materials Science and Engineering (CMSE), DMSE NanoLab, Biophysical Instrumentation Facility (BIF), Institute for Soldier Nanotechnologies (ISN), and Microsystems Technology Laboratories (MTL), all at MIT, for access to the characterization instruments. We thank the Koch Institute Swanson Biotechnology Center for technical support, specifically Kathleen Cormier. We gratefully acknowledge Stephen Rudolph (MIT) for master fabrication and Hui Sun (MIT) for nanoindentation. We thank Miguel Lara (Universidad Nacional Autónoma de México) for providing *Rhizobium tropici* CIAT899. The authors also acknowledge support from the Paul N. Cook Career Development Professorship and the MIT Research Support Committee.

3.4 Supplementary Information

3.4.1 Supplementary analysis

3.4.1.1 Analysis of interaction between Cs and silk fibroin

Cs is family of highly water soluble, negatively charged peptides extracted from silk fibroin heavy chain with a MW between 2-10kDa (Figure S3.1) and a primary structure that accounts for only 10-15% of hydrophobic amino acids. We used Cs to enhance silk fibroin solubility for in planta application to build on the biodegradability and non-toxic nature of silk-based materials. Silk fibroin used in this study has an average MW of 100-150 kDa (Figure S3.1) and we fabricated blends with a weight ratio between 0 to 40% Cs. By molarity, this means that in the blends, the number of Cs molecules is larger than the amount of silk fibroin. For example, for $Cs_{20}SF_{80}$ blends, we have roughly five times more Cs molecules than silk fibroin ones in the final material. Cs is incorporated in silk materials during the assembly process, when hydrogen bonds between silk nanomicelles and water are replaced with intermolecular hydrogen bonds. During this step,

nanomicelles coalesce and form a monolithic material. Cs would then participate in this assembly process as it is made by a portion of the silk fibroin primary structure. However, being of smaller MW, the incorporation of Cs results in the weakening of the interactions/entanglement between large silk fibroin molecules, ultimately enhancing material disassembly upon exposure to water. The intermolecular and intramolecular interaction of hydrophobic amino acid domains may also be weakened. To further explore this mechanism, we have conducted several investigations of silk fibroin-Cs interactions both in water suspension and in solid, monolithic materials (i.e. film format).

In aqueous suspension, Cs does not show noticeable influence on silk nanomicelle size and on the secondary structure of the protein, as supported by DLS and CD measurements (Figure S3.1 and Figure 3.2b, respectively). Additionally, SDS-PAGE analysis of Cs-silk fibroin blends shows no aggregation or dimerization of Cs exposed to silk fibroin (Figure S3.1b). Investigation of the Cs-silk fibroin blends in the solid format was conducted using WAXS, SAXS, TGA, DSC, ATR-FTIR and Raman. WAXS and SAXS showed no difference between silk fibroin and $Cs_{20}SF_{80}$ samples since the materials are not crystal dominant. Given the low impact of this study to the manuscript we did not incorporate the results of crystallography analysis in SI.

ATR-FTIR spectra of silk fibroin mixed with various content of Cs from 0% up to 40% were collected and showed no significant difference (Figure S3.2); all the spectra depicted a wide peak centered around 1645 cm^{-1}, corresponding to random coil. Self-deconvolution and peak fitting were carried out for all the spectra collected to quantify the secondary structure content in each sample. Incorporation of increasing concentrations of Cs in the blends did not result in a change of beta sheet content, showing that Cs did not drive a random coil to beta-sheet transition during silk fibroin assembly. Turns increased slightly as the Cs content increases, which may be attribute

to the intrinsic properties of Cs, which serves as hydrophilic linkers. To further investigate the interactions between silk fibroin and Cs in solid state, Raman spectra were collected for Cs, silk fibroin, and $Cs_{20}SF_{80}$ before (solid line) and after (dotted line) methanol treatment (Figure S3.3). In particular, in this study we focused on the Amide I and III shifts and on the Fermi doublet peaks of the tyrosyl phenolic ring at 853 and 829 cm^{-1}[137]. In all the samples analyzed, analysis of the Amide bands showed that exposure to methanol resulted a random coil to beta-sheet transition of the silk materials, indicating Cs does not hinder polymorphic changes of the structural protein. The intensity ratio I_{853}/I_{829} has been used to study the hydrogen bonding formed by the tyrosyl phenolic-OH – a more hydrophobic tyrosine environment (i.e., reduction of structural water in the protein and of hydrogen bonding) corresponds to higher I_{853}/I_{829} ratio. As shown in Table S3.1, the inclusion of Cs in silk fibroin materials results in an increased I_{853}/I_{829} ratio, which corroborates the proposed mechanism that Cs reduces the formation of intermolecular hydrogen bonds.

Thermal analysis (Figure S3.4) showed decomposition at about 180˚C for Cs, 225˚C for silk fibroin and 205˚C for $Cs_{20}SF_{80}$. Calorimetric analysis depicted a T_g for Cs at 60˚C, for silk fibroin at 77˚C and at 75˚C for $Cs_{20}SF_{80}$. In literature, this is referred to as the first T_g, i.e. $T_g(1)$ of water-containing silk materials and corresponds to the removal of free water molecules entrapped between silk fibroin molecules during the random coil to beta sheet transition of the material. An exothermic peak was depicted at 125˚C for silk fibroin only, followed by a large endothermic process. The exothermic peak is described in literature as formation of more stable structures in silk where water is present and acts as a plasticizer. The endothermic process is present in SF and $Cs_{20}SF_{80}$ samples and it corresponds to the release of some of the bound water molecules as free water and subsequent evaporation. The lack of the exothermic peak in the $Cs_{20}SF_{80}$ blend may be used as an evidence that Cs weakens the entanglement of silk fibroin molecules and reduces the

formation of new, stable conformations between adjacent silk molecules upon water release. Both silk fibroin and $Cs_{20}SF_{80}$ blend showed an exothermic peak at 222°C and 214°C, respectively, which corresponds to a non-isothermal crystallization peak of silk material[138,139].

3.4.1.2 Payload release profiles from SF and $Cs_{20}SF_{80}$

Payload release profiles in silk fibroin constructs have been studied extensively in controlled drug release applications[130,131,153,168], with most studies indicating that diffusion, swelling, and proteolytic degradation are primary drivers in this process. As targeted plant tissues are not protease-rich, we used simulated sap to investigate payload release profile. Rhodamine 6G, azoalbumin, and GFP-expressing *Rhizobium tropici* CIAT 899 (GFP-CIAT 899) were used as representative models for small molecules, large proteins, and bacteria, and their release profiles in SF and $Cs_{20}SF_{80}$ were investigated. GFP-CIAT 899 was used in the release study in lieu of *Agrobacterium* as several attempts of staining *Agrobacterium* were inconclusive due to interaction between silk fibroin and the dyes used for live/dead assays. Silk fibroin and $Cs_{20}SF_{80}$ were found to have negligible effects on fluorescence and absorbance signal. The release profile of all three payloads for both silk fibroin and $Cs_{20}SF_{80}$ follow a power law (**Figure S3.7**a) described by the semi-empirical model developed by Ritger and Peppas[131,168],

$$f_t = \frac{M_t}{M_\infty} = kt^n, \quad \text{(S1)}$$

which can be rewritten as $\lg(f_t) = lg(k) + nlg(t)$, where f_t is the fraction of released payload at time *t*, M_t is the amount of released payload over time *t* (unit: hour), M_∞ is the amount of released payload at infinity time, (i.e., the total payloads loaded), *k* denotes the release velocity constant determined by the structural and geometric characteristic of the system, and *n* denotes the exponent of release indicating the release mechanism. Parameters for the power law were obtained by linear fitting, shown in Table S3.2. Figure S3.7b depicts film surfaces of $Cs_{20}SF_{80}$ samples before release

(silk fibroin samples have similar surfaces). Surface erosion is observed for all three releases from silk fibroin (Figure S3.7c), while much faster payloads release and combination of surface and bulk erosion is observed for release from $Cs_{20}SF_{80}$ (Figure S3.7d). Rhodamine 6G release from SF (n = 0.93) is *anomalous* and dominated by both diffusion and swelling. Azoalbumin release (n = 1.13) indicates a *Super Case II* release mechanism, possibly resulting from the secondary structure of azoalbumin (primarily α-helices) that lowers the interaction among silk fibroin chains and facilitates the disaggregation of swollen silk fibroin samples. GFP-CIAT 899 release is nearly identical to azoalbumin, but the sample surface shows protrusions, which display similar morphology to GFP-CIAT 899. All three payloads loaded into $Cs_{20}SF_{80}$ possessed a *Super Case II* release mechanism (n>1). This is likely due to the hydrophilicity of Cs, which dissolves easily in simulated sap and expedites the rate of sample degradation. These results show that $Cs_{20}SF_{80}$ allows for faster payload release profiles than SF, from small molecules, to large proteins, and to bacteria.

3.4.1.3 Release and transport model in xylem

The velocity of xylem sap flow is at the order of 10^{-3} m s^{-1} although it varies a lot according to the condition of measured plants during the day[143]. However, the velocity we got here is at the order of 10^{-5} to 10^{-4} m s^{-1}, which may due to the influence of injection. This gives a Péclet number $Pe = Lu/D \sim 10$, where L is the diameter of xylem (~10^{-4} m), u is the velocity of sap flow in xylem, and D denotes the diffusion coefficient of the payload delivered in xylem sap (10^{-10} m^2 s^{-1}). Thus, both advection and diffusion should be taken into consideration in this scenario. The common form of the advection-diffusion equation for an impressible fluid without source and sink is

$$\frac{\partial c}{\partial t} = \nabla \cdot (D\nabla c) - \boldsymbol{v} \cdot \nabla c \quad \text{(S2)}$$

Since we focus on the longitudinal transport along xylem, Equation S1 can be simplified to one dimensional (1D) condition as

$$\frac{\partial c}{\partial t} = D\frac{\partial^2 c}{\partial x^2} - u\frac{\partial c}{\partial x} \quad \text{(S3)}$$

The initial condition (IC) and boundary conditions (BCs) are as follow

IC: $c(x,0) = 0$

BCs: $c(0,t) = c_0(t)$, $c(\infty,0) = 0$.

Once a phytoinjector is injected into xylem, the payload is released following the power law, contributing to the concentration change at x=0 at time t $c_0(t)$ (Schematic S3.1). Mass conservation, i.e. payload released equals to that in the xylem, can be used to determine $c_0(t)$.

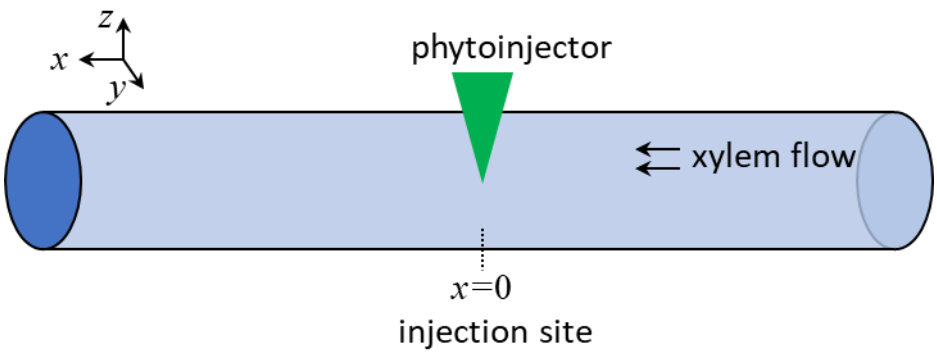

Schematic S3.1. Schematic of the model for release.

To solve this problem, let

$$c(x,t) = \Gamma(x,t)e^{\frac{ux}{2D} - \frac{u^2 t}{4D}} \quad \text{(S4)}$$

the Equation S3 can be rewritten as

$$\frac{\partial \Gamma}{\partial t} = D\frac{\partial^2 \Gamma}{\partial x^2} \quad \text{(S5)}$$

IC: $\Gamma(x,0) = 0$

BCs: $\Gamma(0,t) = f(t) = c_0(t)e^{\frac{u^2 t}{4D}}$, $\Gamma(+\infty,0) = 0$.

Considering the Laplace transform of a function $f(x,t)$,

$$\bar{f}(x,s) = \mathcal{L}[f(x,t)] = \int_0^{+\infty} e^{-st} f(x,t)dt. \quad \text{(S6)}$$

The Laplace transform of Equation S5 is

$$\frac{d^2\bar{\Gamma}(x,s)}{dx^2} - \frac{s}{D}\bar{\Gamma}(x,s) = 0 \quad \text{(S7)}$$

subjecting to boundary conditions

$\bar{f}(s) = \bar{\Gamma}(0,s) = \int_0^{+\infty} c_0(t) e^{\frac{u^2 t}{4D} - st} dt$, and $\bar{\Gamma}(+\infty, s) = 0$.

The solution of Equation S7 is

$$\bar{\Gamma}(x,s) = \bar{f}(s) e^{-x\sqrt{\frac{s}{D}}} = \mathcal{L}[f(t) * g(x,t)] \quad \text{(S8)}$$

which can be considered as the Laplace transform of the convolution of two functions $f(t)$ and $g(x,t)$, where $g(x,t) = \mathcal{L}^{-1}\left[e^{-\frac{x}{\sqrt{D}}\sqrt{s}}\right] = \frac{x}{\sqrt{4\pi D t^3}} e^{-\frac{x^2}{4Dt}}$.

The inversion of $\bar{\Gamma}(x,s)$ gives

$$\Gamma(x,t) = \int_0^t f(\tau) g(x, t-\tau) d\tau = \frac{x}{\sqrt{4\pi D}} \int_0^t \frac{c_0(\tau)}{\sqrt{(t-\tau)^3}} e^{\frac{u^2\tau}{4D} - \frac{x^2}{4D(t-\tau)}} d\tau. \quad \text{(S9)}$$

The concentration thus is

$$c(x,t) = \frac{x}{\sqrt{4\pi D}} e^{\frac{ux}{2D} - \frac{u^2 t}{4D}} \int_0^t \frac{c_0(\tau)}{\sqrt{(t-\tau)^3}} e^{\frac{u^2\tau}{4D} - \frac{x^2}{4D(t-\tau)}} d\tau, \text{ (x>0)} \quad \text{(S10)}$$

$$c(x,t) = \frac{-x}{\sqrt{4\pi D}} e^{\frac{ux}{2D} - \frac{u^2 t}{4D}} \int_0^t \frac{c_0(\tau)}{\sqrt{(t-\tau)^3}} e^{\frac{u^2\tau}{4D} - \frac{x^2}{4D(t-\tau)}} d\tau, \text{ (x<0)} \quad \text{(S11)}$$

Thus the concentration for the whole field is

$$c(x,t) = \frac{|x|}{\sqrt{4\pi D}} e^{\frac{ux}{2D} - \frac{u^2 t}{4D}} \int_0^t \frac{c_0(\tau)}{\sqrt{(t-\tau)^3}} e^{\frac{u^2\tau}{4D} - \frac{x^2}{4D(t-\tau)}} d\tau. \quad \text{(S12)}$$

In addition, the concentration must meet mass conservation

$$M_t = M_\infty k t^n = \int_{-\infty}^{+\infty} c(x,t) dx. \quad \text{(S13)}$$

This integral equation determines boundary condition $c(0,t) = c_0(t)$ and thus $c(x,t)$. While it is hard to explicitly solve the integral equation, we can solve it numerically. By Taylor series, we have

$$\left(\frac{\partial c}{\partial t}\right)_i^n = \frac{c_i^{n+1} - c_i^n}{\Delta t} + O(\Delta t),$$

$$\left(\frac{\partial c}{\partial x}\right)_i^n = \frac{c_{i+1}^n - c_{i-1}^n}{2\Delta x} + O(\Delta x^2)$$

$$\left(\frac{\partial^2 c}{\partial x^2}\right)_i^n = \frac{c_{i+1}^n - 2c_i^n + c_{i-1}^n}{\Delta x^2} + O(\Delta x^2)$$

Where *n* denotes time *t* and *i* is position *x*.

Equation S3 can be approximated as

$$\frac{c_i^{n+1} - c_i^n}{\Delta t} = D\frac{c_{i+1}^n - 2c_i^n + c_{i-1}^n}{\Delta x^2} - u\frac{c_{i+1}^n - c_{i-1}^n}{2\Delta x} + O(\Delta t, \Delta x^2) \quad \text{(S14)}$$

and

$$c_i^{n+1} = c_i^n - \frac{u\Delta t}{2\Delta x}(c_{i+1}^n - c_{i-1}^n) + \frac{D\Delta t}{\Delta x^2}(c_{i+1}^n - 2c_i^n + c_{i-1}^n) \quad \text{(S15)}$$

The code was written in MATLAB R2019a. Parameters to carry out the simulation used are $D = 4 \times 10^{-10} m^2/s$, $u = 5 \times 10^{-5} m/s$, $k = 0.038$ (for time unit minute), and $n = 1.61$. The power law release describes well the first 60% payload release but not for 100%. Thus, our model well describes the release and transport in the first 5 minutes only. For longer time period, the payload loaded to other parts of the phytoinjector may also be released and contributes as payload source at the injection site, which invalidates the mass conservation assumption used here.

3.4.1.4 Lucas-Washburn model for phytosampler

Reswelling of the phytoinjectors and diffusion of metabolite and catabolite in silk phytosampler was modeled with a Lucas-Washburn equation[149]. The fitting was carried out in MATLAB R2019a

Curve Fitting Toolbox on collected data of penetration depth of water frontier in a phytosampler over time.

The fitting equation is

$$H = 36.42\sqrt{t - 54.32}, \quad \text{(S16)}$$

where H is the penetration depth, t is time (unit second). The adjusted R^2=0.9932. The time t_0=54.32 s may attribute to the cone shape of the phytosampler, which does not match the 1D case for Lucas-Washburn model.

3.4.1.5 Estimation of the amounts of payloads delivered by phytoinjectors

We have estimated the amount of cargo molecules delivered for a payload equivalent to 10wt% and compared it with the functional amount found in several plant tissues. In particular, we found that the deliverable weight of cargo molecules is in the order of 10s of ng per phytoinjector.

The total volume of xylem and phloem phytoinjector (V_{phyt}) is 18.74±1.05 nl and 9.11±1.83 nl, respectively. Given that Cs-silk fibroin blends have a density of 1.40 g cm^{-3} (which is equal to 1.4 µg nl^{-1}), the weight of xylem and phloem phytoinjector is 26.24 µg and 12.75 µg, respectively. Let's define that the phytoinjector tip volume of V_{tip}=3% of V_{phyt} (the tip length 100 - 200 µm). Assuming to load the phytoinjector with a 10wt% payload, this would correspond to the loading of 78.7 ng of cargo molecules for xylem phytoinjector and of 38.3 ng of cargo molecules for phloem phytoinjector (Table S3.3).

Plant hormones level is usually in the range of 0.1-50 ng g^{-1} of fresh weight[169]. As hormones are found in specific tissues such as shoot apical meristem and leaves, which have a weight in the order of tens to hundreds of milligrams, the delivered level of hormones by phytoinjectors would provide the plant with physiologically relevant quantities of hormones.

Micronutrients are present in plant tissues at concentration of ppm per dry weight, which approximately equals to 100ng g^{-1} fresh weight. This makes phytoinjectors suitable for delivering a wide range of micronutrients, including Cu, Mo, and Ni. (Table S3.4[170]). Note that micronutrients deficiency does not mean we need to deliver adequate concentration of micronutrients to plants. In addition, according to our experience, less than 1 ng of siRNA per leave of *Nicotiana benthamiana* result in the suppression of chlorophyll synthesis, indicating a very low functioning quantity of iRNA

3.4.1.6 MATLAB code for payloads release

```
function release
%This function is used to solve the release of payloads from
%phytoinjector and transport in xylem and phloem.
%The model is 1D advection-diffusion equation.

%Constants
%D=7.0*10^(-10);  %Diffusion coefficient of Mg2+ ion in water
%D=4.0*10^(-10);  %Diffusion coefficient of R6G/5(6)-Carboxyfluorescein diacetate in water
%D=6.1*10^(-11);  %Diffusion coefficient of albumin in water
%u=10^(-3);       %Velocity of sap in xylem
%u=10^(-4);       %Velocity of sap in phloem

D=4.0*10^(-10);
u=5*10^(-5);
k=0.038;        %M=Minf*k*t^(nn), M/Minf<=60, tmax is calculated
nn=1.61;
Minf=1;

tmax=round(60*(0.6/k)^(1/nn));%Total time,unit second
%tmax=300;
dt=0.001;          %Time step,
tN=tmax/dt;

L=0.1;        %2N+1 is the number of points along x L=0.1m
N=10000;
dx=L/(2*N);

%Matrice
c_tn=zeros(1,2*N+1); %t=n*dt Concentration of payloads at each point
c_tn1=zeros(1,2*N+1); %t=(n+1)*dt Concentration of payloads at each point
c_x0=zeros(1,tN+1);  %c_x0(t), Concentration at x=0, c(N+1). t=0,c0(1)=0
```

```
cinf=0;          %Concentration at infinite, c(1)=c(2*N+1)=0

x=-L/2:dx:L/2;

t_output=[60 180 300];   %used to determine when to write c(x,t), -L/2<=x<=L/2
ct=zeros(length(t_output),2*N+1);
ij=0;

for n=0:tN-1
   t=(n+1)*dt;
   cn_tem=c_tn;

   m_err=1e-6;
   aa_lower=0;aa_upper=1;aa=1;
   while abs(m_err)>1e-8
      if aa>0
         [aa,aa_upper,aa_lower]=increase(m_err,aa,aa_upper,aa_lower);
      %else
       %   aa_lower=-1;aa_upper=0;aa=-1;
       %   [aa,aa_upper,aa_lower]=increase(m_err,aa,aa_upper,aa_lower);
      end

      %Initialization
      M_tn=Minf*k*(dt/60)^nn*((n+1)^nn-(n)^nn); % material released at tn
      c_x0(n+2)=c_x0(n+1)+aa*M_tn/dx;  %c0(x=0,t)
      cn_tem(N+1)=c_x0(n+2);

      c_tn1(1)=cinf;       %BCs x=-L/2
      c_tn1(2*N+1)=cinf;   %x=L/2
      for i=2:N*2
         c_tn1(i)=cn_tem(i)-...
               u*dt/(2*dx)*(cn_tem(i+1)-cn_tem(i-1))+...
               D*dt/(dx)^2*(cn_tem(i+1)-2*cn_tem(i)+cn_tem(i-1));
         if c_tn1(i)<0
            c_tn1(i)=0;
         end
      end
      %material released error during n to n+1 dt period
      m_err=sum((c_tn1-c_tn))*dx-M_tn;
   end

   c_x0(n+2)=c_tn1(N+1);  %c(x=0,t=t)
   c_tn=c_tn1;

   %used to determine when to write c(x,t), at every 0.1*tmax
   if ismember((n+1)*dt,t_output)
```

```
        ij=ij+1;
        ct(ij,:)=c_tn;
    end

end


t=0:dt:tmax;
fileID = fopen('concentration vs time.txt','w');
fprintf(fileID,'%10s %12s %12s %12s\r\n','x','t0','t1','t2');
fprintf(fileID,'%10.8f %12.8f %12.8f %12.8f\r\n',[x;ct]);
fclose(fileID);

fileID2 = fopen('c_x0 vs time','w');
fprintf(fileID2,'%10s %12s\r\n','time(s)','c_x0');
fprintf(fileID2,'%10.8f %12.8f\r\n',[t;c_x0]);
fclose(fileID2);

figure
ax1=subplot(2,1,1);
grid on
plot(ax1,t,c_x0)
title('concentration at x=0 vs. time')
xlabel(ax1,'Time(s)')
ylabel(ax1,'Concentration')

ax2=subplot(2,1,2);
grid on
plot(ax2,1000*x,ct(:,:))
title('concentration distribution at different time')
xlabel(ax2,'x(mm)')
ylabel(ax2,'Concentration')
end

function [aa,aa_upper,aa_lower]=increase(m_err,aa,aa_upper,aa_lower)
    if m_err>0
        aa_upper=aa;
    else
        aa_lower=aa;
    end
    aa=(aa_lower+aa_upper)/2;
end
```

3.4.2 Supplementary figures

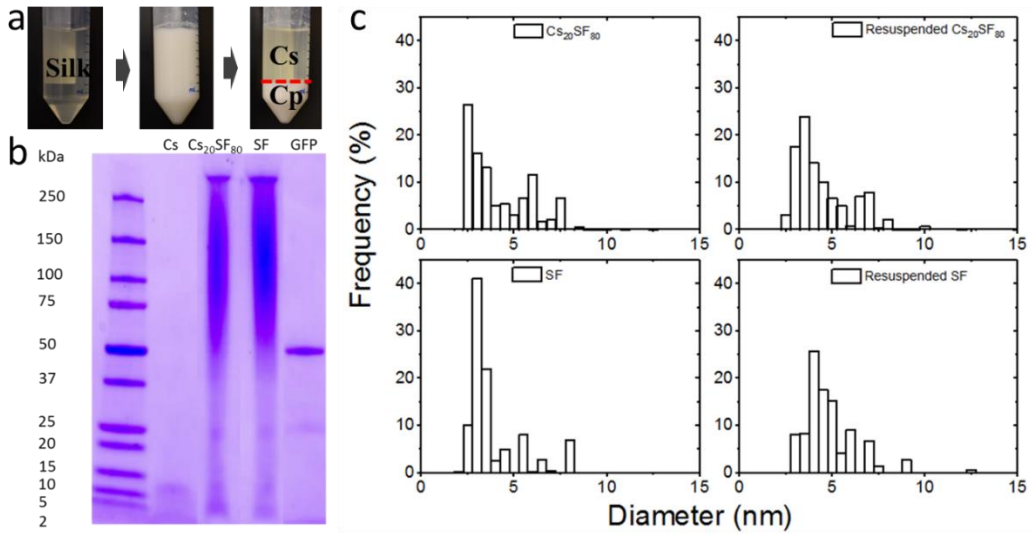

Figure S3.1. Cs fabrication and material size distribution. a, Photographs of: silk fibroin solution, gel formed after 24 h incubation at 37 °C of silk fibroin and alpha-chymotrypsin, and Cs after centrifuge. **b,** SDS-PAGE of silk fibroin (SF), Cs, $Cs_{20}SF_{80}$, and GST tagged GFP (~53kDa). **c,** Size distribution of as prepared $Cs_{20}SF_{80}$, SF and resuspended $Cs_{20}SF_{80}$ and SF. Pure Cs solution has a hydrodynamic radius below 1 nm.

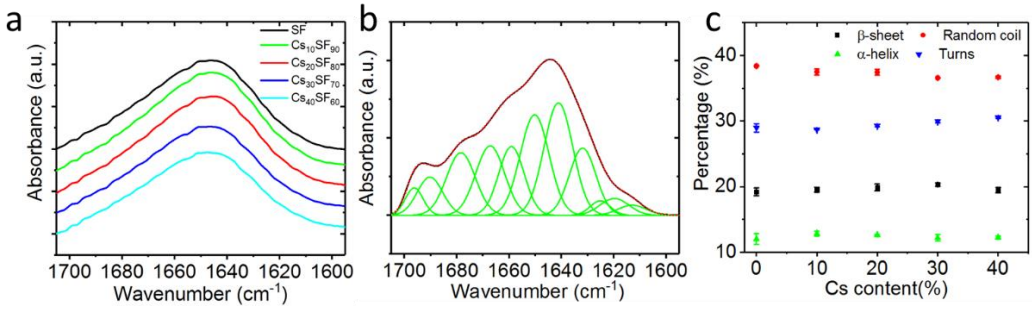

Figure S3.2. ATR-FTIR spectra of CsSF blend and quantification of secondary structure. a, ATR-FTIR spectra of CsSF blend with increasing Cs content. All the investigated ratios of silk:Cs showed similar spectra with a strong peak at 1645 cm^{-1} indicating water-soluble random coil conformation. **b,** Self-deconvolution curve of the ATR-FTIR spectrum of SF and peak fitting. Black solid line is the self-deconvoluted curve, red dot line is the fitted curve by individual peaks (green). **c**. Percentage of secondary structures in CsSF blends with increasing Cs content. Error bar means s.d.

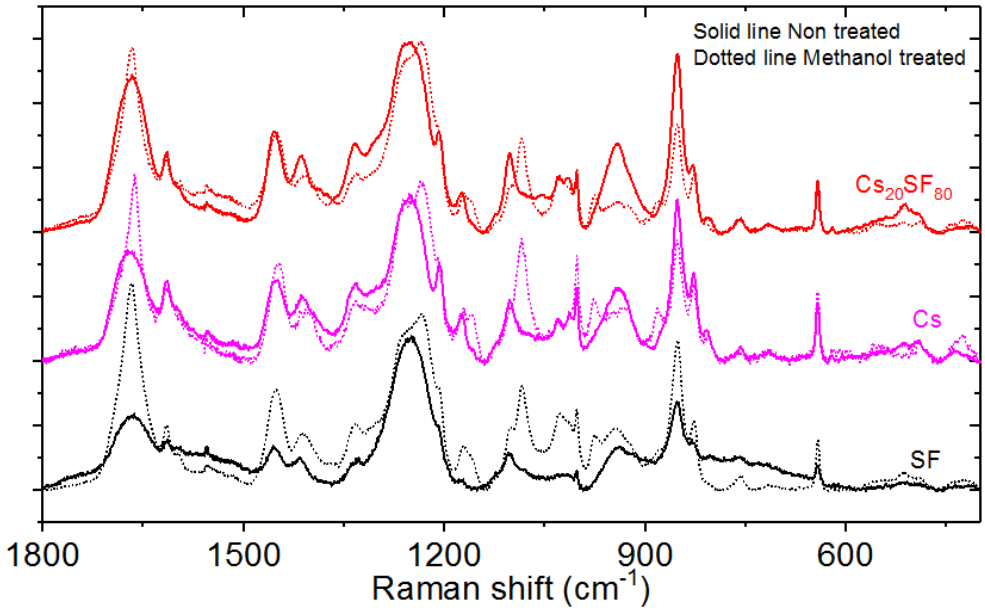

Figure S3.3. Raman spectra of Cs, $Cs_{20}SF_{80}$, and SF. Solid lines indicates samples that are as prepared while dotted lines refer to samples treated in 80% v/v methanol. Cs shows a polymorphic behavior upon exposure to methanol as it undergoes a random coil to beta-sheet transition (changes in Amide I and III bands).

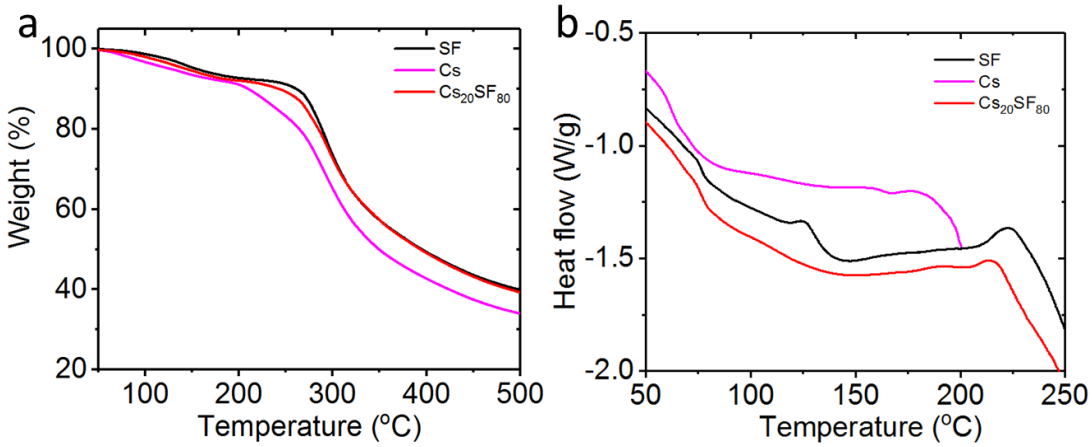

Figure S3.4. TGA (a) and DSC (b) thermograms of Cs, $Cs_{20}SF_{80}$, and SF.

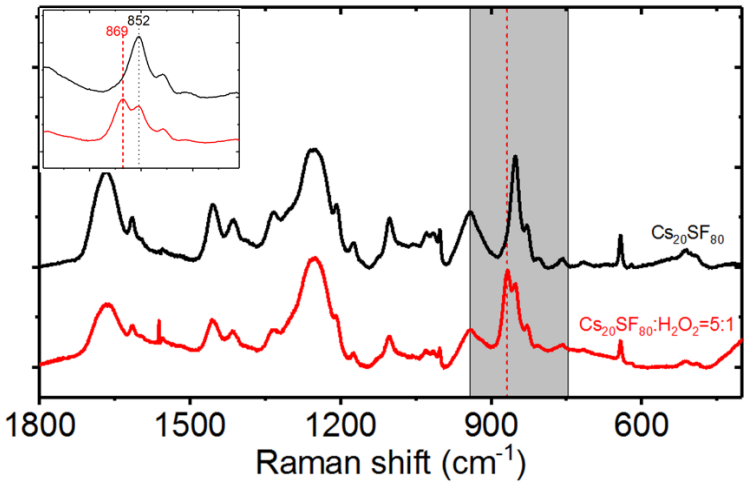

Figure S3.5. Raman spectra of $Cs_{20}SF_{80}$ with and without H_2O_2. The characteristic band of H_2O_2 880 cm^{-1} shifts to 869 cm^{-1} due to the contribution of a protein band at 852 cm^{-1}.

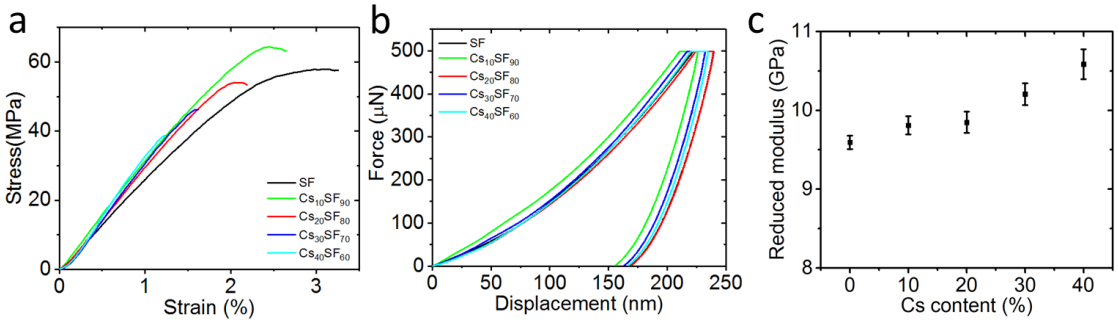

Figure S3.6. Mechanical properties of CsSF blend. a, Stress-strain curves of CsSF blends. **b,** Force-displacement curves of nanoindentation of CsSF blends. **c,** Reduced Young's modulus of CsSF blends. Error bar means s.d.

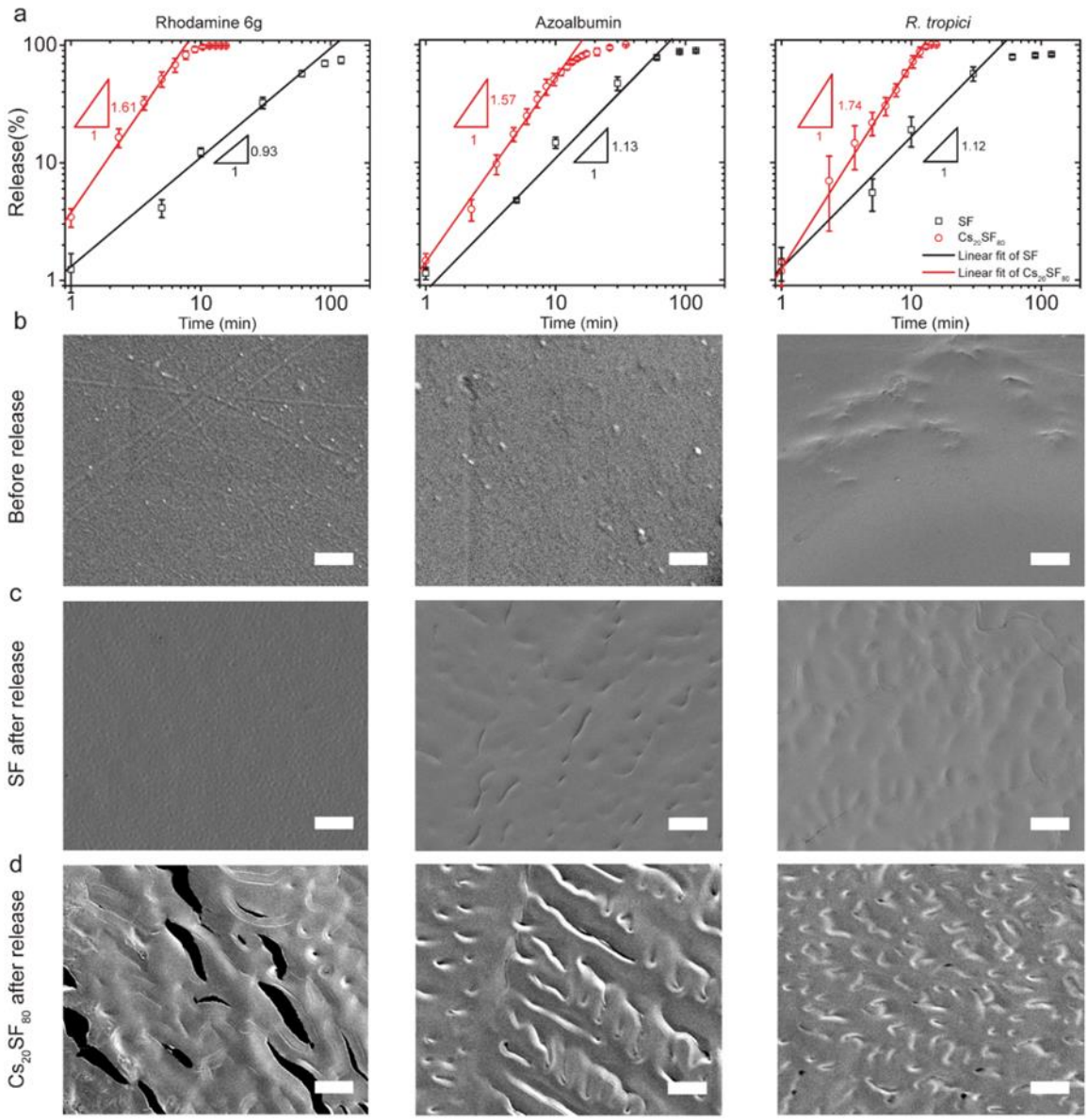

Figure S3.7. Release of payload models in simulated sap. a, Rhodamine 6g (left), azoalbumin (middle), and *R. tropici* (right) preserved in SF and $Cs_{20}SF_{80}$ release in simulated sap. All the payloads encapsulated in the two materials follow a power law release. $Cs_{20}SF_{80}$ showed an increased release rate than SF. **b,** Scanning electron micrographs of $Cs_{20}SF_{80}$ with different payloads. The surfaces of rhodamine 6g and azoalbumin loaded are flat and smooth, while the surface of *R. tropici* loaded materials shows the bacteria profiles. **c** and **d,** SEM images of SF and $Cs_{20}SF_{80}$ materials after 5 mins exposure to simulated sap. Scale bar, 10 μm. Data are mean ± s.d (n=3).

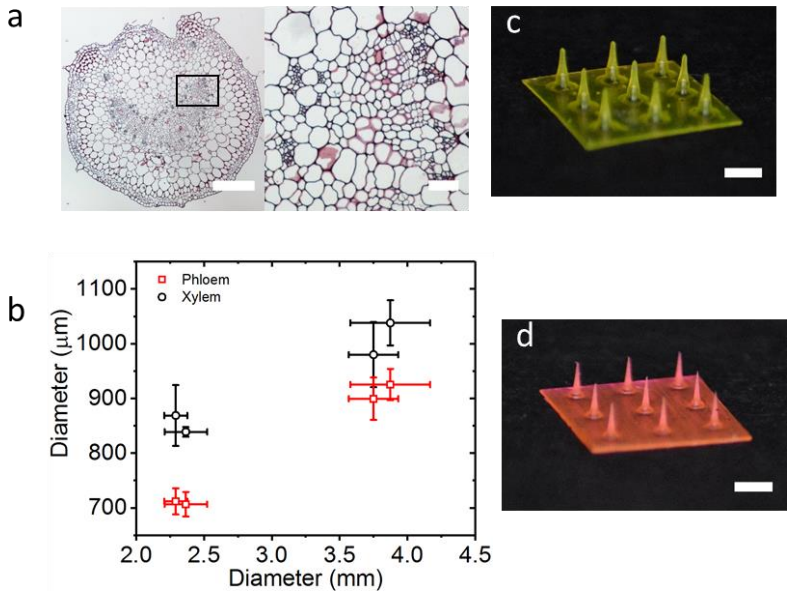

Figure S3.8. Phytoinjectors targeting on xylem and phloem of tomato plants. **a**, Tomato petiole cross section. Phloem (deep green) and xylem (pink) are regularly arranged. Scale bar 500 μm for the left and 50 μm for the right. **b**, Depth of phloem and xylem in tomato petiole. **c** and **d**, photograph of phytoinjectors for xylem and phloem, respectively. Scale bar 1 mm. Error bar means s.d.

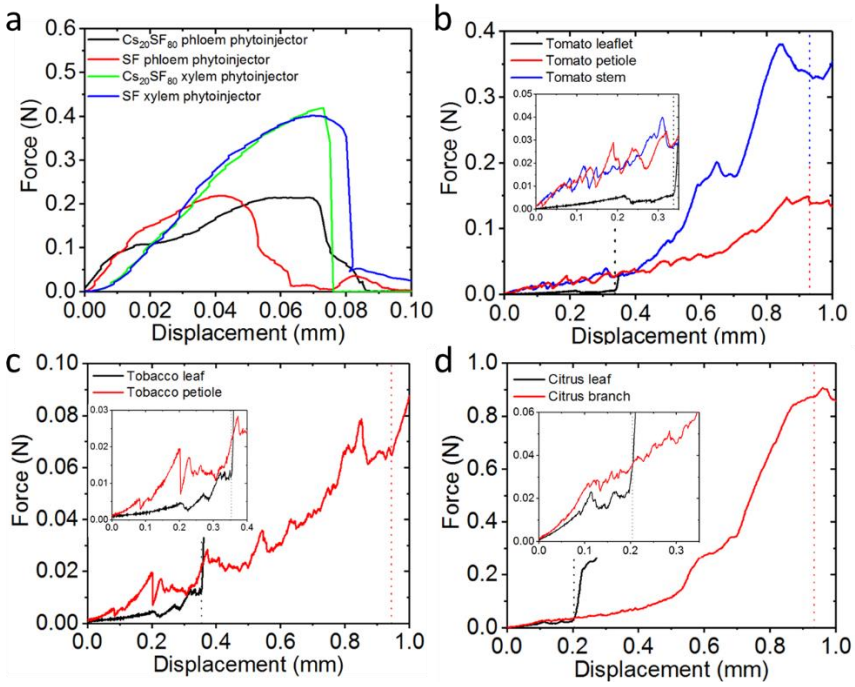

Figure S3.9. Mechanical behavior of phytoinjectors and plant tissues during injection with a xylem phytoinjector. a, Mechanical behavior of xylem and phloem phytoinjectors fabricated from $Cs_{20}SF_{80}$ and SF under compression. The phytoinjectors mainly break due to bending because the inevitable lateral force exerted during compression. The phloem phytoinjector fabricated from $Cs_{20}SF_{80}$ may undergo material cracking as the force was maintained around 0.1 N where the

displacement is from 15 µm to 25 µm (The tip of a phloem injector is < 10 µm in diameter). Reaction forces during injection of a xylem phytoinjector into tomato (**b**), tobacco (**c**), and citrus (**d**). Dotted lines represent the completion of the injection, where the whole phytoinjector was inside the tissue plant or the tissue (leaf) was injected through.

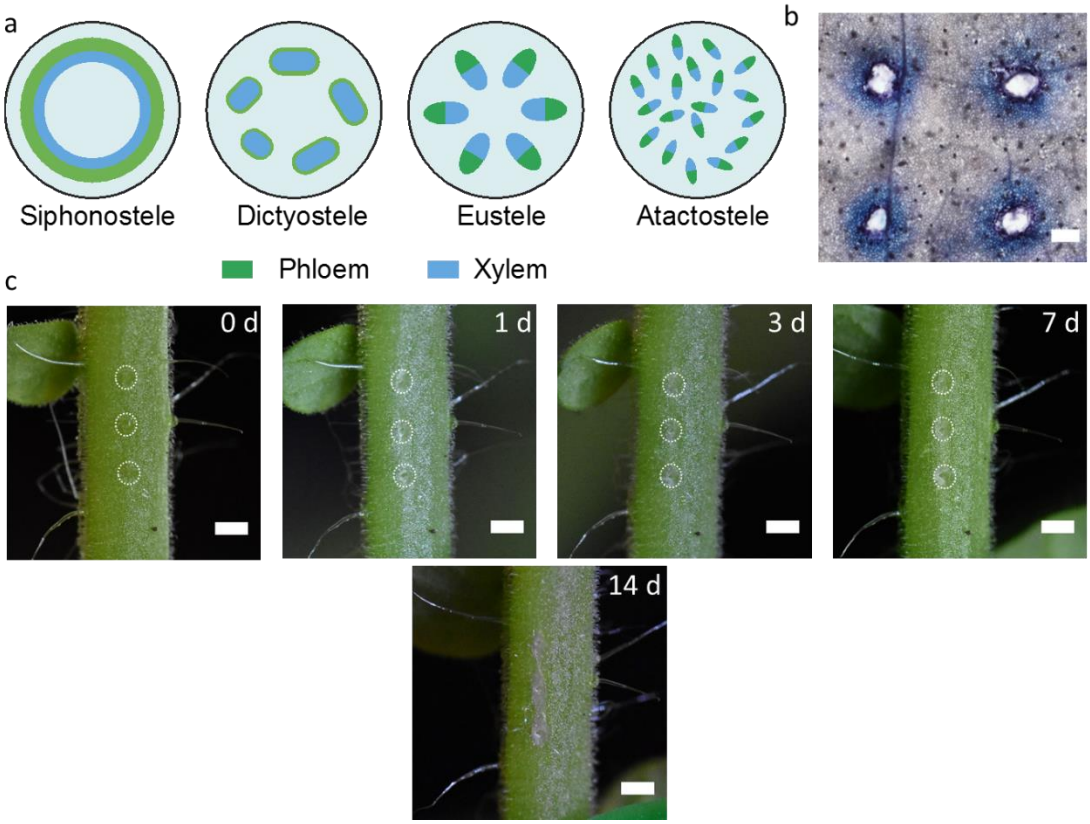

Figure S3.10. Stele types and wound caused by phytoinjectors a, Different types of steles. **b,** Leaf cell viability post injection. Cells stained blue by toluidine blue are dead while not stained are alive. Scale bar 100 µm. **c,** Wound on tomato petiole caused by xylem phytoinjectors, immediate, 1, 3, 7, and 14 days post injection. Scale bar 1 mm.

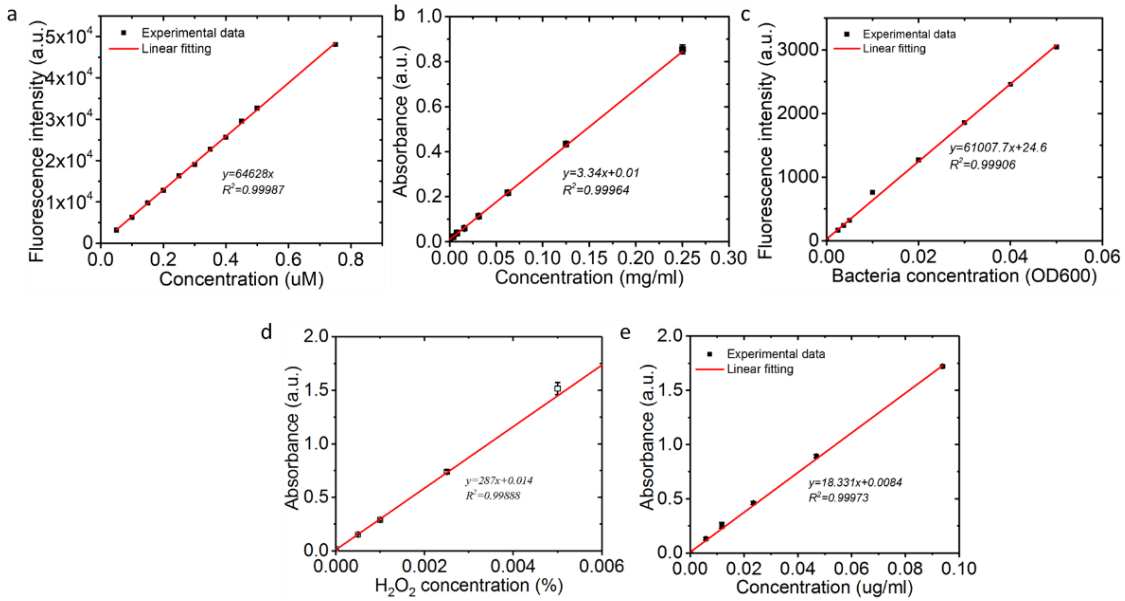

Figure S3.11. Standard curves. **a**. rhodamine 6G, **b**. azozlbumin, **c**. *R. tropici*, **d**. H_2O_2, and **e**. HRP, respectively. R^2 is adjusted R-squared. Error bar means s.d.

3.4.3 Supplementary tables

Table S3.1. I_{853}/I_{829} ratio of Raman spectra

I_{853}/I_{829}	Silk fibroin	Cs	$Cs_{20}SF_{80}$
Non treated	1.69	1.94	2.47
Methanol treated	2.26	2.84	1.94

Table S3.2. Power law fitting parameters of payloads release. Data are mean ± s.d.

Material	SF			$Cs_{20}SF_{80}$		
	k[a)]	n	R^2	k[a)]	n	R^2
Rhodamine 6G	0.59±0.04	0.93±0.06	0.9823	27.54±5.51	1.61±0.07	0.9926
Azoalbumin	0.82±0.34	1.13±0.16	0.9395	8.63±0.72	1.57±0.04	0.9957
R. tropici	1.22±0.17	1.12±0.08	0.9850	15.52±1.22	1.74±0.04	0.9973

[a)]The unit for time *t* is hour for paramater k.

Table S3.3. Estimation of the amount of payload delivered by a phytoinjector.

	Volume (nl)	Weight (µg)[a]*	Tip weight (µg)	Payload weight (ng)[b]*
Xylem phytoinjector	18.74±1.05	26.236	0.787	78.7
Phloem phytoinjector	9.11±1.83	12.754	0.383	38.3

[a]* The density of 1.40 g cm^{-3} is used to do calculation.
[b]*The payload weight is supposed to be 10% of the phytoinjector.

Table S3.4. Micronutrients concentration in plant.[8]

Element	Range of Concentrations (ppm)	Adequate Concentration (ppm)	Adequate Concentration (ng per gram fresh weight)
Cu	2–50	6	600
Mo	0.01–10	0.1	10
Ni	0.01–5	0.05	5

Chapter 4 Efficient Deployment of Hormones in Plants with Minimal Wounding Using Silk-based Microneedles

The contents of this chapter were submitted as Yunteng Cao[1,5], Sally Shuxian Koh[2,3,5], Yangyang Han[4], Javier Jingheng Tan[2], Doyoon Kim[1], Nam-Hai Chua[2,4], Daisuke Urano[2,3,4]*, Benedetto Marelli[1,4]*

[1]Department of Civil and Environmental Engineering, Massachusetts Institute of Technology, Cambridge, MA, USA

[2]Temasek Life Sciences Laboratory, National University of Singapore, Singapore, Singapore

[3]Department of Biological Sciences, National University of Singapore, Singapore, Singapore

[4]Singapore-MIT Alliance for Research and Technology, Singapore, Singapore

[5]These authors contributed equally: Yunteng Cao, Sally Shuxian Koh.

"Efficient Deployment of Hormones in Plants with Minimal Wounding Using Silk-based Microneedles"

4.1 Abstract

New systems for agrochemical delivery in plants will foster precise agricultural practices and provide new tools to study plants and design crop traits, as standard spray methods suffer from elevated loss and limited access to remote plant tissues. Silk-based microneedles can circumvent these limitations by deploying payloads directly in plants' tissues. However, plant response to microneedles' application and microneedles' efficacy in deploying physiologically relevant biomolecules are unknown. Here, we show that gene expression associated with *Arabidopsis thaliana* wounding response decreases within 24-hours post microneedles' application. Microinjection of gibberellic acid (GA_3) in *A. thaliana* mutant *ft-10* is more effective and efficient than spray in activating GA_3 pathways and accelerating bolting. Microneedles' efficacy in delivering GA_3 is also observed in several crop species, i.e., tomato (*Solanum lycopersicum*), romaine lettuce (*Lactuca sativa*), and carmel spinach (*Spinacia oleracea*), underpinning the use of this new tool in plant science and agriculture.

4.2 Introduction

Escalating growing conditions associated with climate change (e.g., extreme weather, the spread of plant diseases and pests, lower soil quality), an ever-increasing human population, scarcity of arable land, and limited resources are pressuring the AgriFood systems to adopt sustainable and precise practices that foster minimization of inputs (e.g., water, fertilizers, and pesticides) and mitigation of environmental impacts[21]. A critical step in this direction is the development of new delivery systems that deploy agrochemicals such as, micronutrients, pesticides, and antibiotics in crops to guarantee high productivity and high produce quality while minimizing waste of resources[171]. To date, the two most common practices for actives delivery *in planta* are foliar spray and soil application. These two methods benefit from being rapid, easily deployable, cost-effective, and effortless. These qualities made *spray* the current standard delivery method in agriculture, albeit it suffers from very low efficiency due to off-target application (at least 30-40% loss to the air[14]), quick run-off (67.2% in 2 minutes in 44 mm h^{-1} rain for oxytetracycline[16]), actives' rapid degradation (43.8% in natural sunlight within 1 day for oxytetracycline[16]), and being blocked and trapped by cuticles (>70% for ~8 nm rod-shaped CeO_2 nanoparticles[15]). Spray of agrochemicals is also associated with significant environmental side effects, such as water and soil contamination, biodiversity loss and degraded ecosystems[172,173], and public health concerns[19]. In plant science, spray is also commonly used to deliver nutrients[174], pesticides, plant growth regulators[7,175], and stimulants[176,177], often in the form of nanomaterials[9,14,28,109,178], to study plant response to biochemical cues. Despite the ease of applications of these actives by spray, only a few tissues can be targeted and with limited knowledge on the effective dose deployed, resulting in a dire need for new delivery tools to study plants and design new crop traits.

In response to these limitations, numerous nanomaterials have been developed to make drug delivery *in planta* more effective via modification of physicochemical properties and decoration with physiologically functional molecules[9,14,28,178]. Nanomaterials protect labile compounds from fast degradation, increase the adhesion of payloads to plants, control the release of payloads, and even enhance the permeability of payloads through cuticles[178,179]. For instance, clay nanosheets extend dsRNA life from 20 days to at least 30 days and the virus protection window of dsRNA from 5–7 days to at least 20 days[109]. However, nanomaterials are commonly applied by spray and suffer from the method-associated low uptake efficiency (in the order of 0.1% for root application and no more than 30% via leaf[14]). Alternative delivery methods such as foliar infiltration are labor-intensive, limiting their use in the field and in many plant models.

To address these challenges, it was previously proposed to use silk-based microneedles to precisely deliver biomarkers (e.g., fluorescent dyes) to several plant tissues, including leaves, vasculature, and meristem[26]. Silk brings merits of non-toxicity, dissolution in contact with sap, edibility (GRAS approved material), and mechanical robustness[26,47,128,129,180-184]. Here, we build on this study to establish silk-based microneedles as a new tool in plant science that enables the precise deployment of known amounts of physiologically relevant molecules to plants with minimal invasiveness.

Microneedle injection on *Arabidopsis thaliana* mutant *ft-10* caused minimal formation of scar and callus. Transcriptomic analyses showed minimal wounding responses and activation of GA_3 responses post injection of GA_3-loaded microneedles, which was corroborated by promoted bolting and inhibited flower formation. This method was proved to be more efficient and effective than foliar spray. Potential applications of the silk-based microneedles in agriculture were also

confirmed by the successful deployment of GA_3 in several crops, including tomato (*Solanum lycopersicum*), romaine lettuce (*Lactuca sativa*), and carmel spinach (*Spinacia oleracea*).

4.3 Results

4.3.1 Rational design of microneedles for GA_3 delivery to *ft-10*

GA_3 is a bioactive member of the gibberellins family and one of the most popular plant growth regulators (PGRs) used in agriculture[7,185,186]. While GA_3 has shown ubiquitous promotion for vegetative growth, its effect on the transition to developmental growth is complex and specific to plant species[187-192]. To better assess the physiological functions of GA_3 delivered with microneedles and study the injection effects on signaling pathways, we selected *A. thaliana* as a model plant due to its well-documented genetic activities. Furthermore, it has been demonstrated that application of gibberellins in *Arabidopsis* promotes termination of vegetative growth, inhibits flower formation, fosters early bolting, and results in plants with fewer rosette leaves and more cauline leaves30. However, wild-type *A. thaliana* Col-0 plants produce only 14 rosette leaves during vegetative growth when inflorescence emerges on day 23 (stratification time excluded) under a 16h day length condition[193] (our data indicate 11-13 rosette leaves on day 21-24, Figure S4.1a). Such small leaf size, few leaves, and the rapid developmental transition make it challenging to investigate plants' responses to the application of GA_3 using different delivery methods (i.e., spray *vs.* injection). To overcome these challenges, knock-out of the non-GA_3 related, dominant pathways for flowering regulation under long-day conditions (i.e., the photoperiod pathway[194]) is necessary. We therefore selected the mutant *ft-10,* whose *ft* genes lose function and show a late-flowering phenotype under long-day conditions. One-month-old *ft-10* plants growing under long-day conditions showed rosette leaves with suitable size (the largest leaf around 4-5 cm in length, petiole wider than 2 mm), making it a suitable candidate for studying delivery methods and were used in our experiments.

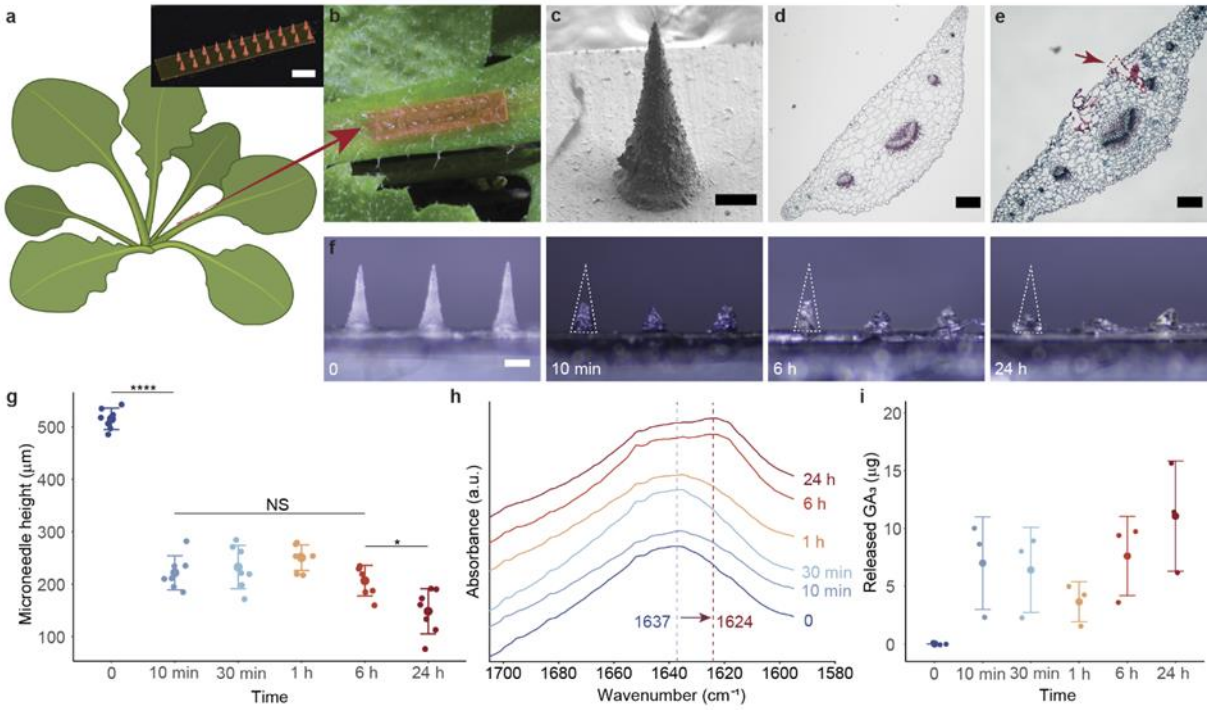

Figure 4.1. **Rational design of microneedles for payload delivery to *ft-10*. a.** Schematic of GA_3-loaded silk materials-based microneedles' injection on *Arabidopsis* mutant *ft-10*. **b.** Representative image of a petiole of a *ft-10* injected by an array of GA_3-loaded silk materials-based microneedles. Inset shows an array of microneedles. Scale bar 1 mm. R6G was added for display purposes. **c.** SEM image of a GA_3-loaded silk material-based microneedle. Scale bar 100 μm. **d.** Cross-section of a *ft-10* petiole. Xylem is stained red while phloem is blue. Scale bars 200 μm. **e.** Cross-section of a *ft-10* petiole after microneedle injection. The red dash-line triangle highlighted by the red arrow denotes an injected microneedle. **f.** Representative images of GA_3-loaded microneedles before and after injection at various time points. The white triangles estimate the initial shapes of microneedles. Scale bars 200 μm for all. **g.** Height changes of microneedles over time after injection. The height decreased dramatically (57% decrease) within 10 minutes after injection ($p < 0.0001$) and then slowly to 148±43 μm (71% decrease) in 24 h (from 6 h to 24 h, $p = 0.023$). One-way ANOVA was performed, followed by the Tukey test. *$p < 0.05$, ****$p < 0.0001$. Data are mean ± s.d., n = 7 individual samples. **h.** Secondary structure of the residue of silk microneedles over time after injection. The emerging peak at 1624 cm^{-1} over time indicates the transition from random coil (1637 cm^{-1}) to beta-sheets. **i.** GA_3 release from a unit array of microneedles after injection. Data are mean ± s.d., n = 3 individual samples.

GA_3 functions both locally and systematically[195]. To effectively deliver GA_3, we targeted the systematic material transport system in *ft-10* (Figure 4.1a-c), i.e., through vasculature via injection on the petiole of a rosette leaf, building on our previously reported strategy[26] (Figure 4.1d,e). Vasculature of *ft-10* used in our experiments was generally located 370-508 μm beneath the

adaxial surface (Figure S4.1b). While rationally designed microneedles have shown the capability to precisely deliver payloads to various tissues, including xylem and phloem, we propose that the delivery of GA_3 does not require precise access to the vasculature. We hypothesize that the small size of GA_3 (346.37 g/mol) enables its apoplast diffusion to the xylem and potential loading into the phloem and subsequent systematic transport upon it is released *in planta*. Therefore, the deployment of GA_3 behind the adaxial cuticle barrier of the petiole is the essential function of microneedles, which may also reach the proximity of vasculature to further facilitate GA_3 transport *in planta*. To achieve this goal, we fabricated cone-shaped silk materials-based microneedles with a height of 531.10±39.25 μm and a base diameter of 225.59±3.40 μm (Figure 4.1c, Figure S4.1c, Table S4.1). These microneedles were utilized for GA_3 delivery in terms of easiness of operation, relatively high loading capacity, high adhesion on the petiole, minor damage to plants, and deployment of the cargo molecules behind the cuticle close to the vasculature (Figure 4.1e). Microneedles of other dimensions were also tested (Figure S4.1d, Table S4.1); larger microneedles caused noticeable wounding on *ft-10*, while shorter microneedles were readily detached from petioles. Thus, they were not used with *ft-10* in this study.

To assess the effectiveness of microneedles in deploying GA_3, we loaded in a microneedle array the same amount of GA_3 used in each foliar spray treatment, which atomized 0.640±0.018 g (n = 10) of 100 μM GA_3 solution containing 22.2±0.6 μg of GA_3. GA_3-loaded microneedles were prepared by casting a mixture of 5 mM GA_3 and 60 mg/ml silk-based materials in silicone molds to obtain an array of 2x11 microneedles. Each device weighed 0.834±0.016 mg (n = 7) and contained 23.3±0.5 μg GA_3, comparable with that of foliar spray. Each 2x11 microneedle array was considered the unit of injection treatment, if not otherwise specified. In preliminary tests (Fig. S1e), GA_3-loaded microneedle injection resulted in similar phenotypes of *ft-10* (e.g., bolting time,

the numbers of rosette leaf and cauline leaf, and leaf size) to those treated by GA_3 foliar spray, which were remarkably different from those injected by microneedles without GA_3. These results suggest GA_3 was successfully delivered to *ft-10* by microneedles and affected plant metabolism.

In-planta release profile of GA_3 from microneedles was also evaluated. The height of GA_3-loaded microneedles dramatically decreased from 515±20 μm to 222±32 μm (57% decrease) after only 10 minutes of exposure to plant tissues and further decreased to 148±43 μm (71% decrease) after 24 hours (Figure 4.1f,g, Figure S4.1f). The rapid size decrease and morphology change after injection are ascribed to silk-based materials' dissolution *in planta*, which agrees with our previous results[26] in tomato and tobacco (*Nicotiana benthamiana*), using different payloads (Figure 4.1f-i). The extended exposure (particularly after 6 h and 24 h) of silk fibroin to sap and high humidity post-injection resulted in the secondary structure transition from random coils to beta-sheets, which is indicated by the shift of the Amide I peak from 1637 cm^{-1} to 1624 cm^{-1} (Figure 4.1h) and makes silk water-insoluble. While this is the first time the disorder to order transition of silk materials is documented in plants, the phenomenon was previously reported in human tissues[130] and corroborated silk degradation measurements, where a rapid silk degradation in the first 10 minutes post-injection was followed by a slower degradation profile (Figure 4.1f,g). The kinetic of GA_3 released in plants supported the kinetic of silk microneedle degradation upon injection (Figure 4.1i, Figure S4.1g). Microneedle bodies in an array (excluding the supporting substrate) contain approximately 6.11 μg of GA_3. Within 10 minutes post-injection, all the GA_3 contained in the microneedles was released into the surrounding plant tissues; higher amounts of GA_3 delivered to plant tissues at extended time points were likely due to the diffusion of the payload from the microneedles' substrate into the plant.

4.3.2 Wounding responses of *ft-10* induced by microneedles

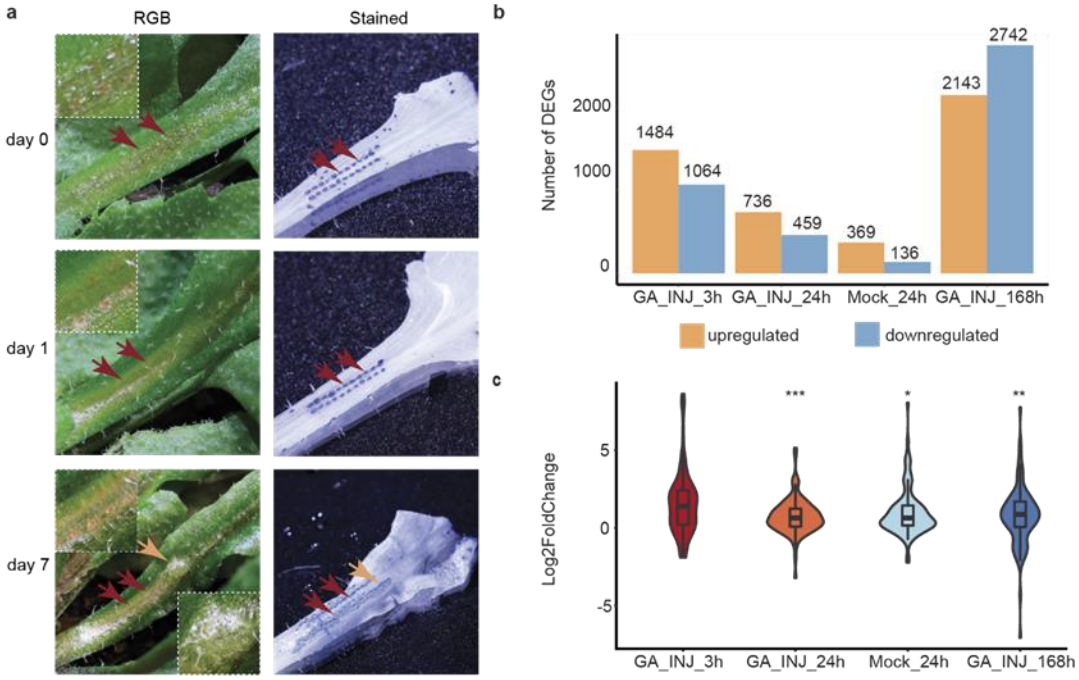

Figure 4.2. Wounding responses of *ft-10* induced by microneedles. a. Representative images of *ft-10* petioles immediately, 1, and 7 days after injected by silk materials-based microneedles. R6G was added to microneedles for display purposes in the left RGB column, and trypan blue was used to stain the dead cells (blue) in the right stained column. Red arrows indicate the scar left by microneedles, and orange arrows show callus. The inlets show the zoomed image of scars (top left) and the callus (bottom right). **b.** Bar plot showing the number of differentially expressed genes (DEGs) 3, 24 or 168 h after GA_3 microneedle injection (GA_INJ_3h, GA_INJ_24h, GA_INJ_168h) or 24 h after mock microneedle injection (Mock_24h) (cut off threshold, $|\log_2 FC| > 1$, FDR < 0.01). The total numbers of upregulated and downregulated genes are shown above each bar. Each timepoint has 3 biological replicates, except 168 h (n = 2) **c.** Changes in expression of 103 wounding response genes found in response to wounding (GO:0009611) Gene Ontology (GO) term. Violin plots show the distribution of gene expression within each time point, while the boxplot displays the minimum and maximum non-outlier observations (whiskers), lower quartile (Q1), median, and upper quartile (Q3). Multiple t-tests (using 3 h as a reference) were performed, and changes in the mean expression of wounding genes within each group were significant. * $p < 0.05$, ** $p < 0.01$, *** $p < 0.001$.

Microneedles are a painless tool used for medical applications due to their tiny size incapable to reach pain receptors in the human dermis. However, they do cause damage to the stratum corneum. We previously reported scars on tomato stem upon microneedles' injection, which did not noticeably impact growth19. Here, scars were also observed, and callus formed on *ft-10* petioles

after injection (Figure 4.2a, Figure S4.2). Dead cells stained by trypan blue were located close to the injection site (Figure 4.2a), likely due to mechanical damage.

To gain insight into the transcriptomic dynamics of plant-biomaterial interactions following GA_3 and mock (i.e., without GA_3) microneedle injection, we performed time-course RNA-sequencing experiments (0 h, 3 h, 24 h, and 168 h). Transcriptomic analyses yielded a total of 9033 differentially expressed genes (DEGs) over all treatments and time points (Figure 4.2b, Figure S4.3). Gene Ontology (GO) enrichment analyses showed that GO:0009611 response to wounding was enriched at 3 hours post-injection with GA_3-loaded microneedles (FDR = 1.77×10^{-12}) and 24 hours post-injection of the mock injector (FDR = 2.19×10^{-4}) (Figure S4.4). To better understand the changes in wounding-related gene expressions over time, *A. thaliana* genes annotated within the Response to Wounding GO terms were extracted from the TAIR10 genome release. There are a total of 240 genes annotated in the response to wounding GO term, of which 103 genes were DEGs at any of the time points within our transcriptome. The expressions of these genes (Figure 4.2c) showed the reduction in the enrichment of wounding-related genes with time ($p < 0.05$, t-test). In the Mock_24h samples, we observed a reduction in expressions of "Response to Wounding" genes ($p = 0.018$); however, this significance was less than the reductions seen in the GA_INJ_24h ($p = 0.0022$) and GA_INJ_168h ($p = 0.012$) groups. It could be highly likely that in the GA_INJ_24h sample, changes in other gene expressions were more significant than changes in wounding responses, suggesting the minor role of wounding at the 24 h timepoint. Therefore, using microneedles to deliver substances such as GA_3 to plants presents a minimally invasive and highly effective technique.

4.3.3 Phenotype-based evaluation of microneedles for GA_3 delivery to *ft-10*

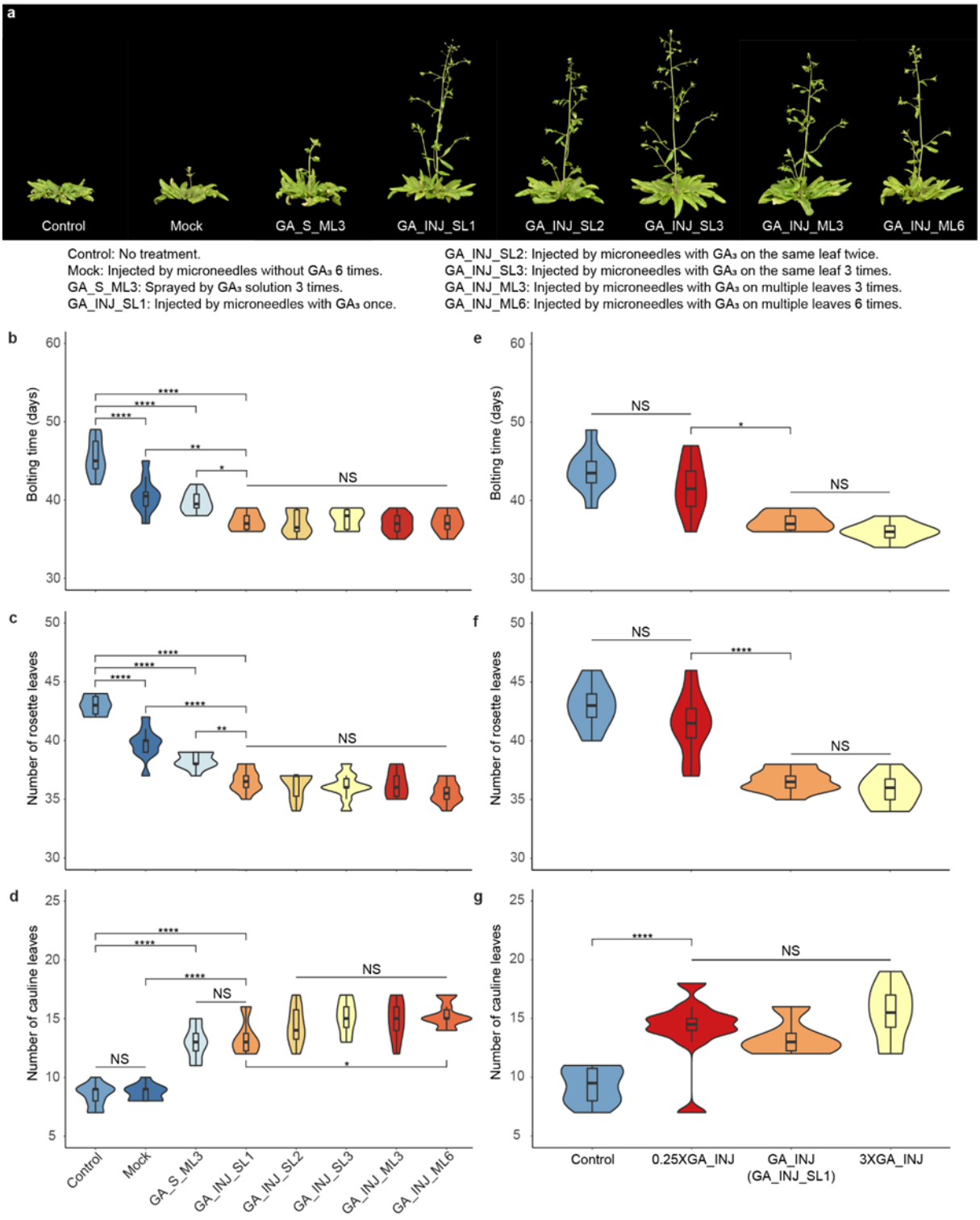

Figure 4.3. Phenotype-based evaluation of microneedles for GA_3 delivery to *ft-10*. a. Representative images of *ft-10* 16 days after the first treatment. Injection of microneedles and spray were carried out every three days. 8 groups of *ft-10* treatment were conducted: no treatment (Control), injection by microneedles without GA_3 for 6 times (Mock), spray with GA_3 solution

(excluding shoot apex by covering the central part of rosette) for three times (GA_S_ML3), injection by GA_3-loaded microneedles on a single leaf once, twice, and three times (GA_INJ_SL1, GA_INJ_SL2, and GA_INJ_SL3, respectively), and injection by GA_3-loaded microneedles on multiple leaves three and six times in total (GA_INJ_ML3 and GA_INJ_ML6, respectively). **b-d.** Bolting time (**b**) and the number of rosette leaf (**c**) and cauline leaf (**d**) of *ft-10* under various treatments. All treated groups showed early bolting and fewer cauline leaves, and the single injection displayed remarkably better performance than spray for 3 times ($p = 0.029$ for bolting time and $p = 0.0023$ for rosette leaf number). Negligible phenotype differences were observed among the five groups of injection except the cauline leaf number between GA_INJ_SL1 and GA_INJ_ML6 ($p = 0.044$). **e-g.** Bolting time (**e**) and the number of rosette leaf (**f**) and cauline leaf (**g**) of *ft-10* injected by microneedles loaded with different amounts of GA_3. 0.25XGA_INJ and 3XGA_INJ contain 0.25 and 3 times GA_3 in GA_INJ, which is the same data as GA_INJ_SL1 in **b-d**. 0.25XGA_INJ showed no difference with Control in bolting time and rosette leaf number, but a remarkable difference in cauline leaf number ($p < 0.0001$). On the other hand, it had significant differences with GA_INJ in bolting time ($p = 0.012$) and rosette leaf number ($p < 0.0001$), but no difference in cauline leaf number. 3XGA_INJ did not display enhanced effects than GA_INJ. Violin plots show the distribution of data points, while the boxplot displays the minimum and maximum non-outlier observations (whiskers), lower quartile (Q1), median, and upper quartile (Q3). One-way ANOVA was performed, followed by the Tukey test. One-way ANOVA assuming unequal variances was used, followed by the Games-Howell test if homogeneity of variances was violated. * $p < 0.05$, ** $p < 0.01$, *** $p < 0.001$, **** $p < 0.0001$.

To investigate microneedle-based GA_3 delivery to *ft-10*, we studied plant responses to the increasing number of injections ($n_{injection} = 1, 2, 3, 6$) – and consequently the total amount of GA_3 delivered – and to different injection positions (same leaf *vs.* multi-leaf), using GA_3 foliar spray as positive control. In total, 8 groups (n = 10 for each group) of *ft-10* treatment were considered: no treatment (Control), injection by microneedles without GA_3 6 times (Mock), spray with GA_3 solution (excluding shoot apex) three times (GA_S_ML3), injection by GA_3-loaded microneedles on a single leaf once, twice, and three times (GA_INJ_SL1, GA_INJ_SL2, and GA_INJ_SL3, respectively), and injection by GA_3-loaded microneedles on multiple leaves three and six times in total (GA_INJ_ML3 and GA_INJ_ML6, respectively).

Mock, GA_S_ML3, and all groups of *ft-10* injected by GA_3-loaded microneedles displayed early bolting (Figure 4.3a,b). Despite the differences in the amount of delivered GA_3 and delivery position, negligible phenotype differences among the groups of GA_3-injected *ft-10* were observed. Statistical analysis confirmed no significant difference in bolting time, rosette leaf number, and

cauline leaf number among all five cases, except for the cauline leaf number between GA_INJ_SL1 and GA_INJ_ML6 (p = 0.044) (Figure 4.3b-d). These results suggest that a single injection of microneedles containing 23.3±0.5 μg GA_3 was sufficient for regulating vegetative to the reproductive transition of *ft-10*. The results also demonstrate that the injection position does not influence the function of GA_3 on flowering, which may ascribe to the long-distance transport of GA_3. Therefore, a one-time injection of an array of 2x11 microneedles has been used as the standard treatment in the remaining studies. Increasing the loading amount of GA_3 in microneedles by 3 times (3XGA_INJ) did not show enhanced effects (Figure 4.3e-g). However, decreasing to a quarter of the amount of GA_3 loaded in microneedles (0.25XGA_INJ) resulted in no statistically significant difference in bolting time (p = 0.44) and rosette leaf number (p = 0.22) with the negative control (n = 10). Interestingly, 0.25XGA_INJ samples possessed a similar number of cauline leaves to samples with 12 times the amount of GA_3, i.e., 3XGA_INJ, and higher than the negative control (p < 0.0001) (Figure 4.3g). In addition, tuning the amount of loaded payloads (up to 8.0% by dry mass weight) did not significantly impact the secondary structure of silk materials and their properties in microneedles during fabrication (Figure S4.5a).

Foliar spray efficiency is significantly influenced by the spray setup, the amount of GA_3 delivered onto the leaves, the delivery position (direct exposure of shoot apex vs. covered shoot apex) (Figure S4.5b), and the weather. To mimic standard procedures, we avoided direct exposure of shoot apex to spray and maintained a high percentage (47.7±3.4%) of solution sprayed onto the leaves. Such foliar spray was used as positive control and did show effective delivery of GA_3, i.e., induced phenotype differences (Figure 4.3a, Figure S4.5b). GA_INJ_SL1 showed remarkably earlier bolting (p = 0.029) and fewer rosette leaves (p = 0.0023) than GA_S_ML3, indicating the efficacy and efficiency of the microneedles to deliver the hormone (Figure 4.3a-d). Notably, the

leaf length of GA_INJ_SL1 was smaller than that of GA_S_ML3 (p = 0.040) (Figure S4.5c). This may result from the different translocation of GA_3 after delivery; we suggest that GA_3 was systematically transported from the injection site to distal leaf cells, however, in foliar spray it directly affected leaf cells upon entering leaves via stomata or through the leaf cuticle. Mock samples showed earlier bolting and fewer rosette leaves with wide variation compared to Control ones, but no significant difference was observed in cauline leaves. This phenotype difference may result from wounding caused by the regular injection and accumulation of wounding signals (6 times injection), as 0.25XGA_INJ did not cause early bolting (Figure 4.3e,f).

4.3.4 GA_3 response induced by GA_3-loaded silk microneedle injection

To further evaluate the microneedle-based delivery of GA_3 to *ft-10*, we investigated similarity of the microneedle transcriptome (a total of 9033 DEGs in Figure 4.2b) to two previously published RNA-sequencing datasets that focused on GA_3 response in *A. thaliana* shoots[196,197]. DEGs extracted from the published datasets using a threshold of $|\log_2 FC| > 1$ and FDR < 0.01 demonstrated significant overlaps with those from the microneedle transcriptome ($p < 0.0001$ with Fisher's exact test), suggesting induction of GA_3-response in the microneedle dataset. The transcriptome comparison revealed 232 DEGs commonly present in the microneedle transcriptome and two GA_3-response RNA-sequencing datasets (Figure 4.4a). These 232 genes showed distinct temporal expression patterns post injection of GA_3-loaded microneedles. Gene clustering analysis using Euclidean distances and a complete clustering method was performed and yielded five gene clusters (Figure 4.4b).

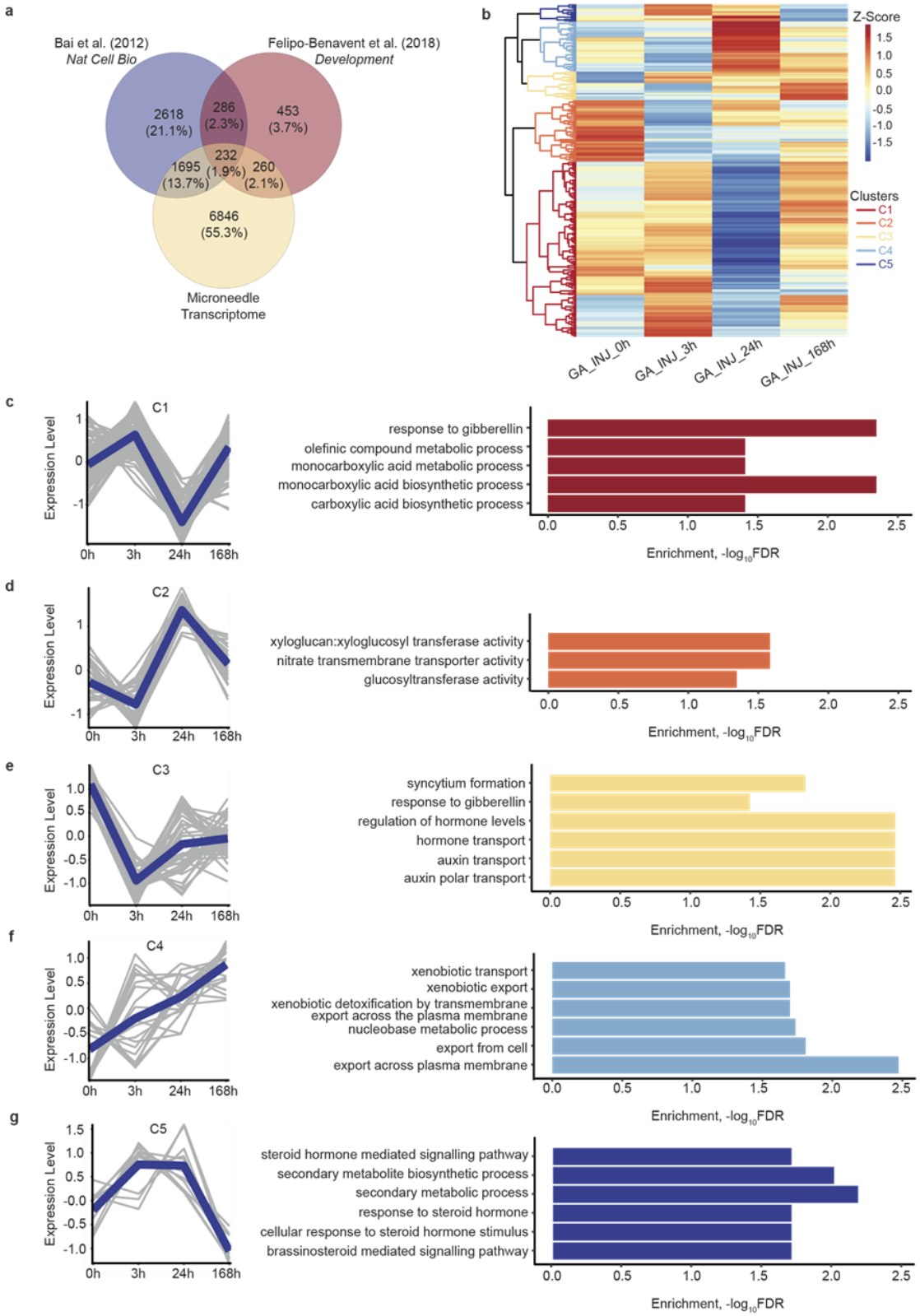

Figure 4.4. Transcriptome analysis following the application of GA_3-loaded silk-based microneedles on *ft-10 Arabidopsis* plants. a. Venn diagram showing the overlap between the

GA_3 microneedle transcriptome and two previously published GA_3 response RNA-sequencing datasets[196,197]. Fisher's Exact Test showed that DEG lists from both datasets significantly overlap with our microneedle dataset ($p < 0.0001$). **b**. Heatmap showing Z-scored expression levels of 232 genes commonly found in the three datasets as shown in the intersection of Venn diagram a. Five distinct clusters were observed, and each cluster is highlighted on the dendrogram with different colors. The distances between clusters on the dendrogram are Euclidean distances. **c-g**. Clustering analysis of time-course RNA-sequencing data showing five distinct transcriptional changes (clusters) induced by GA_3 microneedle treatment. Line graphs in the left panel show the overall expression of genes within each cluster. Grey lines show the Z-scored expression levels of individual genes, while the blue lines show the mean expression values of genes within each cluster. Gene Ontology (GO) enrichment analysis of each cluster of genes was also carried out, and the top 6 enriched GO terms (FDR < 0.01) from each cluster are displayed on the bar plot on the right panel. Each cluster is represented by different colored bars. The size of each bar represents the $-\log_{10}$(FDR). The full lists of DEGs and GO terms from enrichment analyses can be found in Dataset S1 and S2, respectively.

Clustering analyses revealed different expression patterns for the diverse processes associated with microinjection of GA_3 into *ft-10*. Genes within cluster 1 reached maximum expression levels at 3 h. GO terms such as "response to gibberellins" were highly enriched within cluster 1, suggesting that genes in cluster 1 are directly related to GA_3-responses (Figure 4.4c). Gene expression in cluster 2 showed a transient decrease at 3 h, with maximum expression levels being reached at 24 h. There were no GO terms related to biological processes that were enriched within cluster 2, and only three molecular processes were enriched, possibly reflecting downstream changes in response to GA_3 pathway induction (Figure 4.4d). Within cluster 3, we observed a sharp reduction in gene expression following GA_3 treatment at all time points. In addition to "responses to gibberellins", numerous hormone-responsive GO terms were enriched, suggesting that other hormone responses were gradually changed following microneedle-assisted delivery of GA_3 (Figure 4.4e). Cluster 4 genes had a higher expression level relative to the 0 h time point following microneedle-assisted delivery of GA_3. Further GO enrichment analysis revealed GO terms related to xenobiotic substances and export, suggesting that genes involved in the export of exogenous chemical substances were gradually induced in the microneedle transcriptome (Figure 4.4f). Within cluster 5, genes reached maximum expression between 3 h and 24 h, followed by a sharp decrease at 168

h. The enriched GO terms were related to secondary metabolites and steroid hormone responses, suggesting that the plants could be metabolically adjusting and internally regulating to prepare for phase transition from vegetative to flowering stages (Figure 4.4g). This corroborated the observation of bolting stems (~2 mm) 4-8 days after injection (Figure 4.3e). Overall, these data demonstrate the effectiveness of microneedle-assisted delivery of GA_3 in inducing GA_3 response within plants.

4.3.5 Microneedle utility in diverse plant species

To demonstrate the utility of silk-based microneedles to deliver PGRs in crops, we investigated the delivery of GA_3 to different plant species, including tomato, romaine lettuce, and carmel spinach. Microneedles' dimension was adapted to plant anatomy (cross-section of the stem, midrib, or petiole, Figure S4.6a,b, S4.7a,b). For injection in the tomato stem, we used microneedles with height =1006.1±65.3 µm and base diameter = 258.66±7.84 µm, (Figure S4.1c). For lettuce and spinach, we used the same microneedles used for *ft-10*. Tomato plants (n = 7) injected with GA_3-loaded microneedles (GA_INJ) showed a significant increase in height (Figure 4.5a,b) and similar diameters of the stem compared to other treatments, including GA_3 foliar spray (GA_S) (Figure S4.6c). While both GA_3-treated groups showed a noticeable color difference from 4^{th} to 6^{th} leaf (newly emerging leaves, length < 2 cm when treated), in GA_INJ this difference was more apparent than in GA_S (Figure 4.5c), likely due to accelerated growth. All three treatments did not significantly influence carotenoids content (Figure S4.6d-g). GA_INJ showed significantly decreased contents of chlorophyll *a* (p = 0.0049) and *b* (p = 0.0025) in the newly emerging leaf (4^{th} leaf) when compared to Control, but in GA_S only chlorophyll *b* decreased (Figure 4.5d). Mature leaves (2^{nd} leaf) were less sensitive to GA_3 application (Figure S4.6f). However, GA_3 injection was effective in causing a decrease in chlorophyll *b* content (p = 0.039). The expanding leaves (3^{rd} leaf) were affected by GA_3 in both GA_INJ and GA_S (Figure S4.6g). These findings

indicate GA_3 delivered by microneedles influenced growth at various stages and is more effective than foliar spray.

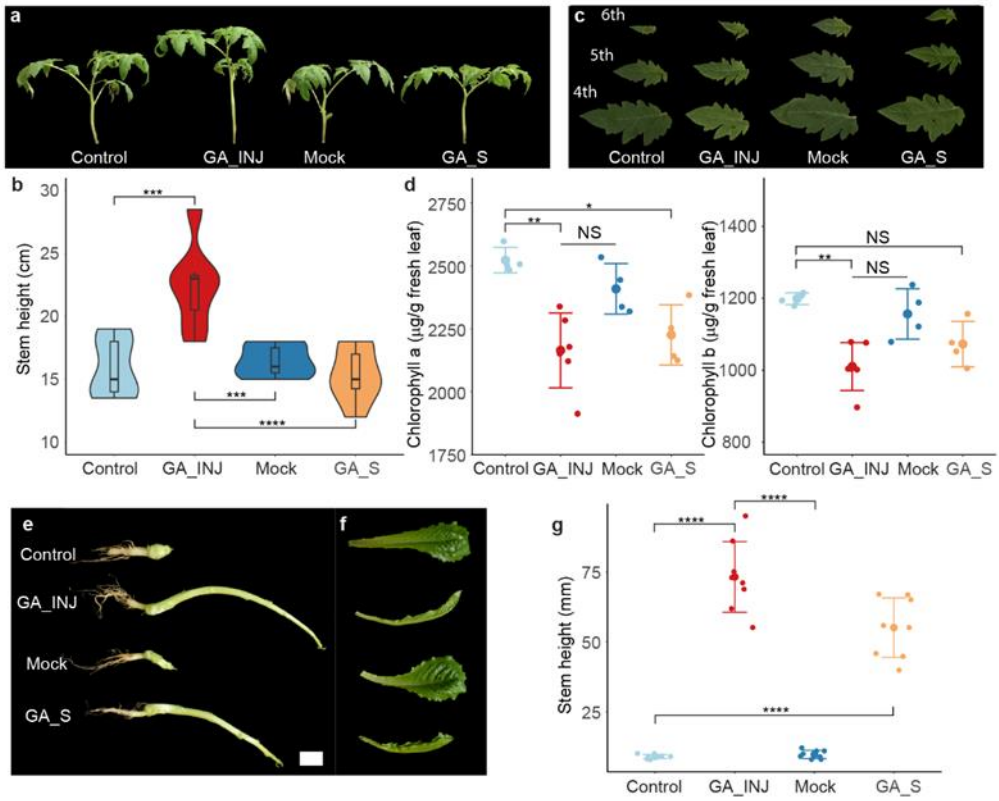

Figure 4.5. Microneedle utility in diverse plant species. a. Representative images of tomato plants 7 days after treatment. Control indicates no treatment, GA_INJ is injection with GA_3-loaded microneedles, Mock denotes injection with microneedles without GA_3, and GA_S is foliar spray of GA_3 solution (100 µM). **b.** Height of the stem of tomato plants in **a**. Tomato plants injected by GA_3-loaded microneedles were much higher than other groups. ($p < 0.001$ with Control, $p < 0.001$ with Mock, and $p < 0.0001$ with GA_S). Violin plots show the distribution of data points, while the boxplot displays the minimum and maximum non-outlier observations (whiskers), lower quartile (Q1), median, and upper quartile (Q3). **c.** The 4^{th}, 5^{th}, and 6^{th} leaves (newly growing leaves after treatments) 10 days after treatment in **a**. The application of GA_3 (both by microneedles and spray) caused lighter leaf color compared to groups without GA_3. **d.** Chlorophyll *a* and chlorophyll *b* content in the 4^{th} leaf (10 days after treatment) of tomato plants in **a**. GA_3 injection induced a significant decrease of chlorophyll *a* ($p = 0.0049$) and *b* ($p = 0.0025$) in the leaf, but spray only caused a reduction of chlorophyll *a* ($p = 0.034$). Data are mean ± s.d.. **e-f.** Representative images of stems (**e**) and newly growing leaf (**f**) of lettuce 7 days after treatments. The application of GA_3 induced stem elongation and leaf morphology changes. **g**. Stem height of lettuce in **e**. Data are mean ± s.d.. One-way ANOVA was performed, followed by the Tukey test. One-way ANOVA assuming unequal variances was used, followed by the Games-Howell test if homogeneity of variances or equal group size assumption were violated. * $p < 0.05$, ** $p < 0.01$, *** $p < 0.001$, **** $p < 0.0001$.

Lettuce displayed an elongated stem and morphology differences in emerging leaves after GA_3 treatment (n = 8, Figure 4.5e-g). While such treated lettuce is not suitable for marketing, it confirmed the effective delivery of GA_3 by microneedles and may be used in breeding where accelerated maturity is desired. In addition, such phenotypes ascribe to an excessive amount of GA_3[198], which can be readily tuned to a suitable range for vegetative growth. Spinach also showed an elongated stem after injection with GA_3-loaded microneedles, confirming the versatility of microneedles (n = 5, Figure S4.7c).

4.4 Discussion

This work establishes the use of silk-based microneedles as a new tool to deliver physiologically functional actives, using GA_3 as a model for plants. We targeted several plants, including the model plant *A. thaliana* mutant *ft-10* and economically important crop vegetables such as tomato, romaine lettuce, and carmel spinach. Several merits of microneedles-mediated deployment of cargo molecules were demonstrated, including precise dosage, reduced off-target and runoff, higher efficacy, and the possibility of targeting different plant tissues. This study is also the first to investigate transcriptomic dynamics post-microneedle injection in *A. thaliana*. GA_3-responsive gene activation was observed in response to microneedle application. Wounding responses were enriched at 3 hours post-injection and reduced to minimal levels within 24 hours. Minimal scar and callus formation were also observed, suggesting minimal injection-induced wounding to the plant.

Future work may extend to delivering other widely used plant hormones (e.g., auxin). Microneedles-based delivery may also enable the broad application of hormones, such as jasmonic acid, that hold high potential to positively affect plant growth but are currently restricted from agricultural practices due to limited productivity and high costs[7,186,199,200]. Nanomaterials can also be incorporated into microneedles both in the form of payloads or carriers for other actives, such

as metal nanoparticles for micronutrients and mesoporous silicon nanoparticles for controlled release, where on-site *in vitro* aggregation and thus dysfunction of nanomaterials may be prevented[14]. The properties of microneedles can also be tuned to decrease burst release and target a sustained release of payloads. The proof-of-concept provided in this study opens the door to plant microneedles' application in plant biology and agronomy, enabling new means to regulate plant physiology and study metabolisms via efficient and effective delivery of payloads.

4.5 Materials and Methods

Plant material and growth conditions

Arabidopsis thaliana ft-10 mutant seeds (TAIR Germplasm: CS9869) and ecotype Columbia (Col-0) seeds were sterilized by soaking for 1 minute in 70% ethanol and then for 10 minutes in 20% bleach, followed by five to seven times rinsing with sterile distilled water. Sterilized seeds were placed on Murashige and Skoog (MS)[201] plate and kept at 4 ˚C for 2 days. The plate was placed in a plant growth chamber (Caron 7304-22-1) at 22 ˚C with long day (day/night 16 h/8 h) conditions, 70-100% relative humidity, and light intensity 100 µmol m^{-2} s^{-1}. Seedlings were transferred to pots (2.5×2.5×3 in^3) with soil (Miracle-Gro Moisture Control Potting Soil Mix) on day 7 and watered regularly. Tomato (*Solanum lycopersicum*) seeds were purchased from The Seed Plant. Romaine lettuce (*Lactuca sativa*) seeds were purchased from Organo Republic. Carmel spinach (*Spinacia oleracea*) seeds were purchased from David's Garden. Tomato and Romaine lettuce were grown in pots (3.5×3.5×3 in^3) in the plant room under long day (day/night 16 h/8 h) at 80 µmol m^{-2} s^{-1}, 70-90% relative humidity, day and night temperatures of 26 °C and 20 °C, respectively. Seeds of carmel spinach (*S. oleracea*) were sown in pots (2.5×2.5×3 in^3) and kept in a plant growth chamber (Caron 7314-50-2) at 22 ˚C with long day (day/night 16 h/8 h) conditions with a light intensity of 120 µmol m^{-2} s^{-1}, and 70-90% relative humidity.

Preparation of silk materials

Silk fibroin and silk fibroin-derived highly hydrophilic peptides (Cs)[26]. Briefly, *Bombyx mori* cocoons were boiled for 45 minutes in 0.02 M Na_2CO_3 solution and fibers were dried overnight after a thorough rinse in MilliQ water. Dried fibers were dissolved in 9.3 M LiBr solution at 60 ˚C for 4 h at a mass to volume ratio of 1:4. The solution was dialyzed against MilliQ water for 48 h in dialysis tubing (Spectrum™ Labs Spectra/Por™ 3 3.5 kDa MWCO Standard RC, Repligen Corporation, Waltham, MA). The supernatant was obtained after centrifugation at 20000 x *g* for 1 h and was stored at 4 ˚C prior to use. The concentration of silk fibroin is around 7% w/v, determined by weighing the residual. Silk fibroin was digested in an aqueous solution by alpha-chymotrypsin at an enzyme-to-substrate weight ratio of 1:100. The mixture became white gel after incubation at 37 ˚C for 24 h. The gel was centrifuged at 20000 × *g* for 30 minutes, followed by heat treatment at 80 ˚C for 20 minutes to denature the enzyme. The supernatant (Cs) was obtained after an additional round of centrifugation and was stored at 4 ˚C prior to use. The concentration was determined by weighing dry residual.

GA_3 solution preparation

100 mM stock solution of GA_3 was prepared by dissolving 34.6 mg GA_3 in 1 ml 40% ethanol solution. GA_3 spray solution was prepared by diluting stock solution 1000X to a final concentration of 100 μM. Silwet-77 was added to get a final concentration of 0.01% in the GA_3 spray. 0.04% EtOH with 0.01% Silwet-77 in water was used as the mock spray solution.

Microneedle fabrication

Silk materials-based microneedles were prepared following the previously published method[105] with modification. PDMS molds of microneedles were fabricated by laser ablation (Blueacre Technology Ltd., Dundalk, Ireland) with predesigned dimensions. Silk fibroin and Cs solution were mixed at a dry material ratio of 4:1 with a final silk material concentration of 60 $mg \cdot ml^{-1}$.

The gibberellic acid stock solution was added slowly to the silk-Cs solution to a final concentration of 5 mM by diluting 20X. Lower and higher concentrations of gibberellic acid in silk-Cs solution (1.25 mM and 15 mM, respectively) were used to prepare microneedles for 0.25XGA_I and 3XGA_I, respectively. Rhodamine 6G (R6G) was added to the final solution (concentration 20 μM) if necessary. The solution was put in the PDMS mold and centrifuged at 2000 x *g* for 10 mins. The mold was left in a fume hood to dry overnight. Microneedles were peeled off from the molds and cut into the desired array for use. Loading mass ratio (GA_3 : silk materials) is 0.72%, 2.8%, and 8.0% for 1.25 mM, 5 mM, and 15 mM initial GA_3 concentrations, respectively. Mock microneedles were prepared from silk-Cs solution without GA_3. The final microneedle array (11x11 microneedles) weighed around 4.6 mg.

GA_3 application to ft-10

30-day-old *ft-10* plants (n = 10 per treatment group) were used in experiments. The GA_3 solution was sprayed via a fine mist sprayer on the leaves of *ft-10* with the shoot covered by a piece of paper towel (1 cm x 1 cm). The solution sprayed on the leaves was measured by weighing. Microneedles were cut into 2x11 arrays and applied to the petioles of the plant leaves (leaf size ~4 cm in length). Multi-injection was carried out every three days. The bolting date was recorded as the date an observable stem (~2 mm) appeared. The number of rosette leaves and cauline leaves and the bolting time were recorded. 25-day-old tomato plant (n = 7), 17-day-old lettuce (n = 8), and 3-week-old spinach (n = 5) were used for experiments. Microneedles were applied to these plants in a similar manner to *ft-10 A. thaliana* plants.

Histology

Histology was prepared following the method described previously[26]. Plant (*ft-10*, tomato, lettuce, and spinach) tissues of interest were kept in 10% formalin for 24 h at room temperature after

collection. They were then immersed in 70% ethanol before processing by a Rapid Biopsy Processing on the Vacuum Infiltrating Tissue Processor for paraffin filling. 10 μm thick slices were prepared and stained with Safranin O solution (1% for 1 h) and Fast Green (0.1% for 10 seconds) after deparaffinization. The slides were covered by coverslips after dipping in 100% ethanol and xylene.

Fourier Transform Infrared Spectroscopy (FTIR)

IR spectra of microneedles were collected from 4000 to 650 cm^{-1} on a Spectrum 65 (PerkinElmer, Waltham, MA) equipped with an attenuated total reflection (ATR) generic UATR crystal, with a resolution of 4 cm^{-1} and accumulation of 32 scans.

Imaging and image analysis

Scanning electron microscopy (SEM) images were taken using a Zeiss Merlin high-resolution scanning electron microscope. Samples were coated with 10 nm gold and observed on a 45˚ sample holder at 0.8-1 kV and 80 pA. Histological slides were imaged via an Eclipse TE2000-E Inverted Microscope equipped with a DS-Fi3 camera (Nikon, Japan). Optical images of plants were taken using a Nikon D3400 camera (AF-P DX NIKKOR 18-55mm lens) and a Canon EOS 5D Mark IV camera (Canon MACRO 100mm lens). Images of microneedles after injection were taken via a stereomicroscope (AmScope, USA) with a Canon EOS 5D Mark IV camera. ImageJ2 was used to measure distances and analyze images. Adobe PhotoShop 2021 was used to extract the plants and applied a black background for display purposes.

Quantification of GA_3

The amount of delivered GA_3 was quantified by measuring its residue in a microneedle array peeled off at predetermined time points using LC-MS/MS[106]. Each array was dissolved in 1 ml MilliQ water by vigorous vortex and kept at 4 ˚C overnight. The supernatant was collected by

centrifugation at 20000 x *g* for 10 minutes and further diluted 20X to prepare the samples, 25 µl of the sample were run on an Agilent 1100 HPLC using a Thermo Hypersil Gold column (50 mm x 2.1 mm i.d., 3 µm) attached to a Thermo Q Exactive mass spectrometer. Solvent A was 0.1% formic acid in water and solvent B was 0.2% formic acid in 50% methanol. The gradient conditions were 0% B (0-3 min at 300 µl/min), 0-100% B (3-4 min, 300 µl/min), 100% B (4-14 min, 300 µl/min), 100-0% B (14-14.1 min, 300 µl/min), 0% B (14.1-30 min, 300 µl/min). The mass spectrometer was operated in a PRM (Parallel Reaction Monitoring) mode set in the negative mode. The parameters for the full scan MS were: resolution of 35,000 across 75-1000 m/z and maximum IT 50 ms. The PRM targeted GA_3 with a mass of 345.133 m/z. PRM parameters were: resolution of 17,500, maximum IT 100 ms and collision energy set to NCE 20. Data analysis was done in Thermo Xcalibur Qual Browser manually. The area under the curve for the precursor ion 345.133 were recorded for each of the samples and standards. The concentrations of the samples were calculated using the standard curve $y = 2.68 \times 10^8 x$ (adjusted $R^2 = 0.998$) in the range of 1-100 pmol.

Chlorophyll content determination

Leaf tissue was incubated with 96% ethanol (v/v) to completely extract chlorophyll overnight at 4 ˚C in the dark. Samples were centrifuged at 4800 x *g* for 10 minutes. The supernatant was collected and its absorbance was measured from 400-700 nm by a UV-Vis spectrometer in a cuvette with 1 cm light path. The concentration of chlorophyll *a* (C_a) and chlorophyll *b* (C_b) and the total amounts of carotenoids (C_{x+c}) [unit: µg·(ml of plant extract)$^{-1}$] is calculated by the following equations[202]

$$C_a = 13.95A_{665} - 6.88A_{649}$$

$$C_b = 24.96A_{649} - 7.32A_{665}$$

$$C_{x+c} = \frac{1000A_{470} - 2.05C_a - 114.8C_b}{245}$$

RNA sequencing

For RNA-sequencing experiments, silk microneedles with GA_3 (mass ratio of silk to GA_3 = 60 mg: 5.19 mg) were applied to petioles of 30-day-old *ft-10 Arabidopsis thaliana* plants. Leaf samples were collected after 0, 3, 24 and 168 h of microneedle injection. Microneedles were removed prior to harvesting leaf samples. A mock microneedle without GA_3 was used as a vehicle control, and a separate group of samples were injected with mock microneedles for 24 h. Samples were collected in a similar manner to GA_3-injected leaves. Leaf samples were collected from the same leaf in which microneedle injection was carried out. 3 biological replicates (except 168 h, n=2) were made for each group. Total RNA was isolated from the harvested leaf samples using the RNeasy Plant Mini Kit (Qiagen). Library preparation, poly(A) enrichment, and sequencing of 150 bp paired end reads (PE150) was performed by Novogene (Singapore) using the NovaSeq 6000 platform.

Raw sequence reads were mapped to the *Arabidopsis thaliana* (TAIR10) reference genome using STAR 2.7.7a[203] with default settings. Only uniquely mapped reads and properly paired reads were considered. Differentially Expressed Genes (DEGs) were identified using DESeq2[204] in R. Pairwise comparisons to expression levels at the 0 h time point were made, with a threshold of $|\log_2\text{Fold Change (FC)}| > 1$ and FDR < 0.01. Gene Ontology (GO) enrichment analysis was performed using the R package ClusterProfiler[205]. Statistically significant GO terms (FDR < 0.05) were visualized as bar charts using ggplot2 in R.

To monitor the changes in wounding response over time, the R package biomaRt was used to extract *A. thaliana* genes associated with the response to wounding GO term (GO:0009611). A total of 240 unique genes were annotated to the response to wounding GO term, of which 103 were DEGs found in at least one time point in the microneedle transcriptome. The expression values ($\log_2$FC) of these genes were extracted from all time points, then plotted using the R package

ggplot2. Multiple t-tests were performed using the R package ggpubr, using 3 h GA injection timepoint as a reference for comparison, with $p < 0.05$ considered a statistically significant change observed.

In the meta-analysis, a Fisher's Exact Test was performed using R to determine the degree of similarity between our microneedle transcriptome and two GA_3-response transcriptomes from literature[196,197]. DEGs from the GA_3-response transcriptomes were identified based on a threshold of $|\log_2FC| > 1$ and FDR or $p < 0.01$. After calculating enrichment, the expression levels of 232 genes found in common in all 3 datasets were plotted as the Z-score values of $\log_2FC$s in a heatmap constructed using the R package pheatmap. Complete-linkage hierarchical clustering using Euclidean distances was performed, resulting in the identification of five distinct clusters of gene expression dynamics. The overall expression patterns of the genes within each cluster were plotted using the R package ggplot2. GO enrichment analysis was performed using ClusterProfiler on genes within each cluster, and the top 6 GO terms with FDR < 0.05 from each cluster were visualized using ggplot2.

All statistical analyses were performed in R and are described in the figure legends of RNA-sequencing figures.

Statistics and data analysis

Significance was measured with one-way ANOVA with Tukey's test when the population variances are not significantly different at the 0.05 level according to Levene's test. One-way ANOVA assuming unequal variances was used, followed by the Games-Howell test if homogeneity of variances was violated. Student t-test for two-sample assuming unequal variances was used. * $p < 0.05$, ** $p < 0.01$, *** $p < 0.001$, **** $p < 0.0001$. Violin plots show the distribution of data points, while the boxplot displays the minimum and maximum non-outlier observations

(whiskers), lower quartile (Q1), median, and upper quartile (Q3). Data are mean±s.d. in plots with raw data points.

Data Availability

RNA-sequencing data that support the findings of this study have been deposited in NCBI Gene Expression Ombibus (GEO) with the primary accession code GSE202552.

Code Availability

No custom-made code was used in this study.

Acknowledgements

This work was supported by the Singapore-MIT Alliance for Research & Technology, National Research Foundation, Prime Minister's Office, Singapore under its Campus for Research Excellence and Technological Enterprise (CREATE) program. B.M. acknowledges a Paul M. Cook Career Development Professorship and a Singapore Research Professorship. We thank the Koch Institute's Robert A. Swanson (1969) Biotechnology Center for technical support, specifically Kathleen Cormier from the Hope Babette Tang (1983) Histology Facility and Richard P. Schiavoni from the Biopolymers and Proteomics core Facility.

Author contributions

Y.C., N.-H.C. and B.M. conceived the project and designed preliminary experiments. Y.C., B.M., S.S.K., and D.U. designed the study and wrote the manuscript. Y.C. and S.S.K. performed the majority of experiments and data analysis. Y.H., J.J.T., D.K. assisted with experiments and result discussions. All authors have revised the manuscript and given their approval of the final version.

Competing interests

B.M. is co-founder of a company, Mori Inc., that uses silk fibroin-based materials as edible food coatings to increase the shelf-life of perishable food. The use of silk fibroin as an edible coating,

seed coating, and to fabricate microneedles for drug delivery in plants is protected by multiple IP positions where B.M. is listed as a co-inventor.

4.6 Supplementary Information

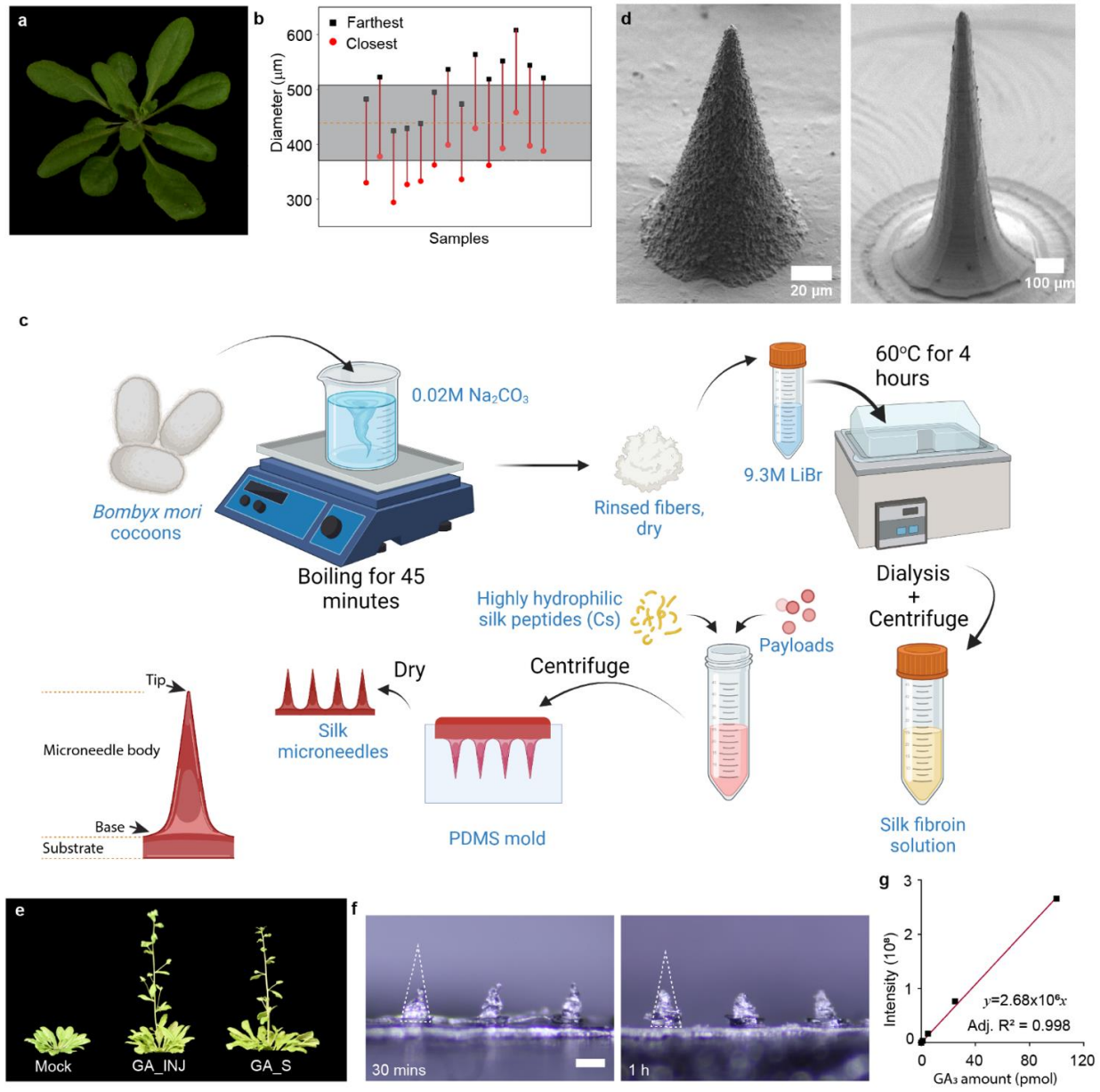

Figure S4.1. Silk-based microneedles-mediated GA_3 delivery to *ft-10*. a. Representative image of a bolting wild-type *Arabidopsis thaliana* Col-0 plant on day 23 with 12 rosette leaves. **b.** The distribution (closest and farthest distance) of the vasculature to the adaxial surface of the petiole in 30-day-old *ft-10*. The gray area of 439±69 μm (mean of the middle point of vasculature ± half of mean thickness of vasculature, 370-508 μm) highlights the location of the vasculature. **c.** Schematic of silk-based microneedle fabrication. Created with BioRender.com. **d.** SEM images of

the smaller and larger microneedles compared to Figure 4.1c. Their dimensions are listed in Table S4.1. **e.** Representative images of *ft-10* treated by microneedles without (Mock) and with (GA_INJ) GA_3 and spray (GA_S). Both groups of GA_3 treated *ft-10* showed remarkable phenotype differences (e.g., bolting time, the numbers of rosette leaf and cauline leaf, and leaf size) with Mock. Images were taken 21 days after the first treatment. These pre-experiments were carried out on 5-week-old *ft-10* growing under long-day conditions with 25 ˚C in the day and 19 ˚C at night. Treatments were carried out every other day for two weeks. **f.** Representative images of GA_3-loaded microneedles 30 minutes and 1 hour after injection. The white triangles estimate the initial shapes of microneedles. Scale bars 200 µm for both. **g**. The standard curve of GA_3 quantification using LC-MS/MS. The standard curve showed great linearity (adjusted $R^2 = 0.998$) in the range of 1-100 pmol, corresponding to 0.04-4 µM GA_3. Sample concentrations fell within this range.

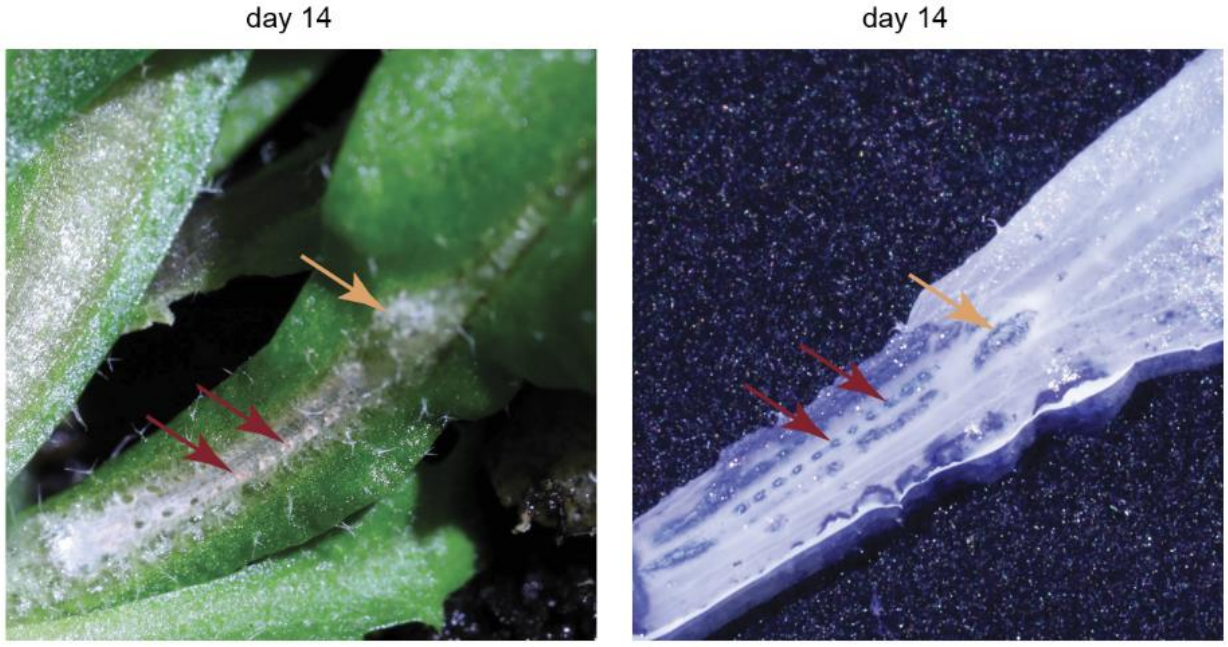

Figure S4.2. Wounding responses of *ft-10* to microneedle injection. Representative images of *ft-10* petioles 14 days after injected by silk materials-based microneedles. R6g was added to microneedles for display purposes (left), and trypan blue was used to stain the dead cells (blue) (right). Red arrows indicate the scar left by microneedles, and orange arrows show callus.

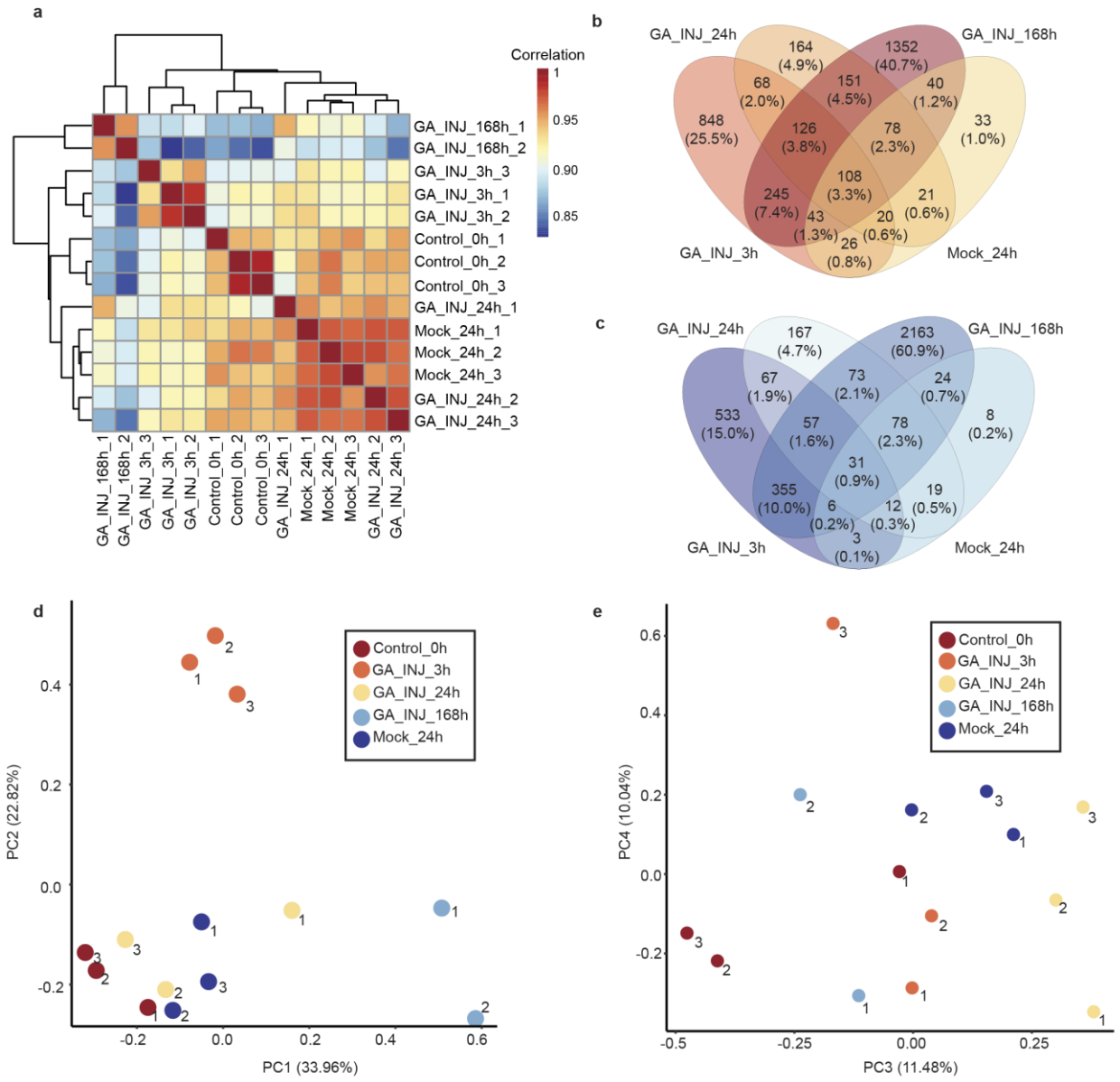

Figure S4.3. Overview of the GA_3 microneedle transcriptome. RNA-sequencing was carried out on leaf samples that were injected with GA_3-loaded silk microneedles. **a**. Heatmap showing correlation of expression patterns of each sample. Samples from the same treatment group should cluster with each other, suggesting good sample quality. **b-c**. Venn diagrams summarizing the overlap of DEGs between each treatment group. Overlap between upregulated DEGs is displayed above (**b**, red), and overlap between downregulated DEGs is shown below (**c**, blue). **d-e.** Principal Component Analysis (PCA) of the samples sent for RNA-sequencing analysis. **d** displays PC1 and PC2, while **e** displays PC3 and PC4. Numbers on each datapoint reflect the sample number (biological replicate) within each group, while different colors represent different treatments. The full list of DEGs can be found in Supplementary Data 1.

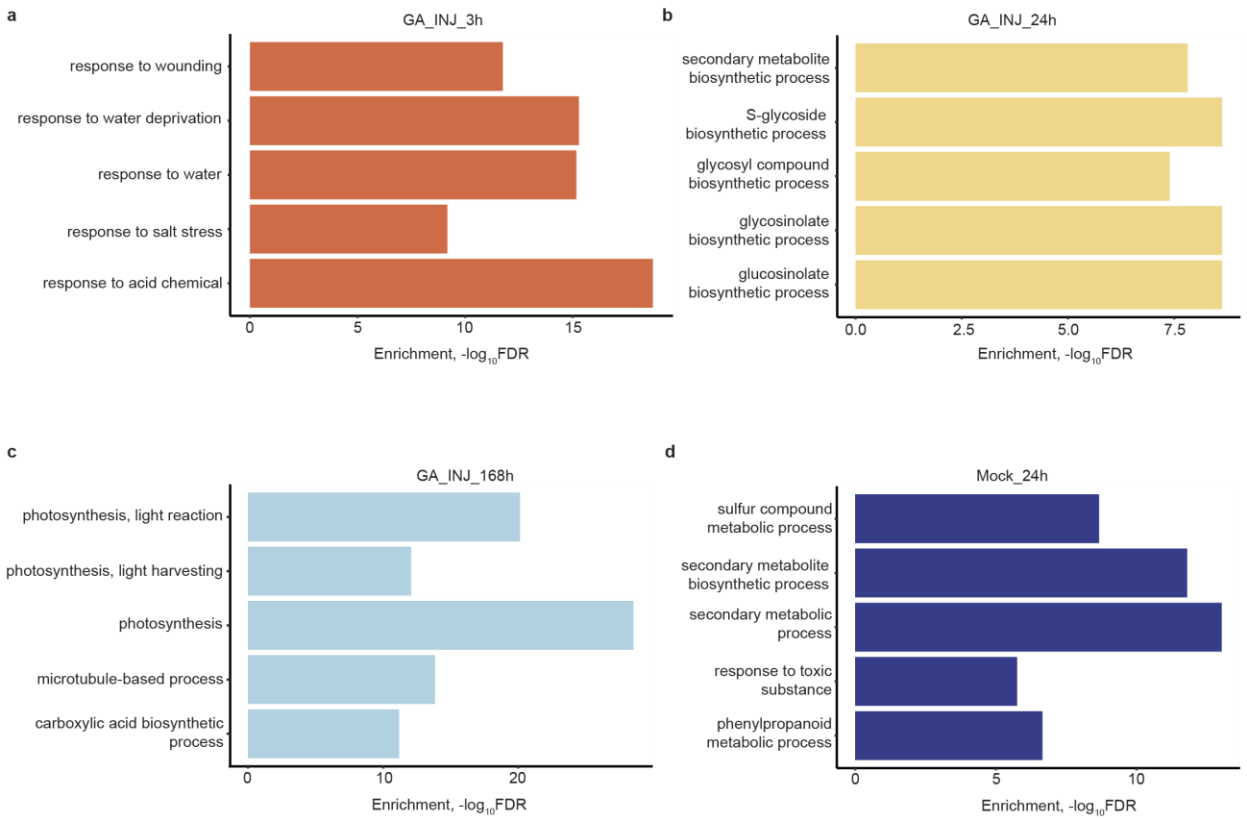

Figure S4.4. Gene Ontology (GO) enrichment analysis of DEGs identified in the GA_3 microneedle transcriptome. GO enrichment analysis was carried out on the DEG lists at each timepoint. Enriched GO terms are defined as GO terms with FDR < 0.01. The top 5 enriched GO terms from (**a**) 3 hours GA_3-loaded microneedle treatment, (**b**) 24 h post microneedle treatment, (**c**) 168 h post microneedle treatment, and (**d**) 24 h mock injector treatment are displayed. The full lists of GO terms from enrichment analyses can be found in Supplementary Data 2.

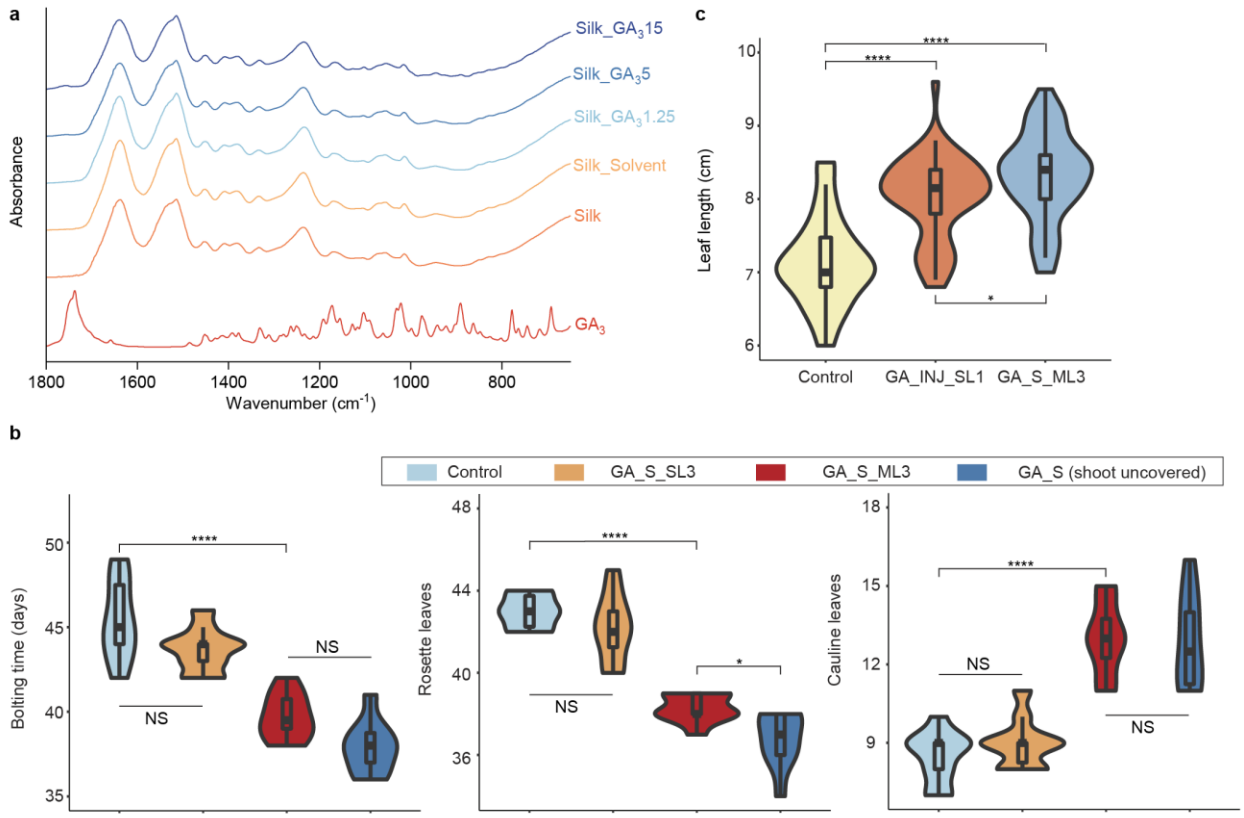

Figure S4.5. Microneedle-mediated GA_3 delivery to *ft-10* and comparison with spray. a. IR spectra of GA_3 and GA_3-loaded silk materials-based microneedles. Silk_solvent, Silk_$GA_3$1.25, Silk_$GA_3$5, Silk_$GA_3$15 denote microneedles fabricated from 0, 1.25 mM, 5 mM, and 15 mM GA_3 originally. While GA_3 stock solution contains ethanol that can cause the beta-sheet formation of silk, no apparent difference was observed from the spectra during microneedle fabrication. **b.** Bolting time, rosette leaf number, and cauline leaf number of *ft-10* treated with GA_3 solution by spray. Spraying on a single leaf three times (GA_S_SL3) had 7.1±1.8% solution sprayed on leaves while spraying all leaves with shoot apex covered three times (GA_S_ML3) has 47.7±3.4% solution on leaves. In each treatment, around 0.64 g solution was applied. There was no difference between GA_S_SL3 and Control, likely due to the limited amount of GA_3 delivered. GA_S_ML3 showed remarkable differences with Control (p < 0.0001), indicating a reasonable amount of applied GA_3 and suitable positive control. Indeed, careful spray application can apply 60-70% of the solution onto leaves. In our experiments, plants were sprayed individually; the plant could not get sprayed when its adjacent plant was treated. Thus, our spray method is acceptable. Direct exposure of shoot apex to spray did have some privilege compared to covered shoot apex in spray, as indicated by the difference in rosette leaf number of GA_S (shoot apex uncovered) and GA_S_ML3 (p = 0.033). Since shoot apex is generally well protected and may get limited exposure to spray, we used GA_S_ML3 as the positive control in *ft*-10 treatment. **c.** Leaf length of *ft-10* 10 days after various treatments. As indicated by the results, both microneedle injection (GA_INJ_SL1) and spray (GA_S_ML3) significantly promoted leaf growth. The spray showed larger leaf sizes than microneedle injection (p = 0.040). Violin plots show the distribution of data points, while the boxplot displays the minimum and maximum non-outlier observations (whiskers),

lower quartile (Q1), median, and upper quartile (Q3). One-way ANOVA was performed, followed by the Tukey test. * $p < 0.05$, ** $p < 0.01$, *** $p < 0.001$, **** $p < 0.0001$.

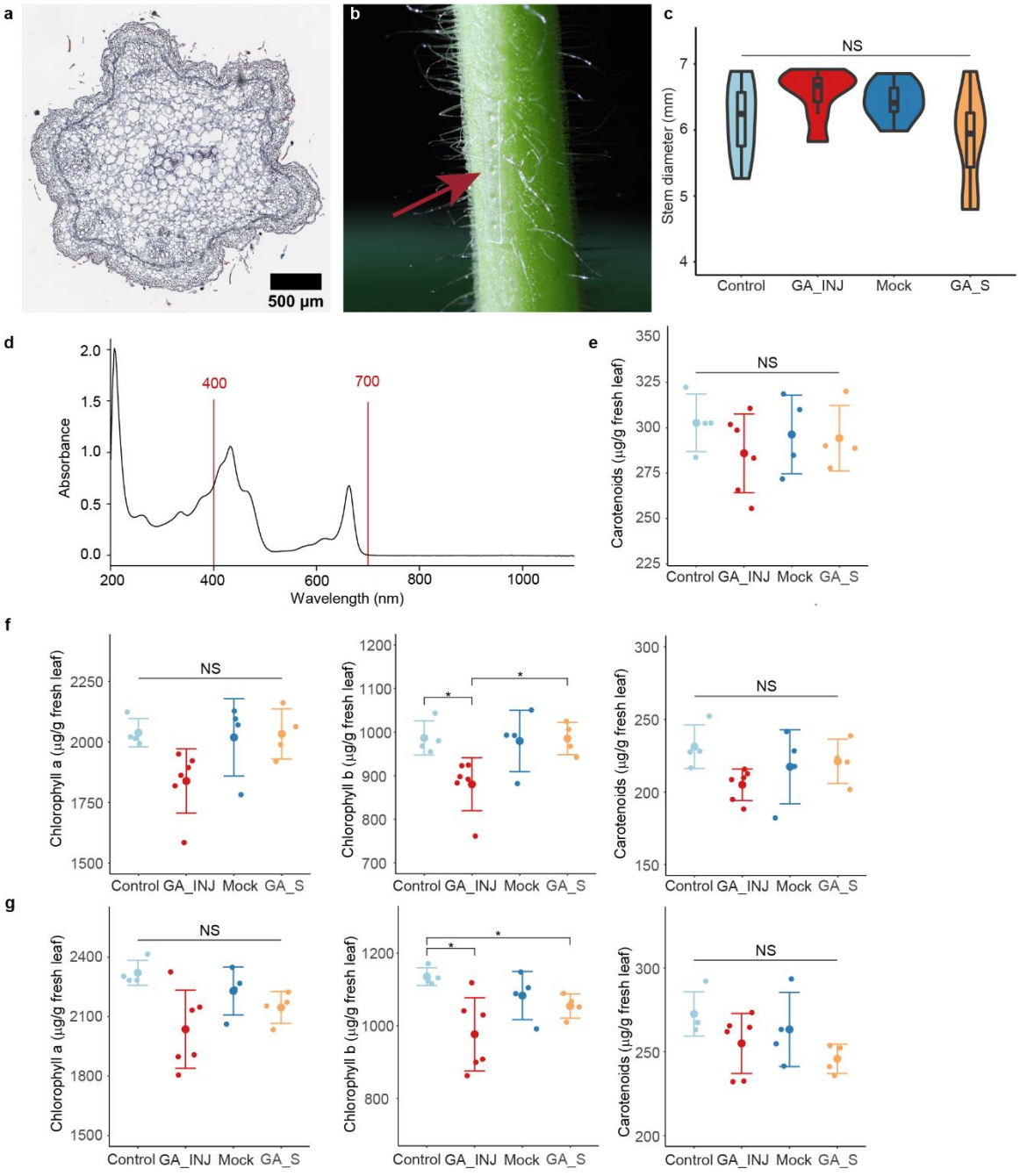

Figure S4.6. Utility of microneedles to deliver GA_3 to tomato plants. a. Cross-section of the stem of a tomato plant, Xylem is stained red while phloem is blue. Scale bar 500 µm. **b.** GA_3-loaded microneedles were injected into a 25-day-old tomato plant. The red arrow points to the clear microneedle array. **c.** Stem diameter of tomato plants 7 days after various treatments. Control indicates no treatment, GA_INJ is injection with GA_3-loaded microneedles, Mock denotes

injection with microneedles without GA_3, and GA_S is the foliar spray of GA_3 solution (100 µM). Data are mean ± s.d.. **d.** The absorption spectrum of tomato leaf extract. Absorbance in 400-700 nm was collected for all samples. **e.** Carotenoids in the 4th leaf (newly emerging leaf, length < 2cm when treated) of treated tomato plants. All treatments did not cause the contents of carotenoids to be different. **f-g.** Chlorophyll a, chlorophyll b, and carotenoids in treated tomato plants' second and third leaf, respectively. The second leaf was mature, and the third was expanding when the treatments were applied. Both chlorophyll a and carotenoids were not affected by treatments in the 2nd and 3rd leaf. For the 2nd leaf, GA_3 delivered by microneedles induced chlorophyll b content decrease compared to both Control (p = 0.039) and spray (p = 0.039), while spray showed no difference from Control. For the third leaf, both spray (p = 0.035) and microneedle (p = 0.040) delivered GA_3 induced chlorophyll b content decrease. Violin plots show the distribution of datapoints, while the boxplot displays the minimum and maximum non-outlier observations (whiskers), lower quartile (Q1), median, and upper quartile (Q3). One-way ANOVA was performed, followed by the Tukey test. One-way ANOVA assuming unequal variances was used, followed by the Games-Howell test if homogeneity of variances or equal group size was violated. * p < 0.05, ** p < 0.01, *** p < 0.001, **** p < 0.0001.

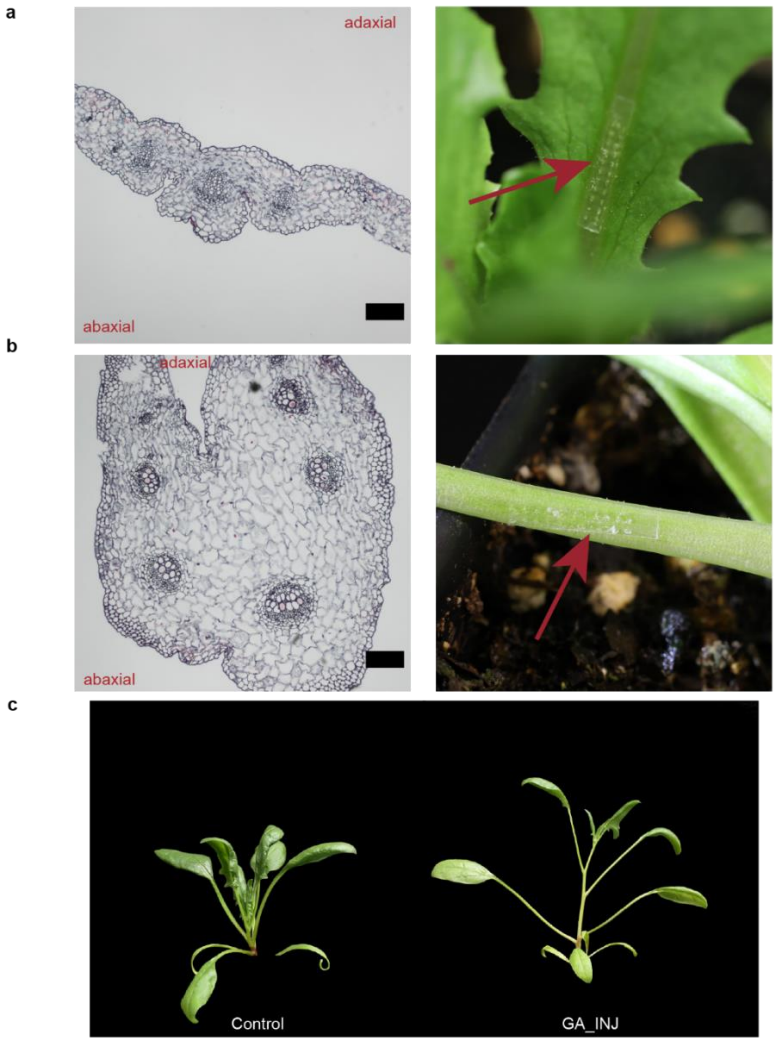

Figure S4.7. Utility of microneedles to deliver GA_3 to lettuce and spinach. a. Cross-section of the midrib of lettuce (left) and GA_3-loaded microneedles injected on the midrib of 17-day-old lettuce (right). **b.** Cross-section of the petiole of spinach (left) and GA_3-loaded microneedles injected on the petiole of 3-week-old spinach. **c.** Representative images of two spinaches without treatment (Control) and injected by GA_3-loaded microneedles (GA_INJ). Images were taken 7 days after treatments. The injected spinach has a much longer stem than Control.

Table S4.1. Dimensions of microneedles.

	Height (μm)	Base diameter (μm)	Tip diameter (μm)	Center to center distance (μm)	Volume (nL)
Figure 4.1c	531.10±39.25	225.59±3.40	<5	580	7.08
Figure S4.1d (left)	141.55±1.79	82.21±0.95	<3	200	0.25
Figure S4.1d (right)	1006.1±65.3	258.66±7.84	<40	1500	17.6

Dataset S1, See Appendix A.1.

Dataset S2, See Appendix A.2.

Chapter 5 Phase Front Assembly of Biopolymers for Mesostructured Materials Design

The contents of this chapter were submitted as Doyoon Kim[1], Yunteng Cao[1], Zheng Li[2], Federica Rigoldi[1], Hui Sun[1], Rajeev J. Ram[2], and Benedetto Marelli[1]*

[1]Department of Civil and Environmental Engineering, Massachusetts Institute of Technology, Cambridge, MA, USA

[2]Department of Electrical Engineering, Massachusetts Institute of Technology, Cambridge, MA, USA

"Phase Front Assembly of Biopolymers for Mesostructured Materials Design"

5.1 Abstract

Condensation phenomena at the interface between biopolymer matrices and inorganic ions modulate many biological processes (e.g., biomineralization) and have inspired high-performing materials design. However, little is known about inorganic ions orchestration of biopolymers assembly; thus, the use of ions to direct protein assembly is mostly limited to uncontrollable and disordered "salting out" processes. Here, we report the simultaneous manipulation of silk fibroin assembly and inorganic nucleation at their phase front to drive the formation of three-dimensional, ordered, nanoporous and hollow microstructures. Using one-pot manufacturing of mesostructured microneedles as an example, we show that phase front assembly enables the fabrication of microneedles with hollow and nanoporous tips, unattainable with other fabrication methods. These mesostructured microneedles provide new tools to bridge the biotic/abiotic interface by interrogating pathways for biomolecules transport in plants and detecting early-stage bioaccumulation of environmental contaminants, such as cadmium and arsenic.

5.2 Introduction

Ever-increasing human population pressures stakeholders in the manufacturing, agro-food, and water-energy infrastructures to rapidly raise their outputs using already available and cost-efficient technological solutions[184,206-208] based on linear materials and resource models that follow

make-take-discard practices[209,210]. The development of new materials that combine large-scale production with performance and mitigation of environmental impact is therefore an instrumental step to addressing the challenges that society will face this century. Among several new materials currently considered renewable and biodegradable, natural polymers offer many merits, including large availability, non-toxicity, processing in water, ease of regeneration, and fabrication into several formats[209,211]. However, manufacturing biopolymers at the nanoscale into pre-defined structures and morphologies remains a technological challenge due to the complexity of material condensation[10]. Currently, nano and mesostructures in biopolymer-based materials are often achieved with top-down techniques or with multi-step, bottom-up approaches that are costly, time-consuming, and limited in material size[212,213], hindering their large-scale applications.

In living materials, condensation at the interface between inorganic ions and pre-formed biopolymer matrices modulate the formation of nano and mesostructured materials – such as bone and nacre[214-216] – that have outstanding mechanical properties and have inspired bottom-up strategies to fabricate high-performing materials[217-219]. Alternatively, inorganic-organic templating has been explored to guide the assembly of biopolymers on well-defined mineral surfaces to design sensors and catalytic domains[220]. Nonetheless, little is known about how the concurrent condensation of inorganic ions and biopolymers is modulated to form ordered materials with pre-defined porosity, shape, and structure. Here, we report the simultaneous manipulation of silk fibroin (SF) assembly and nucleation of salt crystals at their phase front to drive the formation of mesostructures unattainable with current fabrication methods (Figure 5.1). The one-pot, bottom-up process is easily scalable and yields 2D or 3D nanoporous or hollow structures on a cm-scale within several hours (Figure 5.1a–i). In addition, microneedles with nanoporous tips and hollow structures were fabricated for delivery to and sampling from plants, demonstrating proof-of-

concept of the capabilities of phase front assembly (PFA) and such microneedles bridging the biotic/abiotic interface in living systems.

5.3 Results and Discussion

5.3.1 Atomistic modeling and nanoscale study of SF–cations interactions

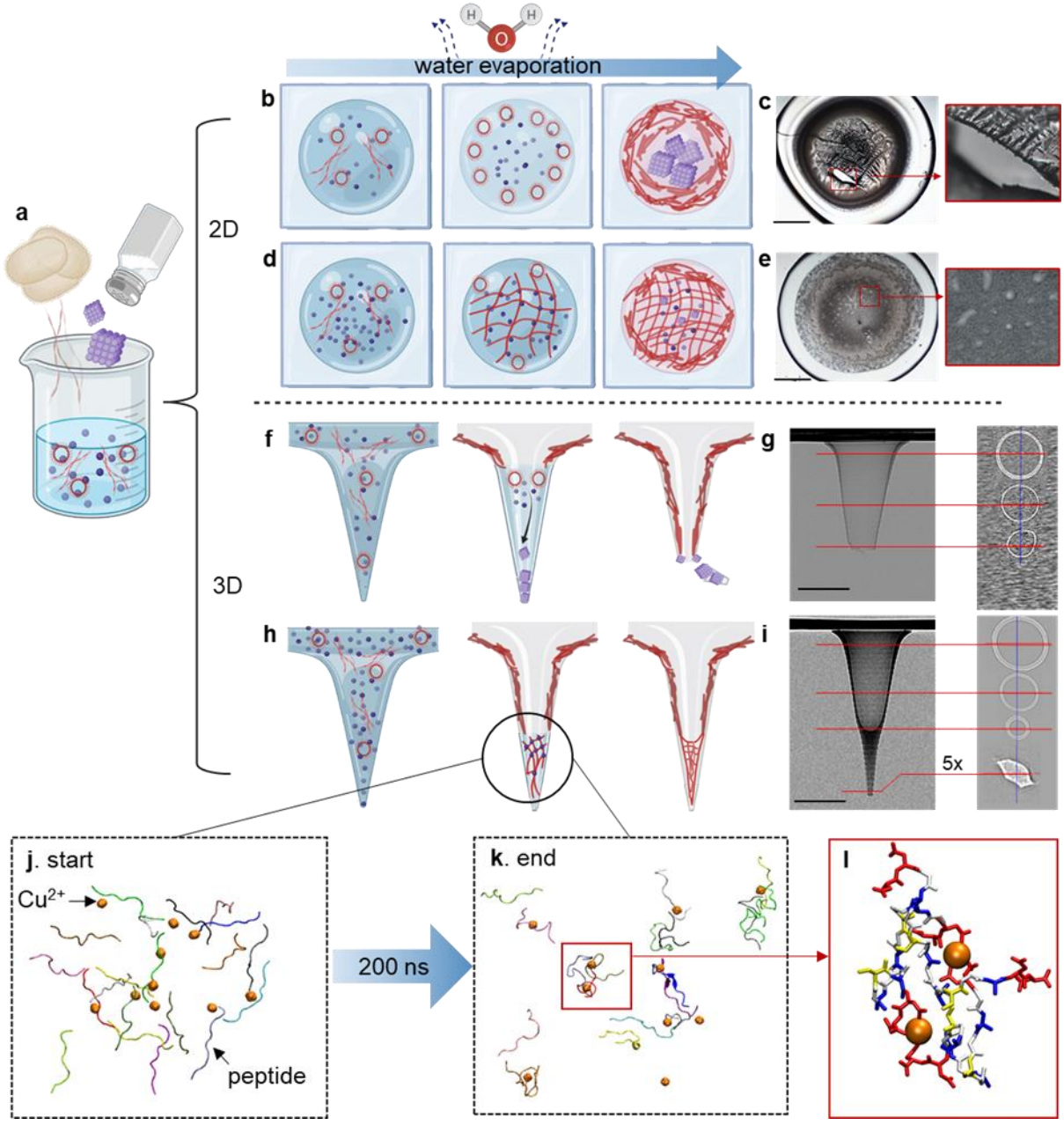

Figure 5.1. **Phase front assembly for the fabrication of silk-based hollow/porous microneedles**. **a**, Preparation of regenerated SF solution extracted from Bombyx mori cocoons with the addition of ionic salt. **b-e**, Fabrication of films (2D structure). **b**, At a moderate ionic

strength, ionic salts are concentrated at the center of the film while SFs assemble from the edge (salt-out). This condition forms a film with two separable regions (silk-heavy ring and salt crystal-dominant center). **c**, Optical microscope images of a film prepared from a 5 µL droplet containing 0.5% NaCl and 5% SF_S (NaCl:SF_S=1:10). **d**, Elevation of ionic strength (salt concentration or use of multi-valent ions) traps metal ions in the SF network (gelation). Drying of the silk-gel film leaves microscale pores. **e**, Optical microscope images of a film prepared from a 5 µL droplet containing 1% $CuSO_4$ and 5% SF_S ($CuSO_4$:SF_S=1:5). **f–i**, Fabrication of microneedles (3D structure). **f**, Ionic salts are concentrated at the tip of the microneedle, while SFs assemble from the base at moderate ionic strength. This condition can form a film with two separable regions (silk-heavy ring and salt crystal-dominant center). **c**, Optical microscope images of a film prepared from a 5 µL droplet containing 0.5% w/v NaCl and 5% w/v SF_S (NaCl:SF_S=1:10, w:w). **d**, Elevation of ionic strength (salt concentration or use of multi-valent ions) traps metal ions in the SF network (gelation). Drying of the silk-gel film leaves microscale pores. **e**. Optical microscope images of a film prepared from a 5 µL droplet containing 1% w/v $CuSO_4$ and 5% w/v SF_S ($CuSO_4$:SF_S=1:5, w:w). Scale bars are 500 µm (**c**, **e**, **g**, **i**). **j–I**, Atomistic representation of silk mimic peptides ($DD(GAGSGA)_2DD$) aggregation- state at time 0 (**j**) and 200 ns (**k**). Copper ions (Cu^{2+}, orange sphere) make inter-peptides 'ionic-bridges', stabilizing the resulting aggregates. Interaction detail shows that Cu^2 are chelating by interstrand interactions by the charged portion of silk-mimic peptides (**l**). Peptides strands are colored by restype (red for ASP, yellow for ALA, white for GLY, and blue for SER).

To understand the concurrent condensation of SF and inorganic ions, we used an atomistic model to explore the interactions in solution between a silk-mimic peptide (i.e., $DD(GAGSGA)_2DD$) and two naturally abundant cations known to stabilize the *Bombyx mori* silk dope: Na^+ and Cu^{2+} [221]. A Cu^{2+} ion stabilizes aggregates of several silk-mimic peptides by forming stable 'ionic bridges' (Figures. 5.1j-k and 5.2a–c). A detailed view of the peptide-dication interaction model depicts how Cu^{2+} is chelated through interstrand interactions mainly formed with the charged portion of silk-mimic peptides (Figure 5.1l). On the other hand, Na^+ cation-peptide interactions were less stable (average stability pair is about 20% of simulation time, opposite to > 80% induced by Cu^{2+}), and resultant peptide assemblies involved a single strand-ion pair (average number of contacts < 1.5 for 85% of pairs) (Figure 5.2b). The Na^+ system also showed a two-order of magnitude increase in ion mobility (measured as mean square displacement, Figure 5.2c) compared to Cu^{2+}. At the macroscale, these results are corroborated by the Cu-mediated SF hydrogel formation from the SF suspension with increased Cu^{2+} content (Supplementary Figure 5.1) and other structural proteins[222].

Atomic force micrographs validate the atomistic model simulation at the nanoscale, showing that the Cu^{2+} promoted the aggregation of nanowhiskers assembled from silk-mimic peptides $(GAGSGA)_2$ compared to Na^+ (Figure 5.2d,e). Less Na^+ cations were involved in ionic bridges, which increased the cation availability in solution and resulted in the heterogeneous nucleation of NaCl crystals on the peptides (Figure 5.2d inset), indicating the concurrent condensation of peptides and inorganic crystals during water evaporation. Furthermore, the hydrodynamic radius of the nanowhiskers was smaller in the presence of Na^+ compared to the same molar concentrations of Cu^{2+} (Figure 5.2f).

5.3.2 Salt crystallization during silk film formation

To further investigate the simultaneous condensation of SF and inorganic ions across several scales, we investigated the crystallization of NaCl and $CuSO_4$ from their ionic species in droplets of SF suspension on a polydimethylsiloxane (PDMS) substrate (Figure 5.2g–j). SF suspensions with two average molecular weights of ~270 kDa (larger SF, SF_L) and ~200 kDa (smaller SF, SF_S) were used for comparison (Supplementary Figure 5.2)[165]. We hypothesize that SF_L with more intrinsic folding of hydrophobic regions may promote salting out at lower salt concentrations. Due to the high surface energy between the salt solution without SF and the hydrophobic PDMS, the contact angle of the droplet (>80º) remains mostly constant during water evaporation (Figure 5.2g), forming a single NaCl or $CuSO_4$ particle at the end (Figs. 2i,j). The SF addition reduces the surface energy, pinning the contact line during evaporation and inducing a coffee-stain effect, accumulating more SF at the pinned edge (Figure 5.2h)[223,224]. With relatively low SF concentrations (e.g., 0.5% NaCl+0.25% SF_S (w:w=2:1, Figure 5.2i) and 0.05% $CuSO_4$+0.05% SF_S (w:w=1:1, Figure 5.2j)), crystals mainly form near the contact lines. As suggested by the atomistic model and atomic force micrographs, the negatively charged SF segments rich in carboxylic acids attract crystals' ionic precursors[133] and drive heterogeneous nucleation on SF's surface[225]. An

increase in SF concentrations, from 0.25% to 0.5 or 1% SF_S (NaCl:SF_S=1:1 and 1:2, Figure 5.2i), results in more NaCl particles but of smaller size, following classical nucleation theory[226].

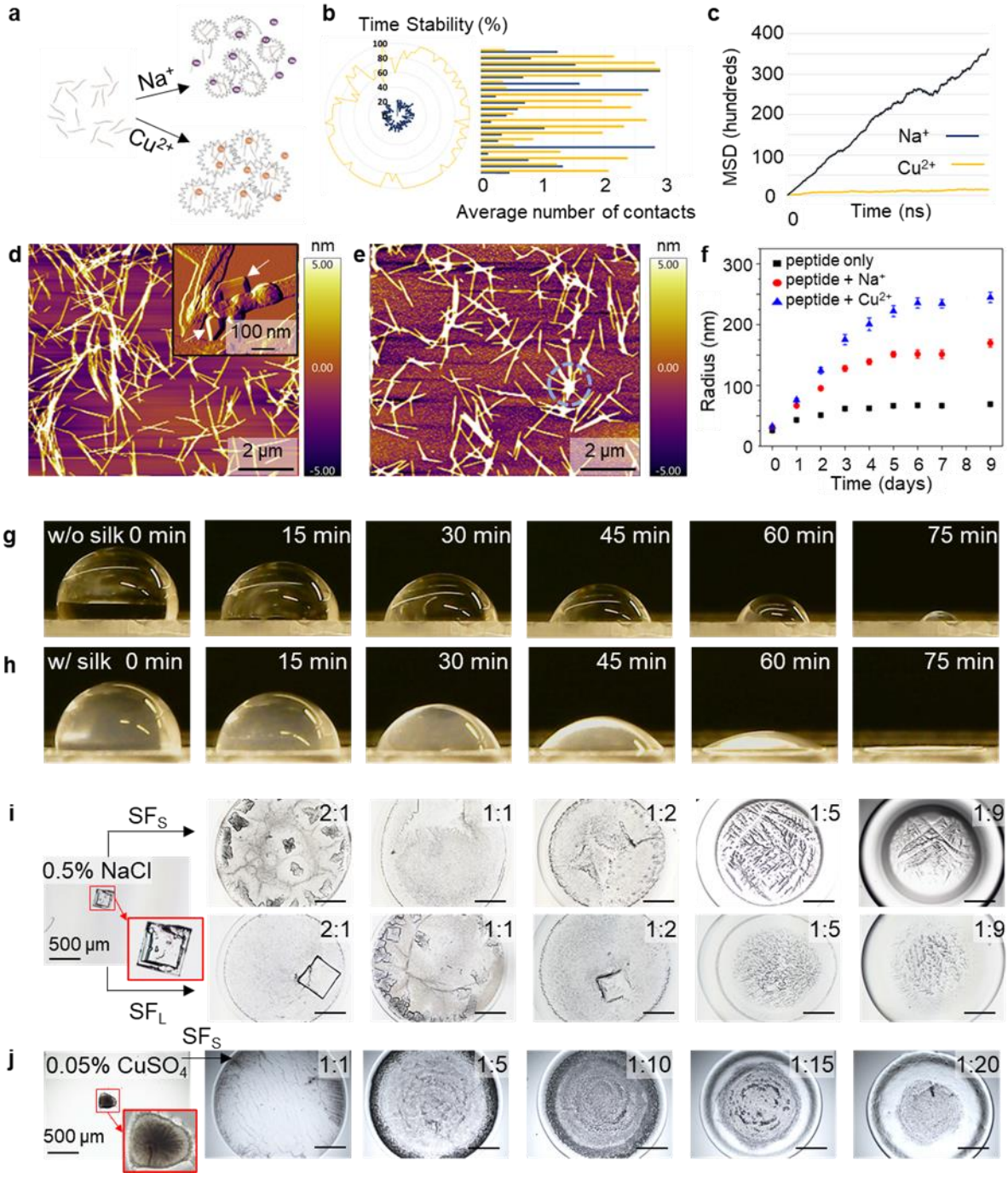

Figure 5.2. **Silk-ionic salt interactions in solutions and films**. **a**, Schematic of interactions between homologues ion species (Na^+-blue spheres and Cu^{2+}-orange spheres) with randomly places SF-mimicking peptides ($DD(GAGSGA)_2DD$). **b-c**, Molecular dynamics simulation insights in peptides aggregation state. Time stability of ion-bridges and aggregates dimension estimation

(**b**) and mean square displacement (MSD, **c**) in the presence of the two different ions species (Na^+: blue and Cu^{2+}: yellow). For the time stability (%), we evaluate the ion-peptide pairs (pairs are defined with cut-off distance = 0.4nm) and pursue a hierarchical classification of the formed aggregates as an estimate of the average number of peptide-peptide pairs during simulation. **d–f**, Assembly of SF-mimicking peptides (0.244 mM, $(GAGAGS)_2$) in the presence of 1.22 mM of Na+ or Cu^{2+}. Atomic force micrographs (height images) show that peptides assembled into nanowhiskers either with Na+ (**d**) and Cu^{2+}(**e**) on day 6. Inset of **d** is a zoomed-in amplitude image showing the formation of NaCl nanocrystals (white arrows) at the junction of multiple nanowhiskers. With Cu^{2+}, nanowhiskers are more heavily aggregated at a junction (circled area in **e**). Dynamic light scattering characterization shows that the hydrodynamic radius of the peptide assemblies increases more rapidly with Cu^{2+} than Na^+ (**f**). Data in **f** are mean ± SD from three measurements. **g–h**, Side view monitoring of the evaporation of $CuSO_4$ solution (0.2% w/v, 5 µL) on PDMS without (**g**) and with SF_S (**h**, $CuSO_4$:SF_S=1:5, w:w). **i–j**, Optical microscope images of 5 µL droplets on PDMS after evaporation. Initial solutions contained 0.5% w/v NaCl (**i**) and 0.05% w/v $CuSO_4$ (**j**) with SF_S and SF_L. The ratios are weights of salts to silk fibroins. Scale bars are 500 µm. $CuSO_4$ with SF_L was not tested because of immediate gelation.

The salt-forming pattern changes significantly when the relative fibroin concentration increases enough to fabricate self-standing films. SF form micelles where hydrophobic chains surround hydrophilic intermolecular spacers[227], repelling ionic precursors from the silk-accumulating contact line and forcing particle formation close to the center of the film (e.g., 0.5% NaCl+4.5% SF_L (w:w=1:9, Fig.2i) and 0.05% $CuSO_4$+1% SF_S (w:w=1:20, Fig.2j)). Consequently, two weakly bound phases appear in the film: a silk-dominated edge and a central area with high salt inclusions (also shown in Figure 5.1c). Due to the stronger interaction of Cu^{2+} with SF than Na^+, this phase-separation in the film was more clearly observed with the addition of $CuSO_4$ than NaCl (Figure 5.2i,j). Further increases in Cu^{2+} concentration resulted in gelation of SF solutions, leading to another phase separation of SF dense (via aggregation) and sparse regions (Figure 5.1e and Figure S5.1). The highly viscous environment of the copper-mediated SF gel further inhibits crystallization or growth of $CuSO_4$ crystals and hinders material reflow in the SF sparse region during water evaporation, resulting in the formation of pores. These two different phase separation phenomena directed by Cu^{2+} provide the basis for the PFA described below.

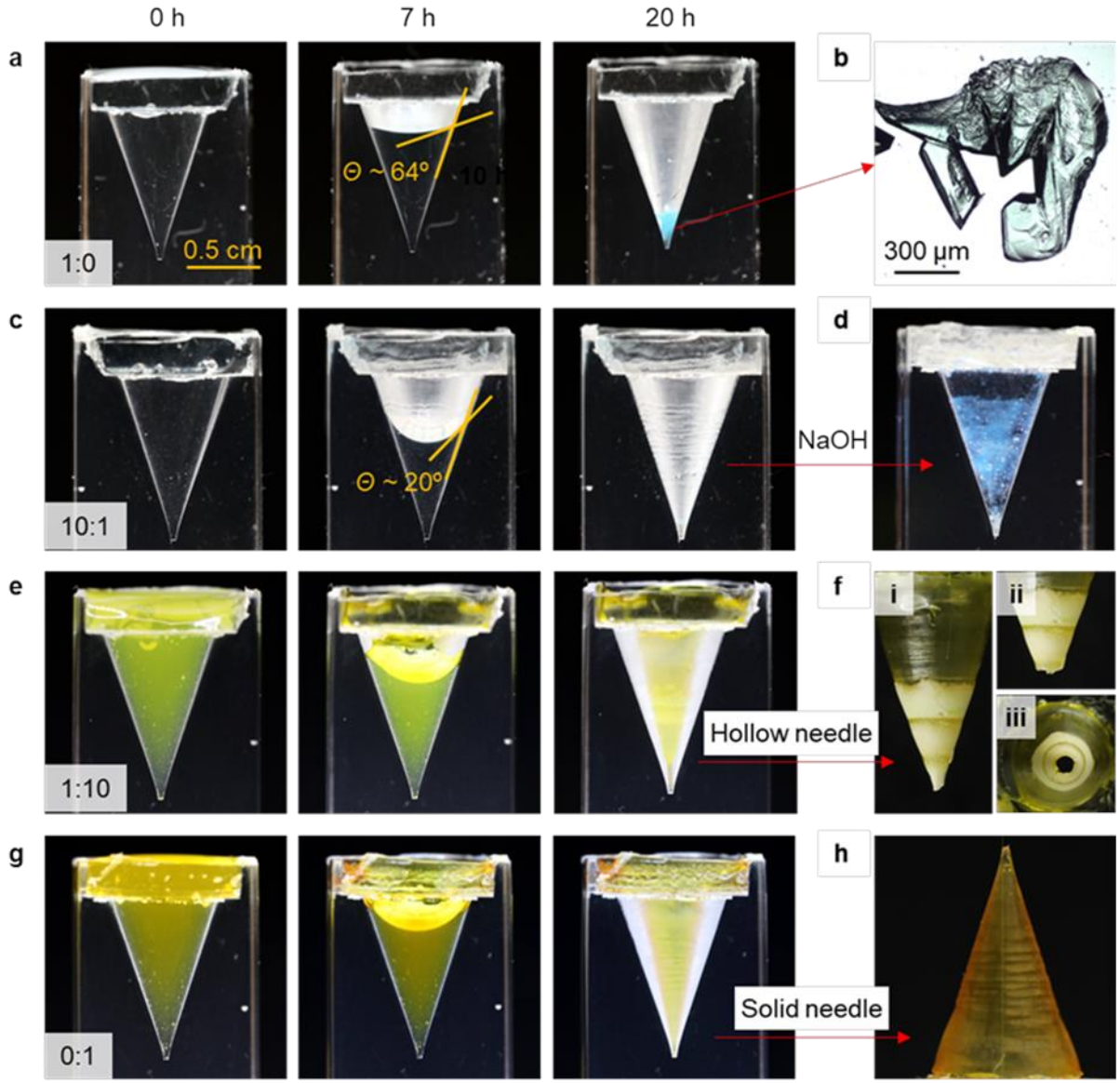

Figure 5.3. **Macroscopic view of crystallization of $CuSO_4$ in silk fibroin solutions during needle formation.** Photographs of 0.5% $CuSO_4$ solutions evaporating in a PDMS mold (0.6 cm base diameter × 0.9 cm long) at 0, 7, and 20 h with $CuSO_4$ to SF_S weight ratios at 1:0 (**a**), 10:1 (**c**), 1:10 (**e**), and 0:1 (**g**). **b**, Optical microscope of the $CuSO_4$ precipitates from the solution without silk ($CuSO_4$:SF_S=1:0, w:w). **d,** Addition of 0.1 N NaOH forms blue hydroxide mineral and visualizes Cu distribution on PDMS wall after evaporation of the solution with low SF concentration ($CuSO_4$:SF_S=10:1, w:w). **f**, At high silk fibroin ($CuSO_4$:SF_S=1:10, w:w), $CuSO_4$ precipitated heavily at the tip (**i**) that is easily separated from the column region to form a hollow microneedle structure (**ii, iii**). **h**, Solid microneedle with mechanical integrity formed by pure silk solution. 0.005% phenol red is added to solutions with high fibroin concentrations ($CuSO_4$:SF_S=1:10 and 0:1, w:w) for display purpose.

5.3.3 Structural manipulation of three-dimensional silk structures via phase front assembly

Using time-lapse photography, we monitored salt crystallization and 3D silk assembly in a conical PDMS well representing a scaled-up version of a microneedle replica mold (Figure 5.3). From the initial 0.5% $CuSO_4$ solution without SF, hydrated crystals with a clear blue color precipitated at the bottom tip of the mold (Figure 5.3a,b). The addition of 0.05% SF_S ($CuSO_4$:SF_S=10:1) inhibited crystal precipitation at the tip (Figure 5.3c); the mold wall was covered uniformly with white residues, presumably aggregates of silk fibroins bound with ionic Cu due to the chelating action of SF. Adding 0.1 N NaOH into the dried mold formed blue $Cu(OH)_2$ crystals, confirming that Cu precursors distributed uniformly along the mold wall (Figure 5.3d). As shown in the 2D film formation process, SF decreased the surface energy, lowering the contact angle from ~64º to ~20º at 7 h (Figure 5.3a,c), and attracted SF with Cu ions to the wall. This relationship (i.e., decreasing surface energy and increasing polymer accumulation) observed in evaporating polymer solutions inside a cavity can be explained by the competition between Marangoni effect and capillary flow[228]. When we operated at a sufficient SF concentration to form a cone-like film covering the entire mold wall (0.5% $CuSO_4$+5% SF_S, w:w=1:10), two separate regions appeared and formed a hollow mesostructure (Figure 5.3e,f). Cu^{2+} and sulfate ions, repelled by SF assembly forming a film from the base, were concentrated at the tip region, leading to a clear separation of the silk-dominant transparent column and the Cu-heavy opaque tip (Figure 5.3f-i). The significant $CuSO_4$ inclusion disrupted film integrity and broke the tip, resulting in a complete hollow needle structure (Figure 5.3f-ii,iii). The silk-only solution formed a similar cone-like needle without phase separation or brittle tip formation (Figure 5.3g,h).

We applied PFA to fabricate hollow microneedle arrays using a PDMS mold (10×10 needles, 600 μm base diameter and 1.6 mm long) exposed to SF, NaCl and $CuSO_4$ (Figure 5.4). A detailed description of the results obtained by varying salt to SF ratios can be found in Supplementary Text

1 and Supplementary Figs. 3 and 4. In brief, no salt supplement formed solid microneedles (SMNs) made of a pure SF (5 % w/v, $CuSO_4$:SF_S=0:1, Figure 5.4a). The addition of ionic $CuSO_4$ in the solution resulted in either hollow microneedles (HMNs, Figure 5.4b–e, dominantly fabricated at $CuSO_4$:SF_S=1:100 and 1:50) or porous ones (PMNs, Figure 5.4f–h, dominantly fabricated at $CuSO_4$:SF_S=1:20). Compared to NaCl (Figure 5.4i–k and Figure S5.3), $CuSO_4$ provided more consistent structures during fabrication; lower water solubility[229] induces nucleation at an earlier PFA stage when the solution is less viscous and material reflow allows for the formation of defectless structures. Less viscous conditions and the higher density of the $CuSO_4$ nuclei, when compared to the NaCl ones, also result in a faster Stoke's flow of the forming crystals, which precipitate toward and accumulate at the tip of the mold. Additionally, $CuSO_4$ enabled the fabrication of PMNs. At higher $CuSO_4$ concentrations (>0.5% w/v, $CuSO_4$:SF_S=1:20 and 1:10), Cu^{2+} ions concentrated at the tip induced SF gelation by sticky reptation[221], inhibiting the formation of HMNs due to the limited diffusion of Cu and sulfate ions needed for the growth of $CuSO_4$ crystals, in accordance to atomistic models, AFM measurements, and 2D observations. Micro-computed X-ray tomography (microCT) image shows that the PMN ($CuSO_4$:SF_{30}=1:20) structure consists of a nanoporous tip and a hollow middle column with a wall thickness of ~30–90 μm (Figure 5.1i and Figure S5.4).

5.3.4 Cu distribution along microneedles

Leveraging the robust PFA achieved using SF and $CuSO_4$, we used three $CuSO_4$:SF_S concentrations to achieve microneedles with pre-defined mesostructures: SMN ($CuSO_4$:SF_S=0:1, Figure 5.4a), HMN ($CuSO_4$:SF_S=1:100 and 1:50, Figure 5.4b,c) and PMN ($CuSO_4$:SF_S=1:20, Figure 5.4h) for further characterization and experiments. Scanning electron microscopy/energy dispersive X-ray spectrometry (SEM/EDS) analysis of the nanoporous microneedle ($CuSO_4$:SF_S=1:20) shows the clear interface between the Cu-heavy porous tip and Cu-low smooth

column regions (indicated as * and #, Figure 5.5a and Figure S5.5c) at ~600–700 μm above the tip end. Sub-micron $CuSO_4$ crystals were randomly scattered on the tip surface (Figure 5.5b), resulting in several spikes in the Cu/N weight ratio profile (Figure 5.5c,d). Spatially resolved Raman spectra were collected to analyze silk conformation and the presence of $CuSO_4$ along the microneedle structure[230]. Spectra obtained along the microneedle outer surface from the tip to the middle column (denoted as *z*-direction, Figure 5.5e) show bands corresponding to SO symmetric stretching (~985–1005 cm^{-1})[231] in correspondence of mesoscopic particles present on the microneedle tip. No sulfate peaks were detected in the middle column region above the interface. Instead, peaks corresponding to silk fibroins, such as amide I at ~1660 cm^{-1} [232], became more evident. PMN with low $CuSO_4$ ($CuSO_4$:SF_S=1:100) has a shorter porous region (<100 μm) with negligible Cu signals from SEM/EDS (Figure S5.5a). The pore structures did not correlate with $CuSO_4$ crystal distribution, corroborating that nanopores were mainly generated by Cu-mediated SF assembly in the mold rather than dissolution of $CuSO_4$ precipitates. Pores from particle dissolution were only partially evident at PMNs' ($CuSO_4$:SF_S=1:100) tip end after ethanol treatment (to increase crystallinity (i.e., β-sheet contents and insolubility[135]) followed by a weak acid rinse (Figure S5.5b). Ethanol-treated PMNs ($CuSO_4$:SF_S=1:20) contain ~10 μg Cu per mg of the microneedle, which was removable by deionized water (~60%) and weak acid (~90%) without significant morphological change (Figure 5.5f), alleviating potential safety concerns (Supplementary Text 2). $CuSO_4$ removal changed the microneedles' original blue color to transparent (Figure 5.5f inset) and was confirmed by SEM/EDS and Raman spectra analyses (Figure S5.5 and S5.6). The weak HCl treatment slightly increased β-sheet contents in silk films by dissolving a small portion of soluble regions (random coil dominant) (Figure 5.5g and Figure S5.7a). However, the overall effects of both ethanol treatment and acid rinse on the secondary

protein structures were not significant, especially when prepared at lower $CuSO_4$:SFs ratios. Instead, the β-sheet contents were more influenced by Cu^{2+} addition (showing a maximum at $CuSO_4$:SFs=1:100, which is consistent with a previous report[233]) or film forming environment (Figure S5.7b,c).

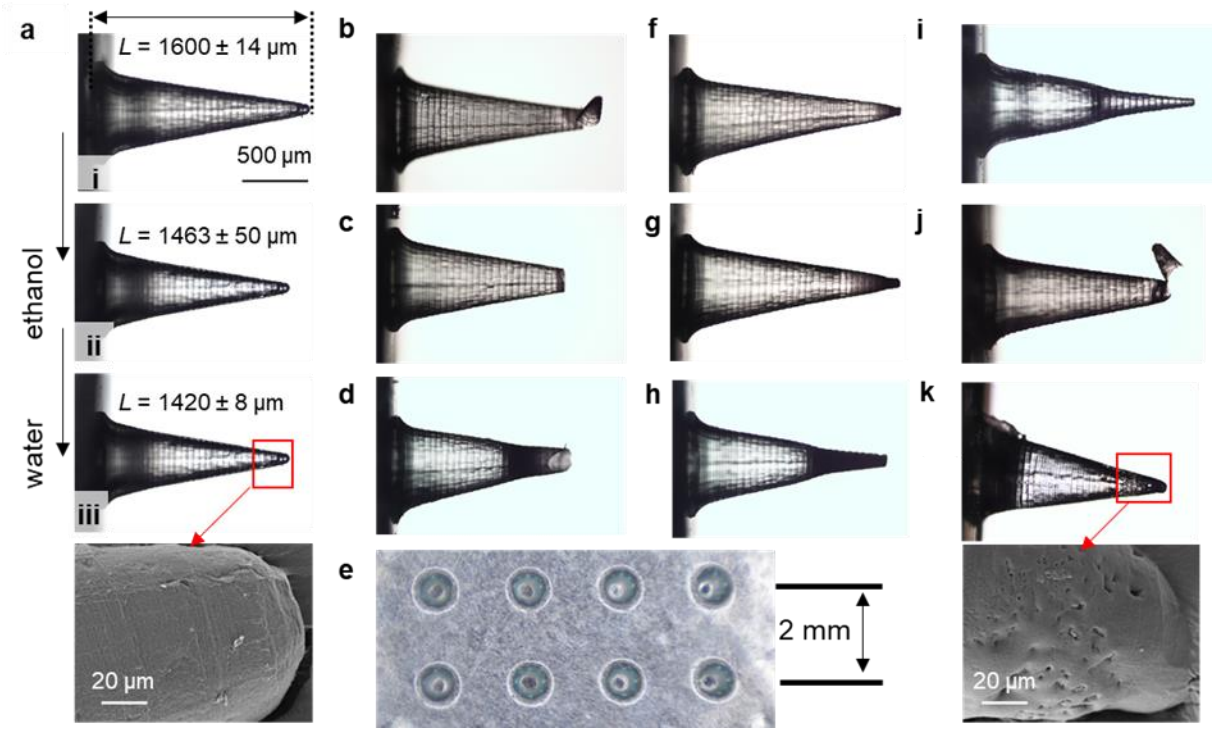

Figure 5.4. **Microneedle fabrication using SFs addition of ionic $CuSO_4$ and NaCl. a**, Solid needles ($CuSO_4$:SFs=0:1) before (**i**) and after ethanol treatment (**ii**), and additional dissolution in water with a zoomed-in SEM image (**iii**). ImageJ (ver 1.53e) was used to analyze the lengths (*L*) of microneedles from optical images (Mean ± SD, *N* = 10). **b–d,** Optical microscope images of hollow microneedle made of SFs and $CuSO_4$ at $CuSO_4$:SFs=1:100 (**b**), 1:50 (**c**), and 1:20 (**d**). **e,** Stereo microscope image (top view) of the hollow microneedle ($CuSO_4$:SFs =1:100). **f–h,** Optical microscope images of porous microneedles made of SFs and $CuSO_4$ at $CuSO_4$:SFs =1:100 (**f**), 1:50 (**g**), and 1:20 (**h**). **i**, Solid microneedle with a narrow tip (NaCl:SFs=1:50). **j,** Hollow microneedle (NaCl:SFs=1:100). **k**, Porous microneedle (NaCl:SFs=1:50) after ethanol treatment and water dissolution for a day with a zoomed-in SEM image.

5.3.5 Microneedles mechanical testing

Mechanical testing of ethanol-treated microneedles showed that the initial breaking forces of HMN were statistically higher than the other two types (1.40 ± 0.39 vs. 0.64 ± 0.26, Figure 5.5h). The tips of SMN and PMN broke by bending due to the unavoidable lateral force exerted during

compression[26], which smoothly declined the force-displacement curve after the initial failure (black arrows in Figure 5.5i). On the other hand, HMN broke by the step-by-step collapse of the column region, causing sudden drops and rebounds of the curves. Regardless of the breaking patterns, the measured breaking forces from all three microneedle types were about an order of magnitude higher than forces required to penetrate human skin[234] or plant tissues[26].

5.3.6 Hollow microneedles for plant applications

The above-described manufacturing of HMNs and PMNs using PFA yields mesostructured materials that can bridge the interface between the biotic and abiotic worlds, providing new means for drug delivery or biological fluid sampling. Below, we explore the application of HMNs and PMNs microneedles in plants, using tomato (*Solanum lycopersicum*, Figure 5.6a) as a model, due to the compelling need to develop new technologies for crop science and precision agriculture[235]. We applied droplets containing fluorescein on the backside of microneedles (i.e., SMN, HMN, and PMN) injected in petioles of three-weeks old plants (Figure 5.6b–d) to study how the model molecules would be transported across the microneedles into the plant tissue. SMNs absorbed the droplets most quickly, but fluorescein only spread locally near the injection spot in the petiole after 2 h, probably because it was retained in the microneedles (Figure 5.6b). Despite the slow droplet absorption, HNMs increased the amount of fluorescein delivered into the plant tissue because its hollow nature created a direct "communication channel" between the plant vascular structure and the inner microneedle surfaces[236], allowing for advection and diffusion directly from the droplet into the plant sap (Figure 5.6c). PNMs were the most inefficient for delivery as the droplet dried out on the backside of the microneedles before it could be absorbed in the silk microstructure and diffuse in plant tissue (Figure 5.6d); $CuSO_4$ inclusion increased the β-sheet contents (Figure 5.5g), which made microneedles' surface more hydrophobic. Additionally, SF-Cu^{2+} increases the stiffness of the microneedles, reducing HMNs and PMNs swelling upon injection and inhibiting

the absorption of droplets placed on the backside due to reduce relaxation phenomena. In the case of HMNs, the inner well became easily wet upon the injection into petioles, dispersing the droplet more easily.

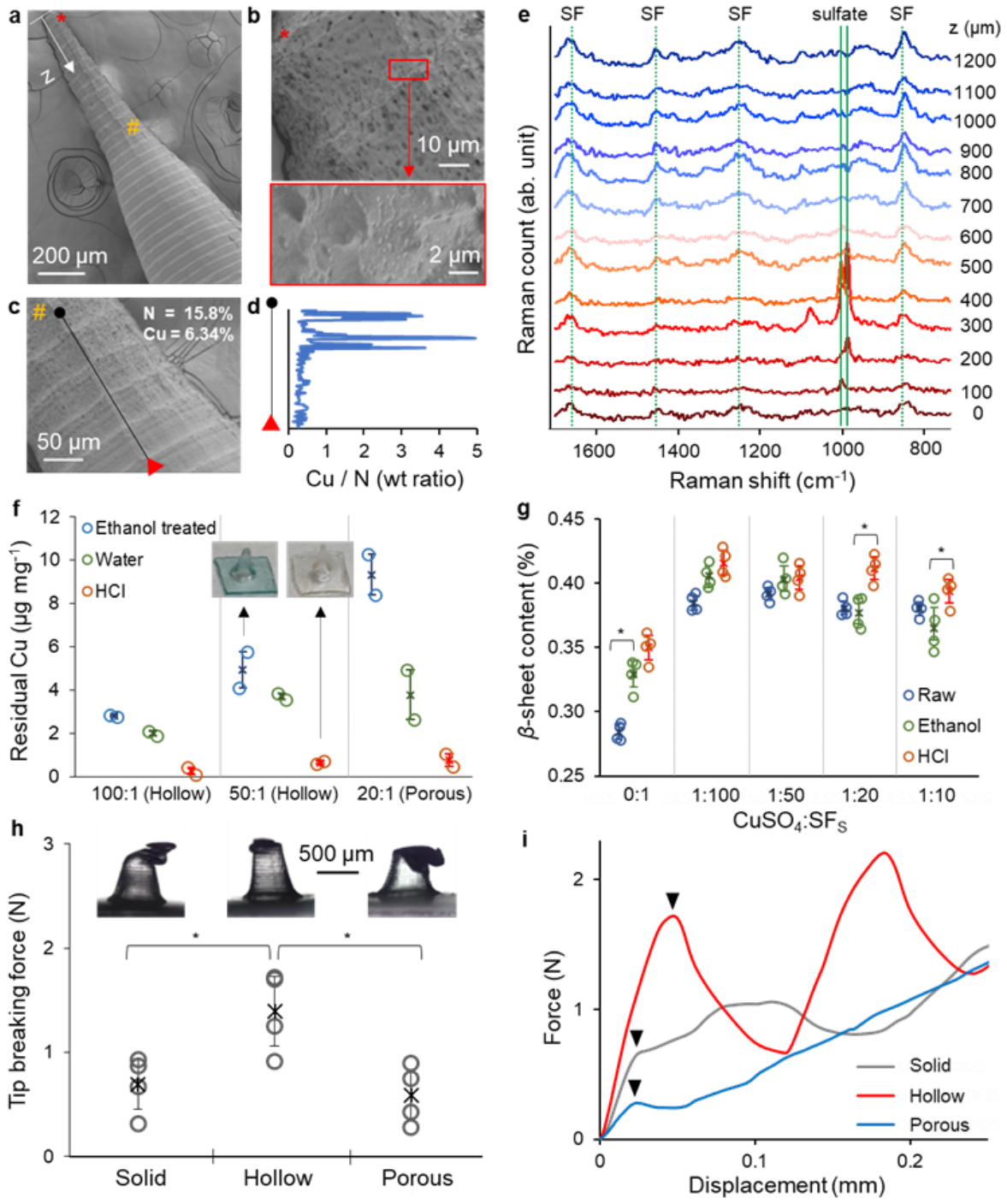

Figure 5.5. **Characterization of solid, hollow, and porous microneedles with $CuSO_4$. a–c**, SEM images of a porous microneedle ($CuSO_4$:SF_S=1:20, w:w). **d**, A profile of Cu / N weight ratio by SEM-EDX along the line shown in **c**. **e**, Raman spectra collected along *z*-direction of the porous needle shown in **a**. Bands corresponds to sulfate minerals, and silk fibroins are indicated with solid and dotted green lines. **f**, Residual Cu concentrations in the ethanol-treated hollow ($CuSO_4$:SF_S=1:100 and 1:50, w:w) and porous microneedles ($CuSO_4$:SF_S=1:20, w:w) after soaking in deionized water or 0.1 mM hydrochloric acid. Inset images are the hollow microneedle before (left) and after (right) acid wash. (N = 2, independent experiments) **g**, FTIR analyses for β-sheet contents of SF_S films with $CuSO_4$ prepared in PDMS molds mimicking a microneedle molding environment. Comparison of SFs films prepared on flat surfaces is in Figure S5.7b–c. * symbol is marked when a statistical significance ($p < 0.05$) was observed by treatments (i.e., raw vs. ethanol or ethanol vs. raw) of the film at the same ratio. (N = 4 from independent experiments). **h**, Initial breaking forces of solid ($CuSO_4$:SF_S=0:1, w:w), hollow ($CuSO_4$:SF_S=1:50, w:w), and porous ($CuSO_4$:SF_S=1:20, w:w) microneedles. Inset optical microscope images are microneedles after mechanical testing. * symbol indicates a statistically significant difference ($p < 0.05$) between two groups (N = 4 from independent experiments). **i**, Displacement-force curves from the mechanical testing of three microneedle types with indications of initial breaking points with the black arrows. For f-h, plots show mean (cross marks) ± SD (error bars) and individual data points (open dots). One- (h) or two-way (f,g) ANOVA with the Tukey HSD post-hoc tests were conducted for the statistical comparison.

Using one HMN as a source of payload supply (closer to a canopy, HMN_{source}), we applied a second HMN at 0.5 cm from the source (i.e., towards roots) for sampling purposes ($HMN_{sampling}$, Figure 5.6e,f). Fluorescein transported from HMN_{source} through the vascular tissue, i.e., phloem given the flow direction (Figure 5.6g), and successfully extracted by the downstream $HMN_{sampling}$ over a period of 20 h (Figure 5.6h). Moreover, we were able to accumulate additional fluorescein in a rolled-tissue paper, as an attachable collector, inserted in $HMN_{sampling}$. PNMs were able to extract fluorescein from plant tissues but were less effective in delivering fluorescein to the collecting tissue paper (Figure 5.6i). Plant growth continued upon injection and removal of the microneedles, with no sign of adverse effects on leaf growth.

To further explore HMNs and PMNs as technologies to collect plant fluids, we exposed tomato plants to cadmium (Cd) or arsenic (As) by addition of Cd^{2+} or AsO^{3-} in a plant medium and evaluated their concentration in sap via microneedle-mediated plant sap sampling. Both Cd and As are toxic for human consumption, and their bioaccumulation in agricultural products is a

significant concern even at lower concentrations in water sources[237]. A single SMNs injection into petiole effectively extracted Cd (~0.21 ± 0.10 ng Cd per needle equivalent to ~0.27 ng Cd per mg of microneedle) for a day from the tomato plant exposed to 1 mg L^{-1} Cd in a plant medium (Figure 5.6j). Cd captured in SMNs (even without any chemical modification) was >5% of Cd accumulated in the dry leaves (~5 µg per mg), where the bioaccumulation is typically known to be highest. Quantifying sufficient Cd from a single SMN was particularly interesting as it allows continuous monitoring without sacrificing tissues, typically followed by complicated digestion protocols. It is noteworthy that no surface modification of SMN was conducted to increase Cd binding affinities, indicating a potential improvement in future studies. Both HMNs and PMNs did not extract Cd at a detectable level because of their limited swelling capacity. However, we extracted ~0.14 ± 0.07 ng Cd by attaching a low-cost collector (a rolled-up laboratory tissue paper) to HMN, proving that HMN performed as an effective channel between the plant sap and the collector (Figure 5.6k). When exposed to 10 mg L^{-1} Cd, HMNs and PMNs extracted up to 1.8 and 1.2 ng Cd per needle, although less effective than SMNs (Figure S5.8a). None of the microneedles and attached collectors extracted a significant amount of As from the plants exposed to 1 mg L^{-1} as after 24h upon injection, possible due to the different plant uptake mechanisms; typically Cd uptake is via Ca^{2+}, Fe^{2+}, Mn^{2+}, and Zn^{2+} transporters while arsenite uptake is through the members of the nodulin 26-like intrinsic protein[238]. However, after 3 days of injection, the collectors attached to SMNs, HMNs, and PMNs extracted 31.2, 47.5, and 29.6 times more As than the needles themselves (Figure S5.8b), indicating that the collector can be used for a broader range of contaminant species than microneedles. No significant damage to plants, such as leaf withering, was observed during the three days of Cd and As extraction experiments except for scars left behind the injection. Altogether, the results highlight the potential of single microneedle application for the early

prediction of bioaccumulation of toxic contaminants existing at low concentrations in the environment.

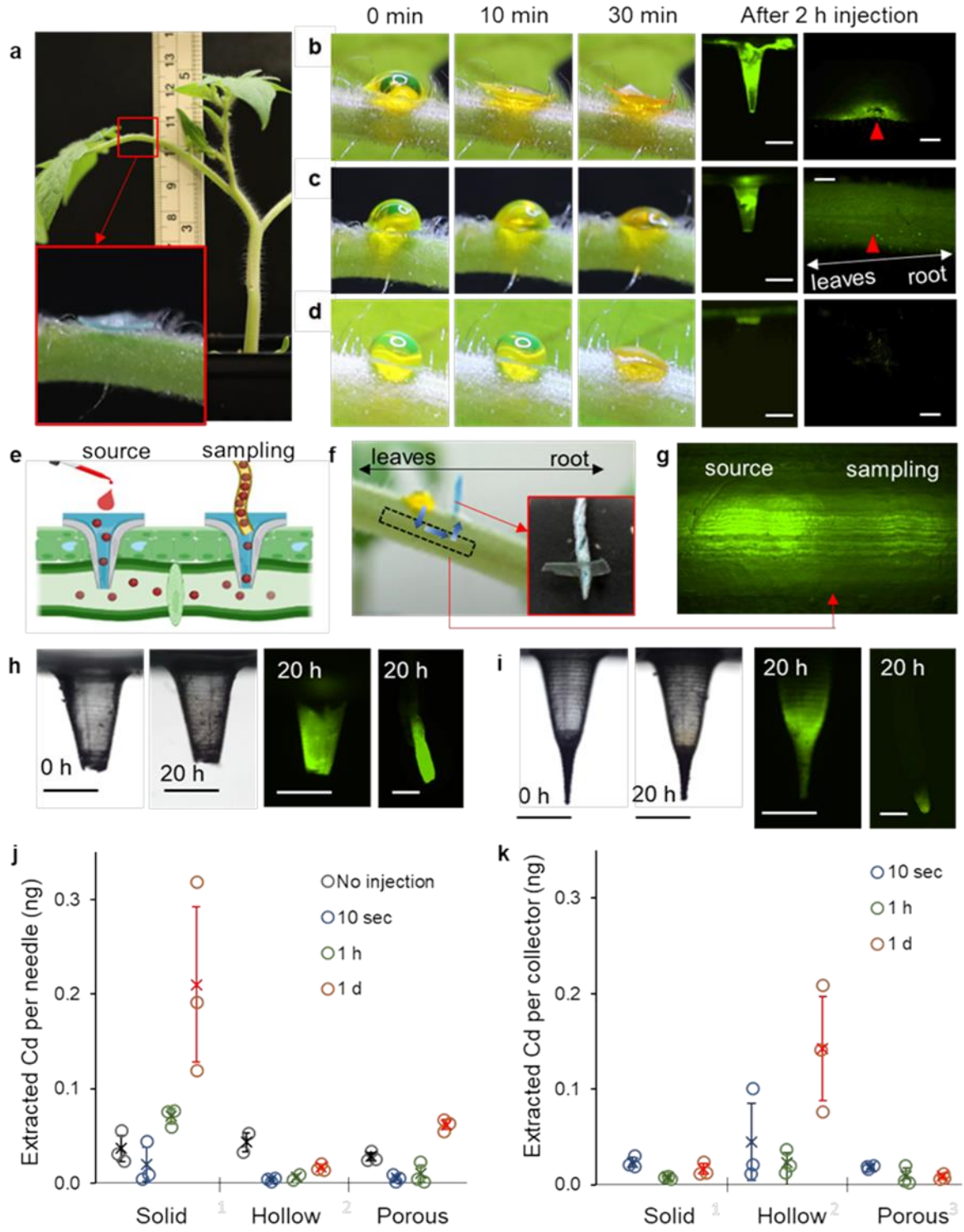

Figure 5.6. **HMN and PMN applications to tomato plants**. **a**, Microneedle injection into tomato petiole about 10 cm above the root. **b–d**, Gravitational delivery of biomolecules to plants through the solid (**b**, $CuSO_4$:SF_S=0:1, w:w), hollow (**c**, $CuSO_4$:SF_S=1:20, w:w), and porous (**d**, $CuSO_4$:SF_S=1:20, w:w) microneedles. Photo images were collected from the microneedles injected into tomato petiole after placing 2.5 μL droplets containing 0.2% sodium fluorescein. Fluorescence microscope images of the microneedles and injection spots in the petioles were obtained after 2 h of injection. **e–i**, Combination of gravitational delivery and accumulative sampling. Schematic illustration (**e**) and a photo image of actual application to a tomato petiole (**f**) show a continuous delivery and accumulative collection using two HMN. Fluorescein (2.5 μL droplets containing 0.2% sodium fluorescein) was delivered to plants through one HMN ($CuSO_4$:SF_S=1:50, w:w). After being transported via the phloem (as shown in a fluorescence image of petiole cross-section, **g**), fluorescein was extracted from the microneedles and accumulated in tissue paper attached to another HMN. Optical and fluorescence images of hollow (**h**, $CuSO_4$:SF_S=1:50, w:w) and porous (**i**, $CuSO_4$:SF_S=1:20, w:w) microneedles and attached tissue paper collector before and after 20 h of the sampling. **j–k**, Cd extraction using one microneedle (**j**) and attached tissue paper (**k**) applied to a petiole of a tomato plant growing in a plant medium containing 1 mg L^{-1} Cd. Plots show mean (cross marks) ± SD (error bars) and individual data points (open dots, N = 3, independent experiments).

5.4 Conclusions and Outlook

In this study, we presented a simple strategy to fabricate mesostructured materials with complex 3D geometries by controlling the kinetics and extents of formation of nanocrystals and the phase front with silk fibroin assembly. Manipulation of PFA allowed manufacturing microneedles with hollow and porous structures that are unattainable with current fabrication techniques and stably operate in plant tissues for the continuous cargo delivery from external sources and accumulative collection. These results open the door to the design of hollow microstructures that can host sensors and create an active interface with living tissues.

5.5 Methods

Preparation of Silk Fibroin Solution. The regenerated silk fibroin was extracted from *Bombyx mori* silkworm cocoons following an established protocol[165]. In brief, cocoons (purchased from a local farm in Jeollanam-do, South Korea) were cut into small pieces (~2 × 2 cm^2) and boiled in 0.02 M sodium carbonate for 10 min (SF_L) and 30 min (SF_S) to remove the sericin. The obtained degummed silk fibers were then washed with ultrapure water, dried overnight, and dissolved in 9.3 M lithium bromide for 4 h at 60°C. The dissolved silk fibroins were dialyzed against ultrapure

water in a dialysis cassette (molecular weight cut-off: 3500 Da) for 2 days with frequent replacements. The resulting silk fibroin solutions were then centrifuged to remove impurities. The final silk fibroin solution was diluted with water to 5 wt %, and then stored at 4℃ before use. Size distribution of SF_L and SF_S were determined by sodium dodecyl sulfate-polyacrylamide gel electrophoresis (SDS-PAGE, Bio-Rad Laboratories) as described in elsewhere[26].

Fabrication and monitoring of silk films and needles. Silk fibroin solutions (5wt%, SF_L and SF_S) ratio were mixed with ionic salts (5wt%, NaCl and $CuSO_4$) at varying ratios. Then, 5 μL droplets of each mixture were placed on a flat PMDS (Sylgard 184, Dow-Corning) surface and air-dried at room temperature and humidity. Changes in droplet sizes and contact angles were monitored using a portable USB digital microscope (Jiusion). NaCl was chosen as a representative salt with high water solubility enabling the monitoring of its crystallization behavior at a wide range of concentrations. $CuSO_4$ is also investigated as a highly soluble salt, and its blue color allows us to monitor its phase separation more easily under a microscope. The completed dried droplets were imaged under an optical microscope (Nikon Eclipse TE2000-E).

The macroscale needles were prepared by casting the mixture of 5% w/v SF_S and 5% w/v ionic $CuSO_4$ solutions in a negative PDMS mold (0.6 cm base diameter and 0.9 cm long). The needle formation process was imaged every 30 minutes by a digital single-lens reflex camera (Canon EOS5 mark iv) with a macro lens (EF 100mm f/2.8). The microneedle arrays were fabricated by casting the mixture of 3.6 mL silk fibroins (5 wt %, SF_S and SF_L) with a varying volume of ionic salt solutions (5 wt %, NaCl and $CuSO_4$) in negative PDMS molds (10 × 10 microneedles, 600 μm base diameter, 1,600 μm long, and 2 mm spacing between needles). The molds filled with the mixed solutions were centrifuged (4,000 rcf, 5 min) and placed under a vacuum for 30 minutes to remove air bubbles entrapped between the molds and the solutions. The

arrays were peeled off from the mold after air-drying and cut into small pieces with the desired number of microneedles for further experiments or characterization. As a post-treatment, microneedles were soaked in 80% ethanol for a day for silk crystallization. If needed, the crystallized silk microneedles were washed with deionized water or 0.1 mM hydrochloric acid for another day to remove NaCl and $CuSO_4$ crystals precipitated in the microneedles.

Atomistic modeling and simulation. We performed molecular dynamics simulations of silk -repetitive domain like- dodecapeptide, with sequence $(GAGSGA)_2$, covalently bonded to two Aspartic Acid residues on the C and T terminal ends, in the zwitterionic state. Asp residue was not protonated. The all-atom additive CHARMM36m protein force field[239] was used to represent the peptides. Two different systems with/ without Cu^{2+} ions were prepared. For each system, the initial configuration was prepared by placing ten homologues -peptides, with random orientation, in a cubic 80 $Å^3$ box. The total number of TIP3P water molecules in each system was approximately 45.000. A total of 10 Cu^{2+} ions parametrized through a dummy model, including Jahn–Teller effect[240], were added in one system to understand Cu^{2+} role in peptides aggregation. For each system, Sodium ions were added for neutralizing the net charge of the system. First, energy minimization was performed using the steepest descent protocol, followed by the conjugated gradient. Subsequently, each system was equilibrated using the NAMD code[222] under constant pressure and temperature conditions, maintained constant at 1atm and 300 K, respectively, with a coupling constant of 1.0 ps, in order to relax the volume of the periodic box while using a time step of 2 fs, a non-bonded cut-off of 9 Å, rigid bonds, and particle-mesh Ewald long-range electrostatics. Finally, the production run was performed using NAMD code for a total time of 200ns in NVT ensemble. All the analyses were performed using *in-house* TCL scripts and VMD

integrated tools. We evaluated the time stability of ion-peptides pairs over 200 ns long simulation and estimated aggregates dimensions using pairwise inter-peptide contact analysis.

Characterization of silk-mimicking peptides-metal ions interactions. The dodecapeptide $(GAGSGA)_2$ used in this study was synthesized by GenScript (Piscataway, NJ), with free N- and C termini. In brief, peptides were synthesized using standard fluorenylmethyloxycarbonyl (Fmoc)-based solid-phase peptide synthesis and purified by reverse-phase high-performance liquid chromatography to a purity of 95% or higher. Peptides were dissolved in pure Milli-Q water to 0.2 mg mL^{-1} (i.e., 0.244 mM), partially denatured at 70°C for 15 min, then cooled down to room temperature, followed by immediate addition of metal ions (i.e. NaCl and $CuCl_2$) to the peptide solution at a molar ratio of peptide monomer:metal ion = 1:5.

Atomic force micrographs were obtained using a Cypher VRS AFM (Asylum Research). A 10 μL aliquot of diluted samples (30 μg/ml peptides) was dropped on a freshly cleaved mica surface (ϕ = 10 mm, Ted Pella) and dried before imaging. All morphological characterization was performed by tapping mode in air, at a scan rate of 4 - 6 Hz and a resolution of 256 × 256 pixels per image, using FS-1500 (Asylum Research) probes. DLS measurements were performed on a DynaPro NanoStar Light Scatterer (Wyatt Technology). All samples were measured in plastic cuvettes (UVette, Eppendorf). The laser was at 658 nm, and its power was automatically adjusted to an optimized range of counts by the built-in auto-attenuation capability. The acquisition time for each data point was 5s, and 10 data points were acquired for each sample. The autocorrelation curve for each sample was examined to make sure there were no severe aggregates.

Characterization of microneedles. The optical images of individual silk microneedles and were obtained with a microscope (Nikon Eclipse TE2000-E). The microneedles were sputter-coated with gold for 10 nm for collecting SEM images (Zeiss Merlin High-resolution SEM and JEOL

JSM-6010LA). Line profiles of Cu/N weight ratios along the microneedles were collected by SEM/EDS (Zeiss Merlin High-resolution SEM).

The spatially resolved Raman spectra were collected for PMNs using a home-built confocal Raman microscope in the Physical Optics and Electronics Group at MIT. Previously reported instrumental setup is used[230] without polarization selection on the Raman signal. A 785 nm single-frequency DBR diode laser (Photodigm Inc.) was used as the excitation source. A 0.6 NA objective (40X, Olympus Inc.) was used to focus the laser beam on the sample and collect the back-scattered Raman signal. The lateral and axial full-width at half-maximum (FWHM) of the instrument point spread function (PSF) was approximately 700 nm and 5 μm, respectively. The excitation laser power was approximately 4 mW on the sample, and the excitation polarization was perpendicular to the scan direction. The integration time was 60 seconds with two repetitions at each spatial point. The sample was scanned at a step size of 100 μm and re-focused at each spatial point using a manual XZY translational stage (Thorlabs Inc.). The raw spectra in the range of 200–1900 cm^{-1} were post-processed sequentially using cosmic-ray removal, Lieber fit[241] for fluorescence background subtraction, and Savitzky-Golay filtering (order 2, frame length 11) for smoothing.

A hollow microneedle was scanned by the 3D X-ray micro-computed tomography system (ZEISS Versa 520 micro-CT System) with the following parameters: source setting 80kV and 7W, source filter air, camera binning 1, and exposure time 5 seconds. The objective was 4X, and the pixel size was around 1.55 μm. Total 1601 projections were taken while the sample rotated 360˚.

Residual Cu contents in the microneedles were analyzed by using an inductively coupled plasma-optical emission spectrometer (Agilent 5100 DVD). Samples were prepared by digesting three microneedles in 500 μL NaOH (3 N, 60℃) for 5 h. The digested solutions were added to 4.5 mL nitric acid (5%) and filtered through 0.2 μL cellulose acetate syringe filter.

Mechanical testing of microneedles. The tip breaking forces of the microneedles were evaluated by the static compression strength test by a Dynamic Mechanical Analysis (TA Instruments Q850) at a loading speed of 1 mm min^{-1}.

Analyses of secondary silk protein structures. Fourier-transform infrared spectroscopy (FTIR, Perkin Elmer Spectrum 65) was used to evaluate the effects of $CuSO_4$ addition and post-treatments silk materials on the secondary protein structure. For the evaluation, silk films were prepared with 400 µL SFs (5%) and 0–40 µL $CuSO_4$ (5%) solutions in PMDS mold with rectangular wells (1×1×0.3 cm^{-3}) that mimicked silk curing environment in the microneedle molds. FTIR spectra were collected at a wavelength range of 4,000 to 650 cm^{-1}, with a resolution of 4 cm^{-1} and an accumulation of 64 scans. The relative fractions of *β*-sheet and random coil were determined by Fourier self-deconvolution of the amide I band (1705–1595 cm^{-1}) and Gaussian curve-fitting of the deconvoluted spectra.

Sampling and delivery experiments. The tomato (*Solanum lycopersicum*) plant was chosen as a working model in this study because of their well-known vascular structure and importance in agriculture. They were grown in pots for 4–6 weeks from seeds with regular water and fertilizer feeding at room temperature with 12 h photoperiod per day. Microneedles were injected into petioles of plants in pots, at approximately 10 cm above the root, for delivery and sampling of fluorescein (from sodium salt, Mw 376.27 g mol^{-1}, pK_a ~6.4, Sigma), used as a model biomolecule. The petioles with a diameter of around 2–2.5 mm were selected as injection spots so the microneedles can reach both xylem phloem located at the depths around 700 and 850 µm, respectively[26]. For the delivery, a 2.5 µL droplet of 0.2% sodium fluorescein was placed on the backside of the microneedle that facings up so the droplet can be absorbed into the microneedle or directly inside the petiole (in the case of the hollow microneedle) with the gravitation force. A

piece of laboratory tissue paper (0.3 cm × 0.5 cm, Leica Microsystems 3P BIO-WRAPS) was rolled and inserted into the well of the sampling microneedle from the backside as a collector of fluorescein delivered from another microneedle used as an injector. For the sampling of Cd and As, tomato plants (4–6 weeks) were transferred to 100 mL plant media (Hoagland′s No. 2 Basal Salt Mixture) containing cadmium nitrate tetrahydrate (1 or 10 mg Cd L^{-1}, Sigma-Aldrich) or sodium arsenite (1 mg As L^{-1}, Spectrum Chemical) one day before the microneedle injection. The injected microneedle was digested in 500 µL NaOH (3 N, 60°C) for 5 h, then transferred to 2 mL nitric acid (5%). The tissue paper collector attached to the microneedle was transferred to 1 mL nitric acid (5%) and heated at 60°C for 5 h. After heating, additional 1.5 mL nitric acid (5%) were added for dilution. Bioaccumulated Cd and As in the plant leaves after sampling experiments were extracted in concentrated nitric acid and hydrogen peroxide by the microwave digestion system (Milestone UltraWave). Solutions extracting Cd and As from the microneedle, tissue paper, and leaves were filtered through 0.2 µL cellulose acetate syringe filters and analyzed by an inductively coupled plasma-mass spectrometer (ICP-MS, Agilent 7900).

Acknowledgments

B.M., Y.C, R.R. and Z.L acknowledge support from a Singapore-MIT Alliance for Research & Technology, National Research Foundation, Prime Minister's Office, Singapore under its Campus for Research Excellence and Technological Enterprise (CREATE) program. This work was partially supported by the Office of Naval Research (Award N00014-21-1-2402, Award N00014-19-1-2317) and the US National Science Foundation (Award CMMI-1752172).

Conflict of Interest

B.M. is co-founder of a company, Mori Inc., that uses silk fibroin-based materials as edible food coatings to increase the shelf-life of perishable food. The use of silk fibroin as an edible coating,

seed coating, and to fabricate microneedles for drug delivery in plants is protected by multiple IP positions where B.M. is listed as a co-inventor.

Data Availability

The data that support the findings of this study are available from the corresponding author upon reasonable request.

Code Availability

All code used in this work is available from the corresponding authors upon reasonable request.

5.6 Supplementary Information

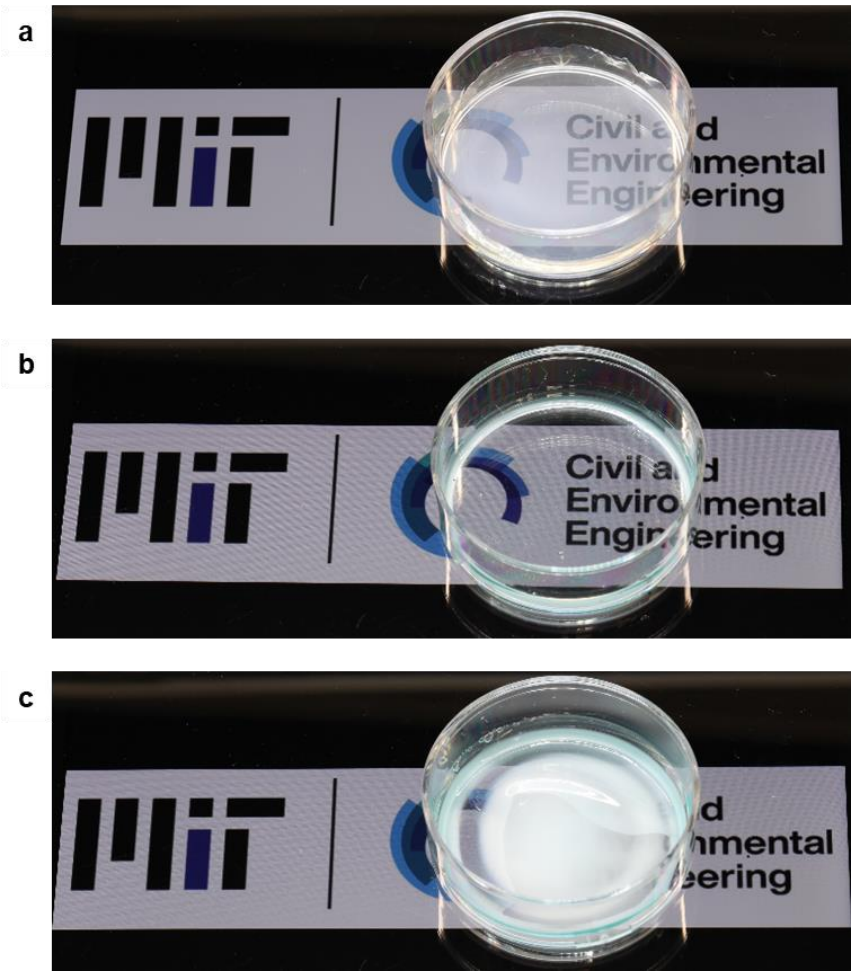

Figure S5.1. Photo images of films prepared with SF_S with a varying weight ratio of ionic $CuSO_4$ in Petri-dishes. $CuSO_4$:SF_S= 0:1 (**a**), 1:10 (**b**), and 1:5 (**c**).

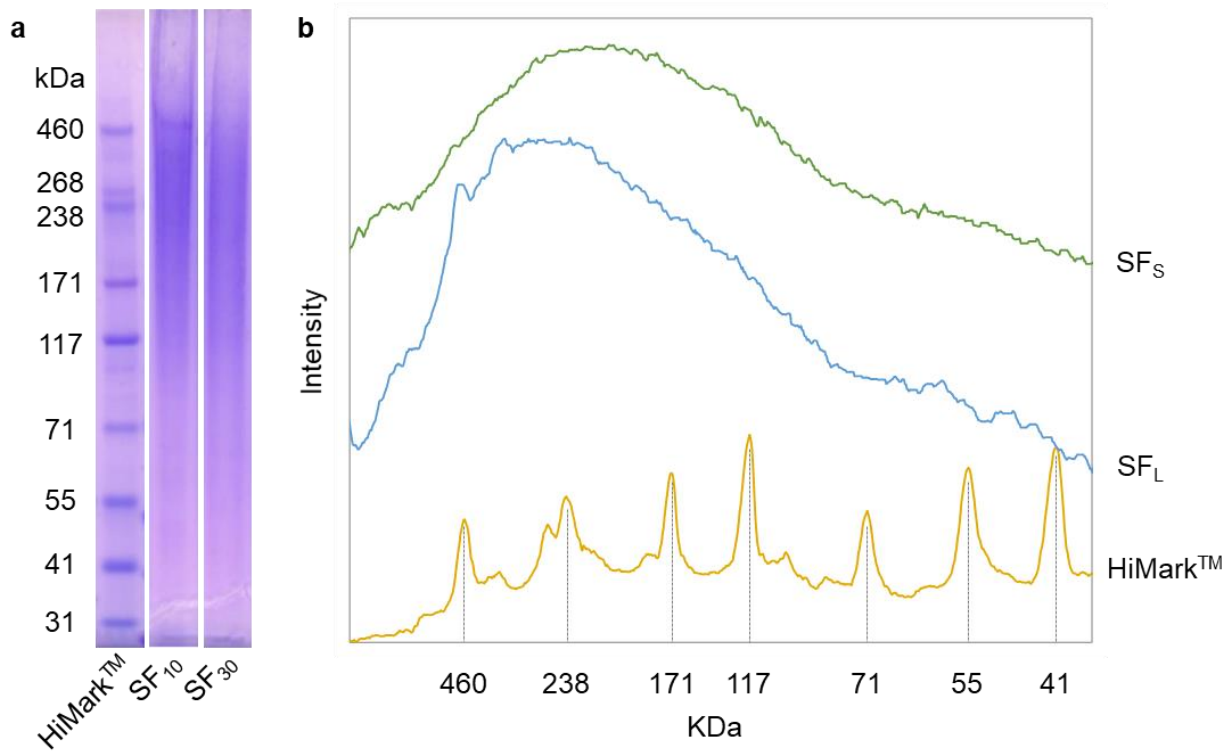

Figure S5.2. Size distribution of silk fibroin by Sodium dodecyl sulfate-polyacrylamide gel electrophoresis (SDS-PAGE). (**a**) Photo images after gel electrophoresis of pre-stained protein standard (HiMark™), larger silk fibroin (SF_L), and smaller silk fibroin (SF_S). (**b**) Color intensity plots converted from gel images using ImageJ (ver. 1.53e).

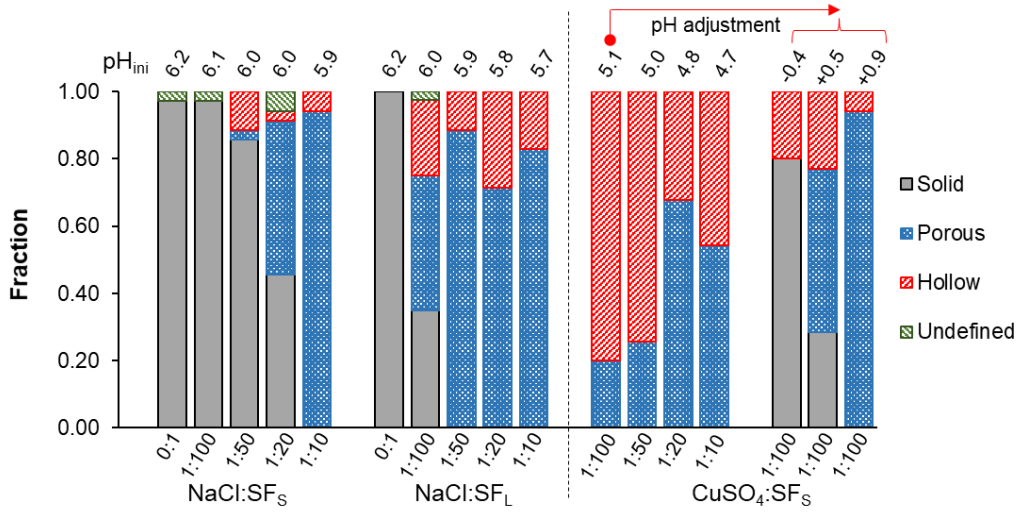

Figure S5.3. Microneedle fabrication using SF_S and SF_L with the addition of ionic NaCl and $CuSO_4$. Fractions of microneedle types prepared in an array. More than 30 individual needles were observed under a microscope to categorize them into solid, hollow, and porous tip structures.

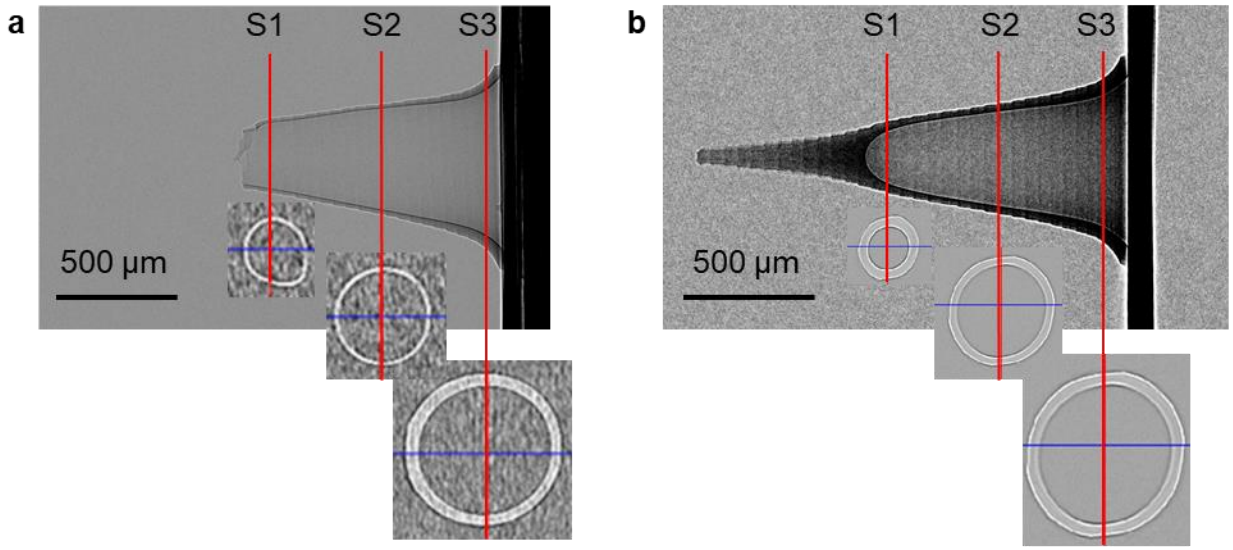

c

	Hollow (a)		Porous (b)	
	Thickness (µm)	Inner diameter (µm)	Thickness (µm)	Inner diameter (µm)
S1	27.2 ± 2.9	239.5 ± 14.9	40.2 ± 3.5	154.7 ± 5.7
S2	31.0 ± 2.9	393.8 ± 3.8	29.9 ± 2.3	323.8 ± 7.4
S3	63.2 ± 4.6	584.7 ± 12.8	88.5 ± 8.0	619.9 ± 6.0

Figure S5.4. **Micro-computed X-ray tomography images of hollow (a) and porous (b) microneedles.** Wall thickness and inner diameter were evaluated from the cross-sectional images (**c**).

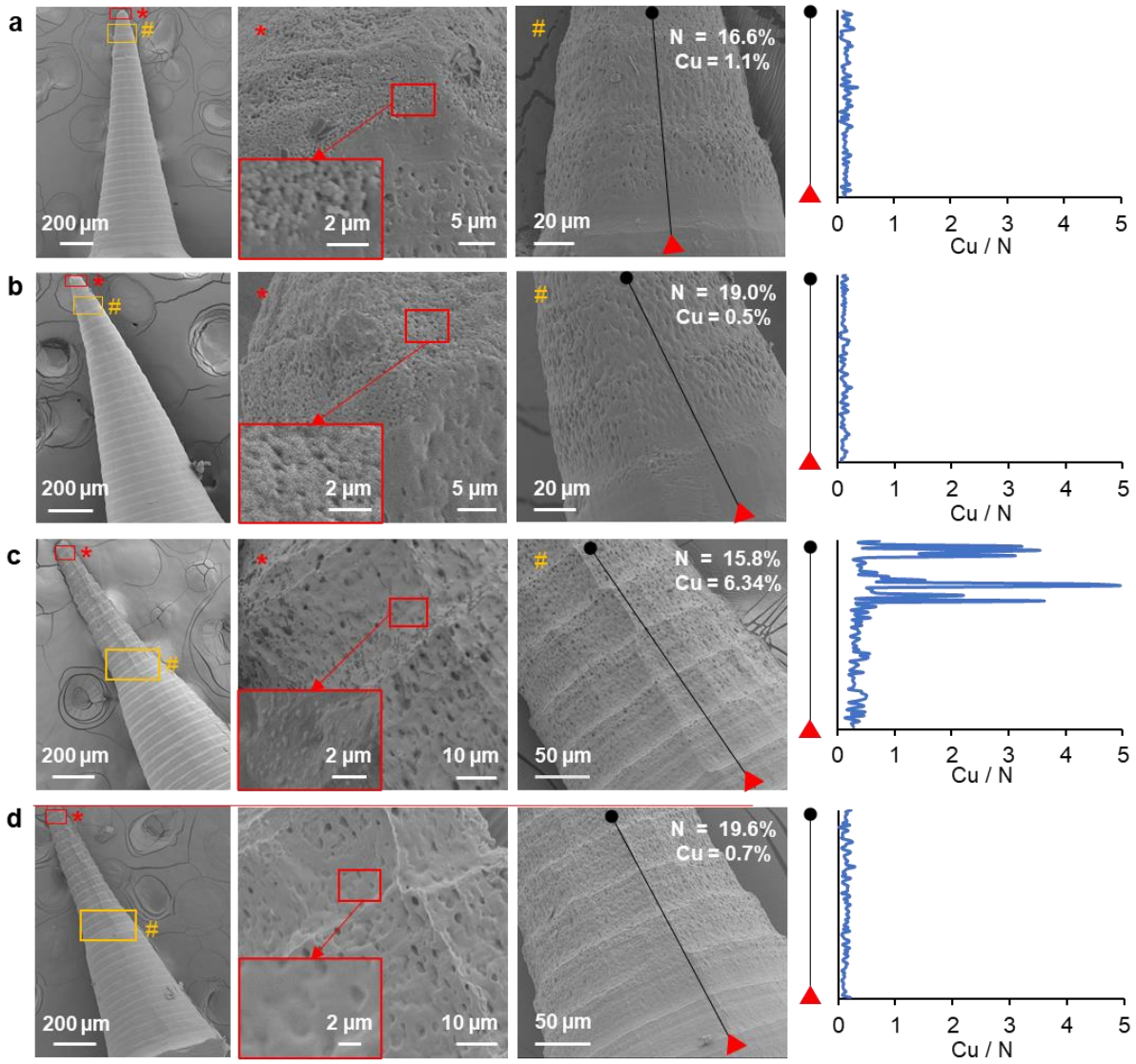

Figure S5.5. **SEM images of porous microneedles and EDX line profiles of Cu / N weight ratio near the interfaces between porous tips and smooth column regions.** (**a**) Raw porous microneedle with low Cu ($CuSO_4$:SF_S=1:100) (**b**) Porous microneedle with low Cu ($CuSO_4$:SF_S=1:100) after ethanol treatment and 0.1 mM hydrochloric acid washing. (**c**) Raw porous microneedle with high Cu ($CuSO_4$:SF_S=1:20) (**d**) Porous microneedle with high Cu ($CuSO_4$:SF_S=1:20) after ethanol treatment and 0.1 mM hydrochloric acid washing.

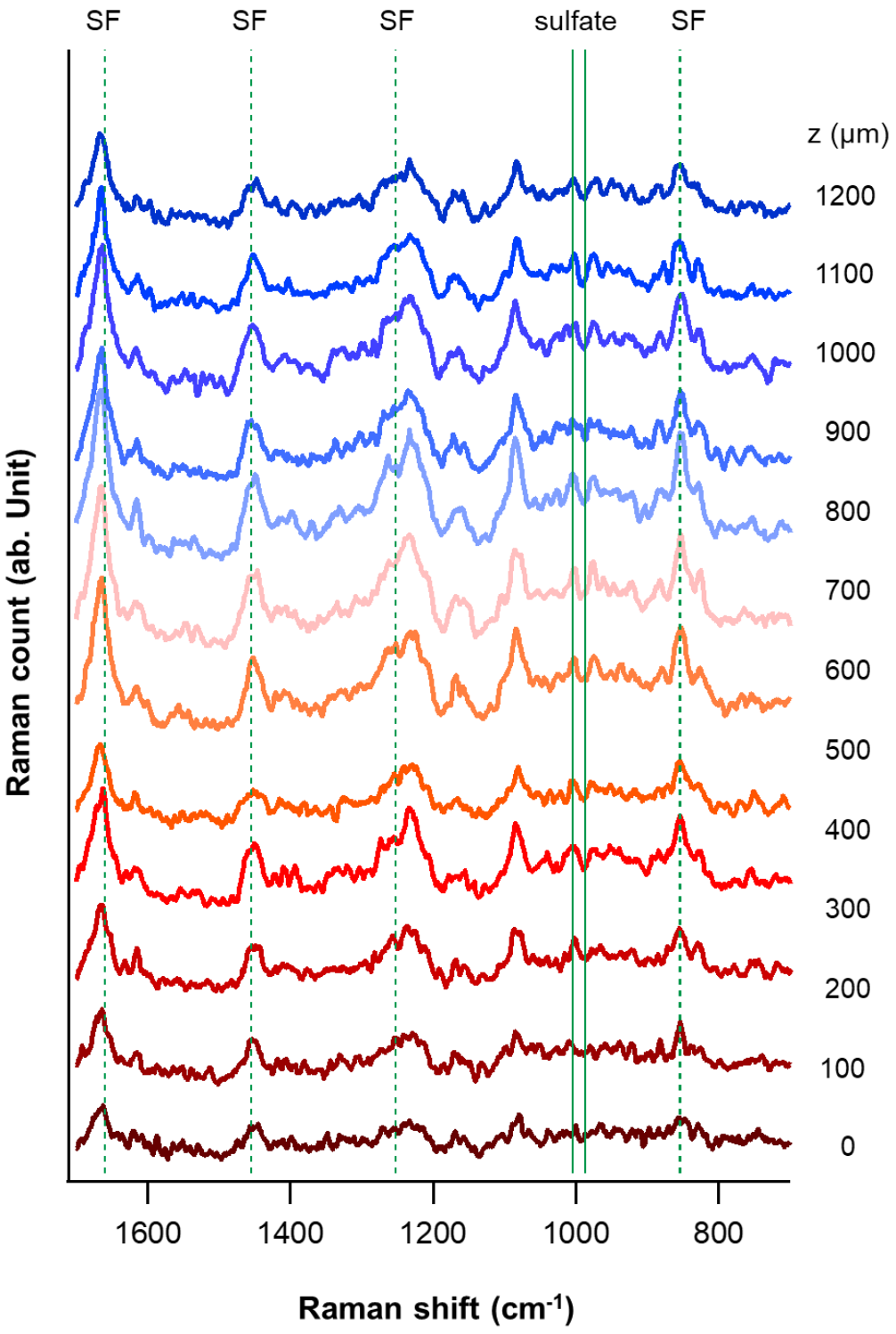

Figure S5.6. **Raman spectra of various sites a porous microneedle.** Raman spectra were collected from the porous microneedle ($CuSO_4$:SF_S=1:20) after ethanol treatment and 0.1 mM hydrochloric acid washing at a distance from the tip end. Bands corresponding to sulfate minerals and silk fibroins are indicated with solid and dotted green lines.

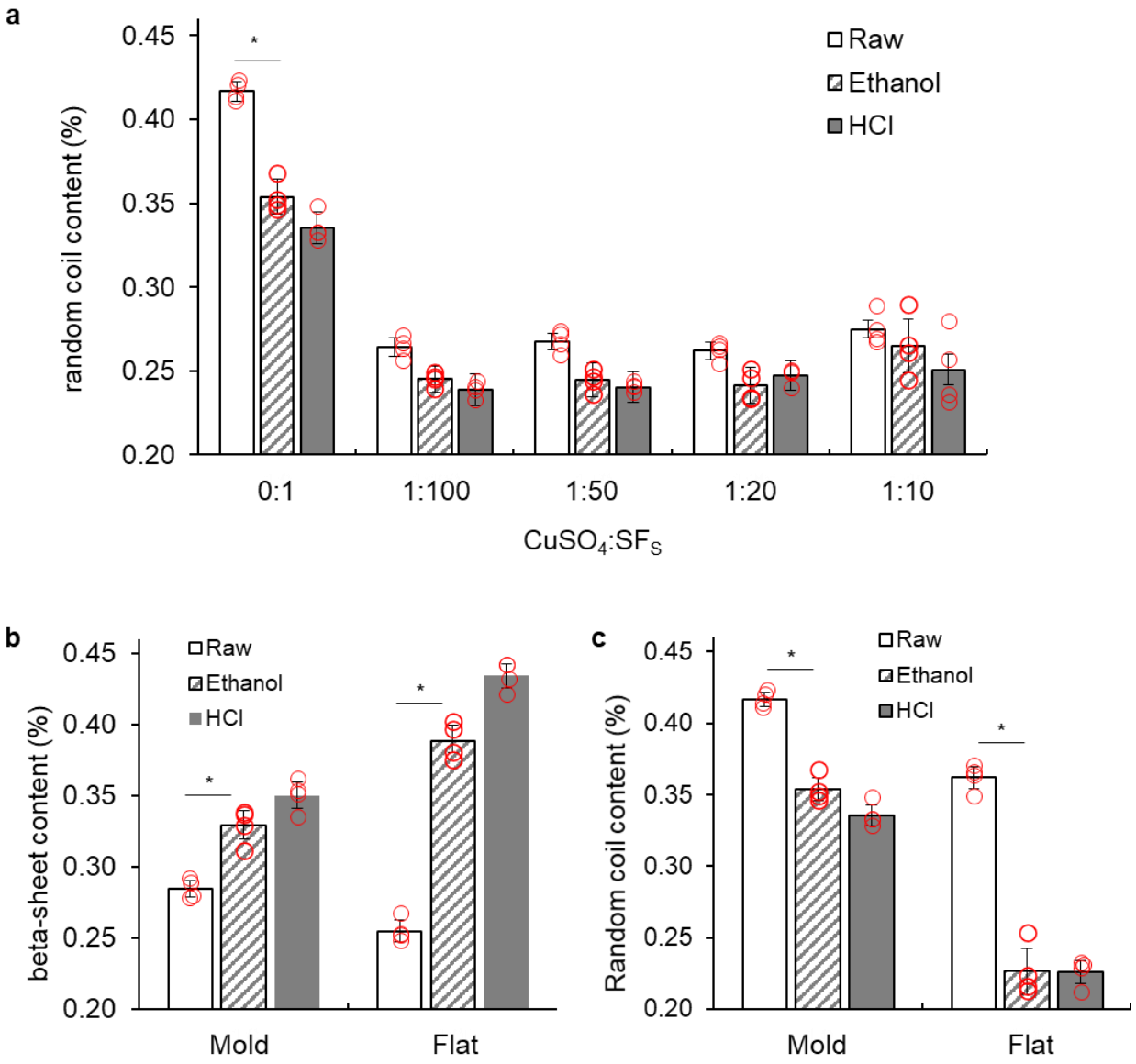

Figure S5.7. **FTIR analyses of SF_S films**. (**a**) Random coil contents in SF_S films with $CuSO_4$ prepared in PDMS molds with a rectangular well (1×1×0.3 cm^{-3}). (**b–c**) Comparison of beta-sheet and random coil contents in pure SF_S films ($CuSO_4$:SF_S=0:1) prepared in PDMS molds and flat PDMS surfaces. Films prepared in the flat surfaces show more drastic changes in β-sheet structures by ethanol treatment and acid washing compared to the films prepared in the mold due to the smaller sample thickness (136.7 ± 12.5 μm vs. 51.3 ± 9.0 μm) and faster water evaporation rate (40.4 mg h^{-1} vs. 21.8 mg h^{-1}). Bar graphs with error bars represent means and standard deviations. Red circles are individual data points. Two-way ANOVA with the Tukey HSD post-hoc tests were conducted for the statistical comparison. N = 4 from independent experiments.

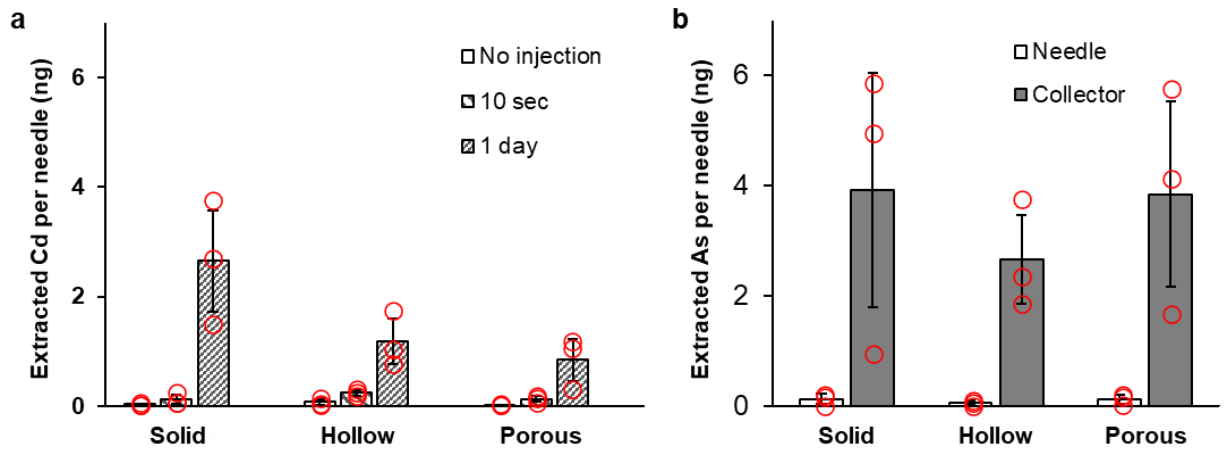

Figure S5.8. Contaminants extraction. (**a**) Cd extraction using one microneedle injected to a petiole of a tomato plant growing in a plant medium containing 1 mg L^{-1} Cd. As a control, porous needles injected into the plant without Cd spike extracted 0.03 ± 0.02 ng Cd per needle. (**b**) As extraction using one microneedle and attached tissue paper as a collector applied to a petiole of a tomato plant growing in a plant medium containing 1 mg L^{-1} As for 3 days. Bar graphs with error bars represent mean and standard deviation. Red circles are individual data points (N = 3, independent experiments).

Supplementary Text 1: Microneedle formation under different conditions

Without any salt, both SF_S and SF_L solutions fabricated an array of cone-like, solid microneedles (SMNs) that replicate the exact shape and size of the mold (Figure 5.4a). SMNs transport target molecules from or to injected tissues mainly via swelling and diffusion[236]. Regulation of silk polymorphism (non-ordered to ordered molecular structure transition) with ethanol enhanced stability in wet environments, also resulting in ~8.6% reduction in length (Figure 5.4b-I,ii). SMNs were the dominant type of microneedles fabricated for salt to SF weight ratios 0:1, 1:100, and 1:50 (e.g., 0–0.1% w/v NaCl + 5% w/v SF_S, Figure S5.3). Tips became narrower with further NaCl addition (Figure 5.4i), possibly because the concentrated ions could lead silk fibroin molecules to aggregate to each other (known as a sticky reptation concept[221]), preventing adhesion to the mold wall. At NaCl concentrations higher than 0.25% (NaCl:SF_S=1:20 and 1:10), a few hollow microneedles (HMNs, Figure 5.3j) and more porous microneedles (PMNs, Figure 5.3k) were fabricated. NaCl crystals (<10 µm) sporadically formed at the PMNs tip, and their dissolution

during ethanol treatment was the main mechanism for pore generation. Using SF_L resulted in more fractions of HMN and PMN at lower NaCl concentration. We can speculate that the longer chain lengths in SFs have a stronger tendency aggregate than the shorter SF_L counterpart (i.e., larger salt-out effect), thus ionic precursors could be condensed in a liquid phase that promotes nucleation of NaCl crystals and their precipitation at the tip.

At all ratios, $CuSO_4$ addition resulted in either hollow (Figure 5.4b–e) or porous (Figure 5.4f–h) structures, and Cu-heavy tip regions of both needle types became longer with more $CuSO_4$ addition. The HMNs tips were removed or partially detached from the column when peeling off from the mold while the PMN tips were intact. HMNs were the dominant type (>74%) at low $CuSO_4$ concentrations ($CuSO_4$:SF_S=1:100 and 1:50). Compared to NaCl, $CuSO_4$ has lower water solubility, inducing nucleation at an earlier point of evaporation when the solution is less viscous. This condition is favorable for $CuSO_4$ nuclei, which are heavier than NaCl nuclei, to precipitate down at the tip. At higher $CuSO_4$ concentrations (>0.25% w/v $CuSO_4$, $CuSO_4$:SF_S=1:20 and 1:10), PMN with narrow tips becomes dominant. Micro-computed X-ray tomography (microCT) image of a PMN ($CuSO_4$:SF_S=1:20) shows an empty well inside the middle column of the needles, with a wall thickness of 30–90 μm (Figure S5.4). The opaque, narrow, porous tip indicates that the concentrated $CuSO_4$ gelated the silk solution at the tips by sticky reptation, inhibiting the formation of HMNs due to the limited diffusion of Cu and sulfate ions needed for the growth of $CuSO_4$ crystals. This result is in accordance with atomistic models, AFM measurements, and 2D observations where at $CuSO_4$:SF_S=1:5, early gelation during the sol-gel-solid transition resulted in opaque films, another sign of SF premature aggregation during fabrication (Figure S5.1). We hypothesized that gelation was caused by a pH decrease below SF isoelectric point as Cu ions complex with hydroxides. A similar result may be achieved at $CuSO_4$:SF_S=1:100 by an artificial

decrease in the initial solution pH, preventing HMNs formation (Figure S5.3). Additionally, NaOH injection to balance pH did not yield uniform HMN, probably due to local spikes in pH that promoted heterogenous $CuSO_4$ nucleation.

Supplementary Text 2: Safety concern about using Cu

The ethanol-treated PMN ($CuSO_4$:SF_S=1:20) contains ~10 µg Cu per mg of microneedle (Figure 5.5f). It means that one PMN (~0.76 mg) can supply adequate Cu in 13 g of the fresh plant, and the total Cu in 115 PMNs is equivalent to the Daily Value. Thus, we do not consider that Cu in these PMNs and other HMNs prepared with lower amounts of $CuSO_4$ would cause significant concern for food/agricultural and biomedical applications. Cu is one of the plant micronutrients with an adequate concentration of 600 ng per gram fresh weight[170,242] and has been widely used in antimicrobial compounds for crop protection for more than a century[243]. Cu is also an essential mineral present in natural foods, such as beef, and also available as a dietary supplement with 900 µg of Daily Value for adults[244].

Chapter 6 Conclusion and Future Work

6.1 Conclusion

This thesis studies the use of biomaterials and drug delivery principles to engineer the precise deployment of payloads in plants. A novel silk-based biomaterial is designed and fabricated into a microneedle-like device capable of delivering a variety of payloads ranging from small molecules to large proteins into specific loci of various plant tissues. We show that silk-based microneedles can be used to deliver payloads into plant vasculature to study material transport in xylem and phloem and to perform complex biochemical reactions in situ. It is also demonstrated *Agrobacterium*-mediated gene transfer to shoot apical meristem and leaves at various stages of growth. Tuning the material composition changes the properties of the microneedles and enables precise sampling from plants. We demonstrate silk-based microneedles as a precise payload delivery tool as well as a sampling tool.

Based on this study, we further establish silk-based microneedles as a new tool in plant science that enables the precise deployment of known amounts of physiologically relevant molecules to plants with minimal invasiveness. Microneedle injection on *Arabidopsis thaliana* mutant *ft-10* causes minimal formation of scar and callus. Transcriptomic analyses show minimal wounding responses and activation of GA_3 responses post injection of GA_3-loaded microneedles, which is corroborated by promoted bolting and inhibited flower formation. Silk-based microneedle-mediated delivery is proved to be more efficient and effective than foliar spray. Potential applications of the silk-based microneedles in agriculture are also confirmed by the successful deployment of GA_3 in several crops, including tomato (*Solanum lycopersicum*), romaine lettuce (*Lactuca sativa*), and carmel spinach (*Spinacia oleracea*).

We previously demonstrated silk-based microneedles could sample from plants but the capability is limited by their volume. Therefore, we further develop hollow microneedles via simultaneous

manipulation of silk fibroin assembly and inorganic nucleation at their phase front, which are unattainable with other fabrication methods. These hollow silk-based microneedles build the channel between inside and outside the plants, enabling biomarkers delivery to plants and detection of early-stage bioaccumulation of environmental contaminants, such as cadmium and arsenic. In sum, this thesis provides a versatile tool for precise payloads delivery to plants and sampling from plants.

6.2 Future Work

Unlike the extensive research done in the biomedical field, using microneedles for precision delivery to plants is emergent, and its versatility is far from being fully unveiled. To narrow the gap, we foresee three main fields to explore for future work. The first lies in investigating microneedles via combining advanced microneedle fabrication techniques (i.e., drawing, 3D printing, molding, and layer-by-layer fabrication) with rational modification of biomaterials (i.e., formation of micro/nano particles and functionalization of surface groups). Adaption and modification specific to plant species are desired. Further modification of microneedles for easier access to phloem and shoot apical meristem will be a game-changer.

The second is the incorporation of other payloads into microneedles, particularly those functioning in plants at a trace concentration, such as micronutrients, small interfering RNA (siRNA), and self-replicating microorganisms. Integration of nanomaterials (e.g., nanosized payloads[33], nanocarriers[109], nanosensors[11]) into microneedles is also of great importance because the properties of nanomaterials can be easily tuned for controlled release and stimuli-responsive release, which are the trend in sustainable agriculture. It will also provide a powerful tool for plant science since most reported nanocarriers for plants are currently delivered via foliar and vacuum infiltration to plant leaves and explants.

The third is associated with polymeric hollow microneedles, which break the biological barriers and connect the inside and outside of the plants. They overcome the capacity limit of solid microneedles in delivery and sampling, enabling continuous cargo delivery from external sources and accumulative collection. However, the healing process of plants may interfere with the proper functioning of hollow microneedles. The exposure of the inside of the plants will also enable the application of direct detection techniques with limited penetration depth.

Bibliography

1 Global report on food crises 2018. 1 -202 (Food Security Information Network, 2018).

2 The state of the world's land and water resources forfood and agriculture—systems at breaking point. (Food and Agriculture Organization of the United Nations Rome, Italy, 2021).

3 Sun, H., Cao, Y., Kim, D. & Marelli, B. Biomaterials technology for agrofood resilience. *Adv. Funct. Mater.*, 2201930, (2022).

4 World fertilizer trends and outlook to 2020. (Food and Agriculture Organization of the United Nations, Rome, 2017).

5 Agricultural micronutrients market by type, mode of application, form, crop type and region - global forecast to 2027. (ReportLinker, 2022).

6 Sharma, A. *et al.* Worldwide pesticide usage and its impacts on ecosystem. *SN Appl. Sci.* **1**, 1-16, (2019).

7 Rademacher, W. Plant growth regulators: backgrounds and uses in plant production. *J. Plant Growth Regul.* **34**, 845-872, (2015).

8 Cunningham, F. J., Goh, N. S., Demirer, G. S., Matos, J. L. & Landry, M. P. Nanoparticle-mediated delivery towards advancing plant genetic engineering. *Trends Biotechnol.* **36**, 882-897, (2018).

9 Demirer, G. S. *et al.* Nanotechnology to advance CRISPR-Cas genetic engineering of plants. *Nat. Nanotechnol.* **16**, 243-250, (2021).

10 Giraldo, J. P. *et al.* Plant nanobionics approach to augment photosynthesis and biochemical sensing. *Nat. Mater.* **13**, 400-408, (2014).

11 Lew, T. T. S. *et al.* Real-time detection of wound-induced H2O2 signalling waves in plants with optical nanosensors. *Nat. Plants* **6**, 404-415, (2020).

12 Kwak, S. Y. *et al.* A nanobionic light-emitting plant. *Nano Lett.* **17**, 7951-7961, (2017).

13 Wong, M. H. *et al.* Nitroaromatic detection and infrared communication from wild-type plants using plant nanobionics. *Nat. Mater.* **16**, 264-272, (2017).

14 Su, Y. *et al.* Delivery, uptake, fate, and transport of engineered nanoparticles in plants: a critical review and data analysis. *Environ. Sci. Nano* **6**, 2311-2331, (2019).

15 Hong, J. *et al.* Evidence of translocation and physiological impacts of foliar applied CeO2 nanoparticles on cucumber (Cucumis sativus) plants. *Environ. Sci. Technol.* **48**, 4376-4385, (2014).

16 Christiano, R. S. C., Reilly, C. C., Miller, W. P. & Scherm, H. Oxytetracycline dynamics on peach leaves in relation to temperature, sunlight, and simulated rain. *Plant Dis.* **94**, 1213-1218, (2010).

17 Lawrencia, D. *et al.* Controlled release fertilizers: a review on coating materials and mechanism of release. *Plants* **10**, (2021).

18 Archer, L., Crane, J. H. & Albrecht, U. Trunk injection as a tool to deliver plant protection materials-an overview of basic principles and practical considerations. *Horticulturae* **8**, 552, (2022).

19 Nicolopoulou-Stamati, P., Maipas, S., Kotampasi, C., Stamatis, P. & Hens, L. Chemical pesticides and human health: the urgent need for a new concept in agriculture. *Front. Public Health* **4**, 148, (2016).

20 Yin, H. *et al.* Soil sensors and plant wearables for smart and precision agriculture. *Adv. Mater.* **33**, e2007764, (2021).

21 Lew, T. T. S. *et al.* Species-independent analytical tools for next-generation agriculture. *Nat. Plants* **6**, 1408-1417, (2020).
22 Kim, Y. C., Park, J. H. & Prausnitz, M. R. Microneedles for drug and vaccine delivery. *Adv. Drug Deliv. Rev.* **64**, 1547-1568, (2012).
23 Li, S., Xia, D. & Prausnitz, M. R. Efficient drug delivery into skin using a biphasic dissolvable microneedle patch with water-insoluble backing. *Adv. Funct. Mater.* **31**, 2103359, (2021).
24 Prausnitz, M. R. Microneedles for transdermal drug delivery. *Adv. Drug Deliv. Rev.* **56**, 581-587, (2004).
25 Kundu, A., Nogueira Campos, M. G., Santra, S. & Rajaraman, S. Precision vascular delivery of agrochemicals with micromilled microneedles (microMMNs). *Sci. Rep.* **9**, 14008, (2019).
26 Cao, Y., Lim, E., Xu, M., Weng, J. K. & Marelli, B. Precision delivery of multiscale payloads to tissue-specific targets in plants. *Adv. Sci.* **7**, 1903551, (2020).
27 Fiorello, I. *et al.* Plant-like hooked miniature machines for on-leaf sensing and delivery. *Commun. Mater.* **2**, (2021).
28 Wang, P., Lombi, E., Zhao, F. J. & Kopittke, P. M. Nanotechnology: a new opportunity in plant sciences. *Trends Plant Sci.* **21**, 699-712, (2016).
29 Elmer, W. & White, J. C. The future of nanotechnology in plant pathology. *Annu. Rev. Phytopathol.* **56**, 111-133, (2018).
30 Nair, R. *et al.* Nanoparticulate material delivery to plants. *Plant Science* **179**, 154-163, (2010).
31 Keller, A. A., Huang, Y. & Nelson, J. Detection of nanoparticles in edible plant tissues exposed to nano-copper using single-particle ICP-MS. *J. Nanopart. Res.* **20**, 101, (2018).
32 Larue, C. *et al.* Fate of pristine TiO2 nanoparticles and aged paint-containing TiO2 nanoparticles in lettuce crop after foliar exposure. *J. Hazard. Mater.* **273**, 17-26, (2014).
33 Zhao, L. *et al.* Monitoring the environmental effects of CeO2 and ZnO nanoparticles through the life cycle of corn (Zea mays) plants and in situ mu-XRF mapping of nutrients in kernels. *Environ. Sci. Technol.* **49**, 2921-2928, (2015).
34 Martin-Ortigosa, S., Valenstein, J. S., Lin, V. S. Y., Trewyn, B. G. & Wang, K. Gold functionalized mesoporous silica nanoparticle mediated protein and DNA codelivery to plant cells via the biolistic method. *Adv. Funct. Mater.* **22**, 3576-3582, (2012).
35 Colvin, V. L. The potential environmental impact of engineered nanomaterials. *Nat. Biotechnol.* **21**, 1166-1170, (2003).
36 Fojtů, M., Teo, W. Z. & Pumera, M. Environmental impact and potential health risks of 2D nanomaterials. *Environ. Sci. Nano* **4**, 1617-1633, (2017).
37 Fadeel, B. & Kostarelos, K. Grouping all carbon nanotubes into a single substance category is scientifically unjustified. *Nat. Nanotechnol.* **15**, 164, (2020).
38 Naqvi, S. *et al.* Calcium phosphate nanoparticle mediated genetic transformation in plants. *J. Mater. Chem.* **22**, (2012).
39 Zhang, H. *et al.* DNA nanostructures coordinate gene silencing in mature plants. *Proc. Natl. Acad. Sci. U.S.A.* **116**, 7543-7548, (2019).
40 Douglas, S. M. *et al.* Self-assembly of DNA into nanoscale three-dimensional shapes. *Nature* **459**, 414-418, (2009).
41 Rothemund, P. W. Folding DNA to create nanoscale shapes and patterns. *Nature* **440**, 297-302, (2006).

42 Lee, H. *et al.* Molecularly self-assembled nucleic acid nanoparticles for targeted in vivo siRNA delivery. *Nat. Nanotechnol.* **7**, 389-393, (2012).
43 Li, J., Fan, C., Pei, H., Shi, J. & Huang, Q. Smart drug delivery nanocarriers with self-assembled DNA nanostructures. *Adv. Mater.* **25**, 4386-4396, (2013).
44 Gratton, S. E. *et al.* The effect of particle design on cellular internalization pathways. *Proc. Natl. Acad. Sci. U.S.A.* **105**, 11613-11618, (2008).
45 Wong, M. H. *et al.* Lipid exchange envelope penetration (LEEP) of nanoparticles for plant engineering: a universal localization mechanism. *Nano Lett.* **16**, 1161-1172, (2016).
46 Langecker, M., Arnaut, V., List, J. & Simmel, F. C. DNA nanostructures interacting with lipid bilayer membranes. *Acc. Chem. Res.* **47**, 1807-1815, (2014).
47 Sun, H. & Marelli, B. Polypeptide templating for designer hierarchical materials. *Nat. Commun.* **11**, 351, (2020).
48 Parker, R. M. *et al.* The self-assembly of cellulose nanocrystals: hierarchical design of visual appearance. *Adv. Mater.* **30**, e1704477, (2018).
49 Narkevicius, A. *et al.* Controlling the self-assembly behavior of aqueous chitin nanocrystal suspensions. *Biomacromolecules* **20**, 2830-2838, (2019).
50 Kwak, S. Y. *et al.* Chloroplast-selective gene delivery and expression in planta using chitosan-complexed single-walled carbon nanotube carriers. *Nat. Nanotechnol.* **14**, 447-455, (2019).
51 Tian, Y. & Zhou, S. Advances in cell penetrating peptides and their functionalization of polymeric nanoplatforms for drug delivery. *Wiley Interdiscip. Rev. Nanomed. Nanobiotechnol.* **13**, e1668, (2021).
52 Silva, S., Almeida, A. J. & Vale, N. Combination of cell-penetrating peptides with nanoparticles for therapeutic application: a review. *Biomolecules* **9**, 22, (2019).
53 Lindgren, M., Hallbrink, M., Prochiantz, A. & Langel, U. Cell-penetrating peptides. *Trends Pharmacol. Sci.* **21**, 99-103, (2000).
54 Mae, M. *et al.* Internalisation of cell-penetrating peptides into tobacco protoplasts. *Biochim. Biophys. Acta* **1669**, 101-107, (2005).
55 Eudes, F. & Chugh, A. Cell-penetrating peptides: from mammalian to plant cells. *Plant Signal. Behav.* **3**, 549-550, (2008).
56 Chugh, A. & Eudes, F. Cellular uptake of cell-penetrating peptides pVEC and transportan in plants. *J. Pept. Sci.* **14**, 477-481, (2008).
57 Lakshmanan, M., Kodama, Y., Yoshizumi, T., Sudesh, K. & Numata, K. Rapid and efficient gene delivery into plant cells using designed peptide carriers. *Biomacromolecules* **14**, 10-16, (2013).
58 Numata, K., Ohtani, M., Yoshizumi, T., Demura, T. & Kodama, Y. Local gene silencing in plants via synthetic dsRNA and carrier peptide. *Plant Biotechnol. J.* **12**, 1027-1034, (2014).
59 Lakshmanan, M., Yoshizumi, T., Sudesh, K., Kodama, Y. & Numata, K. Double-stranded DNA introduction into intact plants using peptide–DNA complexes. *Plant Biotechnol.* **32**, 39-45, (2015).
60 Guo, B. *et al.* Native protein delivery into rice callus using ionic complexes of protein and cell-penetrating peptides. *PLoS One* **14**, e0214033, (2019).
61 Ng, K. K. *et al.* Intracellular delivery of proteins via fusion peptides in intact plants. *PLoS One* **11**, e0154081, (2016).

62 Chuah, J. A. & Numata, K. Stimulus-responsive peptide for effective delivery and release of DNA in plants. *Biomacromolecules* **19**, 1154-1163, (2018).
63 Odahara, M. *et al.* Nanoscale polyion complex vesicles for delivery of cargo proteins and Cas9 ribonucleoprotein complexes to plant cells. *ACS Appl. Nano Mater.* **4**, 5630-5635, (2021).
64 Fujita, S., Motoda, Y., Kigawa, T., Tsuchiya, K. & Numata, K. Peptide-based polyion complex vesicles that deliver enzymes into intact plants to provide antibiotic resistance without genetic modification. *Biomacromolecules* **22**, 1080-1090, (2021).
65 Miyamoto, T., Tsuchiya, K. & Numata, K. Dual peptide-based gene delivery system for the efficient transfection of plant callus cells. *Biomacromolecules* **21**, 2735-2744, (2020).
66 Miyamoto, T., Tsuchiya, K. & Numata, K. Endosome-escaping micelle complexes dually equipped with cell-penetrating and endosome-disrupting peptides for efficient DNA delivery into intact plants. *Nanoscale* **13**, 5679-5692, (2021).
67 Hurt, E. C., Pesold-Hurt, B., Suda, K., Oppliger, W. & Schatz, G. The first twelve amino acids (less than half of the pre-sequence) of an imported mitochondrial protein can direct mouse cytosolic dihydrofolate reductase into the yeast mitochondrial matrix. *EMBO J.* **4**, 2061-2068, (1985).
68 Chuah, J. A., Yoshizumi, T., Kodama, Y. & Numata, K. Gene introduction into the mitochondria of Arabidopsis thaliana via peptide-based carriers. *Sci. Rep.* **5**, 7751, (2015).
69 Thagun, C., Chuah, J. A. & Numata, K. Targeted gene delivery into various plastids mediated by clustered cell-penetrating and chloroplast-targeting peptides. *Adv. Sci.* **6**, 1902064, (2019).
70 Santana, I., Wu, H., Hu, P. & Giraldo, J. P. Targeted delivery of nanomaterials with chemical cargoes in plants enabled by a biorecognition motif. *Nat. Commun.* **11**, 2045, (2020).
71 Akelah, A. Novel utilizations of conventional agrochemicals by controlled release formulations. *Mater. Sci. Eng. C* **4**, 83-98, (1996).
72 Aouada, F. A. & de Moura, M. R. in *Nanotechnologies in Food and Agriculture* Ch. Chapter 5, 103-118 (Springer, 2015).
73 Azeem, B., KuShaari, K., Man, Z. B., Basit, A. & Thanh, T. H. Review on materials & methods to produce controlled release coated urea fertilizer. *J. Control. Release* **181**, 11-21, (2014).
74 Dai, C., Yang, L., Xie, J. & Wang, T.-J. Nutrient diffusion control of fertilizer granules coated with a gradient hydrophobic film. *Colloids Surf. A Physicochem. Eng. Asp.* **588**, (2020).
75 Pereira, E. I. *et al.* in *Nanotechnologies in Food and Agriculture* (eds Mahendra Rai, Caue Ribeiro, Luiz Mattoso, & Nelson Duran) Ch. Chapter 11, 241-265 (Springer, 2015).
76 Trenkel, M. E. Slow-and controlled-release and stabilized fertilizers: an option for enhancing nutrient use efficiency in agriculture. (2010).
77 Mohd Ibrahim, K. R., Eghbali Babadi, F. & Yunus, R. Comparative performance of different urea coating materials for slow release. *Particuology* **17**, 165-172, (2014).
78 Xiaoyu, N. *et al.* A novel slow-release urea fertiliser: physical and chemical analysis of its structure and study of its release mechanism. *Biosyst. Eng.* **115**, 274-282, (2013).
79 Eghbali Babadi, F., Yunus, R., Abdul Rashid, S., Mohd Salleh, M. A. & Ali, S. New coating formulation for the slow release of urea using a mixture of gypsum and dolomitic limestone. *Particuology* **23**, 62-67, (2015).

80 Kottegoda, N. *et al.* Urea-hydroxyapatite nanohybrids for slow release of nitrogen. *ACS Nano* **11**, 1214-1221, (2017).
81 Dubey, A. & Mailapalli, D. R. Zeolite coated urea fertilizer using different binders: Fabrication, material properties and nitrogen release studies. *Environ. Technol. Innov.* **16**, (2019).
82 Yang, Y. C., Zhang, M., Li, Y., Fan, X. H. & Geng, Y. Q. Improving the quality of polymer-coated urea with recycled plastic, proper additives, and large tablets. *J. Agric. Food Chem.* **60**, 11229-11237, (2012).
83 Li, L. *et al.* Preparation and performance of polyurethane/mesoporous silica composites for coated urea. *Mater. Des* **99**, 21-25, (2016).
84 Directive on single-use plastics. (The European Parliament; The Council Of The European Union, 2019).
85 Restricting the use of intentionally added microplastic particles to consumer or professional use products of any kind—Annex XV restriction report. (European Chemicals Agency, 2019).
86 Riyajan, S. A., Sasithornsonti, Y. & Phinyocheep, P. Green natural rubber-g-modified starch for controlling urea release. *Carbohydr. Polym.* **89**, 251-258, (2012).
87 Qiao, D. *et al.* Preparation and characterization of slow-release fertilizer encapsulated by starch-based superabsorbent polymer. *Carbohydr. Polym.* **147**, 146-154, (2016).
88 Xiao, X. *et al.* One-step method to prepare starch-based superabsorbent polymer for slow release of fertilizer. *Chem. Eng. J.* **309**, 607-616, (2017).
89 Perez, J. J. & Francois, N. J. Chitosan-starch beads prepared by ionotropic gelation as potential matrices for controlled release of fertilizers. *Carbohydr. Polym.* **148**, 134-142, (2016).
90 Pang, L., Gao, Z., Feng, H., Wang, S. & Wang, Q. Cellulose based materials for controlled release formulations of agrochemicals: A review of modifications and applications. *J. Control. Release* **316**, 105-115, (2019).
91 Ni, B., Liu, M., Lu, S., Xie, L. & Wang, Y. Environmentally friendly slow-release nitrogen fertilizer. *J. Agric. Food Chem.* **59**, 10169-10175, (2011).
92 dos Santos, B. R., Bacalhau, F. B., Pereira Tdos, S., Souza, C. F. & Faez, R. Chitosan-montmorillonite microspheres: a sustainable fertilizer delivery system. *Carbohydr. Polym.* **127**, 340-346, (2015).
93 Rashidzadeh, A. & Olad, A. Slow-released NPK fertilizer encapsulated by NaAlg-g-poly(AA-co-AAm)/MMT superabsorbent nanocomposite. *Carbohydr. Polym.* **114**, 269-278, (2014).
94 Olad, A., Zebhi, H., Salari, D., Mirmohseni, A. & Reyhani Tabar, A. Slow-release NPK fertilizer encapsulated by carboxymethyl cellulose-based nanocomposite with the function of water retention in soil. *Mater. Sci. Eng. C* **90**, 333-340, (2018).
95 Wendels, S. & Averous, L. Biobased polyurethanes for biomedical applications. *Bioact. Mater.* **6**, 1083-1106, (2021).
96 Bortoletto-Santos, R., Ribeiro, C. & Polito, W. L. Controlled release of nitrogen-source fertilizers by natural-oil-based poly(urethane) coatings: The kinetic aspects of urea release. *J. Appl. Polym. Sci.* **133**, (2016).
97 Feng, G. d. *et al.* Polyurethane-coated urea using fully vegetable oil-based polyols: Design, nutrient release and degradation. *Prog. Org. Coat.* **133**, 267-275, (2019).

98 Bortoletto-Santos, R. *et al.* Oil-based polyurethane-coated urea reduces nitrous oxide emissions in a corn field in a Maryland loamy sand soil. *J. Clean. Prod.* **249**, (2020).
99 Liu, J., Yang, Y., Gao, B., Li, Y. C. & Xie, J. Bio-based elastic polyurethane for controlled-release urea fertilizer: Fabrication, properties, swelling and nitrogen release characteristics. *J. Clean. Prod.* **209**, 528-537, (2019).
100 Yang, Y., Tong, Z., Geng, Y., Li, Y. & Zhang, M. Biobased polymer composites derived from corn stover and feather meals as double-coating materials for controlled-release and water-retention urea fertilizers. *J. Agric. Food Chem.* **61**, 8166-8174, (2013).
101 Welch, R. M. & Shuman, L. Micronutrient nutrition of plants. *Crit. Rev. Plant Sci.* **14**, 49-82, (1995).
102 White, P. J. & Brown, P. H. Plant nutrition for sustainable development and global health. *Ann. Bot.* **105**, 1073-1080, (2010).
103 Martins, N. C. T. *et al.* Composites of biopolymers and ZnO NPs for controlled release of zinc in agricultural soils and timed delivery for maize. *ACS Appl. Nano Mater.* **3**, 2134-2148, (2020).
104 Ashfaq, M., Verma, N. & Khan, S. Carbon nanofibers as a micronutrient carrier in plants: efficient translocation and controlled release of Cu nanoparticles. *Environ. Sci. Nano* **4**, 138-148, (2017).
105 Yang, R., Xiao, C. F., Guo, Y. F., Ye, M. & Lin, J. Inclusion complexes of GA3 and the plant growth regulation activities. *Mater. Sci. Eng. C* **91**, 475-485, (2018).
106 Pereira, A., Oliveira, H. C. & Fraceto, L. F. Polymeric nanoparticles as an alternative for application of gibberellic acid in sustainable agriculture: a field study. *Sci. Rep.* **9**, 7135, (2019).
107 Grillo, R. *et al.* Chitosan/tripolyphosphate nanoparticles loaded with paraquat herbicide: an environmentally safer alternative for weed control. *J. Hazard. Mater.* **278**, 163-171, (2014).
108 Patel, S., Bajpai, J., Saini, R., Bajpai, A. K. & Acharya, S. Sustained release of pesticide (Cypermethrin) from nanocarriers: An effective technique for environmental and crop protection. *Process Saf. Environ. Prot.* **117**, 315-325, (2018).
109 Mitter, N. *et al.* Clay nanosheets for topical delivery of RNAi for sustained protection against plant viruses. *Nat. Plants* **3**, 16207, (2017).
110 Liu, Q. *et al.* Clay nanosheet-mediated delivery of recombinant plasmids expressing artificial miRNAs via leaf spray to prevent infection by plant DNA viruses. *Hortic. Res.* **7**, 179, (2020).
111 Shen, Y., Zhu, H., Wang, Y., Cui, H. & Sun, R. in *Polymers for Agri-Food Applications* 67-90 (Springer International Publishing, 2019).
112 Hou, X., Pan, Y., Miraftab, R., Huang, Z. & Xiao, H. Redox- and enzyme-responsive macrospheres gatekept by polysaccharides for controlled release of agrochemicals. *J. Agric. Food Chem.* **69**, 11163-11170, (2021).
113 Hou, X., Pan, Y., Xiao, H. & Liu, J. Controlled release of agrochemicals using pH and redox dual-responsive cellulose nanogels. *J. Agric. Food Chem.* **67**, 6700-6707, (2019).
114 Yang, J. *et al.* MOF-based multi-stimuli-responsive supramolecular nanoplatform equipped with macrocycle nanovalves for plant growth regulation. *Acta Biomater.* **134**, 664-673, (2021).

115 Fischer, J. *et al.* Targeted drug delivery in plants: enzyme-responsive lignin nanocarriers for the curative treatment of the worldwide grapevine trunk disease Esca. *Adv. Sci.* **6**, 1802315, (2019).
116 Peil, S., Beckers, S. J., Fischer, J. & Wurm, F. R. Biodegradable, lignin-based encapsulation enables delivery of Trichoderma reesei with programmed enzymatic release against grapevine trunk diseases. *Mater. Today Bio.* **7**, 100061, (2020).
117 Beckers, S. J. *et al.* Targeted drug delivery for sustainable crop protection: transport and stability of polymeric nanocarriers in plants. *Adv. Sci.* **8**, e2100067, (2021).
118 Beckers, S. J., Wetherbee, L., Fischer, J. & Wurm, F. R. Fungicide-loaded and biodegradable xylan-based nanocarriers. *Biopolymers* **111**, e23413, (2020).
119 Machado, T. O. *et al.* Cellulose nanocarriers via miniemulsion allow Pathogen-Specific agrochemical delivery. *J. Colloid Interface Sci.* **601**, 678-688, (2021).
120 Abdelrahman, T. M. *et al.* Pectinase-responsive carriers based on mesoporous silica nanoparticles for improving the translocation and fungicidal activity of prochloraz in rice plants. *Chem. Eng. J.* **404**, 126440, (2021).
121 Takeda, S. & Matsuoka, M. Genetic approaches to crop improvement: responding to environmental and population changes. *Nat. Rev. Genet.* **9**, 444-457, (2008).
122 Zaidi, S. S., Mukhtar, M. S. & Mansoor, S. Genome editing: targeting susceptibility genes for plant disease resistance. *Trends Biotechnol.* **36**, 898-906, (2018).
123 Gebbers, R. & Adamchuk, V. I. Precision agriculture and food security. *Science* **327**, 828-831, (2010).
124 Paul, R. *et al.* Extraction of plant DNA by microneedle patch for rapid detection of plant diseases. *ACS Nano* **13**, 6540-6549, (2019).
125 Wang, N. *et al.* The Candidatus Liberibacter-host interface: insights into pathogenesis mechanisms and disease control. *Annu. Rev. Phytopathol.* **55**, 451-482, (2017).
126 Bové, J. M. & Garnier, M. Phloem-and xylem-restricted plant pathogenic bacteria. *Plant Science* **163**, 1083-1098, (2002).
127 Holland, C., Numata, K., Rnjak-Kovacina, J. & Seib, F. P. The biomedical use of silk: past, present, future. *Adv. Healthc. Mater.* **8**, e1800465, (2019).
128 Zhou, Z. *et al.* Engineering the future of silk materials through advanced manufacturing. *Adv. Mater.* **30**, e1706983, (2018).
129 Marelli, B., Brenckle, M. A., Kaplan, D. L. & Omenetto, F. G. Silk fibroin as edible coating for perishable food preservation. *Sci. Rep.* **6**, 25263, (2016).
130 Ghezzi, C. E. *et al.* Degradation of silk films in multipocket corneal stromal rabbit models. *J. Appl. Biomater. Funct. Mater.* **14**, e266-276, (2016).
131 Lu, Q. *et al.* Degradation mechanism and control of silk fibroin. *Biomacromolecules* **12**, 1080-1086, (2011).
132 White, M. C. Metal complexation in xylem fluid : I. chemical composition of tomato amd soybean stem exudate. *Plant Physiol.* **67**, 292-300, (1981).
133 Marelli, B. *et al.* Silk fibroin derived polypeptide-induced biomineralization of collagen. *Biomaterials* **33**, 102-108, (2012).
134 Ranjbar, B. & Gill, P. Circular dichroism techniques: biomolecular and nanostructural analyses- a review. *Chem. Biol. Drug Des.* **74**, 101-120, (2009).
135 Hu, X., Kaplan, D. & Cebe, P. Determining beta-sheet crystallinity in fibrous proteins by thermal analysis and infrared spectroscopy. *Macromolecules* **39**, 6161-6170, (2006).

136 De Gelder, J., De Gussem, K., Vandenabeele, P. & Moens, L. Reference database of Raman spectra of biological molecules. *J. Raman Spectrosc.* **38**, 1133-1147, (2007).
137 Freddi, G. *et al.* Tyrosinase-catalyzed modification of Bombyx mori silk fibroin: grafting of chitosan under heterogeneous reaction conditions. *J. Biotechnol.* **125**, 281-294, (2006).
138 McGill, M., Holland, G. P. & Kaplan, D. L. Experimental methods for characterizing the secondary structure and thermal properties of silk proteins. *Macromol. Rapid Commun.* **40**, e1800390, (2019).
139 Hu, X., Kaplan, D. & Cebe, P. Dynamic protein−water relationships during β-sheet formation. *Macromolecules* **41**, 3939-3948, (2008).
140 Smirnoff, N. & Arnaud, D. Hydrogen peroxide metabolism and functions in plants. *New Phytol.* **221**, 1197-1214, (2019).
141 Taylor, R. C. & Cross, P. C. Raman spectra of hydrogen peroxide in condensed phases. I. the spectra of the pure liquid and its aqueous solutions. *J. Chem. Phys.* **24**, 41-44, (1956).
142 Jin, H. J. *et al.* Water-stable silk films with reduced β-sheet content. *Adv. Funct. Mater.* **15**, 1241-1247, (2005).
143 Jensen, K. H. *et al.* Sap flow and sugar transport in plants. *Rev. Mod. Phys.* **88**, (2016).
144 Choat, B., Cobb, A. R. & Jansen, S. Structure and function of bordered pits: new discoveries and impacts on whole-plant hydraulic function. *New Phytol.* **177**, 608-626, (2008).
145 Mullendore, D. L., Windt, C. W., Van As, H. & Knoblauch, M. Sieve tube geometry in relation to phloem flow. *Plant Cell* **22**, 579-593, (2010).
146 Savage, J. A., Zwieniecki, M. A. & Holbrook, N. M. Phloem transport velocity varies over time and among vascular bundles during early cucumber seedling development. *Plant Physiol.* **163**, 1409-1418, (2013).
147 Berger, C. & Laurent, F. Trunk injection of plant protection products to protect trees from pests and diseases. *Crop Prot.*. **124**, (2019).
148 Nakatsu, T. *et al.* Structural basis for the spectral difference in luciferase bioluminescence. *Nature* **440**, 372-376, (2006).
149 Gardner, W. Note on the dynamics of capillary flow. *Physical Review* **18**, 206-209, (1921).
150 Detournay, E. & Cheng, A. H. D. in *Comprehensive rock engineering. Vol. 2* 113-171 (Elsevier, 1993).
151 Desai, P. N., Shrivastava, N. & Padh, H. Production of heterologous proteins in plants: strategies for optimal expression. *Biotechnol. Adv.* **28**, 427-435, (2010).
152 Baskaran, P., Soós, V., Balázs, E. & Van Staden, J. Shoot apical meristem injection: A novel and efficient method to obtain transformed cucumber plants. *S. Afr. J. Bot.* **103**, 210-215, (2016).
153 Tsioris, K. *et al.* Fabrication of silk microneedles for controlled-release drug delivery. *Adv. Funct. Mater.* **22**, 330-335, (2012).
154 Larrañeta, E., Lutton, R. E. M., Woolfson, A. D. & Donnelly, R. F. Microneedle arrays as transdermal and intradermal drug delivery systems: Materials science, manufacture and commercial development. *Mater. Sci. Eng. R Rep.* **104**, 1-32, (2016).
155 Stinson, J. A. *et al.* Silk fibroin microneedles for transdermal vaccine delivery. *ACS Biomater. Sci. Eng.* **3**, 360-369, (2017).
156 Toyota, M. *et al.* Glutamate triggers long-distance, calcium-based plant defense signaling. *Science* **361**, 1112-1115, (2018).

157 Wasternack, C. *et al.* The wound response in tomato--role of jasmonic acid. *J. Plant Physiol.* **163**, 297-306, (2006).
158 Heil, M. & Ton, J. Long-distance signalling in plant defence. *Trends Plant Sci.* **13**, 264-272, (2008).
159 Santner, A. & Estelle, M. Recent advances and emerging trends in plant hormone signalling. *Nature* **459**, 1071-1078, (2009).
160 Ohkubo, Y., Tanaka, M., Tabata, R., Ogawa-Ohnishi, M. & Matsubayashi, Y. Shoot-to-root mobile polypeptides involved in systemic regulation of nitrogen acquisition. *Nat. Plants* **3**, 17029, (2017).
161 Ham, B. K. & Lucas, W. J. Phloem-mobile RNAs as systemic signaling agents. *Annu. Rev. Plant Biol.* **68**, 173-195, (2017).
162 Knoblauch, J., Mullendore, D. L., Jensen, K. H. & Knoblauch, M. Pico gauges for minimally invasive intracellular hydrostatic pressure measurements. *Plant Physiol.* **166**, 1271-1279, (2014).
163 Fisher, D. B. & Cash-Clark, C. E. Sieve tube unloading and post-phloem transport of fluorescent tracers and proteins injected into sieve tubes via severed aphid stylets. *Plant Physiol.* **123**, 125-138, (2000).
164 Wright, J. P. & Fisher, D. B. Direct measurement of sieve tube turgor pressure using severed aphid stylets. *Plant Physiol.* **65**, 1133-1135, (1980).
165 Rockwood, D. N. *et al.* Materials fabrication from Bombyx mori silk fibroin. *Nat. Protoc.* **6**, 1612-1631, (2011).
166 Nanjareddy, K. *et al.* Nitrate regulates rhizobial and mycorrhizal symbiosis in common bean (Phaseolus vulgaris L.). *J. Integr. Plant Biol.* **56**, 281-298, (2014).
167 Bialczyk, J. & Lechowsk, Z. Chemical composition of xylem sap of tomato grown on bicarbonate containing medium. *J. Plant Growth Regul.* **18**, 2005-2021, (1995).
168 Hines, D. J. & Kaplan, D. L. Mechanisms of controlled release from silk fibroin films. *Biomacromolecules* **12**, 804-812, (2011).
169 Porfirio, S., Gomes da Silva, M. D. R., Peixe, A., Cabrita, M. J. & Azadi, P. Current analytical methods for plant auxin quantification--A review. *Anal. Chim. Acta* **902**, 8-21, (2016).
170 Jensen, R. R. *et al.* Chemical element concentrations in black locust (Robinia pseudoacacia L.) and green ash (Fraxinus pennsylvanica Marsh.) leaves at the reclaimed Green Valley coal Mine, Indiana, USA. *Environ. Earth Sci.* **60**, 1391-1405, (2009).
171 Marelli, B. Biomaterials for boosting food security. *Science* **376**, 146-147, (2022).
172 Dudley, N. & Alexander, S. Agriculture and biodiversity: a review. *Biodiversity* **18**, 45-49, (2017).
173 Pilling, D., Bélanger, J. & Hoffmann, I. Declining biodiversity for food and agriculture needs urgent global action. *Nat. Food* **1**, 144-147, (2020).
174 Franke, W. in *Foliar Fertilization* 17-25 (Springer Netherlands, Dordrecht, 1986).
175 Rostami, S. & Azhdarpoor, A. The application of plant growth regulators to improve phytoremediation of contaminated soils: A review. *Chemosphere* **220**, 818-827, (2019).
176 Rouphael, Y. & Colla, G. Editorial: biostimulants in agriculture. *Front. Plant Sci.* **11**, 40, (2020).
177 Laane, H. M. The effects of foliar sprays with different silicon compounds. *Plants* **7**, 45, (2018).

178 Wang, D. *et al.* Nano-enabled pesticides for sustainable agriculture and global food security. *Nat. Nanotechnol.* **17**, 347-360, (2022).
179 Yang, C., Powell, C. A., Duan, Y., Shatters, R. & Zhang, M. Antimicrobial nanoemulsion formulation with improved penetration of foliar spray through citrus leaf cuticles to control citrus huanglongbing. *PLoS One* **10**, e0133826, (2015).
180 Marelli, B. *et al.* Programming function into mechanical forms by directed assembly of silk bulk materials. *Proc. Natl. Acad. Sci. U.S.A.* **114**, 451-456, (2017).
181 Zvinavashe, A. T., Lim, E., Sun, H. & Marelli, B. A bioinspired approach to engineer seed microenvironment to boost germination and mitigate soil salinity. *Proc. Natl. Acad. Sci. U.S.A.* **116**, 25555-25561, (2019).
182 Kim, D. *et al.* A microneedle technology for sampling and sensing bacteria in the food supply chain. *Adv. Funct. Mater.* **31**, 2005370, (2020).
183 Mhada, M. *et al.* Bioformulation of silk-based coating to preserve and deliver Rhizobium tropici to Phaseolus vulgaris under saline environments. *Front. Plant Sci.* **12**, 700273, (2021).
184 Zvinavashe, A. T. *et al.* Programmable design of seed coating function induces water-stress tolerance in semi-arid regions. *Nat. Food* **2**, 485-493, (2021).
185 Hedden, P. & Sponsel, V. A century of gibberellin research. *J. Plant Growth Regul.* **34**, 740-760, (2015).
186 Camara, M. C. *et al.* in *Planta* Vol. 248 1049-1062 (Springer Verlag, 2018).
187 Hedden, P. The current status of research on gibberellin biosynthesis. *Plant Cell Physiol.* **61**, 1832-1849, (2020).
188 Yamaguchi, N. *et al.* Gibberellin acts positively then negatively to control onset of flower formation in Arabidopsis. *Science* **344**, 638-641, (2014).
189 Bao, S., Hua, C., Shen, L. & Yu, H. New insights into gibberellin signaling in regulating flowering in Arabidopsis. *J. Integr. Plant Biol.* **62**, 118-131, (2020).
190 Nagai, K. *et al.* Antagonistic regulation of the gibberellic acid response during stem growth in rice. *Nature* **584**, 109-114, (2020).
191 Galvao, V. C., Collani, S., Horrer, D. & Schmid, M. Gibberellic acid signaling is required for ambient temperature-mediated induction of flowering in Arabidopsis thaliana. *Plant J.* **84**, 949-962, (2015).
192 Tian, H. *et al.* Synthesis of gibberellic acid derivatives and their effects on plant growth. *Molecules* **22**, (2017).
193 Boyes, D. C. *et al.* Growth stage-based phenotypic analysis of Arabidopsis: a model for high throughput functional genomics in plants. *Plant Cell* **13**, 1499-1510, (2001).
194 Fornara, F., de Montaigu, A. & Coupland, G. SnapShot: Control of flowering in Arabidopsis. *Cell* **141**, 550, 550 e551-552, (2010).
195 Binenbaum, J., Weinstain, R. & Shani, E. in *Trends Plant Sci.* Vol. 23 410-421 (Elsevier Ltd, 2018).
196 Bai, M. Y. *et al.* Brassinosteroid, gibberellin and phytochrome impinge on a common transcription module in Arabidopsis. *Nat. Cell Biol.* **14**, 810-817, (2012).
197 Felipo-Benavent, A. *et al.* Regulation of xylem fiber differentiation by gibberellins through DELLA-KNAT1 interaction. *Development* **145**, (2018).
198 Miceli, A., Moncada, A., Sabatino, L. & Vetrano, F. Effect of gibberellic acid on growth, yield, and quality of leaf lettuce and rocket grown in a floating system. *Agronomy* **9**, (2019).

199 Wasternack, C. How jasmonates earned their laurels: past and present. *J. Plant Growth Regul.* **34**, 761-794, (2015).
200 Wasternack, C. & Hause, B. Jasmonates: biosynthesis, perception, signal transduction and action in plant stress response, growth and development. An update to the 2007 review in Annals of Botany. *Ann. Bot.* **111**, 1021-1058, (2013).
201 Murashige, T. & Skoog, F. A revised medium for rapid growth and bio assays with tobacco tissue cultures. *Physiol. Plant.* **15**, 473-497, (1962).
202 Lichtenthaler, H. K. & Wellburn, A. R.
203 Dobin, A. *et al.* STAR: ultrafast universal RNA-seq aligner. *Bioinformatics* **29**, 15-21, (2013).
204 Love, M. I., Huber, W. & Anders, S. Moderated estimation of fold change and dispersion for RNA-seq data with DESeq2. *Genome Biol.* **15**, 550, (2014).
205 Yu, G., Wang, L. G., Han, Y. & He, Q. Y. clusterProfiler: an R package for comparing biological themes among gene clusters. *OMICS* **16**, 284-287, (2012).
206 Webb, P. *et al.* The urgency of food system transformation is now irrefutable. *Nat. Food* **1**, 584-585, (2020).
207 Crippa, M. *et al.* Food systems are responsible for a third of global anthropogenic GHG emissions. *Nat. Food* **2**, 198-209, (2021).
208 Flörke, M., Schneider, C. & McDonald, R. I. Water competition between cities and agriculture driven by climate change and urban growth. *Nat. Sustain.* **1**, 51-58, (2018).
209 Law, K. L. & Narayan, R. Reducing environmental plastic pollution by designing polymer materials for managed end-of-life. *Nat. Rev. Mater.*, 1-13, (2021).
210 Zheng, J. & Suh, S. Strategies to reduce the global carbon footprint of plastics. *Nat. Clim. Change* **9**, 374-378, (2019).
211 Sohn, Y. J. *et al.* Recent advances in sustainable plastic upcycling and biopolymers. *Biotechnol. J.* **15**, e1900489, (2020).
212 Kusama, S. *et al.* Transdermal electroosmotic flow generated by a porous microneedle array patch. *Nat. Commun.* **12**, 658, (2021).
213 Cheung, K. & Das, D. B. Microneedles for drug delivery: trends and progress. *Drug Deliv.* **23**, 2338-2354, (2016).
214 Reznikov, N., Shahar, R. & Weiner, S. in *Acta Biomater.* (2014).
215 Tritschler, U. & Cölfen, H. Self-assembled hierarchically structured organic–inorganic composite systems. *Bioinspir. Biomim.* **11**, 35002, (2016).
216 Boskey, A. L. Mineralization of bones and teeth. *Elements* **3**, 385-391, (2007).
217 Shenhar, R., Norsten, T. B. & Rotello, V. M. in *Adv. Mater.* (2005).
218 Cigler, P., Lytton-Jean, A. K., Anderson, D. G., Finn, M. G. & Park, S. Y. DNA-controlled assembly of a NaTl lattice structure from gold nanoparticles and protein nanoparticles. *Nat. Mater.* **9**, 918-922, (2010).
219 Macfarlane, R. J. *et al.* Nanoparticle superlattice engineering with DNA. *Science* **334**, 204-208, (2011).
220 Pyles, H., Zhang, S., De Yoreo, J. J. & Baker, D. Controlling protein assembly on inorganic crystals through designed protein interfaces. *Nature* **571**, 251-256, (2019).
221 Koeppel, A., Laity, P. R. & Holland, C. The influence of metal ions on native silk rheology. *Acta Biomater.* **117**, 204-212, (2020).
222 Phillips, J. C. *et al.* Scalable molecular dynamics on CPU and GPU architectures with NAMD. *J. Chem. Phys.* **153**, 044130, (2020).

223 Li, Y. *et al.* Evaporating droplets on oil-wetted surfaces: Suppression of the coffee-stain effect. *Proc. Natl. Acad. Sci. U.S.A.* **117**, 16756-16763, (2020).
224 Deegan, R. D. *et al.* Capillary flow as the cause of ring stains from dried liquid drops. *Nature* **389**, 827-829, (1997).
225 Jun, Y. S., Kim, D. & Neil, C. W. Heterogeneous nucleation and growth of nanoparticles at environmental interfaces. *Acc. Chem. Res.* **49**, 1681-1690, (2016).
226 De Yoreo, J. J. Principles of crystal nucleation and growth. *Rev. Mineral. Geochem.* **54**, 57-93, (2003).
227 Jin, H. J. & Kaplan, D. L. Mechanism of silk processing in insects and spiders. *Nature* **424**, 1057-1061, (2003).
228 Babaie, A. & Stoeber, B. Viscous flow separation caused by the Marangoni effect in competition with capillary flow. *Phys. Fluids* **27**, 71702, (2015).
229 Haynes, W. M., David R. Lide, and Thomas J. Bruno. *CRC handbook of chemistry and physics*. (CRC press, 2016).
230 Li, Z., Persits, N., Gray, D. J. & Ram, R. J. Computational polarized Raman microscopy on sub-surface nanostructures with sub-diffraction-limit resolution. *Opt Express* **29**, 38027-38043, (2021).
231 Frost, R. L., Williams, P. A., Martens, W., Leverett, P. & Kloprogge, J. T. Raman spectroscopy of basic copper (II) and some complex copper (II) sulfate minerals: Implications for hydrogen bonding. *Am. Mineral.* **89**, 1130-1137, (2004).
232 Monti, P., Taddei, P., Freddi, G., Asakura, T. & Tsukada, M. Raman spectroscopic characterization ofBombyx mori silk fibroin: Raman spectrum of Silk I. *J. Raman Spectrosc.* **32**, 103-107, (2001).
233 Zhou, P. *et al.* Effects of pH and calcium ions on the conformational transitions in silk fibroin using 2D Raman correlation spectroscopy and 13C solid-state NMR. *Biochemistry* **43**, 11302-11311, (2004).
234 Kochhar, J. S., Soon, W. J., Choi, J., Zou, S. & Kang, L. Effect of microneedle geometry and supporting substrate on microneedle array penetration into skin. *J. Pharm. Sci.* **102**, 4100-4108, (2013).
235 Lowry, G. V., Avellan, A. & Gilbertson, L. M. Opportunities and challenges for nanotechnology in the agri-tech revolution. *Nat. Nanotechnol.* **14**, 517-522, (2019).
236 Samant, P. P. & Prausnitz, M. R. Mechanisms of sampling interstitial fluid from skin using a microneedle patch. *Proc. Natl. Acad. Sci. U.S.A.* **115**, 4583-4588, (2018).
237 Gao, P. *et al.* Effects of nearly four decades of long-term fertilization on the availability, fraction and environmental risk of cadmium and arsenic in red soils. *J. Environ. Manage.* **295**, 113097, (2021).
238 Verbruggen, N., Hermans, C. & Schat, H. Mechanisms to cope with arsenic or cadmium excess in plants. *Curr. Opin. Plant Biol.* **12**, 364-372, (2009).
239 Huang, J. *et al.* CHARMM36m: an improved force field for folded and intrinsically disordered proteins. *Nat. Methods* **14**, 71-73, (2017).
240 Liao, Q., Kamerlin, S. C. L. & Strodel, B. Development and application of a nonbonded Cu2+ model that includes the Jahn–Teller effect. *J. Phys. Chem. Lett.* **6**, 2657-2662, (2015).
241 Lieber, C. A. & Mahadevan-Jansen, A. Automated method for subtraction of fluorescence from biological Raman spectra. *Appl. Spectrosc.* **57**, 1363-1367, (2003).
242 Epstein, E. *Mineral nutrition of plants: principles and perspectives*. (Sinauer Associates, Sunderland, Massachusetts, 1972).

243 Lamichhane, J. R. *et al.* Thirteen decades of antimicrobial copper compounds applied in agriculture. A review. *Agron. Sustain. Dev.* **38**, 28, (2018).
244 Health, N. I. o. (ed Office of Dietary Supplements) (2020).

Appendix A: Supplementary Data for Chapter 4

A.1 Supporting Dataset for Differential Gene Expression Analysis

Table A.1 Differential gene expression analysis

Gene	Z-scored, log2 Fold Changes			
	Control_0h	GA_INJ_3h	GA_INJ_24h	GA_INJ_168h
AT1G01610	0.84655371	0.34155112	-1.5490799	-0.1553849
AT1G01620	0.43736234	0.40622645	-1.6396557	0.24951504
AT1G03310	-0.0131012	-1.2552608	0.85720225	0.69689385
AT1G03870	-0.8094169	0.59369487	-1.0809593	0.93636161
AT1G04350	-0.9724357	-0.559069	1.51588083	0.52091747
AT1G04680	-0.0604917	0.5438685	-1.6615208	0.6243037
AT1G05170	0.25549964	-1.2015992	0.79135699	0.41852822
AT1G05570	-0.9533486	-0.162342	1.52718154	0.09756952
AT1G06360	-0.4347475	0.3918142	-1.1665035	0.82060233
AT1G06460	1.09495028	-1.0714901	0.53387519	-0.3793769
AT1G06850	-1.0420384	0.6646279	-0.755961	0.88138446
AT1G08920	0.51239012	-0.865364	0.76220795	-0.1551648
AT1G10200	1.26318775	-0.8993162	-0.7521802	0.13758191
AT1G11000	-0.4455811	0.84575644	-1.4168996	0.54442434
AT1G11410	-0.3158391	-1.1688532	0.76867826	0.97224013
AT1G12090	0.34522348	0.47757008	-1.8864741	0.43485581
AT1G12500	0.17784385	0.46500984	-1.9011564	0.62458391
AT1G13930	1.51037966	-0.8913265	-0.3701609	-0.3722792
AT1G14440	0.12676155	0.96735665	-1.4461591	-0.1300121
AT1G15550	-0.690642	1.43877841	-0.7120878	-0.2734112
AT1G17020	0.27680048	-0.8782444	1.23853929	-0.2242489
AT1G18250	0.14593888	0.47442688	-1.6932567	0.50847207
AT1G21400	-0.5159149	-0.3748902	1.6001324	-0.1759498
AT1G21680	0.96611957	-0.8528457	0.70935228	-0.5861754
AT1G22640	0.09361046	-0.1741515	1.60626845	-0.9903046
AT1G23090	0.01919978	1.26309471	-1.1938322	-0.4864064
AT1G24625	0.545193	-1.0978709	1.34035029	-0.340889
AT1G25230	-0.4419298	1.11077295	-1.0093418	0.00405138
AT1G25275	0.16910939	1.28055679	-1.0609271	-0.7423815
AT1G25450	0.6696526	0.48482646	-1.749432	0.01180891
AT1G27210	-0.2565492	1.12632611	-1.2662764	-0.0255926
AT1G32900	-0.6135058	-0.9344746	1.1231049	0.79924379
AT1G33240	-0.9461137	0.58555963	-0.798987	0.89321206
AT1G33590	0.46682482	0.80448705	-1.7369232	-0.113363

AT1G41830	-0.0203079	0.09110688	-1.7108214	1.06974859
AT1G44350	1.2844017	-0.9252369	-0.1374565	-0.2675271
AT1G44446	-0.946644	0.55971432	-0.8427146	0.94873943
AT1G48280	0.0585274	0.81385164	-1.5625023	0.16928915
AT1G48480	-0.3838568	0.86732378	-1.4795581	0.50290514
AT1G50260	0.85131346	-0.8974606	0.43829152	-0.2460472
AT1G52342	-0.2630778	-1.1519571	0.63528615	0.99151081
AT1G54730	-1.2737314	0.87531868	0.29910267	0.19901096
AT1G54740	-0.9100659	0.90794832	-0.7804237	0.52240007
AT1G55210	0.94810376	-1.0954446	-0.6810152	0.60135097
AT1G55320	-0.5191051	-0.9850814	1.03351557	0.81517614
AT1G61800	0.97758499	-1.0064127	0.00860204	0.02309299
AT1G62440	-0.2491425	0.56450485	-1.5308296	0.70519076
AT1G62480	1.02834299	0.29433499	-1.4790696	-0.3366316
AT1G62570	0.78871636	-1.2431998	0.6215997	0.04008361
AT1G62810	-0.6819366	-0.2303009	1.89056455	-0.3481389
AT1G64670	0.1603838	0.67974361	-1.5446541	0.18964198
AT1G64760	0.25084882	0.26926227	-1.7878032	0.67175768
AT1G65310	-0.2053137	0.0561815	-1.1794006	0.93539934
AT1G68570	-0.6297651	-0.8133645	1.25895278	0.60382775
AT1G68830	-1.0999898	0.09785285	1.59223649	-0.059354
AT1G69040	-0.0030504	1.11113235	-1.2719709	-0.2601013
AT1G69490	0.12090855	0.03216725	1.56528524	-1.1965993
AT1G69530	-0.1960023	1.04807689	-1.1357426	-0.0949129
AT1G70710	0.10544252	0.60210923	-1.5725237	0.34079737
AT1G71695	-0.2638765	0.49791757	-1.7483845	0.93154857
AT1G71960	-1.4537004	0.70311226	0.30114614	0.54982403
AT1G72510	0.09651187	-1.3243907	1.17391449	0.44526918
AT1G74100	0.97874835	-1.1022285	-0.6016165	0.52455779
AT1G74310	1.04312237	-1.2379259	0.06522564	0.15131977
AT1G74670	-0.850626	0.7247459	-1.0889796	0.85186649
AT1G75780	0.07796965	0.76857373	-1.6221268	0.23487447
AT1G76990	-0.8531068	1.29093394	-0.3966791	-0.1733744
AT1G78070	1.07092622	-1.2953624	0.25687326	0.05318733
AT1G78170	0.47419814	0.85392485	-1.1224513	-0.5798221
AT1G78260	0.03247354	0.81850874	-1.6983132	0.28122648
AT1G78610	-0.0219233	-1.1283986	-0.1120925	1.22505015
AT5G01040	0.02636561	1.14870321	-1.3323393	-0.2868426
AT5G04020	-0.5149751	1.01651502	-1.0291107	0.1845339
AT5G04530	-0.3927396	1.01283536	-1.1813057	0.16744142

AT5G07000	1.39822644	-0.5863462	-0.8021091	-0.2771408
AT5G07830	0.02985627	0.67548541	0.93386199	-1.3279163
AT5G08640	0.65951199	-0.2796145	-1.6611508	0.72753642
AT5G11740	0.08926357	0.14680598	-1.5941861	0.8267212
AT5G12940	-0.2344401	0.14147975	-1.5545822	1.12934852
AT5G13180	0.37543166	-0.6465078	1.30270309	-0.5973925
AT5G14920	0.32359831	1.03847084	-1.644085	-0.2660125
AT5G15350	-0.6090201	0.53018514	-1.1318791	0.83342104
AT5G15580	-0.6423169	1.22242788	-1.2463771	0.25080705
AT5G18270	-0.485798	-0.58392	1.10783366	0.33116227
AT5G20150	0.11043432	-1.1244364	1.46290212	0.03873403
AT5G21100	-0.263655	-1.080698	0.36379293	1.10182435
AT5G22940	-0.4155718	0.65725494	-1.33856	0.65069017
AT5G23860	0.26666001	0.42879939	-1.8980871	0.56993202
AT5G25900	0.43090274	0.14481769	1.0886475	-1.3014854
AT5G38410	0.20065985	0.48893448	-1.9364176	0.60135077
AT5G41761	-0.369194	1.15485844	0.40437177	-1.0552456
AT5G42650	1.14646395	-1.2195883	-0.0041816	0.07591205
AT5G43760	-0.3251917	0.51056547	-1.5250794	0.83134584
AT5G43830	-0.2558887	1.08426527	-1.3547654	0.07480037
AT5G44680	-0.8756038	0.89518142	-0.9265612	0.59812984
AT5G45670	-0.2359197	0.18996701	-1.3737386	0.96177846
AT5G45950	0.75730694	0.31437068	-1.8443895	0.15791536
AT5G46050	1.1290279	-1.0706829	0.6076747	-0.4634615
AT5G46910	1.2515721	-0.4656618	-1.1975532	0.01245849
AT5G47770	-0.5107712	0.76002614	-1.4402239	0.71089428
AT5G49630	-0.6840229	-0.655278	1.65777373	0.23411842
AT5G49800	0.08913793	0.50271824	-1.530731	0.42863116
AT5G50915	-0.1195879	0.60124106	-1.7179394	0.66363973
AT5G51560	-0.5235597	0.67532624	-1.4429202	0.81018025
AT5G55050	1.04286144	-1.1154893	-0.4348493	0.36252742
AT5G55730	0.23391341	-0.0581432	-1.622752	0.90606449
AT5G55860	-0.4995512	-0.298201	1.661377	-0.3098325
AT5G56320	-0.6092087	0.82471201	-1.3219675	0.66580838
AT5G58900	0.24841056	0.42290517	-1.7907991	0.52255034
AT5G59130	0.69890682	-1.2942082	0.58209881	0.20723549
AT5G59290	0.38739071	0.07193889	-1.848979	0.77332306
AT5G60400	-0.3776284	1.39690069	-1.2387676	-0.1934272
AT5G60890	1.29731869	-0.8694194	-0.5443748	-0.0649827
AT5G61440	-0.1974809	0.46727094	-1.373388	0.64580198

AT5G61520	-0.7432565	1.02695263	0.61383811	-0.6929216
AT5G64620	0.29359844	1.18885547	-1.4185288	-0.536768
AT5G65310	0.73425973	0.60816675	-0.8869695	-0.7511135
AT3G02110	0.27896618	0.498544	-1.7159193	0.36643599
AT3G04730	-1.3684789	0.65366203	0.68055748	0.26111191
AT3G05490	-1.0315093	0.56310568	-0.7001602	0.93517716
AT3G06750	-0.7677417	0.51520753	-1.0817233	0.97368297
AT3G07320	0.73030593	0.31903939	-1.8424263	0.17893887
AT3G09520	-0.3039189	-1.0428543	1.35878921	0.4409137
AT3G10450	-1.010594	-0.2486966	1.41225252	0.31778889
AT3G10720	-0.0206843	0.77054168	-1.8377968	0.47534046
AT3G11280	-0.8415589	1.26215298	-0.6603891	0.01966527
AT3G12110	-0.4813515	0.7105267	-1.4976557	0.76926192
AT3G12610	-0.1658191	0.17968224	-1.4785842	0.97185964
AT3G13520	0.45562306	0.16192855	-1.8615799	0.62350167
AT3G14067	0.19215428	-1.2621667	1.43518277	0.11322391
AT3G14440	1.02013627	-1.3394932	0.23554588	0.16232635
AT3G14840	-1.3845552	0.78770672	0.00973293	0.59035983
AT3G15020	-0.5342382	-0.9207043	0.39708952	1.19021622
AT3G16180	0.84996458	0.52549631	-1.7273703	-0.2238807
AT3G16370	-0.073116	0.70400606	-1.8303132	0.58931874
AT3G17100	-1.2849332	1.07741584	0.06682558	0.16296702
AT3G21670	0.64436393	-1.4808262	0.61488973	0.42653576
AT3G21700	1.06627726	-1.1658202	0.64878342	-0.3329794
AT3G21770	0.20912152	0.96137856	-1.581367	-0.1162554
AT3G23530	-0.3632466	0.70607432	-1.6237618	0.73968016
AT3G23730	-0.1512445	0.65239409	-1.5040172	0.50152853
AT3G23880	-0.8173089	1.07462908	-1.2248717	0.55926097
AT3G24420	1.34071728	-0.0424375	-0.5078429	-0.9597179
AT3G24480	-0.3226573	0.20701268	-1.4363548	1.07321451
AT3G25900	0.61075616	0.63119756	-1.7301739	-0.0885045
AT3G26290	1.14198328	-1.0535932	0.76175853	-0.5962291
AT3G27660	1.22664729	-1.1085133	-0.4088197	0.15441251
AT3G28130	0.74344945	-1.3825759	0.12540904	0.55552044
AT3G28180	-0.2630568	0.63477701	-1.5680622	0.67365464
AT3G43720	0.53591861	0.30903679	-1.9551096	0.45845097
AT3G44990	0.67949721	-1.0571308	-0.6248018	0.79416816
AT3G48460	1.17030036	-1.0966177	-0.7474381	0.42460938
AT3G49220	1.01570184	-0.4953318	-1.5268141	0.49750609
AT3G51600	0.96212285	0.54830692	-1.4162171	-0.566285

AT3G52360	-0.8795415	-0.3402499	-0.0637577	1.2622966
AT3G52470	1.23198685	-0.7059156	-0.9975314	0.13894969
AT3G53040	1.12608936	-0.5896927	-0.5962961	-0.1388659
AT3G53480	-0.8941565	-0.465179	1.5935908	0.29694166
AT3G54720	-0.66106	1.21338111	-1.0822197	0.16915871
AT3G55120	-0.0263189	-0.8022942	1.42269585	-0.1198507
AT3G55240	-0.4616531	-0.3643361	1.75069024	-0.3411377
AT3G56060	-1.2226403	0.02375303	-0.0259348	1.21617711
AT3G57630	-0.0398541	-1.1546821	1.15398012	0.42521615
AT3G63010	0.06860792	1.00414296	0.22508237	-1.2228058
AT2G01940	-0.5719448	1.38428709	-0.7424553	-0.3173721
AT2G02850	0.27323788	1.17291154	-0.4774231	-1.1278673
AT2G04240	-0.3687641	1.02351428	0.87310136	-1.2368178
AT2G04780	0.38502347	0.28352858	-1.9125167	0.60645906
AT2G14890	-0.1199945	0.47567602	-1.6673744	0.75590143
AT2G16850	-0.0121396	0.43892242	-1.6051315	0.64330487
AT2G17280	1.41465402	-0.9407311	-0.4287349	-0.1880996
AT2G20835	-0.7048467	-0.5812824	-0.0117843	1.29398532
AT2G26710	-0.659803	1.28362411	-1.0275845	0.06123522
AT2G27385	0.66521089	0.4871588	-1.6596421	-0.0459416
AT2G27840	1.21051546	-0.9752098	-0.7168299	0.24258087
AT2G28200	-0.6004046	-0.5829116	1.29931902	0.31710359
AT2G28470	0.10946315	-1.1848348	-0.102985	1.14402828
AT2G29550	0.04178546	0.63735531	-1.706568	0.45857123
AT2G32560	-0.5390763	0.59193312	-1.546812	0.97835117
AT2G34930	0.52755952	0.28828805	-1.7365083	0.34182463
AT2G35190	0.31032656	0.67664328	-1.8713779	0.26061545
AT2G36970	-0.7046691	0.92142638	0.47081267	-0.5306324
AT2G37640	0.9515023	-0.481675	-1.5673503	0.5750729
AT2G38870	1.2232155	-1.2609938	0.33331546	-0.184432
AT2G39220	-0.1546519	-0.66033	1.3725325	-0.1000398
AT2G39900	1.08143865	0.0696832	-1.6540307	-0.0484347
AT2G40610	0.0217709	-0.1172351	-1.329704	0.9819335
AT2G41090	-1.3669138	0.13470605	0.8899449	0.63891112
AT2G41640	-0.4390633	-0.7787361	0.39044136	0.95750514
AT2G42620	-0.6291072	1.20891227	0.22205765	-0.7278435
AT2G42840	0.1760707	0.80283252	-1.1414208	-0.217956
AT2G43290	-0.7655737	-0.2447463	-0.509045	1.34968341
AT2G45470	0.06927594	0.18732029	-1.7621755	0.91818742
AT2G46530	0.11864891	-1.2877763	1.21616858	0.35834838

AT2G46690	1.25056985	-0.6351525	0.20529093	-0.7522779
AT2G46780	-0.3396995	0.33777783	-1.3494374	0.9015466
AT2G47000	0.51022069	-0.8310272	1.48949621	-0.6721909
AT4G01700	1.16081265	-0.8540458	-0.4390773	-0.0140487
AT4G02330	-0.0902004	0.25832777	-1.5083699	0.83745264
AT4G03200	-0.9298855	-0.4174529	1.67041227	0.23373015
AT4G03210	-0.6522086	0.79429882	-1.2045509	0.66094374
AT4G12420	-0.4243734	0.8621765	-1.5226327	0.57728533
AT4G12730	0.09829178	0.53956326	-1.8838243	0.61802782
AT4G12910	-0.1583005	-1.2946251	1.06436778	0.74334711
AT4G12980	-0.3279607	-0.6680351	-0.5148102	1.33920258
AT4G15230	-0.4834108	1.31944523	-0.6465077	-0.4050293
AT4G18970	-0.431034	0.8463168	-1.6173965	0.66298155
AT4G19170	0.11175247	-0.832652	1.5878838	-0.3376896
AT4G19700	0.00268299	1.10428067	0.17728075	-1.2251508
AT4G20070	-1.2734382	0.43029009	0.34186108	0.61524077
AT4G20320	0.88990362	-1.0151797	0.83818493	-0.4335139
AT4G21850	1.28292605	-0.6372909	-0.3739523	-0.3963336
AT4G22010	-0.2042421	0.73139775	-1.3757457	0.39000816
AT4G22780	-0.1513946	-0.8516863	1.53471247	-0.0200608
AT4G23030	1.34704669	-0.5655226	-0.4858888	-0.4575982
AT4G23710	0.51486411	0.46380072	-1.6234952	0.1036653
AT4G25260	1.11203835	-0.4150434	-1.2460348	0.13369493
AT4G29140	-0.5987184	1.26164563	-0.7622036	-0.1547914
AT4G29190	-0.2433376	0.9527762	0.60796088	-1.1147459
AT4G30190	1.37544933	-0.4309374	-1.1272068	-0.1930407
AT4G30280	-0.1508873	0.55508963	-1.3476903	0.49425783
AT4G30340	0.29107761	1.2431517	-0.671684	-1.08644
AT4G30410	-0.057943	0.62657266	-1.5094937	0.43769952
AT4G34790	-0.2676018	0.61962357	-1.586493	0.70564023
AT4G35110	1.42820928	-0.8812164	-0.3596968	-0.3071951
AT4G37400	-1.3246114	0.51547896	0.67200485	0.36112917
AT4G37450	-0.2779018	0.79264482	-1.5579114	0.52386453
AT4G39070	-0.271126	1.35725259	-0.9082919	-0.4805987
AT4G39330	0.67084093	0.24330042	-1.806417	0.29013667
AT4G39940	-0.0148137	-1.2989897	1.08232741	0.59225182
AT4G39950	0.94292157	-0.7016891	-1.077483	0.47708958
AT4G40060	0.09119413	-0.7474037	1.25690648	-0.181728

A.2 Supporting Dataset for Gene Ontology Enrichment Analysis

Table A.2 Gene ontology enrichment analysis of sample GA_INJ_3h

ID	Description	FDR
GO:0001101	response to acid chemical	1.90E-19
GO:0009414	response to water deprivation	5.19E-16
GO:0009415	response to water	6.83E-16
GO:0009611	response to wounding	1.77E-12
GO:0009651	response to salt stress	6.71E-10
GO:0007623	circadian rhythm	3.68E-08
GO:0048511	rhythmic process	3.68E-08
GO:0009409	response to cold	1.14E-07
GO:0009639	response to red or far red light	3.67E-07
GO:0009408	response to heat	6.05E-06
GO:0019748	secondary metabolic process	4.08E-05
GO:0036293	response to decreased oxygen levels	8.66E-05
GO:0070482	response to oxygen levels	9.00E-05
GO:0080134	regulation of response to stress	9.35E-05
GO:0001666	response to hypoxia	0.00010127
GO:0030490	maturation of SSU-rRNA	0.00014928
GO:0045087	innate immune response	0.00016173
GO:0006972	hyperosmotic response	0.00017794
GO:0009753	response to jasmonic acid	0.00018742
GO:2000026	regulation of multicellular organismal development	0.00024326
GO:0048584	positive regulation of response to stimulus	0.00027376
GO:0070542	response to fatty acid	0.00027376
GO:0009694	jasmonic acid metabolic process	0.00034287
GO:0000462	maturation of SSU-rRNA from tricistronic rRNA transcript (SSU-rRNA, 5.8S rRNA, LSU-rRNA)	0.00036156
GO:0042274	ribosomal small subunit biogenesis	0.00037123
GO:0043200	response to amino acid	0.00042811
GO:0071456	cellular response to hypoxia	0.00042811
GO:0042254	ribosome biogenesis	0.00045307
GO:0006364	rRNA processing	0.00045307
GO:0042538	hyperosmotic salinity response	0.00045307
GO:0036294	cellular response to decreased oxygen levels	0.00045307
GO:0071453	cellular response to oxygen levels	0.00045307
GO:0031347	regulation of defense response	0.00051322
GO:0098754	detoxification	0.00061998
GO:0016072	rRNA metabolic process	0.00061998
GO:0048580	regulation of post-embryonic development	0.00061998
GO:0071229	cellular response to acid chemical	0.00061998
GO:0006979	response to oxidative stress	0.00069273
GO:0032103	positive regulation of response to external stimulus	0.0009712
GO:0022613	ribonucleoprotein complex biogenesis	0.00113723

GO:0016054	organic acid catabolic process	0.00119509
GO:0002682	regulation of immune system process	0.00123606
GO:0050776	regulation of immune response	0.00123606
GO:0007568	aging	0.00139365
GO:0009251	glucan catabolic process	0.00139365
GO:0045089	positive regulation of innate immune response	0.00141928
GO:0002684	positive regulation of immune system process	0.00141928
GO:0002833	positive regulation of response to biotic stimulus	0.00141928
GO:0050778	positive regulation of immune response	0.00141928
GO:0009743	response to carbohydrate	0.0014543
GO:0009620	response to fungus	0.00152818
GO:0051239	regulation of multicellular organismal process	0.0016508
GO:0032101	regulation of response to external stimulus	0.00173209
GO:0010224	response to UV-B	0.00173209
GO:0009914	hormone transport	0.00214253
GO:0002831	regulation of response to biotic stimulus	0.00215166
GO:0006816	calcium ion transport	0.00250517
GO:0002253	activation of immune response	0.00256366
GO:0006360	transcription by RNA polymerase I	0.00279046
GO:0009636	response to toxic substance	0.00279046
GO:0031668	cellular response to extracellular stimulus	0.00293538
GO:0044282	small molecule catabolic process	0.00296403
GO:0060918	auxin transport	0.00323983
GO:0045088	regulation of innate immune response	0.00336629
GO:0071230	cellular response to amino acid stimulus	0.00359156
GO:0010118	stomatal movement	0.00383894
GO:0009744	response to sucrose	0.00383894
GO:0002757	immune response-activating signal transduction	0.00383894
GO:0010114	response to red light	0.00383894
GO:0009642	response to light intensity	0.00383894
GO:0002764	immune response-regulating signaling pathway	0.00447555
GO:0071496	cellular response to external stimulus	0.00449831
GO:0031349	positive regulation of defense response	0.00491126
GO:0002218	activation of innate immune response	0.00491126
GO:1901605	alpha-amino acid metabolic process	0.00491126
GO:0034285	response to disaccharide	0.00491126
GO:0140115	export across plasma membrane	0.00491126
GO:1901606	alpha-amino acid catabolic process	0.00509727
GO:0090696	post-embryonic plant organ development	0.00516469
GO:0009644	response to high light intensity	0.00626676
GO:0046395	carboxylic acid catabolic process	0.00663118
GO:0044275	cellular carbohydrate catabolic process	0.00741551
GO:0009751	response to salicylic acid	0.00741551
GO:0010817	regulation of hormone levels	0.00781649
GO:0044247	cellular polysaccharide catabolic process	0.00798883

GO:0090693	plant organ senescence	0.00798883
GO:0002758	innate immune response-activating signal transduction	0.00798883
GO:0006833	water transport	0.00798883
GO:0042044	fluid transport	0.00798883
GO:0001522	pseudouridine synthesis	0.00816234
GO:0009926	auxin polar transport	0.0082854
GO:0044403	biological process involved in symbiotic interaction	0.0082854
GO:0048366	leaf development	0.00917876
GO:0009411	response to UV	0.00936545
GO:0090697	post-embryonic plant organ morphogenesis	0.00939946
GO:0015804	neutral amino acid transport	0.00985657
GO:0032787	monocarboxylic acid metabolic process	0.01063002
GO:0016036	cellular response to phosphate starvation	0.01074878
GO:1901615	organic hydroxy compound metabolic process	0.01074878
GO:0009404	toxin metabolic process	0.01132107
GO:0034470	ncRNA processing	0.01170708
GO:0044550	secondary metabolite biosynthetic process	0.01183999
GO:0042742	defense response to bacterium	0.01193343
GO:0009991	response to extracellular stimulus	0.01193343
GO:0009845	seed germination	0.01193343
GO:0009267	cellular response to starvation	0.01193343
GO:0009695	jasmonic acid biosynthetic process	0.01193343
GO:0030001	metal ion transport	0.01226145
GO:1905392	plant organ morphogenesis	0.01227862
GO:0072348	sulfur compound transport	0.01322423
GO:0071365	cellular response to auxin stimulus	0.01322423
GO:0008202	steroid metabolic process	0.01333637
GO:0044262	cellular carbohydrate metabolic process	0.01333637
GO:0031669	cellular response to nutrient levels	0.01333637
GO:0009734	auxin-activated signaling pathway	0.01333637
GO:0042908	xenobiotic transport	0.0149632
GO:0009640	photomorphogenesis	0.0149632
GO:0030004	cellular monovalent inorganic cation homeostasis	0.01537455
GO:0010150	leaf senescence	0.01542446
GO:0016052	carbohydrate catabolic process	0.01545382
GO:0098661	inorganic anion transmembrane transport	0.01568219
GO:0006790	sulfur compound metabolic process	0.01568219
GO:0014070	response to organic cyclic compound	0.01633984
GO:0034605	cellular response to heat	0.01775295
GO:2000030	regulation of response to red or far red light	0.01830687
GO:0009626	plant-type hypersensitive response	0.01830687
GO:0046777	protein autophosphorylation	0.01916181
GO:0012501	programmed cell death	0.01961422
GO:0071482	cellular response to light stimulus	0.01990507
GO:0034050	programmed cell death induced by symbiont	0.02079439

GO:0072329	monocarboxylic acid catabolic process	0.02079439
GO:0002213	defense response to insect	0.02081987
GO:0010099	regulation of photomorphogenesis	0.02081987
GO:0051094	positive regulation of developmental process	0.02081987
GO:0016125	sterol metabolic process	0.0212801
GO:0042752	regulation of circadian rhythm	0.0219129
GO:0048582	positive regulation of post-embryonic development	0.0219129
GO:0051702	biological process involved in interaction with symbiont	0.0232111
GO:0006865	amino acid transport	0.02322588
GO:0042542	response to hydrogen peroxide	0.02388532
GO:0006820	anion transport	0.02461019
GO:0000302	response to reactive oxygen species	0.02461019
GO:0090351	seedling development	0.02461019
GO:0048878	chemical homeostasis	0.02498124
GO:0009808	lignin metabolic process	0.02586739
GO:0034284	response to monosaccharide	0.02638299
GO:0120254	olefinic compound metabolic process	0.02638299
GO:0048528	post-embryonic root development	0.02780755
GO:0050832	defense response to fungus	0.02871703
GO:0042592	homeostatic process	0.02964404
GO:0019318	hexose metabolic process	0.02969282
GO:0046618	xenobiotic export	0.03252957
GO:1990961	xenobiotic detoxification by transmembrane export across the plasma membrane	0.03252957
GO:0008272	sulfate transport	0.03252957
GO:0000272	polysaccharide catabolic process	0.03287938
GO:0009624	response to nematode	0.03287938
GO:0048532	anatomical structure arrangement	0.03287938
GO:0007029	endoplasmic reticulum organization	0.03441844
GO:0009698	phenylpropanoid metabolic process	0.0344994
GO:0071478	cellular response to radiation	0.03630529
GO:0010315	auxin efflux	0.03630529
GO:0009746	response to hexose	0.03630529
GO:0005976	polysaccharide metabolic process	0.03634267
GO:0015849	organic acid transport	0.03947165
GO:1900140	regulation of seedling development	0.03947165
GO:0000469	cleavage involved in rRNA processing	0.03947165
GO:0042430	indole-containing compound metabolic process	0.0400527
GO:0010167	response to nitrate	0.0400527
GO:0016126	sterol biosynthetic process	0.0400527
GO:0016998	cell wall macromolecule catabolic process	0.0400527
GO:0042335	cuticle development	0.0400527
GO:0006081	cellular aldehyde metabolic process	0.04093473
GO:0008037	cell recognition	0.04093473
GO:0010646	regulation of cell communication	0.04262876

GO:0009631	cold acclimation	0.04262876
GO:0010286	heat acclimation	0.04262876
GO:1901698	response to nitrogen compound	0.04337074
GO:0009407	toxin catabolic process	0.04337074
GO:0010102	lateral root morphogenesis	0.04353726
GO:0009608	response to symbiont	0.04371231
GO:0098781	ncRNA transcription	0.04371231
GO:0031667	response to nutrient levels	0.04412709
GO:0044042	glucan metabolic process	0.04457631
GO:0070588	calcium ion transmembrane transport	0.04471042
GO:0016115	terpenoid catabolic process	0.04471042
GO:0090501	RNA phosphodiester bond hydrolysis	0.04471042
GO:0140352	export from cell	0.04471042
GO:0055081	anion homeostasis	0.04471042
GO:0042594	response to starvation	0.04471042
GO:0010101	post-embryonic root morphogenesis	0.04697016

Table A.3 Gene ontology enrichment analysis of sample GA_INJ_24h

ID	Description	FDR
GO:0016144	S-glycoside biosynthetic process	2.35E-09
GO:0019758	glycosinolate biosynthetic process	2.35E-09
GO:0019761	glucosinolate biosynthetic process	2.35E-09
GO:0044550	secondary metabolite biosynthetic process	1.52E-08
GO:1901659	glycosyl compound biosynthetic process	4.01E-08
GO:0001101	response to acid chemical	6.58E-07
GO:0009651	response to salt stress	9.40E-07
GO:0009414	response to water deprivation	1.36E-06
GO:0009415	response to water	2.58E-06
GO:0019748	secondary metabolic process	3.72E-06
GO:0016143	S-glycoside metabolic process	4.13E-06
GO:0019757	glycosinolate metabolic process	4.13E-06
GO:0019760	glucosinolate metabolic process	4.13E-06
GO:0044272	sulfur compound biosynthetic process	4.13E-06
GO:0007623	circadian rhythm	5.44E-06
GO:0048511	rhythmic process	5.44E-06
GO:0009639	response to red or far red light	1.49E-05
GO:0006790	sulfur compound metabolic process	1.57E-05
GO:0009409	response to cold	2.20E-05
GO:0048580	regulation of post-embryonic development	7.85E-05
GO:0044262	cellular carbohydrate metabolic process	7.92E-05
GO:0009408	response to heat	0.0001151
GO:0042752	regulation of circadian rhythm	0.00013895
GO:2000026	regulation of multicellular organismal development	0.00016477
GO:0009640	photomorphogenesis	0.00022743
GO:1901657	glycosyl compound metabolic process	0.00051999
GO:0009637	response to blue light	0.00061922
GO:0051239	regulation of multicellular organismal process	0.00078856
GO:0009746	response to hexose	0.00078856
GO:0034284	response to monosaccharide	0.00140955
GO:0005977	glycogen metabolic process	0.00149627
GO:0006112	energy reserve metabolic process	0.00149627
GO:0009749	response to glucose	0.00159849
GO:0000103	sulfate assimilation	0.00229974
GO:0016126	sterol biosynthetic process	0.00386916
GO:0010118	stomatal movement	0.00458668
GO:0010439	regulation of glucosinolate biosynthetic process	0.00504218
GO:0009648	photoperiodism	0.00527943

GO:1901137	carbohydrate derivative biosynthetic process	0.0055297
GO:0006979	response to oxidative stress	0.00571157
GO:0071483	cellular response to blue light	0.0059126
GO:2000030	regulation of response to red or far red light	0.00689409
GO:0007602	phototransduction	0.00696147
GO:0009585	red, far-red light phototransduction	0.00696147
GO:0009808	lignin metabolic process	0.00748467
GO:0042538	hyperosmotic salinity response	0.00960188
GO:0009583	detection of light stimulus	0.01162503
GO:0052386	cell wall thickening	0.0128054
GO:0016125	sterol metabolic process	0.01280882
GO:0048573	photoperiodism, flowering	0.01280882
GO:0051606	detection of stimulus	0.01314357
GO:0051094	positive regulation of developmental process	0.01338194
GO:0009411	response to UV	0.0174987
GO:0010029	regulation of seed germination	0.02038713
GO:0009743	response to carbohydrate	0.02038713
GO:0034605	cellular response to heat	0.02038713
GO:0009809	lignin biosynthetic process	0.02038713
GO:1901617	organic hydroxy compound biosynthetic process	0.02038713
GO:0016051	carbohydrate biosynthetic process	0.020865
GO:0006006	glucose metabolic process	0.0218669
GO:0010099	regulation of photomorphogenesis	0.02207453
GO:1900140	regulation of seedling development	0.02405364
GO:0006813	potassium ion transport	0.02426196
GO:1901615	organic hydroxy compound metabolic process	0.02443838
GO:0009649	entrainment of circadian clock	0.02485092
GO:0042742	defense response to bacterium	0.02642472
GO:0009636	response to toxic substance	0.02642472
GO:0006972	hyperosmotic response	0.02642472
GO:0055075	potassium ion homeostasis	0.03061815
GO:0052543	callose deposition in cell wall	0.03083521
GO:0051607	defense response to virus	0.03083521
GO:0140546	defense response to symbiont	0.03083521
GO:2000070	regulation of response to water deprivation	0.03083521
GO:0009581	detection of external stimulus	0.03513594
GO:0009582	detection of abiotic stimulus	0.03513594
GO:0098754	detoxification	0.03513594
GO:0044247	cellular polysaccharide catabolic process	0.03525673
GO:0048582	positive regulation of post-embryonic development	0.03673431

GO:0005982	starch metabolic process	0.03894866
GO:0006694	steroid biosynthetic process	0.03963258
GO:0098869	cellular oxidant detoxification	0.03963258
GO:0008202	steroid metabolic process	0.04205863
GO:0019318	hexose metabolic process	0.0454805
GO:0009699	phenylpropanoid biosynthetic process	0.04617294
GO:0010119	regulation of stomatal movement	0.04617294
GO:0051240	positive regulation of multicellular organismal process	0.04617294

Table A.4 Gene ontology enrichment analysis of sample GA_INJ_168h

ID	Description	FDR
GO:0015979	photosynthesis	2.96E-29
GO:0019684	photosynthesis, light reaction	7.46E-21
GO:0007017	microtubule-based process	1.45E-14
GO:0009765	photosynthesis, light harvesting	8.49E-13
GO:0046394	carboxylic acid biosynthetic process	6.53E-12
GO:0006091	generation of precursor metabolites and energy	2.89E-11
GO:0016051	carbohydrate biosynthetic process	6.32E-11
GO:0005976	polysaccharide metabolic process	4.17E-10
GO:0044262	cellular carbohydrate metabolic process	8.57E-10
GO:0000226	microtubule cytoskeleton organization	1.01E-09
GO:0015994	chlorophyll metabolic process	1.02E-09
GO:0009768	photosynthesis, light harvesting in photosystem I	1.59E-09
GO:0006778	porphyrin-containing compound metabolic process	1.87E-08
GO:0007018	microtubule-based movement	1.91E-08
GO:0033013	tetrapyrrole metabolic process	2.45E-08
GO:0007010	cytoskeleton organization	2.78E-08
GO:0044264	cellular polysaccharide metabolic process	9.00E-08
GO:0044550	secondary metabolite biosynthetic process	9.32E-08
GO:0006633	fatty acid biosynthetic process	9.32E-08
GO:0042440	pigment metabolic process	1.42E-07
GO:0006520	cellular amino acid metabolic process	1.74E-07
GO:0009767	photosynthetic electron transport chain	1.74E-07
GO:0015995	chlorophyll biosynthetic process	1.74E-07
GO:0000271	polysaccharide biosynthetic process	2.56E-07
GO:0044272	sulfur compound biosynthetic process	3.66E-07
GO:0006790	sulfur compound metabolic process	3.66E-07
GO:0000910	cytokinesis	4.09E-07
GO:0006631	fatty acid metabolic process	6.24E-07
GO:0016144	S-glycoside biosynthetic process	6.24E-07
GO:0019758	glycosinolate biosynthetic process	6.24E-07
GO:0019761	glucosinolate biosynthetic process	6.24E-07
GO:0009657	plastid organization	6.87E-07
GO:0033014	tetrapyrrole biosynthetic process	7.48E-07
GO:0008652	cellular amino acid biosynthetic process	7.67E-07
GO:0006779	porphyrin-containing compound biosynthetic process	7.67E-07
GO:0032787	monocarboxylic acid metabolic process	1.16E-06
GO:0006073	cellular glucan metabolic process	1.32E-06
GO:0006928	movement of cell or subcellular component	2.33E-06

GO:0009409	response to cold	2.63E-06
GO:1901659	glycosyl compound biosynthetic process	3.59E-06
GO:0045489	pectin biosynthetic process	3.66E-06
GO:0015977	carbon fixation	3.66E-06
GO:0044042	glucan metabolic process	4.01E-06
GO:0019253	reductive pentose-phosphate cycle	4.24E-06
GO:0009651	response to salt stress	4.42E-06
GO:0072330	monocarboxylic acid biosynthetic process	6.61E-06
GO:0071555	cell wall organization	7.33E-06
GO:0046148	pigment biosynthetic process	9.21E-06
GO:1901605	alpha-amino acid metabolic process	1.09E-05
GO:0019685	photosynthesis, dark reaction	1.32E-05
GO:0045488	pectin metabolic process	1.61E-05
GO:0022402	cell cycle process	1.95E-05
GO:0010393	galacturonan metabolic process	1.95E-05
GO:0010109	regulation of photosynthesis	2.66E-05
GO:0019748	secondary metabolic process	2.91E-05
GO:0000911	cytokinesis by cell plate formation	3.22E-05
GO:0034637	cellular carbohydrate biosynthetic process	3.57E-05
GO:0009642	response to light intensity	4.71E-05
GO:0009644	response to high light intensity	5.91E-05
GO:0071669	plant-type cell wall organization or biogenesis	6.19E-05
GO:0045229	external encapsulating structure organization	7.47E-05
GO:1901607	alpha-amino acid biosynthetic process	9.08E-05
GO:0010207	photosystem II assembly	9.08E-05
GO:0042548	regulation of photosynthesis, light reaction	9.08E-05
GO:0009658	chloroplast organization	9.08E-05
GO:0006782	protoporphyrinogen IX biosynthetic process	0.00017197
GO:0046501	protoporphyrinogen IX metabolic process	0.00017197
GO:0042546	cell wall biogenesis	0.00017198
GO:0033692	cellular polysaccharide biosynthetic process	0.00023547
GO:1901137	carbohydrate derivative biosynthetic process	0.00024432
GO:0042592	homeostatic process	0.00027518
GO:0019318	hexose metabolic process	0.00032916
GO:0016143	S-glycoside metabolic process	0.00037737
GO:0019757	glycosinolate metabolic process	0.00037737
GO:0019760	glucosinolate metabolic process	0.00037737
GO:0009664	plant-type cell wall organization	0.0003827
GO:0007051	spindle organization	0.00045934
GO:0043467	regulation of generation of precursor metabolites and energy	0.00047741

GO:1905156	negative regulation of photosynthesis	0.00059096
GO:0032544	plastid translation	0.00068699
GO:0051225	spindle assembly	0.00078625
GO:0009414	response to water deprivation	0.00085216
GO:0001101	response to acid chemical	0.00091765
GO:0009415	response to water	0.00091765
GO:0009914	hormone transport	0.00098483
GO:0060918	auxin transport	0.00119848
GO:0006979	response to oxidative stress	0.00120457
GO:0044036	cell wall macromolecule metabolic process	0.00121616
GO:0006006	glucose metabolic process	0.00121616
GO:0010196	nonphotochemical quenching	0.00128586
GO:1990066	energy quenching	0.00128586
GO:0055086	nucleobase-containing small molecule metabolic process	0.00129428
GO:0009832	plant-type cell wall biogenesis	0.00136624
GO:0000278	mitotic cell cycle	0.0017685
GO:0010383	cell wall polysaccharide metabolic process	0.0017685
GO:0009117	nucleotide metabolic process	0.0017685
GO:0007623	circadian rhythm	0.0017685
GO:0048511	rhythmic process	0.0017685
GO:0009926	auxin polar transport	0.00184604
GO:0006753	nucleoside phosphate metabolic process	0.00199468
GO:0009250	glucan biosynthetic process	0.00264863
GO:0010027	thylakoid membrane organization	0.00268768
GO:0010205	photoinhibition	0.00270279
GO:0043155	negative regulation of photosynthesis, light reaction	0.00270279
GO:0009699	phenylpropanoid biosynthetic process	0.00277179
GO:0003013	circulatory system process	0.00303593
GO:0003018	vascular process in circulatory system	0.00303593
GO:0010232	vascular transport	0.00303593
GO:0010233	phloem transport	0.00303593
GO:0043648	dicarboxylic acid metabolic process	0.00310374
GO:0006972	hyperosmotic response	0.00314977
GO:0042538	hyperosmotic salinity response	0.00319414
GO:1901657	glycosyl compound metabolic process	0.00327649
GO:0090407	organophosphate biosynthetic process	0.0036398
GO:0010118	stomatal movement	0.00401182
GO:0048878	chemical homeostasis	0.00401182
GO:0009069	serine family amino acid metabolic process	0.00401182
GO:0051607	defense response to virus	0.00401182

GO:0140546	defense response to symbiont	0.00401182
GO:0005982	starch metabolic process	0.00401182
GO:0051273	beta-glucan metabolic process	0.00428475
GO:0015849	organic acid transport	0.00439296
GO:0006783	heme biosynthetic process	0.00469191
GO:0009991	response to extracellular stimulus	0.00509073
GO:0006109	regulation of carbohydrate metabolic process	0.00511311
GO:0031667	response to nutrient levels	0.00515153
GO:0019725	cellular homeostasis	0.00523344
GO:0009064	glutamine family amino acid metabolic process	0.00536938
GO:0052546	cell wall pectin metabolic process	0.00546285
GO:0009259	ribonucleotide metabolic process	0.00546285
GO:0019693	ribose phosphate metabolic process	0.00553839
GO:0005996	monosaccharide metabolic process	0.00619611
GO:0071496	cellular response to external stimulus	0.00620454
GO:0006536	glutamate metabolic process	0.00658508
GO:0030091	protein repair	0.00658508
GO:0051274	beta-glucan biosynthetic process	0.00733883
GO:1901259	chloroplast rRNA processing	0.00734499
GO:0009668	plastid membrane organization	0.00748762
GO:0018377	protein myristoylation	0.00751789
GO:0051301	cell division	0.00752864
GO:0009769	photosynthesis, light harvesting in photosystem II	0.00799138
GO:1903047	mitotic cell cycle process	0.00799138
GO:0009698	phenylpropanoid metabolic process	0.00827224
GO:0031668	cellular response to extracellular stimulus	0.00827224
GO:0006820	anion transport	0.00833623
GO:0009070	serine family amino acid biosynthetic process	0.0086144
GO:0043255	regulation of carbohydrate biosynthetic process	0.0086144
GO:0031669	cellular response to nutrient levels	0.00887184
GO:0042168	heme metabolic process	0.00928505
GO:0009808	lignin metabolic process	0.00980462
GO:1901606	alpha-amino acid catabolic process	0.00980462
GO:0010119	regulation of stomatal movement	0.00985098
GO:0022900	electron transport chain	0.00985098
GO:0000281	mitotic cytokinesis	0.00988891
GO:0006566	threonine metabolic process	0.00990196
GO:0010206	photosystem II repair	0.00990196
GO:0006813	potassium ion transport	0.01059741
GO:0046149	pigment catabolic process	0.0106431

GO:0009067	aspartate family amino acid biosynthetic process	0.01077537
GO:0010315	auxin efflux	0.01077537
GO:0052325	cell wall pectin biosynthetic process	0.01077537
GO:0009084	glutamine family amino acid biosynthetic process	0.01111176
GO:0009639	response to red or far red light	0.01125195
GO:0006865	amino acid transport	0.01247232
GO:0006644	phospholipid metabolic process	0.01251707
GO:0003008	system process	0.0125972
GO:0006163	purine nucleotide metabolic process	0.01294157
GO:0009066	aspartate family amino acid metabolic process	0.01328127
GO:0030865	cortical cytoskeleton organization	0.01328127
GO:0031365	N-terminal protein amino acid modification	0.01328127
GO:0006637	acyl-CoA metabolic process	0.01344661
GO:0035383	thioester metabolic process	0.01344661
GO:0009615	response to virus	0.01344661
GO:0009637	response to blue light	0.01356813
GO:0030243	cellulose metabolic process	0.01356813
GO:0072521	purine-containing compound metabolic process	0.01487341
GO:0009809	lignin biosynthetic process	0.01491175
GO:0010675	regulation of cellular carbohydrate metabolic process	0.01491175
GO:0072598	protein localization to chloroplast	0.01491175
GO:0015996	chlorophyll catabolic process	0.0163706
GO:0046942	carboxylic acid transport	0.0165043
GO:0017014	protein nitrosylation	0.01688969
GO:0018119	peptidyl-cysteine S-nitrosylation	0.01688969
GO:0045036	protein targeting to chloroplast	0.01779423
GO:0072596	establishment of protein localization to chloroplast	0.01779423
GO:0019319	hexose biosynthetic process	0.01931663
GO:0009624	response to nematode	0.01931663
GO:0045454	cell redox homeostasis	0.02018637
GO:0009743	response to carbohydrate	0.02117576
GO:0042742	defense response to bacterium	0.021342
GO:1901293	nucleoside phosphate biosynthetic process	0.02146432
GO:0006094	gluconeogenesis	0.02166066
GO:0009150	purine ribonucleotide metabolic process	0.02191928
GO:0009408	response to heat	0.02243246
GO:0016049	cell growth	0.02257047
GO:0042744	hydrogen peroxide catabolic process	0.02257047
GO:0009185	ribonucleoside diphosphate metabolic process	0.02290569
GO:0030244	cellulose biosynthetic process	0.02307132

GO:0035384	thioester biosynthetic process	0.02355375
GO:0071616	acyl-CoA biosynthetic process	0.02355375
GO:0009165	nucleotide biosynthetic process	0.02461827
GO:0006498	N-terminal protein lipidation	0.02467404
GO:0006499	N-terminal protein myristoylation	0.02467404
GO:0046486	glycerolipid metabolic process	0.02484423
GO:0006544	glycine metabolic process	0.02517057
GO:0009773	photosynthetic electron transport in photosystem I	0.02517057
GO:0071365	cellular response to auxin stimulus	0.02519582
GO:0009833	plant-type primary cell wall biogenesis	0.02519582
GO:0055081	anion homeostasis	0.02519582
GO:0010439	regulation of glucosinolate biosynthetic process	0.02522692
GO:0043094	cellular metabolic compound salvage	0.02548038
GO:0006085	acetyl-CoA biosynthetic process	0.02548038
GO:0009089	lysine biosynthetic process via diaminopimelate	0.02548038
GO:0046451	diaminopimelate metabolic process	0.02548038
GO:0009063	cellular amino acid catabolic process	0.02778768
GO:0006787	porphyrin-containing compound catabolic process	0.02862749
GO:0033015	tetrapyrrole catabolic process	0.02862749
GO:0006650	glycerophospholipid metabolic process	0.03070526
GO:0030001	metal ion transport	0.03091381
GO:0042743	hydrogen peroxide metabolic process	0.03157895
GO:0072593	reactive oxygen species metabolic process	0.03186278
GO:0006066	alcohol metabolic process	0.03191571
GO:1901615	organic hydroxy compound metabolic process	0.03293044
GO:0009825	multidimensional cell growth	0.03402445
GO:0016311	dephosphorylation	0.03482585
GO:0010817	regulation of hormone levels	0.03615263
GO:0031324	negative regulation of cellular metabolic process	0.03675086
GO:0010167	response to nitrate	0.03725109
GO:0042335	cuticle development	0.03725109
GO:0098657	import into cell	0.03725109
GO:0061640	cytoskeleton-dependent cytokinesis	0.037853
GO:0006084	acetyl-CoA metabolic process	0.03867176
GO:0006636	unsaturated fatty acid biosynthetic process	0.03867176
GO:0006541	glutamine metabolic process	0.03917894
GO:1905392	plant organ morphogenesis	0.03917894
GO:0009088	threonine biosynthetic process	0.03917894
GO:0015976	carbon utilization	0.03917894
GO:0009260	ribonucleotide biosynthetic process	0.03917894

GO:0010087	phloem or xylem histogenesis	0.03917894
GO:0010189	vitamin E biosynthetic process	0.04014975
GO:0042360	vitamin E metabolic process	0.04014975
GO:0019252	starch biosynthetic process	0.04140436
GO:0046390	ribose phosphate biosynthetic process	0.0418159
GO:0010102	lateral root morphogenesis	0.0421795
GO:0045037	protein import into chloroplast stroma	0.04251778
GO:1901401	regulation of tetrapyrrole metabolic process	0.04251778
GO:0000103	sulfate assimilation	0.04274135
GO:0006775	fat-soluble vitamin metabolic process	0.04274135
GO:0010020	chloroplast fission	0.04274135
GO:0042362	fat-soluble vitamin biosynthetic process	0.04274135
GO:0043572	plastid fission	0.04274135
GO:0048509	regulation of meristem development	0.04306018
GO:0010101	post-embryonic root morphogenesis	0.0490168
GO:0009645	response to low light intensity stimulus	0.04968914
GO:0033559	unsaturated fatty acid metabolic process	0.04991711

Table A.5 Gene ontology enrichment analysis of sample Mock_INJ_24h

ID	Description	FDR
GO:0019748	secondary metabolic process	9.41E-14
GO:0044550	secondary metabolite biosynthetic process	1.59E-12
GO:0006790	sulfur compound metabolic process	2.14E-09
GO:0009698	phenylpropanoid metabolic process	2.20E-07
GO:0009636	response to toxic substance	1.76E-06
GO:0009699	phenylpropanoid biosynthetic process	1.78E-06
GO:0050832	defense response to fungus	3.96E-06
GO:0016144	S-glycoside biosynthetic process	4.09E-06
GO:0019758	glycosinolate biosynthetic process	4.09E-06
GO:0019761	glucosinolate biosynthetic process	4.09E-06
GO:0098754	detoxification	4.09E-06
GO:0044272	sulfur compound biosynthetic process	4.64E-06
GO:0009808	lignin metabolic process	4.64E-06
GO:0009620	response to fungus	5.45E-06
GO:1901659	glycosyl compound biosynthetic process	1.69E-05
GO:0016143	S-glycoside metabolic process	4.35E-05
GO:0019757	glycosinolate metabolic process	4.35E-05
GO:0019760	glucosinolate metabolic process	4.35E-05
GO:0006979	response to oxidative stress	9.83E-05
GO:0009611	response to wounding	0.00021903
GO:0009809	lignin biosynthetic process	0.00044634
GO:1990748	cellular detoxification	0.0008614
GO:0098869	cellular oxidant detoxification	0.0008614
GO:0097237	cellular response to toxic substance	0.0009231
GO:1901657	glycosyl compound metabolic process	0.00218014
GO:0010439	regulation of glucosinolate biosynthetic process	0.00240093
GO:0000103	sulfate assimilation	0.00248796
GO:0016052	carbohydrate catabolic process	0.0057734
GO:0006820	anion transport	0.00792102
GO:1901605	alpha-amino acid metabolic process	0.00945841
GO:0009682	induced systemic resistance	0.01093605
GO:1900376	regulation of secondary metabolite biosynthetic process	0.01093605
GO:0006749	glutathione metabolic process	0.02128764
GO:0006575	cellular modified amino acid metabolic process	0.02547993
GO:0009651	response to salt stress	0.0288401
GO:0009404	toxin metabolic process	0.03156723
GO:0009624	response to nematode	0.0319795
GO:0009819	drought recovery	0.03896756

GO:0015849	organic acid transport	0.04407478
GO:0000272	polysaccharide catabolic process	0.04483077
GO:0009407	toxin catabolic process	0.04687894
GO:1901606	alpha-amino acid catabolic process	0.04779912

Table A.6 Meta-analysis gene ontology

ID	Description	p.adjust	Cluster
GO:0072330	monocarboxylic acid biosynthetic process	0.00450386	C1
GO:0009739	response to gibberellin	0.00450386	C1
GO:0046394	carboxylic acid biosynthetic process	0.03902332	C1
GO:0120254	olefinic compound metabolic process	0.03902332	C1
GO:0032787	monocarboxylic acid metabolic process	0.03902332	C1
GO:0015112	nitrate transmembrane transporter activity	0.0260948	C2
GO:0016762	xyloglucan:xyloglucosyl transferase activity	0.0260948	C2
GO:0046527	glucosyltransferase activity	0.0450581	C2
GO:0009926	auxin polar transport	0.00343591	C3
GO:0060918	auxin transport	0.00343591	C3
GO:0009914	hormone transport	0.00343591	C3
GO:0010817	regulation of hormone levels	0.00343591	C3
GO:0006949	syncytium formation	0.01506204	C3
GO:0009739	response to gibberellin	0.0374185	C3
GO:0140115	export across plasma membrane	0.00336984	C4
GO:0140352	export from cell	0.01555157	C4
GO:0009112	nucleobase metabolic process	0.01832971	C4
GO:0046618	xenobiotic export	0.02011687	C4
GO:1990961	xenobiotic detoxification by transmembrane export across the plasma membrane	0.02011687	C4
GO:0042908	xenobiotic transport	0.02177606	C4
GO:0019748	secondary metabolic process	0.00663156	C5
GO:0044550	secondary metabolite biosynthetic process	0.0098665	C5
GO:0009742	brassinosteroid mediated signaling pathway	0.01983243	C5
GO:0043401	steroid hormone mediated signaling pathway	0.01983243	C5
GO:0048545	response to steroid hormone	0.01983243	C5
GO:0071383	cellular response to steroid hormone stimulus	0.01983243	C5
GO:0042430	indole-containing compound metabolic process	0.01983243	C5
GO:0071367	cellular response to brassinosteroid stimulus	0.01983243	C5
GO:0006790	sulfur compound metabolic process	0.02895525	C5
GO:0009741	response to brassinosteroid	0.02895525	C5
GO:0016143	S-glycoside metabolic process	0.03027216	C5
GO:0019757	glycosinolate metabolic process	0.03027216	C5
GO:0019760	glucosinolate metabolic process	0.03027216	C5
GO:0044272	sulfur compound biosynthetic process	0.04453653	C5
GO:0071407	cellular response to organic cyclic compound	0.04515085	C5
GO:1901657	glycosyl compound metabolic process	0.04515085	C5
GO:0034502	protein localization to chromosome	0.04515085	C5

GO:1990414	replication-born double-strand break repair via sister chromatid exchange	0.04515085	C5
GO:0019953	sexual reproduction	0.04515085	C5
GO:0044703	multi-organism reproductive process	0.04515085	C5
GO:0009554	megasporogenesis	0.04515085	C5
GO:0009684	indoleacetic acid biosynthetic process	0.04515085	C5
GO:0010439	regulation of glucosinolate biosynthetic process	0.04515085	C5
GO:0009683	indoleacetic acid metabolic process	0.04515085	C5
GO:0042436	indole-containing compound catabolic process	0.04515085	C5
GO:0010120	camalexin biosynthetic process	0.04515085	C5
GO:0030308	negative regulation of cell growth	0.04515085	C5
GO:0052317	camalexin metabolic process	0.04515085	C5
GO:0009403	toxin biosynthetic process	0.04515085	C5
GO:0009700	indole phytoalexin biosynthetic process	0.04515085	C5
GO:0046217	indole phytoalexin metabolic process	0.04515085	C5
GO:0052314	phytoalexin metabolic process	0.04515085	C5
GO:0052315	phytoalexin biosynthetic process	0.04515085	C5
GO:0040008	regulation of growth	0.04515085	C5
GO:0009310	amine catabolic process	0.04515085	C5
GO:0042402	cellular biogenic amine catabolic process	0.04515085	C5
GO:0052544	defense response by callose deposition in cell wall	0.04515085	C5
GO:0052482	defense response by cell wall thickening	0.0466986	C5
GO:0042343	indole glucosinolate metabolic process	0.04816563	C5
GO:1900457	regulation of brassinosteroid mediated signaling pathway	0.04955801	C5